INFORMATION TO USERS

This manuscript has been reproduced from the microfilm master. UMI films the text directly from the original or copy submitted. Thus, some thesis and dissertation copies are in typewriter face, while others may be from any type of computer printer.

The quality of this reproduction is dependent upon the quality of the copy submitted. Broken or indistinct print, colored or poor quality illustrations and photographs, print bleedthrough, substandard margins, and improper alignment can adversely affect reproduction.

In the unlikely event that the author did not send UMI a complete manuscript and there are missing pages, these will be noted. Also, if unauthorized copyright material had to be removed, a note will indicate the deletion.

Oversize materials (e.g., maps, drawings, charts) are reproduced by sectioning the original, beginning at the upper left-hand corner and continuing from left to right in equal sections with small overlaps. Each original is also photographed in one exposure and is included in reduced form at the back of the book.

Photographs included in the original manuscript have been reproduced xerographically in this copy. Higher quality 6" x 9" black and white photographic prints are available for any photographs or illustrations appearing in this copy for an additional charge. Contact UMI directly to order.

UMI

A Bell & Howell Information Company
300 North Zeeb Road, Ann Arbor MI 48106-1346 USA
313/761-4700 800/521-0600

Low-temperature Hydrogen-atom Ordering in NaOH in Relation to the Deuterium-induced Phase Transition in NaOD

Paul W. R. Bessonette

Submitted in partial fulfilment of the requirements for the degree of
Doctor of Philosophy in Chemistry
at
Dalhousie University
Halifax, Nova Scotia
February 1998

DALHOUSIE UNIVERSITY

FACULTY OF GRADUATE STUDIES

The undersigned hereby certify that they have read and recommend to the Faculty of Graduate Studies for acceptance a thesis entitled "Low-temperature Hydrogen-atom Ordering in NaOH in Relation to the Deuterium-induced Phase Transition in NaOD"

by Paul W.R. Bessonette

in partial fulfillment of the requirements for the degree of Doctor of Philosophy.

Dated: April 8, 1998

External Examiner

Research Supervisor

Examining Committee

DALHOUSIE UNIVERSITY

Date: February, 1998

AUTHOR: Paul W. R. Bessonette

TITLE: Low-temperature Hydrogen-atom Ordering in NaOH in Relation to the Deuterium-induced Phase Transition in NaOD

DEPARTMENT OR SCHOOL: Department of Chemistry

DEGREE: Ph.D. CONVOCATION: Spring YEAR: 1998

Permission is herewith granted to Dalhousie University to circulate and to have copied for non-commercial purposes, at its discretion, the above title upon the request of individuals or institutions.

Signature of Author

Dedicated to all of my family

and friends

Table of Contents:

List of Figures:

List of Tables:

Abstract:

In many solids, the substitution of deuterium for hydrogen causes a change in the polymorphic phase transition temperature. In more extreme cases, however, the deuterated form of a compound undergoes a low-temperature phase transition which is completely absent in the hydrogenated form. These are called deuterium-induced phase transitions. The research work presented in this thesis was focused on the study of a specific example of a deuterium-induced phase transition. A low-temperature phase transition occurs in sodium deuteroxide (NaOD) at a temperature of 153 K which has no analogue in the hydrogenated form, sodium hydroxide (NaOH), at atmospheric pressure.

To explain the anomalous low-temperature behaviour of NaOH, residual entropy or frozen-in disorder for NaOH was postulated. This postulate was tested extensively, by studying NaOH using the techniques of adiabatic calorimetry and dielectric relaxation to see if NaOH exhibited any evidence indicating a glassy phase transition, which would be associated with frozen-in disorder.

An apparatus was designed and constructed to perform dielectric relaxation measurements on powdered solid samples as a function of temperature and electric field frequency. This apparatus was automated and tested by using it to measure some common ionic salts. No evidence for a glassy phase transition was found in NaOH from the dielectric experiments. Furthermore, calorimetric experiments did not show evidence of unusual relaxation effects that could be attributed to glassy phase behaviour. Therefore, it was concluded that residual entropy does not exist in NaOH.

The dielectric measurements of NaOH did reveal a broad anomaly at $T \sim 170$ K which was interpreted as a prelude, at atmospheric pressure, to a phase transition which would occur in NaOH at higher pressures. Some of the NaOH dielectric results provided evidence for the possible observation of this high-pressure phase in metastable form.

Structural differences between the alkali-metal hydroxides and their corresponding deuterated forms allow the deuterated compounds the potential to form stronger (*i.e.*, shorter) hydrogen bonds due to shorter oxygen-to-oxygen distances in the solid structure. It seems that the slight structural differences between NaOH and NaOD are sufficient to allow a phase transition to occur in NaOD that cannot occur for NaOH.

A comparison of the heat capacities of NaOH and NaOD revealed that NaOH has an anomalously high heat capacity at low temperatures. This indicates that NaOH has exclusive access to energy levels that are not available to NaOD. These levels are likely due to quantum-mechanical tunnelling of the hydrogen atoms in NaOH. Tunnelling would help to prevent a phase transition in NaOH, and the entropy removal due to the thermal depopulation of tunnelling levels would also allow it to have zero entropy at a temperature of absolute zero, in accordance with the third law of thermodynamics.

List of Symbols:

α	coefficient of thermal expansion
α, β, γ	crystallographic angles
α	total polarizability
α	width of guard gap
α_{at}	atomic component of polarizability
α_B	polarizability of species B
α_{cc}	Cole-Cole relaxation time distribution parameter
α_{DC}	Davidson-Cole relaxation time distribution parameter
α_{dip}	dipolar component of polarizability
α_{elec}	electronic component of polarizability
β	Fuoss-Kirkwood relaxation time distribution parameter
β_T	isothermal compressibility
δ	distance between two equilibrium sites for hydrogen
δ	volume fraction of solid in a powder
δ_1, δ_2	volume fractions of heterogeneous dielectric components
ϵ, σ	constants in Lennard-Jones potential; ϵ = well-depth
ϵ	dielectric constant
$\epsilon\epsilon_o$	permittivity of a dielectric
$\bar{\epsilon}$	average dielectric constant of medium around a particle

ϵ_o	permittivity of free space (= 8.8542×10^{-12} F·m^{-1})
ϵ_∞, C, T_0	constants in Curie-Weiss Law equation
ϵ^*	complex dielectric constant
ϵ'	real part of dielectric constant (dielectric constant)
ϵ''	imaginary part of dielectric constant (dielectric loss)
$\epsilon(0)$	limiting low-frequency (static) dielectric constant
$\epsilon(\infty)$	limiting high-frequency dielectric constant
ϵ_1, ϵ_2	bulk dielectric constants of dielectric components
ϵ_{air}	dielectric constant of air (= 1.00054)
ϵ_m	dielectric constant of mixture
ϵ_m''	maximum in dielectric loss curve
ϵ_p	dielectric constant of powder
ϵ_p'	real part of powder dielectric constant
ϵ_p''	imaginary part of powder dielectric constant (loss)
ϵ_s	dielectric constant of bulk solid in powder
ϵ_s'	real part of bulk solid dielectric constant
ϵ_s''	imaginary part of bulk solid dielectric constant (loss)
η	asymmetry parameter
η	density correction factor
θ, ϕ	spherical-coordinate angles
θ	phase angle between current and voltage
Θ_D	Debye temperature

Θ_E	Einstein characteristic temperature
μ	dipole moment
μ	reduced mass
$\overline{\mu}$	average dipole moment per dipole in direction of field
$\overline{\mu}_{avg}$	total average induced dipole moment per molecule
ν	vibrational frequency
ν_D	Debye model cut-off frequency
ρ	density
ρ_{cryst}	crystallographic density
ρ_{macro}	bulk density from macroscopic measurements
ρ_{powder}	density of powder
ρ_R	resistivity
ρ_{solid}	density of bulk solid
σ	conductivity
σ	standard deviation of Gaussian distribution function
τ	relaxation time
τ_{DC}	Davidson-Cole relaxation time
τ_o	average relaxation time parameter
ϕ_1, ϕ_2, ϕ_3, ϕ_4	phase angles of components in Schering bridge
χ	nuclear quadrupole coupling constant
ω	angular frequency
ω_{max}	angular frequency at maximum in dielectric loss curve

ω_{res}	angular frequency at resonance
Ω	total number of quantum states accessible
a, b, c	principal unit-cell axes
(a,b)	(x,y)-coordinates of centre of Cole-Cole plot circle
A	slope of line in geometric isotope effect equation
A	pre-exponential factor in Arrhenius equation
A	area of a capacitor plate
A	constant in Nernst-Lindemann relation
A_D	area of disk electrode
A_R	area of ring electrode
C	capacitance
C	heat capacity
C_{cell}	heat capacity of cell
C_D	disk capacitance
C_o	capacitance in a vacuum
C_p	heat capacity at constant pressure
C_p'	smooth-curve heat capacity
$(C_p)_{ApT}$	heat capacity contribution from Apiezon T grease
$(C_p)_{ind}$	heat capacity contribution from indium seal
$C_{p,m}$	molar heat capacity
$(C_p)_{sample}$	heat capacity of the sample
$(C_p)_{tot}$	total heat capacity

$(C_p)_{vessel}$	heat capacity contribution from sample vessel
C_p/T	encraty
ΔC_p	excess heat capacity
$\Delta C_p/T$	excess encraty
C_R	ring capacitance
C_s	capacitance of variable capacitor
C_{sat}	heat capacity at saturated vapour pressure of sample
C_{unk}	unknown capacitance
C_v	heat capacity at constant volume
$C_v(acoustic)$	acoustic-mode contribution to the heat capacity
$C_v(optic)$	optic-mode contribution to the heat capacity
d	distance between capacitor plates
d	degeneracy ratio (excited state/ground state)
dH	infinitesimal change in enthalpy
dq_{rev}	infinitesimal change in reversible heat
dS	infinitesimal entropy change
dU	infinitesimal change in internal energy
D	dissipation factor
DSC	differential scanning calorimetry
DTA	differential thermal analysis
e	electronic charge (= 1.6022×10^{-19} C)
e	base of natural logarithms (= 2.7182818)

E	electric field
$\|E\|$	magnitude of electric field
E_a	activation energy
E_{loc}	local electric field acting on a molecule
E_o	peak electric field
$\|E_o\|$	magnitude of applied electric field
E_p	intermolecular potential energy
$(E_p)_{avg}$	average intermolecular potential energy
$(E_p)_{rep}$	repulsive potential energy
$E(R)$	electronic ground state energy
ESR	electron spin resonance
$E(t)$	electric field at time t
ΔE	energy difference between two orientations
ΔE_m	most probable value of ΔE in Gaussian distribution
ΔE_{max}	maximum value of ΔE
f	frequency
F	force
$g(\Delta E)$	Gaussian distribution function
G	Gibbs energy
h	Planck's constant (= 6.6261×10^{-34} J·s)
H	enthalpy
H_o	absolute enthalpy at a temperature of absolute zero

$\Delta_{fus}H$	enthalpy of fusion
$\Delta_{trs}H$	enthalpy change during a phase transition
I	nuclear spin quantum number
$\|I\|$	magnitude of current
I_A	ionization energy of species A
I_c	current charging capacitor
$\|I_c\|$	magnitude of charging current
I_l	loss current
I_o	peak current
I_T	total current
j	square root of (-1)
k_B	Boltzmann constant (= 1.3807×10^{-23} J·K^{-1})
k_f	vibrational force constant
k_T	rate constant for reorientation at temperature T
ln	natural logarithm (base e)
L	inductance
m	mass
m	slope of straight line
m_{air}	mass of air in powder
m_{cell}	mass of cell
m_{solid}	mass of solid particles in the powder
n	number of moles of sample

N_1	number of molecules in lower energy orientation
N_2	number of molecules in higher energy orientation
NMR	nuclear magnetic resonance
NQR	nuclear quadrupole resonance
N_v	number of molecules per unit volume
P	pressure
P	polarization of dielectric
P	power
PRT	platinum resistance thermometer
ΔP	difference in power
q	heat
q_p	heat at constant pressure
q_v	heat at constant volume
Q	charge on a capacitor plate
r	true radius of circular electrode
r	radius of circle describing Cole-Cole plot
r_{eff}	effective radius of circular electrode
R	intermolecular distance
R	gas constant (= 8.3145 $J \cdot K^{-1} \cdot mol^{-1}$)
R	resistance
R_0	critical value of R_∞
R_1, R_2, R_3, R_4	resistances in the arms of a Wheatstone bridge

R_1, R_2	resistances of two components of heterogeneous dielectric
R_{heater}	resistance of cell heater
R_{oo}	distance between two oxygen atoms forming hydrogen bond
S	entropy
$S(cal)$	calorimetric entropy
$S(eq)$	entropy determined from equilibrium measurements
S_m	entropy per mole of particles
S_o	entropy at a temperature of absolute zero
$S(res)$	residual entropy
$S(spec)$	entropy determined from spectroscopic data
ΔS_{excess}	excess entropy
$\Delta_{trs}S$	entropy change during a phase transition
t	time
$tan\delta$	loss tangent
T	absolute temperature (*i.e.*, in kelvin)
T_1	spin-lattice relaxation time
T_{avg}	average temperature
T_c	transition temperature
T_f	temperature after the heat pulse
T_{fus}	melting temperature
T_g	glassy phase transition temperature
T_i	temperature before the heat pulse

T_{max}	temperature at which ΔE_{max} occurs
T_{onset}	onset temperature
T_{ref}	temperature of the reference
T_{sample}	temperature of the sample
T_{trs}	temperature of phase transition
ΔT	temperature difference
u, v	segments used to determine τ_o from Cole-Cole plot
U	internal energy
$U(R)$	potential energy
V	molar volume
V	potential difference
V	heater voltage
$\|V\|$	magnitude of voltage
$V(\theta)$	angular-dependent intermolecular potential
$V(t)$	voltage at time t
V_o	well-depth of angular-dependent potential
V_o	peak voltage
V_{powder}	total volume of powder
V_{solid}	volume occupied by solid particles in powder
$\Delta_{trs}V$	molar volume change during a phase transition
x	mole fraction of deuterated compound
x_{crit}	critical content of deuterated form of a compound

x_{thresh}	threshold mole fraction of deuterated compound
y_{int}	y-intercept of straight line
Z	number of formula units per unit cell
$\|Z\|$	magnitude of impedance
Z_1, Z_2, Z_3, Z_4	magnitudes of impedances of components in Schering bridge
Z_A	charge on ion A
Z_B	charge on ion B
Z_c	impedance of a capacitor
$\|Z_c\|$	magnitude of capacitor impedance
$\parallel$	parallel
$\perp$	perpendicular

Acknowledgements:

First of all, I gratefully acknowledge the enthusiasm and support of my supervisor, Dr. Mary Anne White. The experience I have gained in her lab over the past years has been both rare and rewarding.

I am extremely grateful to the Natural Sciences and Engineering Research Council of Canada (NSERC) and the Killam Trust for scholarships which enabled me to pursue my Ph.D. degree. I also thank the Faculty of Graduate Studies and the Department of Chemistry at Dalhousie University for providing me with financial support during my graduate studies through a bursary, scholarships, and teaching assistantships.

I could not have completed my research without the expert technical assistance provided by the technical staff in the Department of Chemistry. I am especially indebted to Brian Millier and Chris Wright of the electronics department, and Rick Conrad, Bud Eisener, and Ross Shortt of the machine shop (Chris and Bud are now with the Psychology Department). Any equipment that needed to be built or fixed during my tenure as a graduate student was always taken care of promptly by their skilful hands.

I would also like to thank the members of Dr. Burford's lab for their help in preparing the NaOH samples in the glove box, and Dr. Glen Rockwell for his assistance in running the NMR spectra.

I have been extremely fortunate to have studied in a lab with coworkers (past and present) who were friendly, helpful, and provided a very pleasant atmosphere in which to work. For this, I express my sincere appreciation to Greg Bednarz, Darek Michalski, Shane Harnish, Chris Smith, Liyan Qiu, and Vladimir Murashov.

I also wish to thank many of my fellow graduate students in the chemistry department for their friendship, and for making graduate student life much more enjoyable.

Finally, although the road leading to my Ph.D. degree has been rich and rewarding, there were some occasional bumps along the way. I express my heartfelt thanks to my family and friends from outside the university for their support and encouragement when it was needed the most.

Chapter 1: Introduction to Disorder in Solids

1.1 Introduction to the Solid State

The solid state is a most interesting phase of matter. All substances (except one) exist in solid form at low temperatures. This fact can be looked upon as satisfying the need for substances in equilibrium to attain perfect order at absolute zero as required by the third law of thermodynamics. Only helium remains liquid down to a temperature of absolute zero.[1] Yet, helium needs to rely on the loophole of extreme quantum effects coupled with the weakest-known intermolecular forces to avoid becoming solid. Even helium, though, will transform to the solid state with the application of a moderate amount of pressure (25 atm or greater for the ^{4}He isotope depending on the temperature[2]). Thus, with one exception, the solid state dominates the low-temperature regime and therefore, the properties of substances at low temperatures are governed by the principles describing the solid state.

Even during the early stages of education, it is commonly taught that motional freedom of the molecules in substances decreases amongst the three fundamental phases of matter in the order of gas to liquid to solid. It is true that the molecules (ions) in a solid are usually much more closely packed than in the liquid and vapour phases, and are confined to occupy a relatively small space due to the close proximity of neighbouring molecules (ions). However, this by no means indicates that the solid state is static and rigid. At temperatures above absolute zero, the molecules (ions) acquire thermal energy

which enables them to undergo vibrational motion about their equilibrium positions in the solid lattice. Furthermore, in many substances, partial or full molecular rotation can occur as well as the motion of molecules or parts of molecules among different orientations. Thus, despite the rigid packing of molecular species, the reality of the various forms of motional freedom in the solid state imparts to the solid a definite amount of disorder.

1.2 Intermolecular Potentials

The formation of a solid could not occur without the existence of overall attractive intermolecular forces.[3,4,5,6,7,8,9] Intermolecular forces are typically divided into two groups, *i.e.*, long-range and short-range intermolecular forces. Short-range forces vary strongly with intermolecular distance (R), whereas long-range forces do not vary so strongly with distance. It is common to speak of intermolecular potential energies (E_p) rather than forces (F) when considering intermolecular interactions mathematically. The two are related by

$$F = -\frac{dE_p}{dR}. \tag{1.1}$$

Long-range forces are usually considered within the approximations that the electron clouds of the interacting particles do not significantly overlap, and that the interparticle distance (R) is large when compared with the dimensions of the particle itself. If the

intermolecular potential energy due to a particular long-range interaction results in a lowering of the total potential energy as the distance between interacting species decreases, the interaction is considered to be attractive. Conversely, if the total potential energy increases with decreasing R, the interaction is repulsive.

There are three types of long-range interactions which must be considered. These are the electrostatic interaction, induction interaction, and dispersion interaction. The electrostatic interaction energy is the result of the Coulombic interaction between molecules which have permanent electric moments (ionic charge, dipole moment, quadrupole moment, etc.). The electrostatic potential energy between two charged ions A and B with charges $Z_A e$ and $Z_B e$, respectively, varies as R^{-1} as follows:

$$E_p = \frac{Z_A Z_B e^2}{4\pi\epsilon_o R}, \tag{1.2}$$

where e is the electronic charge, and ϵ_o is the permittivity of free space. In a similar fashion, the ion-dipole interaction energy varies as R^{-2}, the dipole-dipole interaction as R^{-3}, dipole-quadrupole as R^{-4}, quadrupole-quadrupole as R^{-5}, and so on. Except for the charge-charge interaction, the interaction between two particles with electric moments will have an angular-dependence associated with it in addition to the R-dependence. For example, the equation describing the mutual dipole-dipole interaction is

$$E_p = -\frac{\mu_A \mu_B}{4\pi\epsilon_o R^3}(2\cos\theta_A\cos\theta_B - \sin\theta_A\sin\theta_B\cos(\phi_A - \phi_B)), \tag{1.3}$$

where μ_A and μ_B are the dipole moments of interacting particles A and B, respectively, and θ_A, θ_B, ϕ_A, and ϕ_B are spherical-coordinate angles as defined in Figure 1.1. If R is

Figure 1.1. The mutual dipole-dipole electrostatic interaction[6] between dipoles μ_A and μ_B. The angles θ_A, θ_B, ϕ_A, and ϕ_B are spherical-coordinate angles defining the orientation of the two dipoles whose intermolecular distance is R.

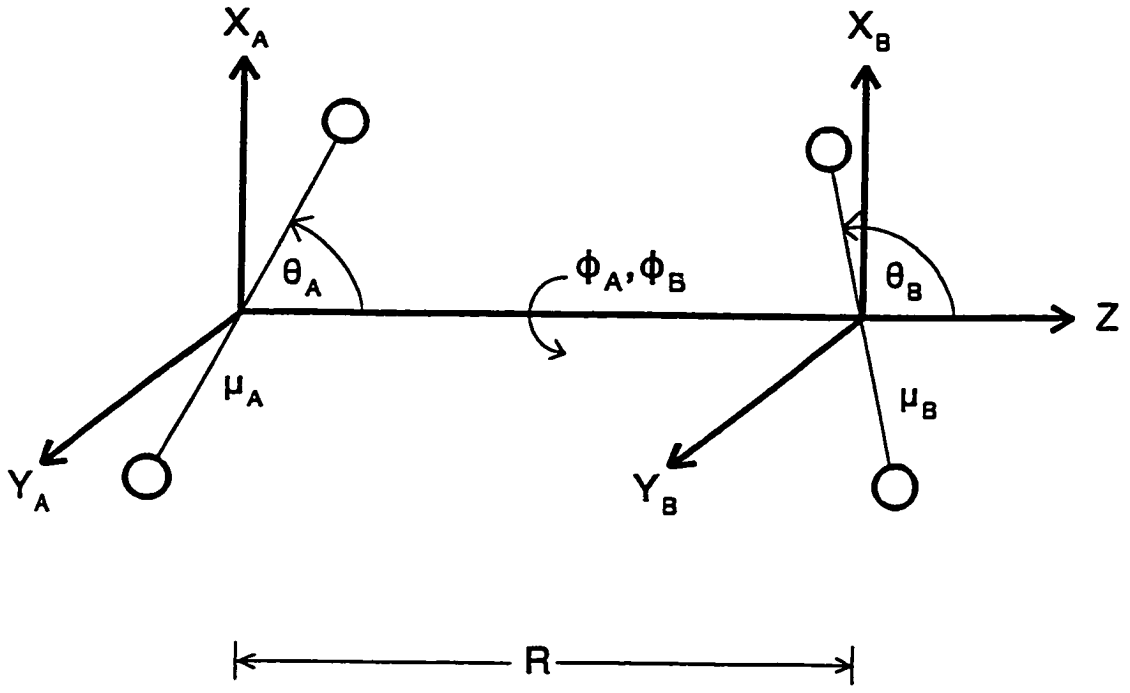

kept fixed and the dipole-dipole interaction energy is averaged over all possible values of the angles θ and ϕ, the following result is obtained:

$$(E_p)_{avg} = -\frac{2\mu_A^2\mu_B^2}{3(4\pi\epsilon_o)^2 k_B T R^6}, \tag{1.4}$$

where T is the absolute temperature, and k_B is the Boltzmann constant. The electrostatic interaction can be attractive or repulsive depending on the charge distributions of the interacting molecular species.

The existence of a permanent electric moment in one molecule can induce a multipole moment in a nearby molecule as shown in Figure 1.2. This is the basis for the induction interaction. For the common case of a permanent point dipole (species A) inducing a dipole moment in a neighbouring neutral molecule (species B), the potential energy of the interaction is given by

$$E_p = -\frac{\mu_A^2\alpha_B(3\cos^2\theta_A + 1)}{2(4\pi\epsilon_o)^2 R^6}, \tag{1.5}$$

where α_B is the polarizability of species B (simply put, a measure of how easily the electron cloud around the molecule can be distorted). Again, this interaction has an angular dependence. Averaging over all possible angles gives the following expression for the average induction potential energy:

$$(E_p)_{avg} = -\frac{\mu_A^2\alpha_B}{(4\pi\epsilon_o)^2 R^6}. \tag{1.6}$$

Since the polarizability α is always a positive quantity, according to equation (1.6) the

Figure 1.2. An example of the long-range induction interaction whereby a permanent dipole in one molecule (left) induces a dipole moment in a nearby neutral molecule (right).

induction energy will always be negative (attractive) which is what would be expected since a dipole would not induce a repulsive dipole in a neighbouring species.

If only the electrostatic and induction interactions existed, there would be no reason for the noble gases to form condensed phases since noble gases are monatomic and thus the interacting particles have no charge or permanent electric moment. However, it is well-established that they do exist as liquids and solids[10] (except helium, which forms only liquid phases at ambient pressure[1]). This occurs entirely as a result of the dispersion interaction. The origin of this interaction arises from the fact that even though the electron distribution around a non-polar species is symmetrical on average, at any given instant the electron distribution can be unsymmetrical which will induce an electric moment in a nearby atom or molecule as shown in Figure 1.3. Thus, the dispersion interaction can be described as the induction of an electric moment in one species due to the instantaneous unsymmetrical charge distribution of a nearby species. The previous two interactions, the electrostatic and induction interactions, were treated in a purely classical sense. However, the dispersion interaction is a purely quantum mechanical effect. London[5] treated the dispersion interaction (which is also known as the London interaction or van der Waals interaction) quantum mechanically in 1930 and arrived at the following expression for the potential energy:

$$E_p = -\frac{3}{2}\frac{I_A I_B}{I_A + I_B}\frac{\alpha_A \alpha_B}{(4\pi\epsilon_o)^2 R^6}, \qquad (1.7)$$

where I_A and I_B are the ionization energies of interacting species A and B, respectively, and α_A and α_B are their corresponding polarizabilities. All of the positive quantities in

Figure 1.3. The long-range dispersion interaction. An instantaneous asymmetry in the electronic charge distribution surrounding one molecular species will induce a dipole moment in a nearby molecule.

equation (1.7) with the negative sign out front assure that the dispersion interaction is a purely attractive one.

The contributions of the three types of long-range interactions to the total potential energy vary depending on the interacting species involved. A list of some representative species along with the contributions of the electrostatic, induction, and dispersion interactions to their total potential energy is provided in Table 1.1[5] for a constant intermolecular distance of 5 Å. Note that only the dispersion interaction contributes to the long-range attractive potential energy for the noble gas atoms. As indicated in Table 1.1, the attractive forces between helium atoms are extremely weak which is responsible for the very low boiling point of helium.[10] For CO with a very small dipole moment of 0.112 D,[11] the electrostatic and induction contributions are very weak with most of the attractive energy being due to the dispersion interaction. For very polar molecules with large dipole moments such as NH_3 and H_2O, the electrostatic interaction becomes more important, although the dispersion interaction continues to play a very significant role.

When two particles are brought closer and closer together, eventually a point will be reached where their electronic charge distributions significantly overlap. Electrostatic repulsion now becomes important, with a corresponding increase in the total potential energy of interaction. The energy of the system will also increase in order to prevent violations to the Pauli Exclusion Principle when the two electron clouds interpenetrate. The point is that short-range interactions between particles are generally repulsive in nature. It is difficult to model short-range interactions in a general manner as was described previously for interactions in the long-range regime. In fact, short-range

Table 1.1. Electrostatic, induction, and dispersion contributions[5] to the total potential energy of some common atoms and molecules for a constant intermolecular separation of 5 Å.

Atom/Molecule	Energy Contributions / J·mol^{-1}		
	Electrostatic	Induction	Dispersion
He	0	0	-4.6
Xe	0	0	-850
CO	-0.012	-0.22	-260
HI	-1.3	-6.5	-1470
HBr	-24	-15.6	-678
HCl	-72	-20.	-405
NH_3	-324	-39	-360
H_2O	-732	-39	-180

interaction calculations are usually determined specifically for the system of interest. It is found, however, that an expression of the form

$$(E_p)_{rep} = \frac{B}{R^{12}}, \tag{1.8}$$

where $(E_p)_{rep}$ is the repulsive potential energy, and B is a constant, satisfactorily represents the short-range repulsive interactions in some cases, especially for the noble gases.[12] Sometimes a decaying exponential term may be used such as

$$(E_p)_{rep} = Ae^{-bR} \tag{1.9}$$

(A and b are constants), depending on the system being studied.

If it is considered that only the dipole-dipole interaction contributes significantly to the electrostatic energy, all of the expressions for the long-range attractive potential energy due to the three types of long-range interactions (equations (1.4), (1.6), and (1.7)) depend on R^{-6}. Thus, both the attractive and repulsive contributions to the total potential energy can be combined into one equation

$$U(R) = \frac{B}{R^{12}} - \frac{A}{R^6} \tag{1.10}$$

($U(R)$ is the potential energy, A and B are constants), which is often written as

$$U(R) = 4\epsilon\left[\left(\frac{\sigma}{R}\right)^{12} - \left(\frac{\sigma}{R}\right)^{6}\right], \tag{1.11}$$

where ϵ and σ are constants. Equation (1.11) is the well-known Lennard-Jones potential, a representative plot of which is shown in Figure 1.4. The Lennard-Jones potential is

Figure 1.4. A plot of a typical Lennard-Jones potential using the best-fit parameters for argon,[12] *i.e.*, $\epsilon = 1006$ J·mol^{-1} and $\sigma = 3.40$ Å.

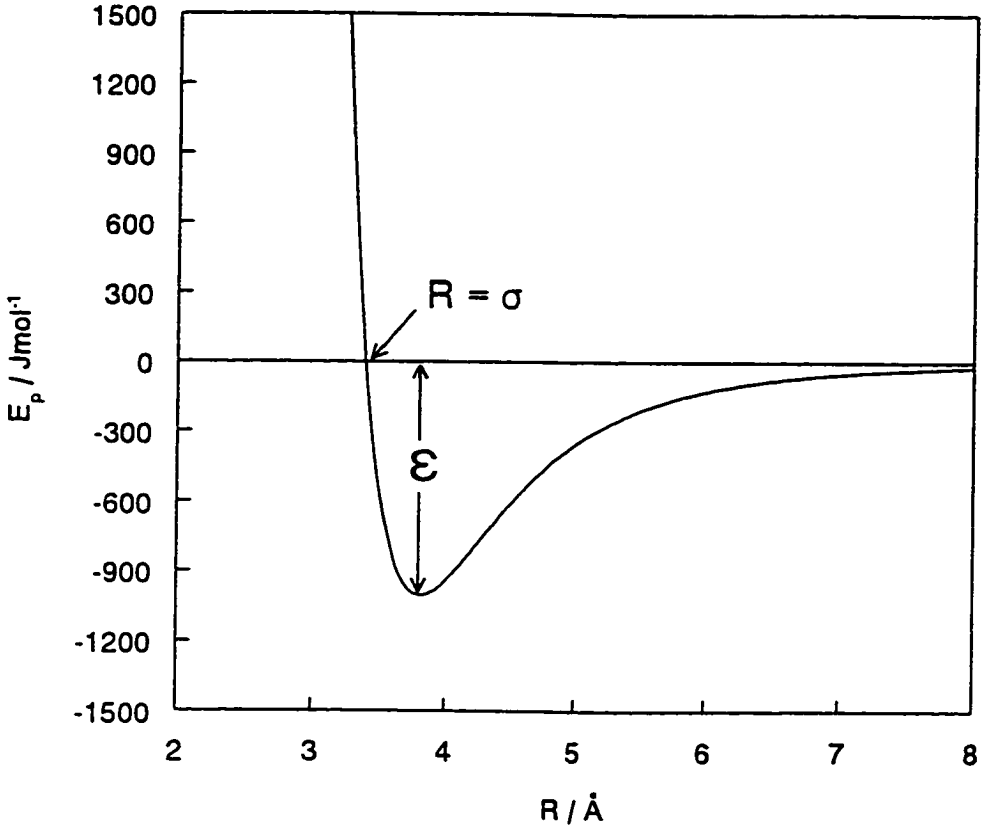

commonly used to describe spherical non-polar molecules. The equilibrium distance between the two interacting particles occurs at the minimum in the potential energy curve which corresponds to $R = 2^{1/6} \times \sigma$. The potential energy curve crosses the R-axis ($U(R) = 0$) at $R = \sigma$, and the well-depth at the equilibrium distance is equal to ϵ.

To treat the potential energy between polar species, a popular equation to use is the Stockmayer potential:

$$U(R,\theta_A,\theta_B,\phi_A,\phi_B) = 4\epsilon\left[\left[\frac{\sigma}{R}\right]^{12} - \left[\frac{\sigma}{R}\right]^{6}\right] - \frac{\mu_A\mu_B}{4\pi\epsilon_o R^3} g(\theta_A,\theta_B,\phi_A,\phi_B). \qquad (1.12)$$

where the function $g(\theta_A, \theta_B, \phi_A, \phi_B)$ is the angular-dependent part of equation (1.3). This equation is simply the Lennard-Jones potential with an added angular-dependent term to describe the orientation dependence of the interaction between two molecular dipoles.

The general potential describing the interaction between two molecules will consist of two components. One of these is the isotropic or radial-dependent component which depends solely on the distance between the molecular centres of mass (R), and can be described, for example, by the Lennard-Jones potential in Figure 1.4. The strength of this potential is characterized by the well-depth ϵ. The general intermolecular potential will also consist of an anisotropic or angular-dependent contribution which describes the dependence of the potential on the relative orientation of one molecule with respect to another. Such a potential ($V(\theta)$) will be periodic and its magnitude can be characterized by the well-depth V_o as shown in Figure 1.5. The angular-dependent potential will be determined by two angles as was shown in Figure 1.1. Figure 1.5 illustrates the dependence upon the angle θ only.

Figure 1.5. (a) A fixed dipole interacting with a reorienting dipole whose orientation with respect to the first is given by the angle θ. (b) The resulting periodic angular-dependent component of the intermolecular potential due to the interaction in (a). This potential is characterized by the well-depth V_o.

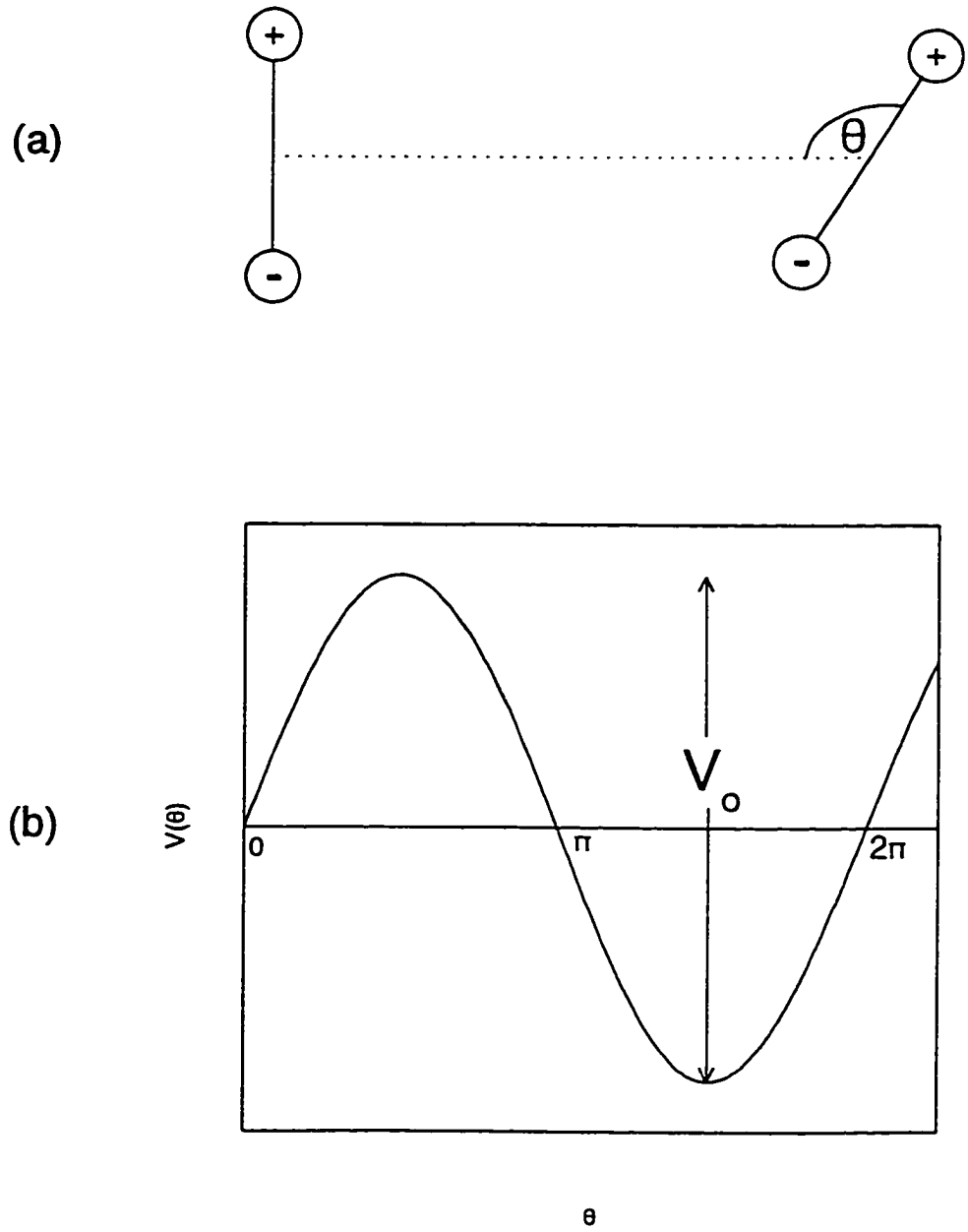

1.3 Types of Disorder in Solids

Comparison of the magnitudes of the radial and angular-dependent components of the intermolecular potential will give some insight into the types of disorder possible in the solid state. If the magnitude of the angular component of the potential is much greater than the magnitude of the radial component ($V_o >> \epsilon$), then the relative orientation of molecules in the solid is more important than their radial distance in determining the intermolecular potential. Such is the case for long rod-shaped molecules which in the solid state will have a fixed orientation (orientational order) but translational disorder may be prominent if there is enough thermal energy available, leading to a liquid crystalline state.

If, on the other hand, the magnitude of the radial component is much greater than that of the angular-dependent part of the intermolecular potential ($\epsilon >> V_o$), then the relative orientation of molecules in the solid is less significant than the distance between molecules in determining the intermolecular potential. This will commonly occur for nearly spherically-shaped molecules. Sufficient thermal energy may lead to partial or free rotation or reorientation of these molecules in the solid state giving an orientationally-disordered crystal (formerly known as a "plastic crystal"[13]).

With any type of reorientational motion there is always an energy barrier that must be overcome in order for the system to switch orientations. In a classical sense, molecules which have enough thermal energy to cross the barrier will be able to reorient. Certain molecules or ions will be able to overcome the barrier quantum mechanically,

especially those whose reorientational motion involves light atoms such as hydrogen or deuterium. These molecules have the extra possibility of going through the barrier rather than going over it. This phenomenon is known as tunnelling.

Disorder in solids can be further broken down into the categories of dynamic disorder and static disorder. Both of these can be distinguished based upon the timescale of observation combined with the rate of reorientation giving rise to the disorder. If the rate of reorientation is such that a molecule reorients many times during the experimental timescale, then the disorder can be described as dynamic. If the opposite is true, that is, molecules are disordered among two or more orientations with negligible reorientation during the experimental timescale, the disorder is referred to as static or frozen-in.

1.4 Polymorphism in Solids

Many substances are found in more than one solid phase. A phase is defined as a collection of particles that is both physically and chemically homogeneous throughout.[14,15] With the suitable manipulation of experimental conditions such as changing the temperature, pressure, or applying an electric field, a concerted reorganization of the molecules or ions in a solid from one solid structure to another can occur corresponding to a new minimum in Gibbs energy. Such a system has undergone a phase transition between two solid phases. When a substance has more than one solid phase, the phenomenon is referred to as polymorphism, and the phase transition between

two different solid phases is known as a polymorphic phase transition.

Many substances exhibit polymorphism. In a typical substance, the solid phase at high temperatures is highly symmetric and disordered in some fashion, but undergoes one or more polymorphic phase transitions as the temperature is lowered to new solid phases which are usually of lower symmetry and are more ordered. By convention, for a solid with more than one solid phase, the high-temperature phase is usually called phase I, and new phases that may form on cooling are labelled phase II, phase III, etc., in order of decreasing temperature.

A prominent example of polymorphism is provided by ice ($H_2O(s)$) which has at least 11 different solid phases[16,17,18,19] upon changing the pressure and temperature. Several of these are shown in the ice phase diagram in Figure 1.6.[16,17,18] For the case of ice, the nomenclature of the different phases is such that the Roman numerals are assigned in order of discovery. In many of the ice polymorphs, the protons are disordered. In fact, the ordinary low-pressure form of ice, hexagonal ice Ih, is especially interesting because it maintains its disorder even down to a temperature of absolute zero.[20,21] This phenomenon will be discussed much more thoroughly in Chapter 4.

1.5 Classifying Phase Transitions

Many attempts have been made at classifying phase transitions of solids.

Figure 1.6. The phase diagram of ice ($H_2O(s)$), styled after references (16), (17), and (18).

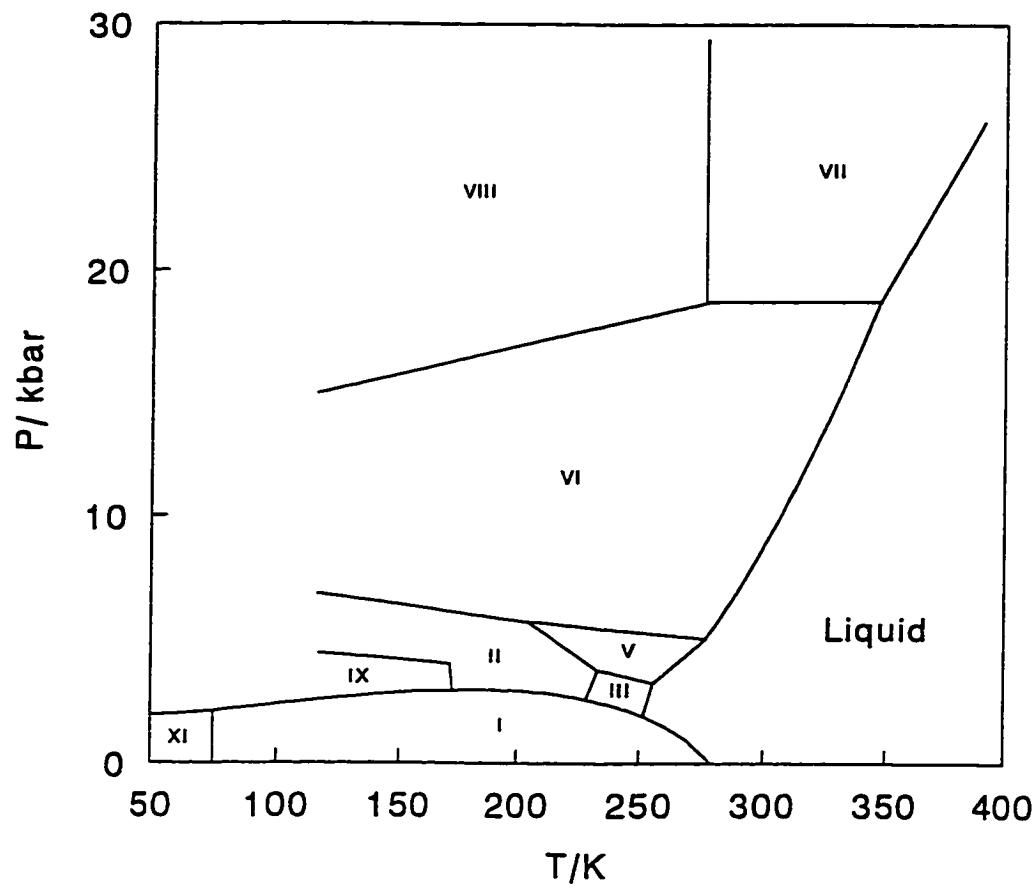

Buerger's classification scheme[22] basically divides phase transitions into two categories: reconstructive and displacive phase transitions. A reconstructive phase transition is one which requires a relatively large amount of energy and involves a major change in the structure of the crystal with bonds being broken and new bonds being formed. An example is the diamond to graphite phase transition in carbon. Displacive phase transitions are generally low-energy, low-entropy phase transitions where bonds are merely distorted rather than broken, with very small changes in structure.[23] An example is the high-low phase transformation that occurs in quartz at a temperature of 843 K.[24]

A useful classification of phase transitions was put forth by Ehrenfest[25] in 1933 based upon the nature of the discontinuity in the Gibbs energy curve for a substance at the phase transition. According to his scheme, a first-order transition is one for which a discontinuity at the transition appears in the first derivatives of the Gibbs energy, given by

$$S = -\left[\frac{\partial G}{\partial T}\right]_P, \tag{1.13}$$

and

$$V = \left[\frac{\partial G}{\partial P}\right]_T, \tag{1.14}$$

where S is the entropy and V is the molar volume. Therefore, such a transition will have an abrupt, finite, non-zero entropy change ($\Delta_{trs}S \neq 0$) and volume change ($\Delta_{trs}V \neq 0$) at the transition temperature. Furthermore, the enthalpy will also exhibit a finite discontinuous change during the transition, since $\Delta_{trs}H = T \times \Delta_{trs}S$. As a consequence

of the discontinuities in S and V, the heat capacity at constant pressure (C_p) and the thermal expansion (α) as defined by

$$C_p = T\left[\frac{\partial S}{\partial T}\right]_p = -T\left[\frac{\partial^2 G}{\partial T^2}\right]_p, \tag{1.15}$$

and

$$\alpha = \frac{1}{V}\left[\frac{\partial V}{\partial T}\right]_p = \frac{1}{V}\left[\frac{\partial}{\partial T}\left[\frac{\partial G}{\partial P}\right]_T\right]_p, \tag{1.16}$$

must go to infinity at the transition temperature. Measurement of the thermal properties of a substance undergoing a first-order phase transition in the heating and cooling directions will reveal hysteresis. A familiar example of a first-order phase transition is melting (solid → liquid transition).

Ehrenfest defined a second-order transition as one for which the first derivatives of the Gibbs energy (S, V) are continuous through the transition, but the second derivatives of G are discontinuous. This means that the entropy change (and thus, the enthalpy change) and the molar volume change will be zero at the transition temperature. However, quantities involving the second derivatives of the Gibbs energy, such as the heat capacity and thermal expansion (equations (1.15) and (1.16)) must show finite jump discontinuities at the phase transition temperature. The anomalous effects associated with a second-order phase transition are observable over a range of temperatures. An illustrative example of a second-order transition is the normal phase to superconducting phase transition in tin.[26]

Third-order and higher-order phase transitions can be defined in a completely

analogous fashion based upon which derivative of the Gibbs energy contains the first discontinuity in *G*. Ehrenfest's classification of phase transitions has been extended and further developed by Pippard.[27]

1.6 Methods for Studying Solid-State Properties

The Ehrenfest phase transition classification system as just described clearly suggests methods which could be used to detect phase transitions in solids, such as the measurement of the heat capacity, enthalpy, entropy, and volume as a function of temperature (or any other thermodynamic variable). A multitude of techniques for this purpose and for the general study of the solid state have been developed over the years,[28,29,30,31] and these methods generally complement each other. A brief survey of the more popular and widely used techniques will now be presented.

Diffraction techniques[32,33] are very important for the determination of the molar volume of the solid. The two common diffraction methods are X-ray diffraction and neutron diffraction, with the principle behind these techniques being the scattering of X-rays or a beam of neutrons by planes of atoms which exist in a solid crystal, and detecting the resulting diffraction pattern. X-rays are scattered by the electrons surrounding the nuclei whereas in neutron diffraction, the nuclei themselves are the scattering centres. These experiments enable the elucidation of the positions of the atoms, the lattice parameters, and the space group symmetry of a particular solid. From this

information, the molar volume is readily obtained. Neutron diffraction has advantages over X-rays in that neutrons penetrate further and are much less energetic than X-rays thereby determining bulk properties while minimizing damage to the sample. Also, neutron scattering is much better for detecting the positions of light atoms (especially hydrogen) which are not adept at scattering X-rays due to their typical lack of electron density. The technique of inelastic neutron scattering can be used to determine such fundamental quantities as the frequencies of normal modes of vibration, phonon dispersion curves, and tunnelling frequencies. The monitoring of the molar volume (V) of a solid as a function of temperature is useful for finding phase transitions (and the order of these transitions) through the observation of kinks or discontinuities in the volume *versus* temperature curve. Furthermore, the slope of such a curve is directly related to the thermal expansion.

The methods which have been developed for the measurement of the thermal expansion of a solid sample are usually grouped under the general heading of dilatometry. The observation of an infinite (very high) or a finite jump in the thermal expansion coefficient provides direct evidence for the occurrence of a first-order or second-order phase transition, respectively. Also, the measurement of the thermal expansion is necessary for the conversion of the experimentally determined heat capacity at constant pressure (C_p) to the more theoretically useful heat capacity under constant volume conditions (C_v). The thermal expansion is commonly determined using diffraction methods (*vide supra*), or by capacitance dilatometry, since the capacitance of a parallel plate capacitor is related to the distance between the plates which can be correlated with

the dimensions of the sample. The latter method is much more sensitive.

Vibrational spectroscopy (infrared spectroscopy, Raman spectroscopy) is principally used to determine the fundamental frequencies of the normal modes of vibration for the internal modes and for the lattice vibrations in solids. Infrared and Raman spectroscopy are used in a complementary fashion as the differing selection rules for the two techniques mean that modes of vibration observable by one method may not be observable by the other. The selection rule for infrared is that the vibration must give rise to a change in the dipole moment. The corresponding restriction for Raman-active vibrations requires that the polarizability must oscillate upon vibration. Measurement of the normal-mode frequencies of solids by vibrational spectroscopy as a function of temperature and/or pressure can probe polymorphic phase transitions as certain vibrational peaks may disappear to be replaced by new peaks in the spectrum as conditions change. These measurements are also useful for analyzing the vibrational contribution to the heat capacity of solids. In addition, vibrational spectroscopy can be used to determine potential barrier heights for internal rotational motion in solids, and also can detect the presence of hydrogen bonding and determine the relative strength of hydrogen bonds in solids.

A popular technique for studying solids is solid-state nuclear magnetic resonance spectroscopy (NMR)[34,35] which is useful for studying nuclei in solids which have a non-zero spin quantum number (I). The nuclear-spin degeneracy of such magnetically active nuclei is lifted upon application of a large magnetic field and, simply put, NMR spectroscopy involves probing the energies of transition between these nuclear spin

energy levels. The NMR spectrum of a solid is dependent upon several interactions. The Zeeman interaction is basically the interaction of the nucleus of interest with the applied magnetic field. Other interactions include the chemical shift interaction, the dipolar interaction, the spin-spin coupling interaction, and the quadrupolar interaction (for nuclei with $I > 1/2$). Many of these interactions are orientation-dependent. For a powdered solid, all possible orientations with the magnetic field will exist and the resulting NMR spectrum will be very broad. However, special techniques such as magic-angle spinning (and others) have been developed which minimize the broadening effects and high resolution NMR spectra of solids can be obtained. The applications of NMR spectroscopy to solids are too numerous to give a thorough survey here, but a few will be mentioned. Each magnetically active nucleus of the same type in a chemically different environment will give rise to a different peak in the NMR spectrum. This is obviously useful for structural information. NMR can also be used to study dynamics of molecules in the solid state through the observation and analysis of narrowing bandwidths or linewidths upon increasing the temperature, and also through the measurement of spin-lattice relaxation times. Information about the site symmetry of a particular nucleus in a solid can also be obtained. Bond lengths in the solid state can be determined through the suitable observation of the powder pattern due to the dipolar interaction. Such a study has been done to measure the two carbon-carbon bond lengths in solid Buckminsterfullerene (C_{60}).[36] Other resonance techniques that are commonly used besides NMR are nuclear quadrupole resonance (NQR) and electron spin resonance (ESR).

Other techniques which are used to study solids include thermal conductivity

measurements, electrical conductivity measurements, calorimetry (heat capacity measurements), and dielectric measurements. The determination of the heat capacity provides direct evidence for phase transitions in solids, and is necessary for the evaluation of the standard thermodynamic properties of a sample as a function of temperature such as the enthalpy, entropy, and Gibbs energy. Dielectric measurements probe the mechanisms of polarization in a sample, and are useful for detecting polymorphic phase transitions as well as the evaluation of kinetic parameters for molecular dynamics in the solid state. These latter two techniques will be discussed and described in much more detail in later chapters, as they are the focus of the research work performed in this thesis.

1.7 Introduction to the Research Objectives

Before embarking on any Ph.D. project in the physical sciences, the scientific problem that is to be the focus of the research should be clearly defined. The next three chapters are designed to do exactly that, and also provide the necessary background information for reasonable understanding of the research problem itself, the experimental results presented in this thesis, and the subsequent discussion of the results.

The major emphasis of this work was directed toward a detailed look at a particular example of a deuterium-induced phase transition involving the compounds NaOH and NaOD. Specifically, a low-temperature polymorphic phase transition occurs

in NaOD which has no analog in NaOH at atmospheric pressure. It was the purpose of this research to gain some insight as to why such an extreme isotope effect is observed for these substances through detailed studies by adiabatic calorimetry and dielectric relaxation.

Several substances are known which show similar deuterium-induced behaviour to NaOH and NaOD, *i.e.*, only the deuterated form exhibits a particular polymorphic phase transition. An examination of the characteristics of these substances along with the explanations that have been put forth in an attempt to explain their anomalous deuterium-induced effects will prove very useful in the understanding of this effect in NaOH and NaOD. A literature survey of the deuterium-induced phase transition phenomenon is provided in the next chapter.

Chapter 2: Deuterium-Induced Phase Transitions

2.1 Introduction

There are many known cases where deuteration causes a change in phase transition temperature. It is well known that ordinary ice ($H_2O(s)$) melts at a temperature of 273.15 K. When the hydrogen atoms in ice are replaced by deuterium, the melting point[37] becomes 276.97 K. A similar effect of deuteration occurs in polymorphic phase transitions as well. For example, the well-studied order/disorder phase transition in ammonium chloride[38] (NH_4Cl) occurs at 242.5 K while the deuterated version of this compound (ND_4Cl) displays an analogous transition[39] at 249.7 K. A more extreme deuteration effect occurs in potassium dihydrogen phosphate (KH_2PO_4, abbreviated KDP) which is ferroelectric. The ferroelectric-paraelectric phase transition in the hydrogenated form of KDP[40] occurs at T = 122 K. When KDP is deuterated, the transition temperature[41] rises to 220 K, an increase of almost 100 K. As should be expected, for all of the cases just described (for many more examples of this phenomenon, see reference (31)), the hydrogen (deuterium) atoms play a very significant role in the phase transition.

Certain substances, however, show a more dramatic effect of deuteration. When these compounds are deuterated, they undergo a low-temperature phase transition which is completely absent in the hydrogenated form. These are appropriately called deuterium-induced phase transitions. There are several known families of compounds which exhibit

this phenomenon; a list of the examples known to date along with their corresponding phase transition temperatures is provided in Table 2.1. Each of these families of compounds will be looked at in more detail in Sections 2.3 - 2.5.

2.2 The Born-Oppenheimer Approximation

In attempting to come up with an explanation for deuterium-induced effects on phase transition temperatures, the first step is to determine the possible ways in which substitution of hydrogen with deuterium could affect the properties of the solid state. The most obvious effect which comes to mind is the increase in mass which occurs on substitution since a deuterium atom has twice the mass of a hydrogen atom. As described in Chapter 1, the intermolecular potential is fundamental to determining the properties in a particular solid. In order to examine whether or not the intermolecular potential would be affected by a change in mass, one has to look to the Born-Oppenheimer approximation.

The Born-Oppenheimer approximation[42,43,44] is a very useful method for simplifying quantum-mechanical considerations and calculations of molecules. In the exact Hamiltonian for a molecular system, the motion of the nuclei and the motion of the electrons are coupled together which results in very complicated equations which must be solved. By invoking the Born-Oppenheimer approximation, the molecular Schrödinger equation is transformed into a much more manageable form.

Table 2.1. Phase transition temperatures for all substances known to show a deuterium-induced phase transition upon substitution of hydrogen with deuterium. These are listed by compound family. Also listed are related members of each family that do not show a deuterium-induced phase transition but, nonetheless, show anomalous deuterium-induced effects. Where available, temperatures obtained by calorimetry are listed; otherwise, dielectric phase transition temperatures are used. See the text for references concerning each individual compound. For a general source, see reference (45).

(a) $M_3H(XO_4)_2$ crystals

M	X = S	
	H	D
K	no	84 K
Rb	no	71 K
	X = Se	
K	20 K	73 K (70% D)
Rb	no	95.4 K
Cs	50 K	180 K

(b) $(NH_4)_2MCl_6$ crystals

M	H	D
Sn	no	no
Pd	no	30.2 K
Pt	no	27.2 K
Pb	no	38.4 K
Te	no	31.9 K, 46.8 K, 48.1 K
Se	24.5 K	48.2 K

Continued...

Table 2.1 (continued).

(c) 9-Hydroxyphenalenone derivatives

	H	D
5-bromo	no	21.5 K, 33.9 K
5-methyl	41 K	44 K

(d) Miscellaneous

Compound	H	D
Tolane	no	313 K
TlH_2PO_4	no	127 K
NaOH	no	153.2 K

The essential principle of the Born-Oppenheimer approximation relies on the fact that because the nuclei are so much more massive than the electrons (by a factor of at least 1840), the electrons will move so much faster than the nuclei that the electrons will be able to instantaneously adapt to a change in nuclear position. Thus the nuclei can be considered to be fixed with respect to the motion of the electrons. With this approximation in place, the total molecular wavefunction can be factored into an electronic wavefunction and a nuclear wavefunction, with the result that the total Schrödinger equation can be separated into two equations, one describing the electrons and one for the nuclei. This effectively decouples the electronic and nuclear motions and allows each to be treated separately.

For the example of a diatomic molecule with internuclear separation R, the Schrödinger equation can be solved using the Born-Oppenheimer approximation as follows. First the electronic equation is solved for several fixed values of R to obtain the electronic ground state energy as a function of the internuclear separation ($E(R)$). The function $E(R)$ becomes the potential in which the nuclear motion occurs (*i.e.*, vibration and rotation). The nuclear equation is then solved using $E(R)$ as the potential energy. The intermolecular potentials described in Chapter 1 are basically determined by the electronic distribution of the molecules (permanent dipoles, induced dipoles, etc.), the energy of which ($E(R)$) is independent of the nuclear mass as long as the Born-Oppenheimer approximation is valid. Thus, the intermolecular potential does not depend on the mass of the nuclei meaning that some other mass-dependent effect is responsible for the changes that occur in the properties of hydrogenated solids *versus* their

corresponding deuterated forms.

One possible mechanism by which deuterium can cause differing solid-state properties as compared to hydrogen is the quantum-mechanical property of tunnelling. Since deuterium has twice the mass of a hydrogen atom, it is a more classical particle than hydrogen and therefore tunnels less efficiently. This was the explanation[46] that was widely accepted for several decades to account for the 100 K increase in transition temperature for deuterated KDP *versus* KDP. In recent years, however, some doubt has been cast on this explanation.[47]

2.3 $M_3H(XO_4)_2$ Family of Crystals

2.3.1 Phase transitions

The $M_3H(XO_4)_2$ group of crystals, where M = NH_4, K, Rb, Cs, and X = S, Se, contains some exclusive members which exhibit deuterium-induced phase transitions as shown in Table 2.1. Interest in this family of compounds began in 1976 when Gesi[48] reported dielectric constant measurements on $(NH_4)_3H(SO_4)_2$. Due to the insertion of the ammonium ion with its high symmetry and extra degrees of freedom available, the possibility of polymorphic phase transitions could be expected for this compound, and this is indeed shown by experiment. Five phases (named phases I-V in order of decreasing temperature) were observed in $(NH_4)_3H(SO_4)_2$ at atmospheric pressure in the

initial measurements by Gesi,[48] with a sixth phase being found in later measurements.[49] All of the phase transitions between these phases showed up as anomalies in the measured dielectric constant (along the c^*-direction of the crystal) as a function of temperature as shown[48] in Figure 2.1. An anomalous broad peak also occurs in the dielectric constant curve at a temperature of approximately -25°C. This peak is too broad to be due to a phase transition. The true nature of this peak was revealed when dielectric constants of this material were measured as a function of applied pressure.[50,51] Upon application of pressure, the anomalous dielectric peak becomes more pronounced until, at a pressure of about 5 kbar, the anomaly splits into two sharp peaks indicating phase transitions with a new phase being stabilized between them. This phase is named phase VI. Further application of pressure resulted in another new phase named phase VII. Both phases VI and VII are ferroelectric as indicated by the observation of the characteristic polarization *vs.* electric field ferroelectric hysteresis loops. The anomaly observed at −25°C at atmospheric pressure is thought to be caused by a fluctuation of electric dipoles that increases and then decreases with decreasing temperature producing the observed hump centred at -25°C without diverging to form the ferroelectric phase that is stabilized only under higher pressures.[51] Phase VII was later found to exist under ambient pressure conditions[49] below about 70 K. The phase transitions in $(NH_4)_3H(SO_4)_2$ have also been studied by heat capacity[52] and thermal expansion[53] measurements. The temperature-pressure phase diagram for $(NH_4)_3H(SO_4)_2$ is shown[49] in Figure 2.2.

When dielectric measurements were carried out on the deuterated form of this compound, vastly different behaviour was observed.[54] At atmospheric pressure, phases

Figure 2.1. Dielectric constant of crystalline $(NH_4)_3H(SO_4)_2$ measured along the c^*-direction as a function of temperature at atmospheric pressure (frequency 100 kHz). Anomalies due to polymorphic phase transitions among the various phases, as well as the broad anomaly centred at -25 °C are the prominent features; from reference (48).

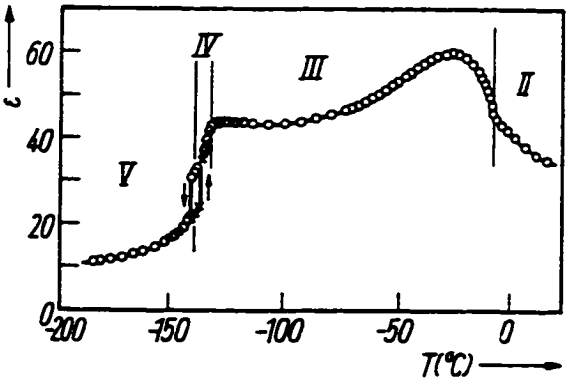

Figure 2.2. Temperature-pressure phase diagram for solid $(NH_4)_3H(SO_4)_2$; styled after reference (49).

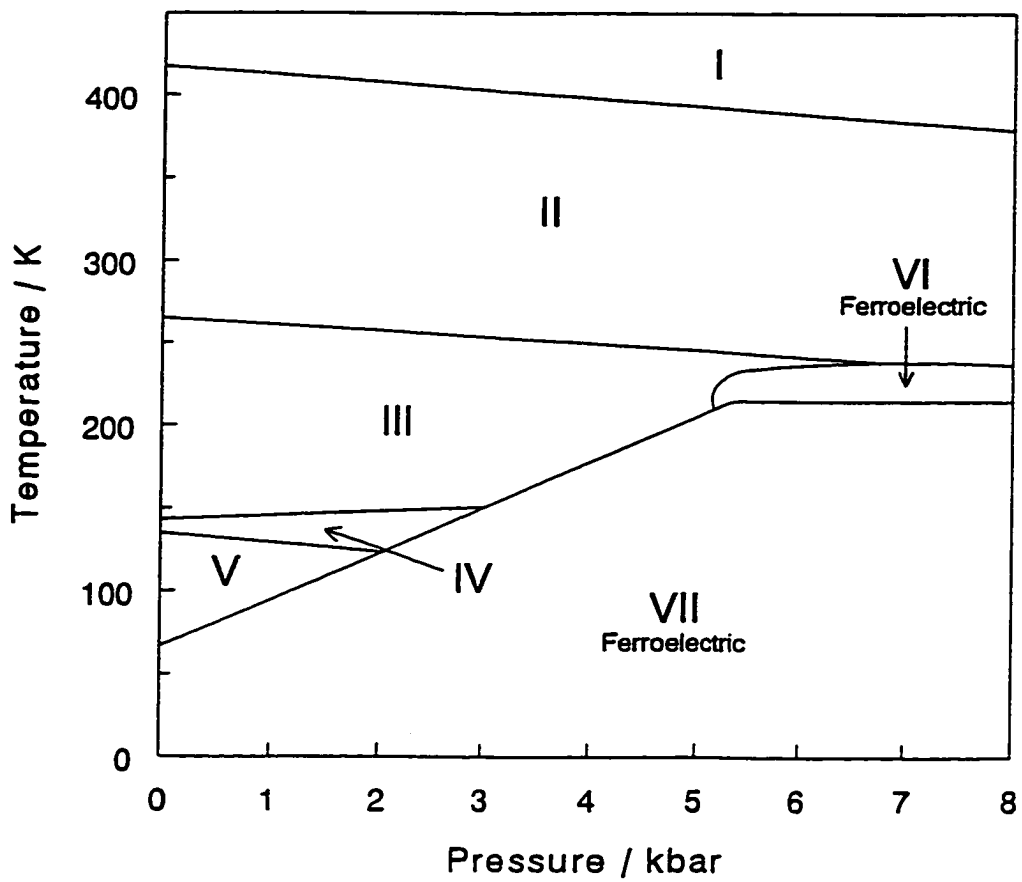

IV and V which were observed in $(NH_4)_3H(SO_4)_2$ were not observed in $(ND_4)_3D(SO_4)_2$. The ferroelectric phases VI and VII, observed in the hydrogenated compound only at high pressures were observed in $(ND_4)_3D(SO_4)_2$ at atmospheric pressure. Dielectric studies were also carried out on the deuterated compound as a function of applied pressure,[54] and also on $\{(NH_4)_3H(SO_4)_2\}_{1-x}\{(ND_4)_3D(SO_4)_2\}_x$ solid solutions[55,56] for several values of x. The temperature-pressure phase diagram for $(ND_4)_3D(SO_4)_2$ is shown[56] in Figure 2.3. It is readily observed that the phase diagram for the deuterated form roughly corresponds to that for $(NH_4)_3H(SO_4)_2$ with an applied pressure of ~ 5 kbar. Thus, for this particular case, deuteration seems to be approximately equivalent to an increase in pressure.

Dielectric[57,58] and dilatometric[59] measurements on the related compound $(NH_4)_3H(SeO_4)_2$ indicate that it also undergoes a number of phase transitions at atmospheric pressure. Five phases were found for $(NH_4)_3H(SeO_4)_2$ above liquid nitrogen temperature (77 K) with the lowest temperature phase (phase V) being ferroelectric. The deuterated version (80% deuteration) of this substance, $(ND_4)_3D(SeO_4)_2$, exhibits the same phase transitions as $(NH_4)_3H(SeO_4)_2$, with the only major difference being that the ferroelectric phase transition temperature occurs 34 K higher in temperature for the deuterated form.[59] A separate dielectric study of a fully deuterated sample found the ferroelectric phase transition to occur 53 K higher than in the hydrogenated form.[60] This again illustrates the important role of the hydrogen (deuterium) atoms in ferroelectric phase transitions. No pressure-induced phase transitions were found for either compound up to about 9 kbar.

Figure 2.3. Temperature-pressure phase diagram for solid $(ND_4)_3D(SO_4)_2$; styled after reference (56).

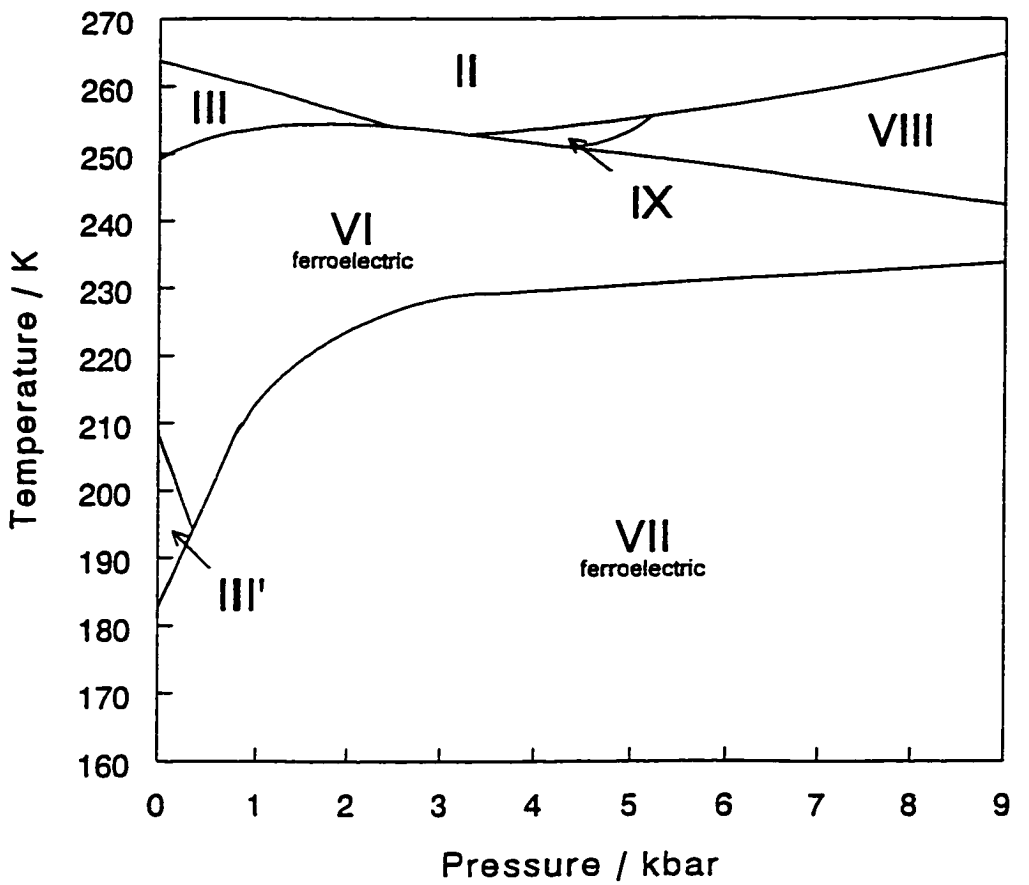

The unusual properties of $(NH_4)_3H(SO_4)_2$ as compared to the deuterated form sparked an interest in the study of the thermal properties of other members of this family of compounds, especially where the ammonium ion is replaced by an alkali-metal cation. The compounds which have been studied to date include $M_3H(SO_4)_2$ where M = K, Rb, and $M_3H(SeO_4)_2$ with M = K, Rb, Cs, as well as their deuterated forms. These substances were initially studied by dielectric measurements,[61,62,63,64] and many of them were later examined by calorimetry.[65,66,67] The compound $Rb_3D(SO_4)_2$ has also been studied by low-temperature ^{87}Rb NMR.[68] The results indicate the occurrence of extreme deuterium-induced effects. All of these compounds undergo a ferroelastic phase transition at high temperatures (above room *T*), but the three compounds $K_3D(SO_4)_2$, $Rb_3D(SO_4)_2$, and $Rb_3D(SeO_4)_2$ all show a low-temperature phase transition in their temperature-dependent dielectric constant curves at 84 K,[61] 71 K,[61] and 95 K,[62] respectively. The interesting point is that the hydrogenated analogues show no low-temperature phase transition at all. As an example, the dielectric constant measurements for $Rb_3H(SeO_4)_2$ and $Rb_3D(SeO_4)_2$ are given[62] in Figure 2.4. The results displayed in this figure clearly show a phase transition in the deuterated form which is noticeably absent in the curve for the H-form. Replacing the hydrogen atoms in $K_3H(SO_4)_2$, $Rb_3H(SO_4)_2$, and $Rb_3H(SeO_4)_2$ with deuterium induces a low-temperature phase transition which does not exist in the H-form. For the other compounds in this family, both the H-form and the D-form display this transition, with the effect of deuteration showing itself as a substantial increase in the transition temperature. The transition occurs in $K_3H(SeO_4)_2$ at a temperature[63] of 20 K with the transition in the deuterated form (70% deuteration)

Figure 2.4. Dielectric constant measured as a function of temperature along the c^*-direction for (a) $Rb_3H(SeO_4)_2$ and (b) $Rb_3D(SeO_4)_2$. All dielectric measurements were taken at a frequency of 1 kHz. A dielectric phase transition is clearly visible in the curve for the deuterated form that is absent in the hydrogenated form; from reference (62).

(a)

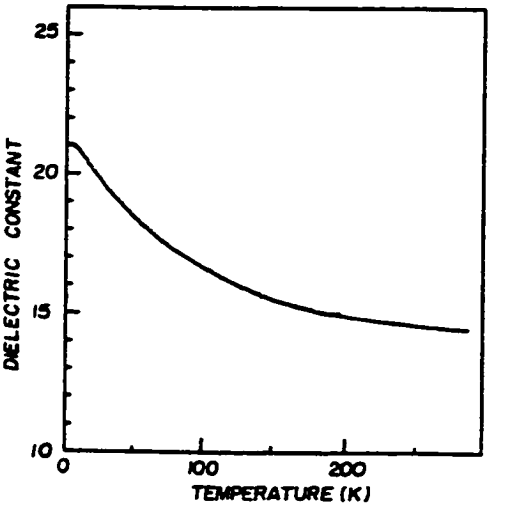

(b)

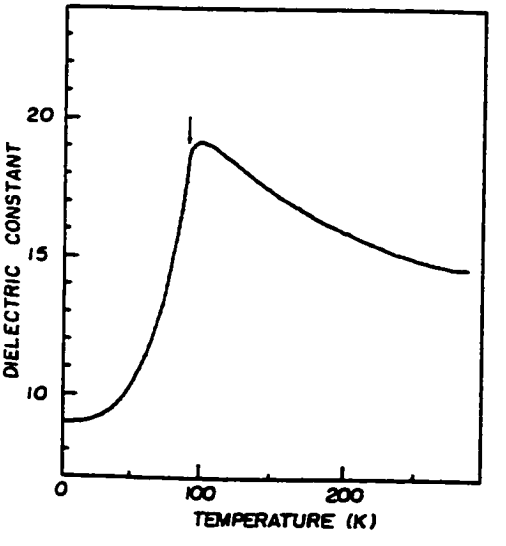

occurring at 73 K. The transition shows up[64] at $T = 50$ K in $Cs_3H(SeO_4)_2$. Deuteration of this compound significantly increases the transition temperature by 130 K to 180 K. These results were summarized in Table 2.1.

For this family, only for $K_3D(SO_4)_2$ has the effect of applied hydrostatic pressure on the phase transition temperature been reported.[69] The transition temperature of $K_3D(SO_4)_2$ was found to increase with pressure at a rate of 8 K / GPa. This is in sharp contrast with other hydrogen-bonded crystals such as KDP which exhibit large, negative pressure coefficients for the transition temperature.[70]

No evidence for ferroelectricity was observed below the transition temperature for any of the compounds that show this transition. Actually, the nature of the anomaly which occurs in the dielectric constant curve is more characteristic of a transition to an antiferroelectric low-temperature phase. Furthermore, when the dielectric constant values are fitted to the standard Curie-Weiss Law,

$$\epsilon = \epsilon_\infty + \frac{C}{T - T_0}, \tag{2.1}$$

where ϵ is the dielectric constant, and ϵ_∞, C, and T_0 are constants, the values for T_0 turn out to be negative, which is also indicative of a transition to an antiferroelectric phase.

Dielectric constant measurements have been performed on hydrogen/deuterium isotopically mixed crystals of the three members of the group which exhibit the deuterium-induced phase transition,[71,72] such as $Rb_3H_{1-x}D_x(SO_4)_2$ for several values of x. In all three cases, the phase transition occurred at intermediate amounts of deuteration above a threshold value of x (x_{thresh}). With $x > x_{thresh}$, decreasing x caused a lowering of

the phase transition temperature until it reached 0 K at an extrapolated value of x_{thresh}. For the $Rb_3H_{1-x}D_x(SO_4)_2$, $K_3H_{1-x}D_x(SO_4)_2$, and $Rb_3H_{1-x}D_x(SeO_4)_2$ isotopically mixed crystals, the threshold values of the mole fraction of the deuterium compound required for the phase transition to occur are x_{thresh} = 0.22, 0.34, and 0.04, respectively.[71,72]

2.3.2 Crystal Structures

Some insight into the cause of the anomalous deuterium-induced behaviour displayed by this family of crystals can be gained through determination of the crystal structures of its members. This has been done for all members by X-ray and/or neutron diffraction. A comparison of the results for all of the compounds shows some striking similarities. All of the compounds,[73,74,75,76,77,78] including $(NH_4)_3H(SO_4)_2$,[79] crystallize in the monoclinic space group *A2/a* (Z = 4) at room temperature, except for $Cs_3H(SeO_4)_2$,[80] which prefers the structurally similar *C2/m* (Z = 2) space group. Between the room-temperature phase and its high-temperature $R\bar{3}m$ phase, however, $Cs_3H(SeO_4)_2$ undergoes a phase transition to an intermediate phase which has the *A2/a* space group.[81] The common *A2/a* structure is shown[82] in Figure 2.5. Some noteworthy features concerning this arrangement are the following. The structure consists of independent dimers made up of two sulfate or selenate tetrahedra that are joined by a hydrogen bond between an oxygen atom of one XO_4^{2-} ion and one of the oxygen atoms of the other XO_4^{2-} ion in the dimer. This is in contrast to the structure of other hydrogen-

Figure 2.5. The common crystal structure (*b*-axis projection) for members of the $M_3(H,D)(XO_4)_2$ family. The space group is *A2/a*. The most notable features in this structure are the isolated hydrogen-bonded XO_4^{2-} dimers; from reference (82).

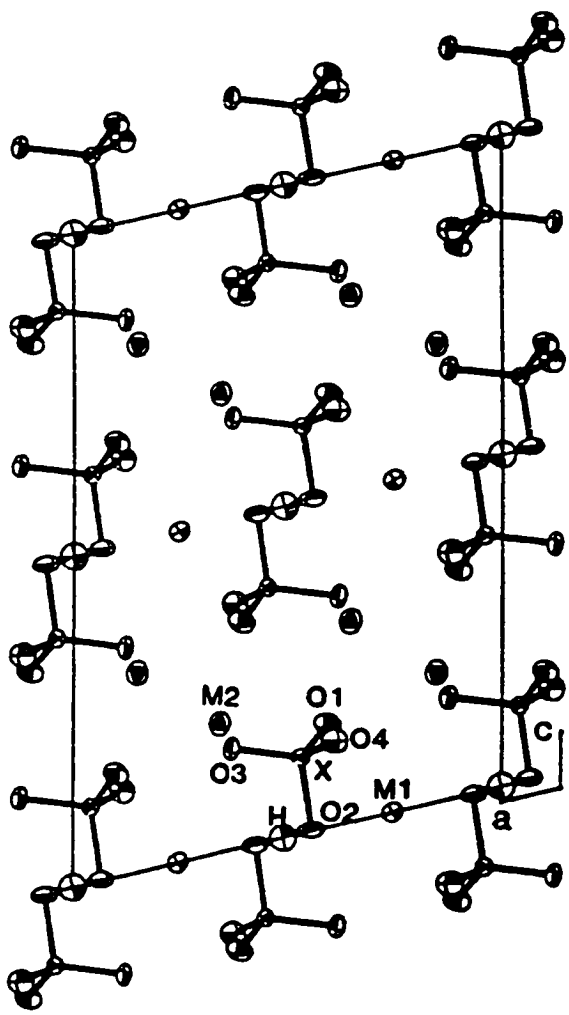

bonded ferroelectric solids such as KDP. In potassium dihydrogen phosphate, the PO_4^{3-} tetrahedra are linked together by an infinite three-dimensional network of hydrogen bonds with the ensuing restriction that the hydrogen atoms in the hydrogen bonds cannot move independently of one another. When one hydrogen atom moves, this has a great effect on the dynamics of other hydrogen atoms since they are all interlinked and must obey the Bernal-Fowler or ice rules.[83,84] Similar restrictions apply to the two-dimensional hydrogen-bonded network of solid squaric acid, and the one-dimensional hydrogen-bonded chains of solids such as cesium dihydrogen phosphate and lead hydrogen phosphate.[82] The hydrogen bonds in the room temperature structure of the $M_3(H,D)(XO_4)_2$ family of crystals have no such limitations since the XO_4^{2-} dimers are not interconnected and thus, the dynamics of the hydrogen (deuterium) atoms are mostly independent of one another. This situation has been dubbed a zero-dimensional hydrogen-bond network.[85] This is considered an advantage to the study of phase transitions in hydrogen-bonded materials because of freedom from the complication of the correlation of the dynamics in the hydrogen bond. To be consistent with the symmetry, the proton must be either located at the centre of symmetry of the hydrogen bond or disordered between two positions surrounding the centre. Evidence points toward the latter interpretation.[78,86,87]

There are two types of cations in the structure. One type of cation occupies a position on a two-fold axis while another type of cation is in a general position. The deuterated versions of these compounds all have the same structure,[86,88,89] the only difference being that the hydrogen atom in the hydrogen-bond making up the dimers is

replaced by a deuterium atom. The *C2/m* structure of $Cs_3H(SeO_4)_2$ and $Cs_3D(SeO_4)_2$[90,91] is similarly composed of isolated hydrogen-bonded dimers but the symmetry of the structure is slightly different.

Crystal structures have been obtained by X-ray diffraction for the low-temperature phases of some of the compounds in this group. The space group of the low-temperature phase of $K_3D(SO_4)_2$ was first reported to be $P2_1/a$ ($Z = 4$),[92] but was later reported as belonging to the *A2* space group ($Z = 16$),[93] while that for $Cs_3D(SeO_4)_2$ is $P2_1/m$ ($Z = 2$).[91] These space groups are compatible with a low-temperature antiferroelectric phase. Surprisingly, the low-temperature phase of $Rb_3D(SeO_4)_2$ was found to belong to space group *A2/a*,[88] the same space group as observed above the transition. Thus, the low-temperature phase transition in this compound is a rare example of a symmetry-invariant transition.

2.3.3 Tunnelling Effect

Due to the extreme isotope effects observed in the low-temperature phase transitions of these solids upon deuteration, it is obvious that the hydrogen (deuterium) atoms are intimately involved in the mechanism of this transition. Two competing explanations have been put forth to explain the isotope effects seen in the low-temperature phase transitions of the $M_3(H,D)(XO_4)_2$ crystals and other hydrogen-bonded solids.

The first of these explanations involves the quantum-mechanical phenomenon of tunnelling. This was first used to account for the isotope effect observed for the phase transition in KDP.[46] Suppose, for example, we have a system in a double-well potential situation with two energy minima and an energy barrier between them as shown in Figure 2.6(a). Classically, a system can only overcome the barrier by acquiring sufficient thermal energy to go over it. However, the minima will contain quantum-mechanical energy levels as indicated in Figure 2.6(b). When probability densities (proportional to the square of the wavefunction) are superimposed over the energy levels, a fundamental consequence of quantum mechanics is revealed. The probability density does not go to zero at the potential barrier. In fact, contrary to classical-mechanical arguments, there is a non-zero probability that a molecular system can be inside the potential barrier. If the barrier is narrow enough, the probability densities on both sides of the barrier will overlap, with the result that there is a non-zero probability that a molecule will go through the barrier. This is the phenomenon known as quantum-mechanical tunnelling, *i.e.*, overcoming a potential barrier by going through it rather than going over it. The tunnelling interaction causes a splitting of the energy levels as shown in Figure 2.6(c), where the magnitude of the splitting depends on the strength of the tunnelling interaction. The energy difference of the split levels can be measured by low-temperature calorimetry, by inelastic neutron scattering, or by suitable NMR measurements.

As indicated in Figure 2.6(b), there will be better probability density overlap, and thus, a system will be more efficient at tunnelling, if its energy levels are higher up in the potential wells. Regardless of whether the double-well potential is describing

Figure 2.6. Diagrams to illustrate the quantum-mechanical tunnelling phenomenon: (a) double-well potential with an associated energy barrier, (b) double-well potential with superimposed energy levels and probability densities, (c) splitting of energy levels due to the tunnelling interaction.

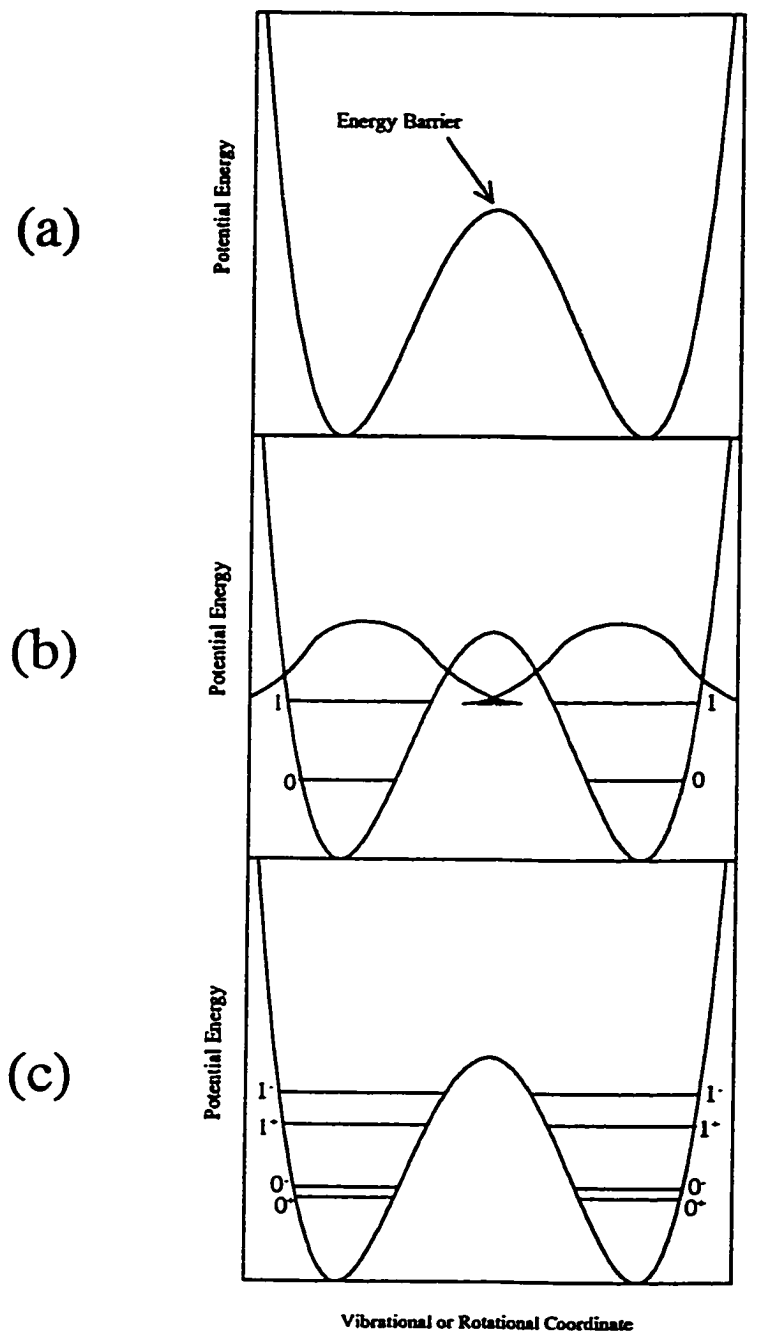

translational, vibrational, or rotational dynamics, the principles of quantum mechanics show that the energies of the quantum levels increase as the mass of the system decreases. Thus, a hydrogen atom with only about half the mass of a deuterium atom will tunnel better than deuterium. Therefore, the tunnelling mechanism satisfies an essential criterion needed to act as a possible explanation for the isotope effects observed in phase transitions: it is mass-dependent.

In the room-temperature *A2/a* phase of the members of the $M_3(H,D)(XO_4)_2$ family of crystals, the hydrogen (deuterium) atoms are dynamically disordered in two positions symmetrically placed about the centre of the hydrogen bond as shown schematically in Figure 2.7. This is a double-well potential situation as just described, with the hydrogen atom switching between a position bonded to one oxygen atom in the hydrogen bond to a position bonded to the other oxygen atom. A consequence of this switching is a reversal of the O-H dipole moment in the hydrogen bond. A hydrogen atom can overcome the barrier in the double-well potential by tunnelling through the barrier. A deuterium atom can tunnel too, but due to its higher mass, it cannot tunnel as effectively as hydrogen. Thus, the motion of the deuterium atom is more classical. The low-temperature phase transition that takes place in hydrogen-bonded solids is due to the electrostatic interactions between dipole moments of neighbouring hydrogen bonds. In a classical sense, as the temperature is lowered, a phase transition should take place when the thermal energy (k_BT) acquired by the molecules is insufficient to overcome the electrostatic interaction between hydrogen bonds. When the transition occurs, it should lead to an ordered low-temperature structure where each hydrogen (deuterium) atom is

Figure 2.7. Dynamic disorder of the protons (deuterons) in two positions about the centre of the hydrogen bond joining two XO_4^{2-} ions.

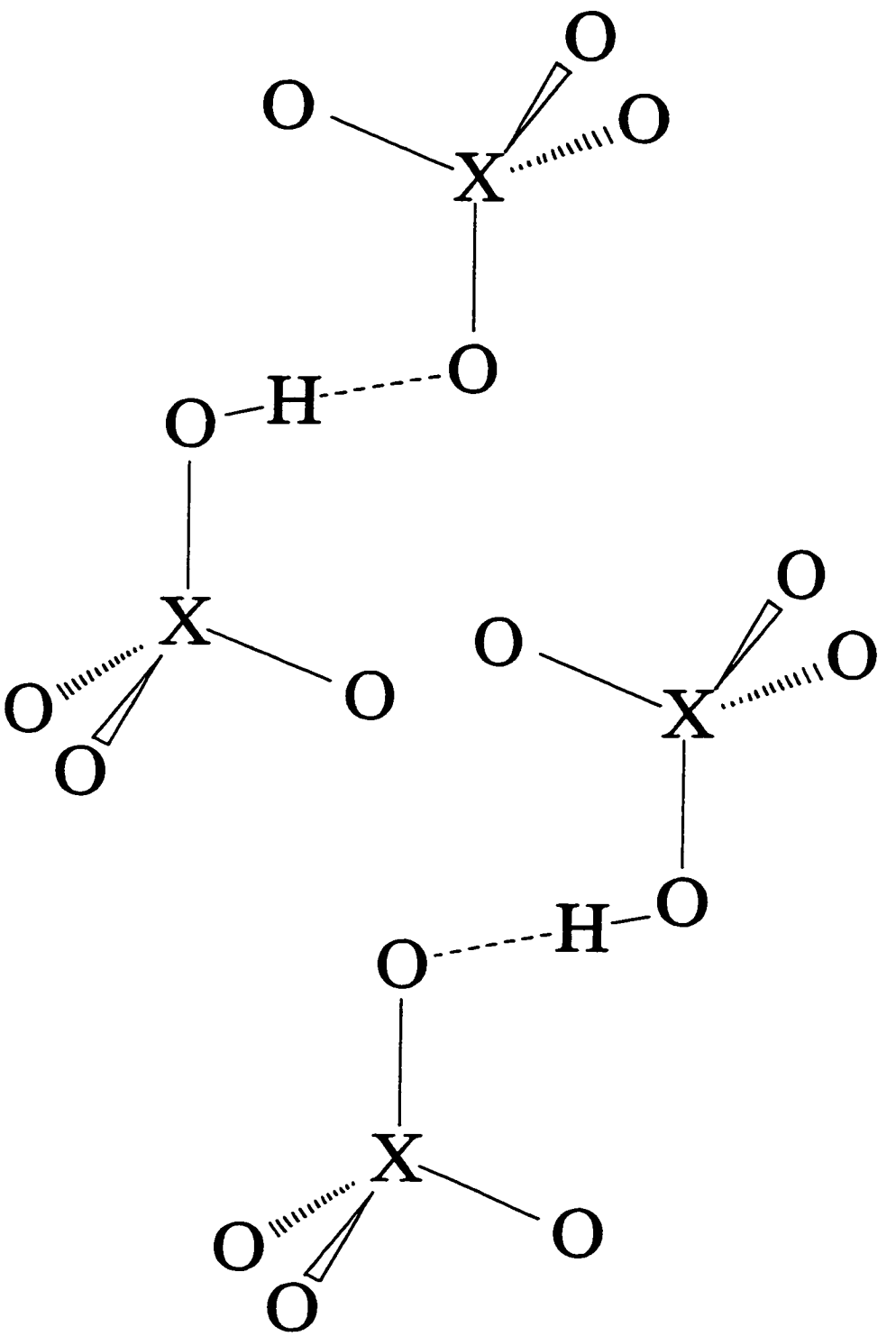

situated in only one well of the double-well potential. This is what happens for the deuterated compounds.

With a hydrogen atom, tunnelling is available as a means to overcome the potential barrier as the probability densities on both sides of the barrier will overlap; the result being that the position of the hydrogen atom between the oxygen atoms becomes "blurred". The effect of this is to reduce the dipole moment of the hydrogen bond with subsequent reduction of the electrostatic interaction between hydrogen bonds, which will hinder the occurrence of the phase transition. This phenomenon is known as quantum paraelectricity.

As can be seen from Figure 2.6, probability distribution function overlap (and therefore tunnelling) decreases as a system moves farther down the potential well. This can be accomplished by decreasing the temperature since when a system is stripped of thermal energy, it no longer has the energy necessary to occupy the high-energy excited levels, and therefore heads toward the lower energy levels. This causes the system to behave more classically and tunnelling is reduced. Thus, the tunnelling argument explains why a phase transition due to ordering of a hydrogen bond occurs at a lower temperature in the hydrogenated form of a compound as compared to the analogous deuterated form. As described earlier, there are extreme cases where the hydrogen compound does not undergo the phase transition at all. This will occur when the electrostatic interaction between neighbouring hydrogen bonds is smaller than the tunnelling splitting associated with the dynamics of the hydrogen atoms,[94] since the tunnelling splitting is a measure of the strength of the tunnelling interaction which opposes the tendency of the

electrostatic interaction to cause a phase transition.

2.3.4 Geometric Isotope Effect

The tunnelling argument was long accepted as a reasonable explanation for isotope effects observed in hydrogen-bonded crystals like KDP. In the last two decades, however, a second competing argument has emerged known as the geometric isotope effect,[82] which was first introduced by Ichikawa.[95,96] The argument is based on an empirical correlation that was found to exist between the transition temperature (T_c) and the hydrogen-bond length (measured at the transition temperature), which is defined in this model as the distance between the two oxygen atoms forming the hydrogen bond (R_{OO}). A similar relationship was also found to exist between the transition temperature and the distance between the two equilibrium sites (δ) for the hydrogen atom in a symmetric hydrogen bond. These correlations were based upon known transition temperatures for several hydrogen-bonded crystals and their hydrogen-bond lengths determined by X-ray diffraction.

Further development revealed that straight-line relationships exist connecting the transition temperatures with the hydrogen-bond distances for several families of hydrogen-bonded solids as shown in Figure 2.8. The figure indicates a straight line relationship for members of the potassium dihydrogen phosphate[47] family of crystals with a 3-D hydrogen-network, one for the 2-D squaric acid family,[97] the 1-D lead hydrogen

Figure 2.8. Plots of phase transition temperatures (T_c) *vs.* hydrogen-bond distance (R_{OO}, measured near T_c) for various families of hydrogen-bonded crystals. Straight-line relationships are depicted for members of the lead hydrogen phosphate (LHP), cesium dihydrogen phosphate (CDP), squaric acid (H_2SQ), potassium dihydrogen phosphate (KDP), and trimetal hydrogen selenate (TMHSe) families. Also listed with each system is the dimensionality of the hydrogen-bonded network; from reference (82).

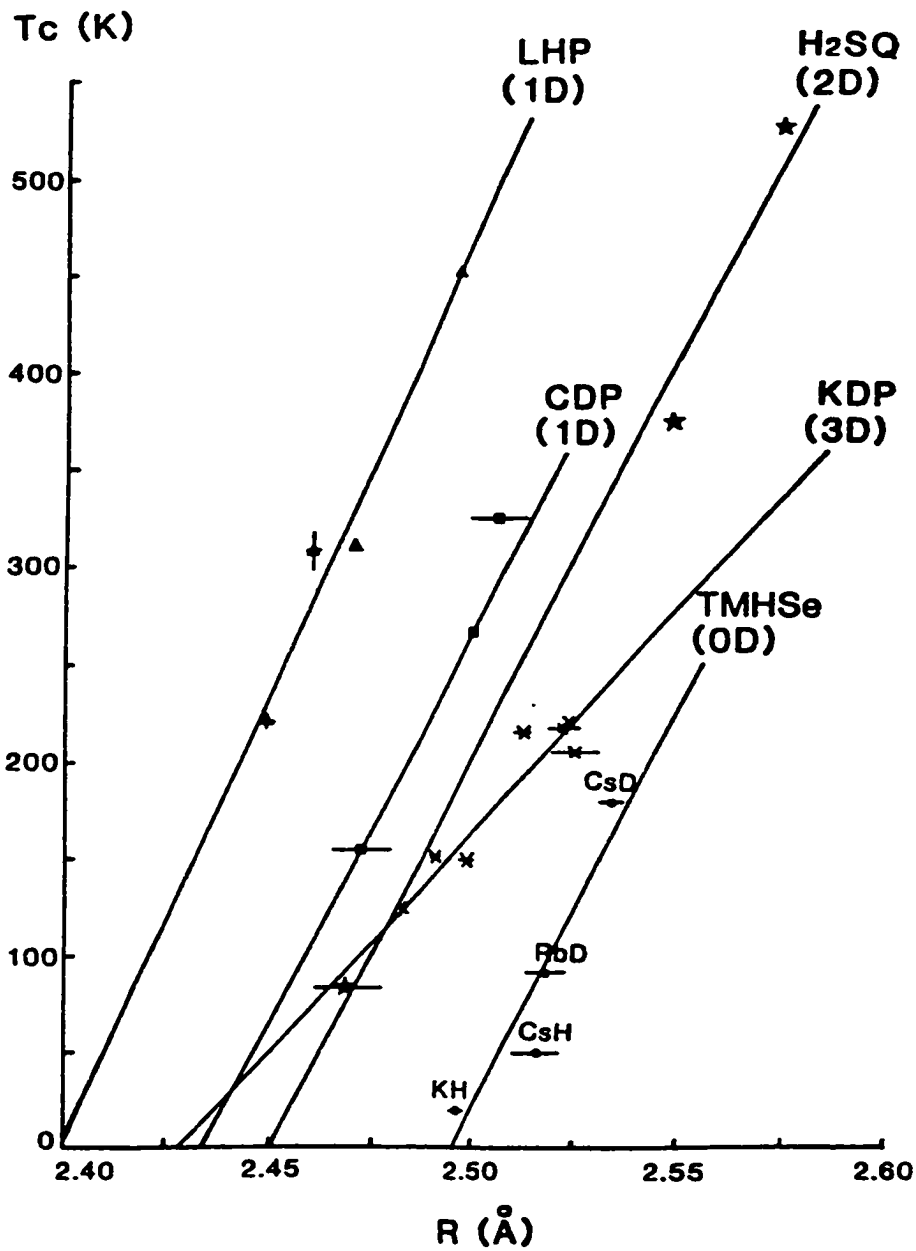

phosphate[98] and cesium dihydrogen phosphate groups,[99] and a linear relationship for the 0-D hydrogen-bonded network of the $M_3(H,D)(SeO_4)_2$ crystals.[100] The raw data for each family were fitted to a linear equation of the form

$$T_c = A(R_{OO} - R_0), \tag{2.2}$$

where A is the slope of the line, and R_0 is the critical value of R_{OO} which causes the phase transition temperature to equal 0 K. For the family of interest here, *i.e.*, the 0-dimensional $M_3(H,D)(SeO_4)_2$ crystals, the obtained parameters[100] for the best fit line are A = 4154 K / Å and R_0 = 2.495 Å. The parameter R_0 has been interpreted[101] as the critical hydrogen-bond distance above which a double-well potential exists for the hydrogen (deuterium) atom in the hydrogen bond, and below which the situation is a single-well potential located in the middle of the two oxygen atoms. This interpretation has been supported by electron-density measurements performed on $K_3H(SO_4)_2$.[87] If the potential is of the single-well type, there is no driving force for the phase transition to occur since there is no orientational disorder associated with the hydrogen atoms.

The data illustrated in Figure 2.8 include experimental values for the hydrogenated forms of the crystals as well as their deuterated forms. The fact that the correlations hold for all members within the same family regardless of whether they are deuterated or not provides evidence against the tunnelling mechanism being involved in the isotope effects observed for these systems. If tunnelling were the key factor in determining the isotope effect, the transition temperatures for the deuterated compounds would be expected to be found above the straight line due to the lower tunnelling probability of deuterium as compared to hydrogen. However, this is not observed.

The geometric isotope effect explains the difference in phase transition temperatures observed between the deuterated and hydrogenated versions of a compound in the following manner. Equation (2.2) gives the relationship between the phase transition temperature (T_c) and the hydrogen-bond length (R_{OO}) measured at the transition temperature. For a compound in this family to have a low-temperature phase transition at a given T_c, it must have the matching hydrogen-bond length at that temperature as given by equation (2.2). Because of thermal contraction, in most hydrogen-bonded substances, the hydrogen-bond length will tend to decrease from its room-temperature value as the temperature is lowered. A typical curve describing this dependence (see, for example, reference (87)) is shown in Figure 2.9(a) where data are presented as temperature *vs.* hydrogen-bond length. The plot has an initial curvature at low temperature, but at higher temperatures, the plot is roughly linear. The average slope of the "linear" portion is usually in the range[87,88,91] 10000 - 15000 K / Å.

When equation (2.2) is superimposed onto the curve in Figure 2.9(a), the result is shown in Figure 2.9(b). According to the geometric isotope effect, a low-temperature phase transition will occur at a given temperature (T_c) if T_c and the hydrogen-bond length at T_c satisfy equation (2.2). Clearly, from Figure 2.9(b), this will be true at the point of intersection of the two curves. Thus, for a given compound in this family of crystals, a phase transition will occur if the curve representing the temperature-dependence of its hydrogen-bond length, and the line described by equation (2.2) intersect.

Consider another situation as described by Figure 2.9(c). In this example, the hydrogen-bond length of the compound is lower at a given temperature when compared

Figure 2.9. Explanation of the geometric isotope effect; (a) a typical curve representing the temperature-dependence of the hydrogen-bond length (R_{oo}), (b) this same curve with the superimposed empirical correlation between transition temperature (T_c) and hydrogen-bond length (measured at T_c); a phase transition will occur where the two curves intersect, (c) an example showing a situation where the two curves do not intersect; in this case, no phase transition will be observed.

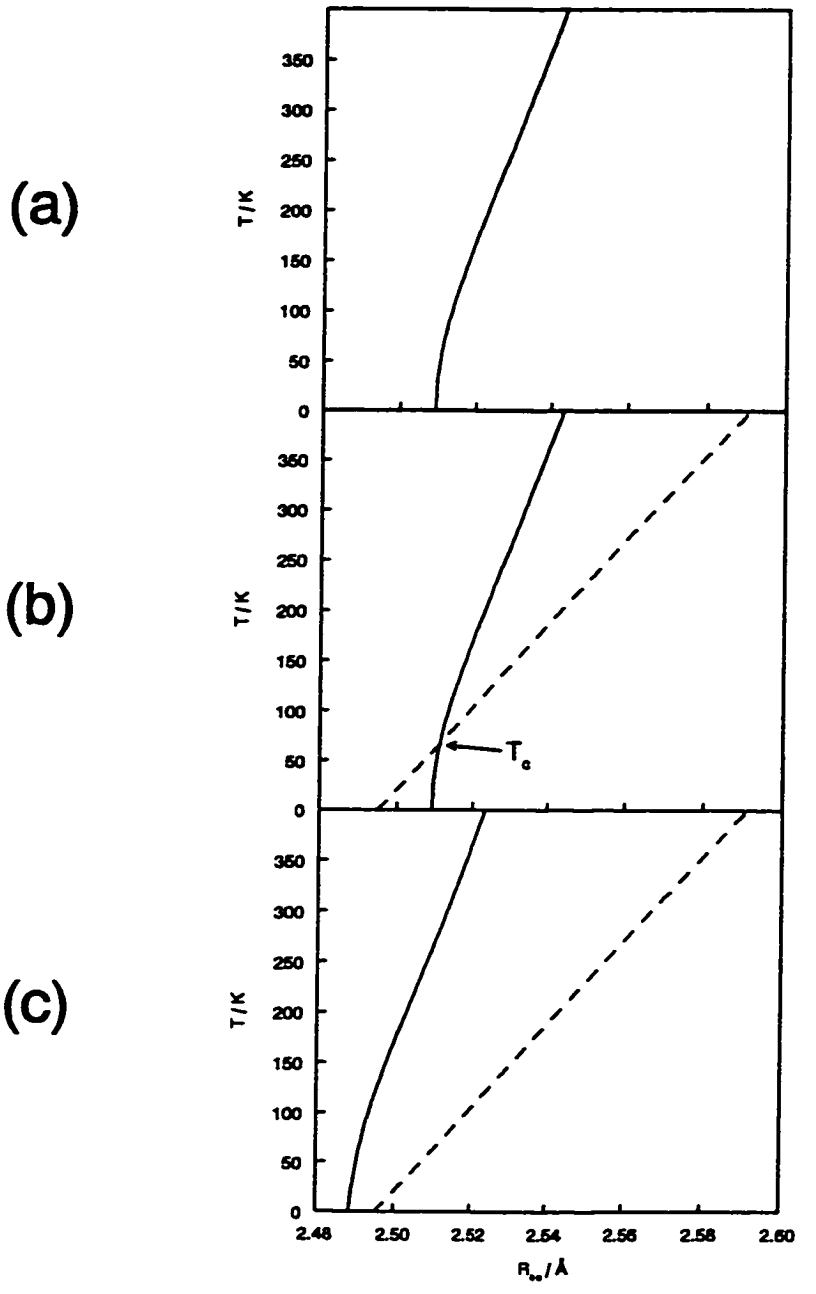

to the compound in Figure 2.9(b). Since the two curves do not intersect in this case, this particular compound will not have a low-temperature phase transition. The results in Figure 2.9(b) and Figure 2.9(c) show that for a substance in this family of compounds, if the hydrogen-bond length at $T = 0$ K is greater than the x-intercept of equation (2.2) (*i.e.*, $R_0 = 2.495$ Å), there will be an intersection of the two curves and the substance will have a low-temperature phase transition at the temperature of intersection. Conversely, however, if the hydrogen-bond length at $T = 0$ K is less than or equal to 2.495 Å, no phase transition will be observed. Those compounds which do show the phase transition will have a higher transition temperature for a longer hydrogen bond.

The argument just presented, along with the diagrams in Figure 2.9, show that a phase transition will be favoured by any condition which tends to lengthen hydrogen bonds. It is known that the substitution of deuterium for hydrogen tends to result in crystals with longer hydrogen bonds (typically an increase of 0.02 - 0.03 Å in R_{oo} for the O---(H,D)---O hydrogen bond).[47,82,95] This is called the Ubbelohde effect.[102] The longer hydrogen bond in the deuterated compound will thus favour the existence of a phase transition. On the other hand, hydrogen atoms tend to form shorter hydrogen bonds than deuterium which will tend to prevent the occurrence of a transition.

Thus, two possible scenarios can be envisaged. For a case where the hydrogenated version of a compound has a phase transition due to ordering of the hydrogen atoms in the hydrogen bond, the corresponding deuterated compound will have the same phase transition but at a higher temperature due to the increased length of the hydrogen bond. Another scenario could occur where the hydrogen-bond length at $T =$

0 K of the H-form of a compound is just below the critical length R_0, and the lengthened hydrogen-bond in the D-form could be above R_0. In this case, the D-form would show the phase transition while the hydrogenated form would not. The latter case is represented by the compounds $Rb_3H(SeO_4)_2$, $K_3H(SO_4)_2$, and $Rb_3H(SO_4)_2$. In fact, the value of R_{OO} for $Rb_3H(SeO_4)_2$ at 0 K has been estimated[82] to be 2.495 $\pm$ 0.009 Å which is consistent with the observation that it does not exhibit a low-temperature phase transition according to equation (2.2). The hydrogen-bond length of $Rb_3D(SeO_4)_2$ at 25 K has been measured by X-ray diffraction[75] and found to be 2.519 $\pm$ 0.004 Å which is clearly greater than R_0. It should be noted that R_{OO} for $K_3H(SeO_4)_2$[76] is 2.4965 $\pm$ 0.0016 Å at 30 K which is just barely larger than R_0 and accounts for the very low phase transition temperature (20 K) observed[63] for this compound.

The effects of thermal contraction with lowering temperature on the energetics of the hydrogen atom in a hydrogen bond have been clearly demonstrated for the case of $K_3H(SO_4)_2$. A detailed X-ray diffraction study of $K_3H(SO_4)_2$ at various temperatures was performed and electron density maps of the hydrogen atoms were obtained as a function of temperature.[87] This study revealed a crossover in the energetics of the hydrogen atom from a double-well to a single-well potential at just below 100 K. Thus, the lack of a phase transition in this compound is explained as being due to thermal contraction causing the hydrogen-bond distance to shrink below the critical value at a temperature above where the phase transition would tend to take place.

Thus, the geometric isotope effect explains the differing phase transition behaviour of hydrogenated compounds *versus* their deuterated analogues simply by using

an empirical correlation between phase transition temperature and hydrogen-bond distance (measured at T_c). This is done without directly invoking the tunnelling mechanism. A study involving the observation of phase transition temperatures of lead hydrogen phosphate and its deuterated form at constant R_{OO} revealed that at least a significant fraction of the increase in the phase transition temperature upon deuteration was due to the geometric isotope effect.[98] The R_{OO} value of the deuterated compound was reduced to that of the hydrogenated compound through the use of applied pressure. Several theoretical models have been put forth to account for the T_c *vs.* R_{OO} correlation.[100,103,104] One of these suggests that the geometric isotope effect is driven by the tunnelling motion of the hydrogen and deuterium atoms.[103] Thus, tunnelling could be indirectly responsible for the geometric isotope effect.

2.3.5 Calorimetry

Among the $M_3(H,D)(XO_4)_2$ compounds, detailed calorimetric studies have only been reported for $Rb_3(H,D)(SeO_4)_2$,[65] $Rb_3(H,D)(SO_4)_2$,[67] and $K_3(H,D)(SeO_4)_2$.[66] The results for the deuterium compounds clearly show an anomaly due to the low-temperature phase transition in contrast to the anomaly-free heat capacity curves for the hydrogenated analogues. The heat capacity results for $K_3H(SeO_4)_2$ show a very subtle anomaly at a very low temperature corresponding to the low-temperature phase transition that appears at T = 20 K in the dielectric measurements. The heat capacity curves for $Rb_3(H,D)(SeO_4)_2$[65]

are given in Figure 2.10, where the curve for the deuterated compound is shifted upwards by 50 $J \cdot K^{-1} \cdot mol^{-1}$ for clarity's sake. The anomaly in the curve for the deuterated form occurs at a temperature of 95.4 K and the entropy change associated with the anomaly was determined to be 4.0 $J \cdot K^{-1} \cdot mol^{-1}$ which is similar in magnitude to the entropy changes of the phase transitions observed for the other crystals in this family which were studied by adiabatic calorimetry.[66,67] Such entropy values are consistent with an order/disorder mechanism for the low-temperature phase transitions in this group of compounds.[66]

Although the compounds $Rb_3H(SeO_4)_2$ and $Rb_3H(SO_4)_2$ do not show a low-temperature phase transition in their heat capacity curves, anomalous behaviour is observed at very low temperatures. This is readily seen when the heat capacity curves for a compound and its deuterated form are superimposed upon each other. At low temperatures, the heat capacity of the H-compound is noticeably larger than that of the corresponding D-compound. This is the opposite of what would be expected from normal vibrational and rotational heat capacity considerations, *i.e.*, the heat capacity of the deuterated form should be larger (see Chapter 9 for further discussion). This inverse isotope effect in the low-temperature heat capacity has been attributed to the presence of extra low-lying energy levels that can be accessed by the hydrogenous compound but are not available for use by the deuterated compound.[94]

Figure 2.10. Heat capacity curves for $Rb_3H(SeO_4)_2$ (closed circles) and $Rb_3D(SeO_4)_2$ (open circles). For clarity's sake the curve for $Rb_3D(SeO_4)_2$ is shifted upwards by 50 $J \cdot K^{-1} \cdot mol^{-1}$; from reference (65).

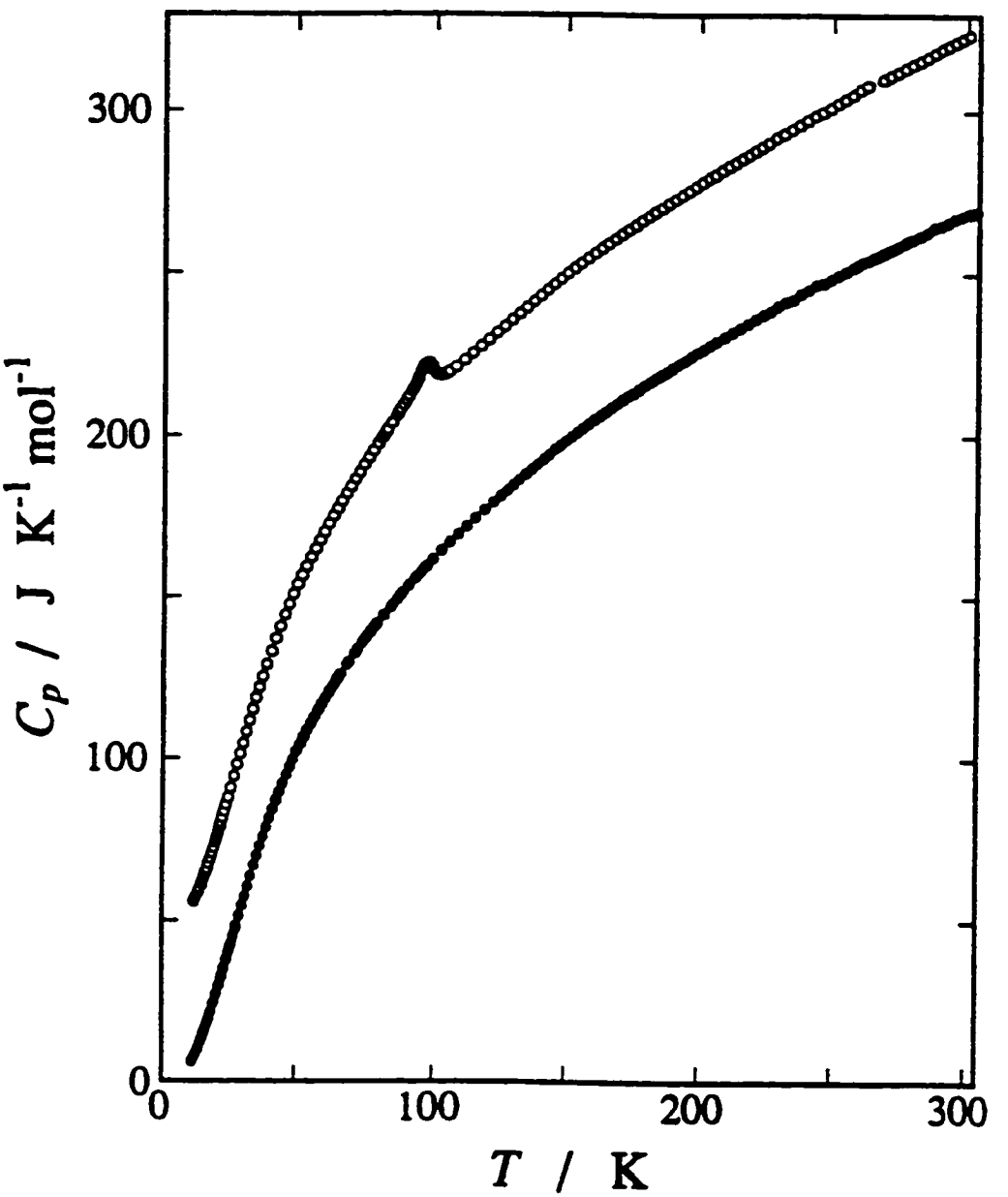

2.4 $(NH_4)_2MCl_6$ Family of Crystals

2.4.1 Phase Transitions and Calorimetry

The deuterium-induced phase transition phenomenon has also been found to exist in a wide variety of crystals with general formula $(NH_4)_2MCl_6$, where M is a tetravalent metal ion. The compounds which have been studied in this regard are those for which M = Pt, Pd, Sn, Pb, Te, Se. Dielectric measurements for these substances are as yet unreported; however, they and their deuterated forms have been studied extensively by calorimetry. A deuterium-induced phase transition in this series was first found serendipitously in $(ND_4)_2PdCl_6$ in a neutron scattering experiment.[105] Subsequent calorimetry revealed[106] a phase transition at T = 30.2 K from the high-temperature cubic phase to a low-temperature tetragonal phase with an entropy change of 16.7 $J \cdot K^{-1} \cdot mol^{-1}$. No anomalies were observed in the corresponding heat capacity curve of $(NH_4)_2PdCl_6$.[107] Calorimetric results for the hydrogenated[108] and deuterated[109] forms of ammonium hexachloroplatinate ($(NH_4)_2PtCl_6$) show similar behaviour with a phase transition in the deuterated salt at T = 27.2 K that is absent in $(NH_4)_2PtCl_6$. More diverse phase transition behaviour is seen in the plumbate and tellurate compounds. The protonated and deuterated plumbate compounds show[110] a second-order anomaly in their heat capacity curves at 78.1 K and 80.7 K respectively. A similar anomaly occurs for the tellurate compounds at 88.0 K (protonated) and 86.7 K (deuterated).[111,112] However, $(ND_4)_2PbCl_6$ has an extra first-order deuterium-induced phase transition at 38.4

K with an associated entropy change[110] of 6.5 $J \cdot K^{-1} \cdot mol^{-1}$.

The heat capacity curves for $(NH_4)_2TeCl_6$ and $(ND_4)_2TeCl_6$ are shown[112] in Figure 2.11, where a wealth of deuterium-induced phase behaviour is revealed. A sharp first-order phase transition is evident at 31.9 K with another more gradual transition peak reaching a maximum at $T \sim 47$ K. Actually the 47 K transition culminates in two sharp closely spaced peaks, one at 46.8 K and the other at 48.1 K. Thus, three deuterium-induced phase transitions occur for $(ND_4)_2TeCl_6$. Neutron powder diffraction measurements of this compound showed that the successive phase structures in order of decreasing temperature are cubic (above 86.7 K), rhombohedral, triclinic, monoclinic, and tetragonal.[111,113] Measurements of the protonated tellurate showed only the cubic-rhombohedral structure change corresponding to the only phase transition in its measured heat capacity curve at 88.0 K. This particular structural change was predicted based upon Raman spectroscopy measurements.[114] The entropy changes of the various phase transitions in $(ND_4)_2TeCl_6$ are 6.69 $J \cdot K^{-1} \cdot mol^{-1}$ (32 K), 4.1 $J \cdot K^{-1} \cdot mol^{-1}$ (including both transitions near 47 K), and 1.9 $J \cdot K^{-1} \cdot mol^{-1}$ (87 K). The small change in entropy at the 87 K transition is characteristic of a displacive-type transition. The higher entropy changes at the deuterium-induced phase transitions are more like an order-disorder transition. As these phase changes occur only in the deuterated compound, they likely involve ordering changes associated with the dynamics of the ND_4^+ ion.

Rounding out this series are $(NH_4)_2SnCl_6$ and $(NH_4)_2SeCl_6$ and their deuterated forms. These substances stand out from the other compounds in this family in that they do not show deuterium-induced phase transitions. In fact, the heat capacity curves of the

Figure 2.11. Heat capacity curves for $(NH_4)_2TeCl_6$ (lower curve) and $(ND_4)_2TeCl_6$ (upper curve). The heat capacity of $(ND_4)_2TeCl_6$ is shifted upwards for clarity. Note the extra deuterium-induced peaks in the curve for the deuterated compound. The middle peak at ~ 47 K can actually be resolved into two peaks; from reference (112).

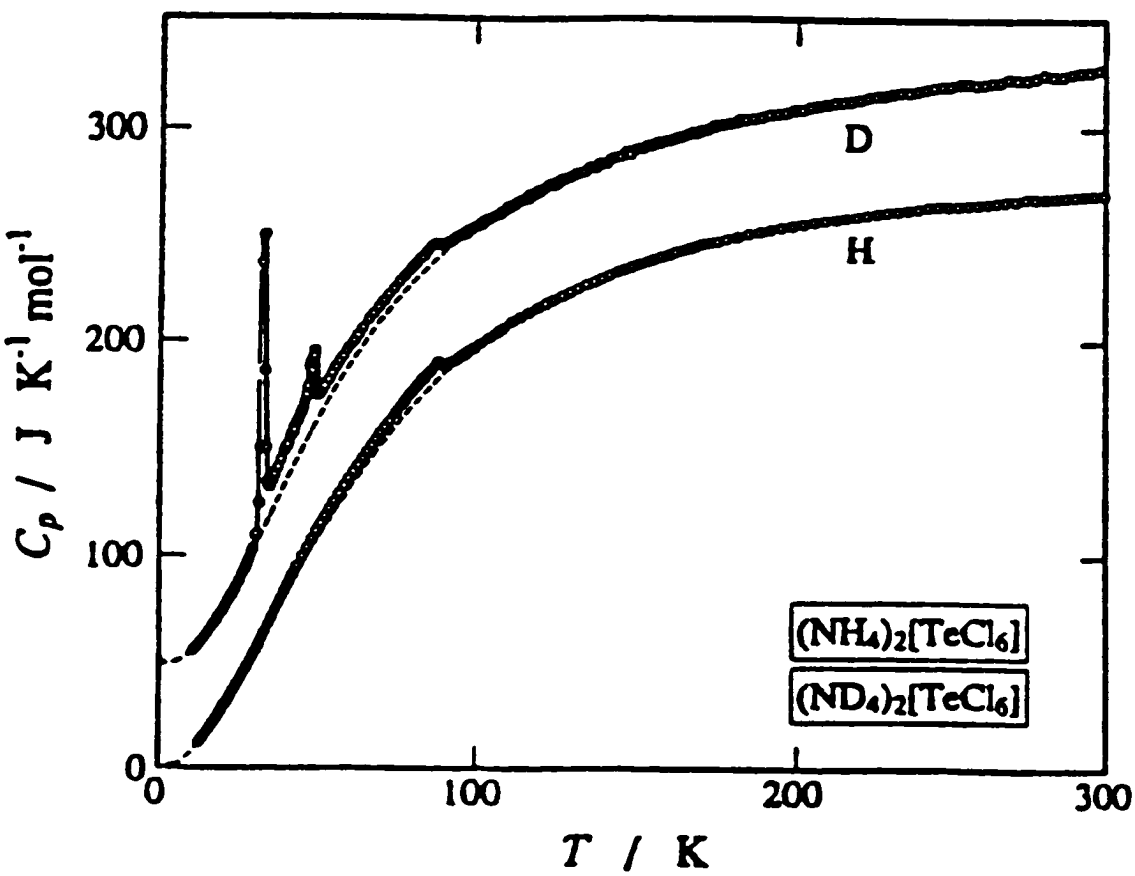

protonated[115] and deuterated[116,117] stannates show no phase transition anomalies at all below room temperature. The selenates show the exact opposite behaviour;[118] both compounds show a single low-temperature phase transition in their heat capacity curves at 24.5 K for the normal salt and 48.2 K for the deuterated salt. Closer inspection of the $(ND_4)_2SeCl_6$ transition revealed a subsidiary peak at 45.7 K. Furthermore, the transition entropy of 12.1 $J \cdot K^{-1} \cdot mol^{-1}$ for $(ND_4)_2SeCl_6$ is eight times larger than the 1.50 $J \cdot K^{-1} \cdot mol^{-1}$ entropy value for the transition in $(NH_4)_2SeCl_6$. This suggests different mechanisms for the phase transitions in the two compounds: an order-disorder mechanism for the deuterated salt *versus* a displacive transition for the normal compound.[118] Thus, the deuterium-induced behaviour in the selenate salts is more subtle than that observed for most of the other members of this series.

Considering the compounds in this series, comparison of the low-temperature heat capacity curves for the protonated salt and deuterated analogue shows a characteristic feature. At very low temperatures, the heat capacity of the protonated compound is higher than that of the deuterated version. This is the same behaviour that was observed in the heat capacity measurements for members of the $M_3(H,D)(XO_4)_2$ series of crystals. Again, the opposite trend is expected based upon the mass effects on vibrations and rotations in the solid state. A higher heat capacity for the deuterated form at low temperatures is typically observed for the vast majority of H/D compound pairs. An explanation for the inverse isotope effect of the low-temperature heat capacity that is observed in systems showing deuterium-induced phase transitions could provide valuable insight into the energetics and dynamics of these systems, especially with respect to the

third law of thermodynamics.

It should be mentioned that the corresponding bromide compounds, *i.e.*, the ammonium hexabromometallates, have not yet been studied in detail for the purpose of looking for deuterium-induced phase transitions. It is anticipated that measurements of these compounds could reveal more examples of anomalous deuterium-induced behaviour similar to that observed for the ammonium hexachlorometallates.[45]

2.4.2 Crystal Structures

All of the compounds in this series have an antifluorite structure of the K_2PtCl_6-type at high temperatures.[45,119,120] The common space group is the face-centred cubic $Fm\bar{3}m$ ($Z = 4$) as illustrated[121] in Figure 2.12. Figure 2.12(a) shows the octahedral MCl_6^{2-} anion with its four-fold axis aligned with the four-fold axis of the (½,½,½) cube, with ammonium ions at the corners. Another perspective of this structure is given in Figure 2.12(b) where the ammonium ions are shown at the centre of a (½,½,½) cube with 12 nearest-neighbour chloride ions. Such an arrangement provides a high-symmetry tetrahedral site for the ammonium ion.

In contrast to the $M_3(H,D)(XO_4)_2$ crystals, hydrogen bonds in the ammonium hexachlorometallates are of the form N-H-Cl which are weak and chemically asymmetric. As the ionic symmetry and the site symmetry for the ammonium ion are both T_d, it cannot be assumed that the ammonium ions in the crystal are orientationally disordered

Figure 2.12. Room-temperature crystal structure for members of the $(NH_4)_2MCl_6$ family of compounds. (a) A view showing the octahedral MCl_6^{2-} ion at the centre with ammonium ions at the corners (only one ammonium ion shown). (b) A view showing the ammonium ion at the centre with each N-H bond exhibiting a trifurcated hydrogen bond with its three nearby Cl^- ions. Both diagrams are (½,½,½) subcubes of the unit cell; from reference (121).

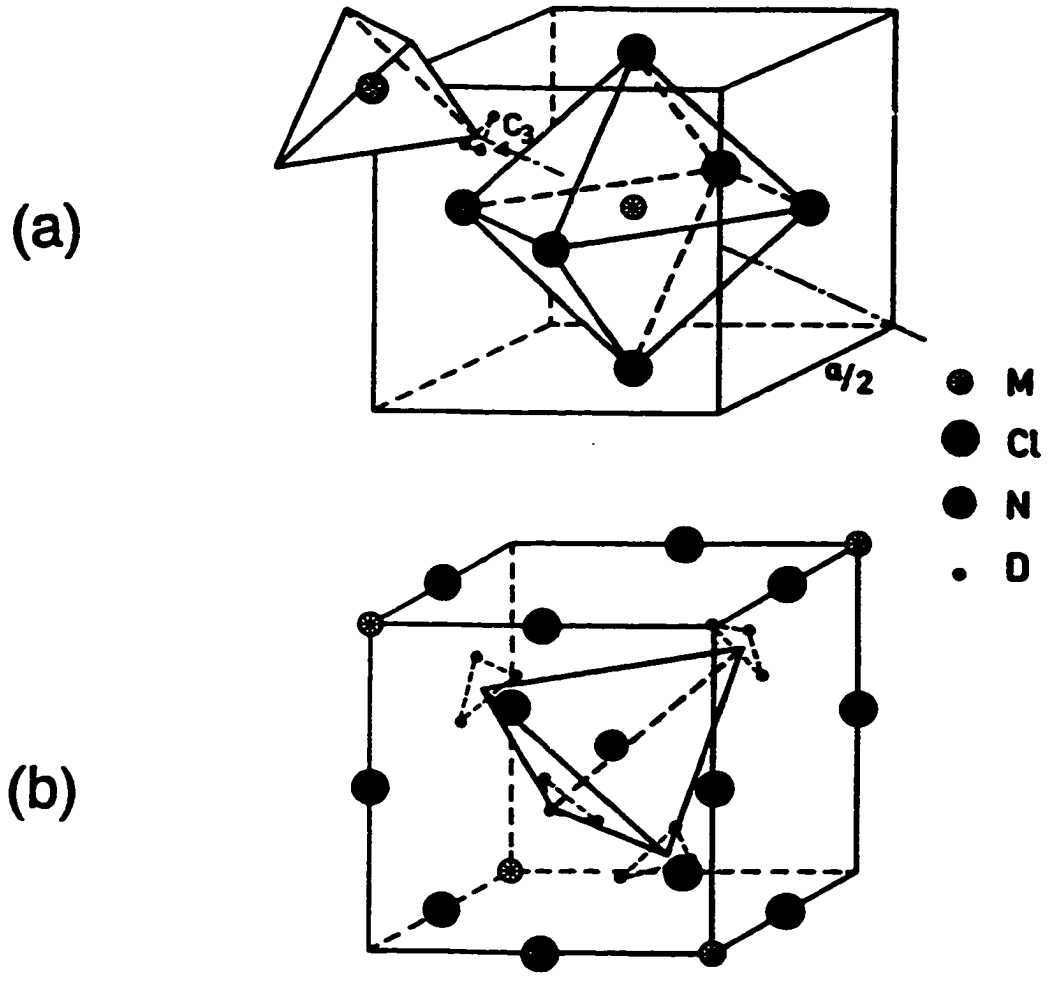

based solely on symmetry arguments. However, most of the deuterated crystals undergo low-temperature phase transitions which involve the deuterated ammonium ion. The entropy changes during these transitions indicate that they occur via an order-disorder process. This means that the ammonium ions are becoming more ordered at low temperatures, which implies orientational disorder at higher temperatures. Some form of classical hindered rotation of the ammonium ions about their three-fold axes is a definite possibility as to the source of this disorder. In fact, evidence for this type of reorientational motion has been observed with ^{1}H NMR.[121] The activation barriers (E_a) for reorientation of the ammonium ions have been determined from the temperature-dependence of the spin-lattice relaxation times (T_1) for this compound family.[122] The resulting values are very low, ranging from 2.6 kJ·mol^{-1} to 6.7 kJ·mol^{-1}, increasing with the metal cation in the order Pd^{4+}, Pt^{4+}, Sn^{4+}, Pb^{4+}, Te^{4+}. When dealing with reorientation of proton-containing species with low activation barriers, tunnelling of the protons should always be suspected as a possible reorientational mechanism. Tunnelling splittings have been observed for these compounds using ^{1}H NMR[121,123,124] and inelastic neutron scattering[125] at low temperatures, and the magnitudes of the splittings show an inverse relationship with the reorientational barrier height, as would be expected.

While the N-H (N-D) bonds would presumably orient themselves so that they are aligned with the three-fold axes of the (½,½,½) cube (Fig. 2.12(b)), measurements by neutron scattering[126,127] and ^{35}Cl NQR[121] indicate that the bonds may be oriented slightly away from these axes. The ammonium ions undergo small rotations in a potential

shaped like an equilateral triangle with the minima corresponding to positions where direct hydrogen bonds can be formed with the three chloride ions close to a particular N-H (N-D) bond (Fig. 2.12(b)). This situation has been called a trifurcated hydrogen bond.[128] Dynamic disorder is expected for the ammonium ions among the three positions in the triangle-shaped potential.

As stated in section 2.4.1, the compounds $(NH_4)_2PbCl_6$, $(NH_4)_2TeCl_6$, and their deuterated varieties show a low-entropy, second-order phase transition near 80 K. The low entropy of this transition suggests a displacive mechanism. For the tellurate compounds, Raman spectroscopy[114] has shown that these transitions involve rotation of the $TeCl_6^{2-}$ octahedra about their three-fold axis. The fact that the ammonium ions do not directly take part in this transition is supported by the observation that the transition temperature is essentially unaffected by deuteration. A similar explanation would account for the transitions in the plumbate compounds near 80 K.

2.4.3 Possible Explanations

As mentioned previously, the hydrogen bonds that are formed in the compounds of this system are weak and chemically asymmetric, so it is unlikely that the geometric isotope effect used as an explanation in the $M_3(H,D)(XO_4)_2$ family of crystals has a pertinent analogue that is applicable to the ammonium hexachlorometallates. The key parameter that accounts for the deuterium-induced behaviour observed in this series

remains undiscovered. Several postulates have been made, however.

Due to the low barriers to reorientation of the ammonium ions in these compounds, tunnelling is very efficient as indicated by the measured tunnelling splittings.[125] The occurrence of deuterium-induced phase transitions could be due to the reduced ability of deuterium atoms to tunnel as compared to the lighter hydrogen atoms. Evidence for dynamic disorder of the ammonium ions in the three-fold potential of a trifurcated hydrogen bond exists, as described in Section 2.4.2. The driving force for a phase transition resulting in ordering of the ammonium ions is the localization of the ions in one of the potential wells in the three-fold potential. This seems to occur in most of the deuterated compounds in this series as shown by the existence of low-temperature phase transitions and the corresponding high entropy changes. But hydrogen atoms tunnel better than deuterium, and the quantum-mechanical delocalization associated with tunnelling resists the classical desire of the ammonium ions to localize in one of the potential wells with decreasing temperature. The motion of the deuterated ammonium ions is more classical and an ordering phase transition can take place. This seems to be a plausible explanation for the observed deuterium-induced phase transitions.

In $(ND_4)_2TeCl_6$, where several deuterium-induced phase transitions take place, it can be postulated that the ND_4^+ ions become more ordered with decreasing temperature. One of the transitions could be due to localization of the deuterium atoms in one of the three potential wells in a random fashion from one ammonium ion to the next. A further decrease in temperature could lead to another ordering phase transition where the interactions between ammonium ions lead to a long-range correlation in their potential-

well localization.[121]

Another mass-dependent effect that could explain the deuterium-induced phase behaviour associated with these systems is the moment of inertia of the ammonium ions. The ammonium ions experience reorientation associated with rotational motion. The rotational constant that determines the rotational energy levels for a system is inversely dependent on the moment of inertia of the rotating species. As the moment of inertia is proportional to the mass, a deuterated ammonium ion will have a larger moment of inertia, and consequently, a lower rotational constant than the NH_4^+ ion. This will cause the rotational energy levels for NH_4^+ to be higher up in the potential wells, as expected, since its lighter mass makes NH_4^+ more of a quantum particle than ND_4^+. Realizing that the potential barriers to reorientation of NH_4^+ and ND_4^+ are very low in these compounds, it is possible that the ground-state level for the hydrogenated substance is above the energy maximum of the potential barrier removing the possibility for a phase transition because potential-well localization is not possible.[129] A transition is possible in such a situation, however, depending on the strength of the collective interaction between neighbouring ammonium ions. For the deuterated compound with lower-energy rotational levels, if the ground state is below the potential maximum, then a phase transition due to ND_4^+ ordering would be possible. As the above ideas are mostly speculative, more studies are needed (especially more neutron diffraction studies of the various deuterium-induced phases) to arrive at a unifying theory to describe the unusual phase transition behaviour for this series of compounds.

2.5 Miscellaneous Examples

2.5.1 5-bromo-9-hydroxyphenalenone

Recently, deuterium-induced phase transitions have been discovered in some solid-state organic molecular crystals, the most notable to date being 5-bromo-9-hydroxyphenalenone.[130] The molecular structure of this compound is shown in Figure 2.13. The system is exceptional in that intramolecular tautomerization can take place with the hydroxyl proton hopping from one oxygen to the other. Furthermore, the O-H-O arrangement forms a strong intramolecular hydrogen bond, and since each hydrogen bond within a molecule is isolated from the other molecules in the solid state, this compound can be said to have a zero-dimensional hydrogen-bonded network by analogy with the $M_3(H,D)(XO_4)_2$ family. The advantage of using this compound to study deuterium-induced behaviour is that the hydrogen-bond distance (R_{oo}) is fixed by the molecular framework and is not significantly affected by isotopic substitution of the hydrogen atom in the hydrogen bond with deuterium.

A study of the solid-state structure of 5-bromo-9-hydroxyphenalenone (hereafter abbreviated as BHP) by X-ray diffraction revealed that the structure is monoclinic[130] with space group *Cc*, and the O-O distance is 2.49 $\pm$ 0.01 Å. This value of R_{oo} is typical of hydrogen bonds where the dynamical motion of the proton is described by a double-well potential, which in this case would be symmetric due to the symmetric nature of the molecule. Dynamical disorder of the proton in the intramolecular hydrogen bond would

Figure 2.13. Molecular structure of 5-bromo-9-hydroxyphenalenone.

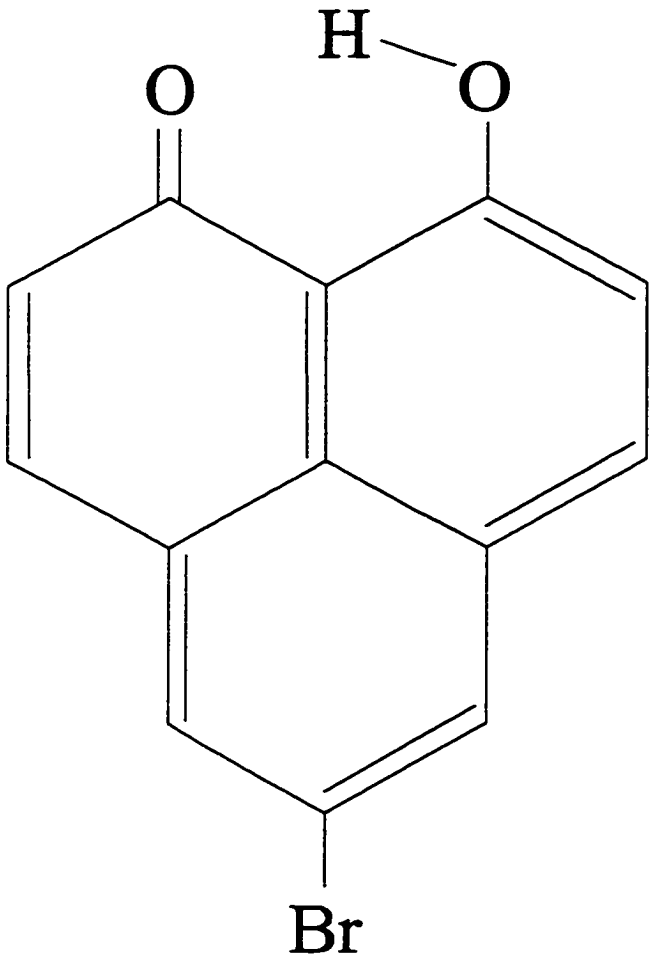

be expected, and this has been verified by ^{13}C solid-state NMR measurements[131] in which the signals from the two carbons attached to the oxygen atoms were found at an averaged position. The hydrogen-bond length in this compound is similar to the corresponding values for other compounds exhibiting deuterium-induced effects.

The low-temperature behaviour of BHP was first studied by dielectric measurements[130] which indicated no phase transitions occurring down to 2 K. The dielectric constant increased gradually with decreasing temperature which is characteristic of paraelectric behaviour. On the other hand, the same experiment performed on a 50%-deuterated sample gave remarkably different results.[130] At 36 K, a broad peak that is typical of a phase transition to an antiferroelectric phase occurred in the dielectric constant curve for the deuterated sample. Further dielectric measurements on a fully deuterated sample (deuterium substitution of H-bonded proton only) showed that two dielectric phase transitions[132] actually exist, with transition temperatures of approximately 20 K and 37 K.

By analogy with the $M_3(H,D)(XO_4)_2$ crystals, an attempt to explain the absence of the low-temperature phase transitions in BHP could be made by invoking the tunnelling effect and the geometric isotope effect. However, the geometric isotope effect depends on an increase in hydrogen-bond length upon deuteration which does not occur to any measurable extent in BHP since R_∞ is fixed by the molecular framework. Thus, the geometric isotope effect should not play a role here, and tunnelling can be studied exclusively.

When intramolecular tautomerization occurs in BHP and its deuterated form, the

dipole moment in the hydrogen-bonded part of the molecule becomes inverted. In a classical sense, motion of the hydrogen (deuterium) atom in the hydrogen bond between the two minima in the double-well potential will occur provided that the temperature is sufficiently high that enough thermal energy is available to surmount the potential barrier between the two minima. At lower temperatures, electrostatic interactions between the dipole moments of neighbouring molecules will become significant and will promote the collective ordering of the hydrogen (deuterium) atoms into one of the two positions, giving rise to a phase transition. Opposing this localization is quantum-mechanical tunnelling which undoubtedly occurs for both deuterated and hydrogenated BHP. Tunnelling causes a blurring effect due to the overlapping of wavefunctions on both sides of the potential barrier which reduces the intermolecular electrostatic interaction and hinders the occurrence of an ordering phase transition.

As mentioned previously, hydrogen atoms are more adept at tunnelling than deuterium due to the smaller mass of hydrogen. In fact, tunnelling frequencies have been measured[133] for the parent compound of BHP, *i.e.*, 9-hydroxyphenalenone, along with 9-deuteroxyphenalenone, and it was found that the tunnelling frequency was reduced from 69 cm^{-1} in the hydroxy compound to 12 cm^{-1} in the deuteroxy version. Thus, the argument that can be made to explain the phase transitions in deuterated-BHP and their absence in BHP is the following. Quantum-mechanical delocalization in the deuterated compound is not effective enough to overcome the electrostatic interactions between neighbouring molecules and ordering phase transitions occur as the temperature is lowered. In the protonated form of BHP, the proton tunnelling is of sufficient magnitude

to render the intermolecular electrostatic interactions insignificant, and the phase transitions are suppressed.[130]

The tunnelling frequency can be varied between the two extremes of full protonation *versus* full deuteration through the use of hydrogen/deuterium isotopically mixed crystals. Such mixed crystals of the protonated and deuterated forms of BHP have been investigated using dielectric measurements for varying values of the mole fraction of the protonated form.[132] The results of these experiments show that the phase transition temperatures decrease with an increase in the mole fraction of the protonated form and eventually disappear for protonated-form mole fractions of 0.25 ± 0.05 and 0.65 ± 0.05 for the 20 K and 37 K transitions, respectively. These results reflect the increase of the tunnelling frequency along the hydrogen bond with increasing mole fraction of the protonated form.

Both forms of BHP have also been studied calorimetrically.[134] Protonated BHP has no anomalies in its low-temperature heat capacity curve whereas the heat capacity curve for the deuterated form reveals two peaks due to phase transitions with maxima at 21.5 K and 33.9 K. This is consistent with the results from the dielectric measurements.[132] The values of the entropy changes for the phase transitions are consistent with an order-disorder mechanism.[129] Also, in contrast with conventional theories of heat capacity, the heat capacity for the hydrogenated form is larger than that for the deuterated form in a low-temperature region. This behaviour seems to be characteristic of substances with deuterium-induced phase transitions.

It should be noted that the methyl derivative, 5-methyl-9-hydroxyphenalenone, and

its deuterated form have also been studied dielectrically.[130] These compounds are isomorphous with BHP and both of them have a characteristic anomaly in their dielectric curves consistent with conversion to an antiferroelectric phase. The phase transition temperatures are 41 K for the protonated form and 44 K for the deuterated form, deuteration causing a slight increase in the transition temperature in this case. The explanation that has been proposed for the appearance of a phase transition in both of the isotopic forms of the 5-methyl derivative is that the tunnelling frequency of the hydrogen atom in the hydrogen bond will be lower in the 5-methyl derivative as compared to the 5-bromo derivative because of the anisotropy of the methyl group.[130] This anisotropy means that the two tautomers in the 5-methyl derivative will be inequivalent and thus the double-well potential for the hydrogen bond will be asymmetric. No such problem exists in the 5-bromo derivative due to the spherical symmetry of the substituent bromine atom. This argument has been supported by molecular orbital calculations.[135]

2.5.2 Other Examples

There are some other rather isolated examples of substances which are known to undergo a phase transition only when deuterated. Recently, a deuterium-induced phase transition was discovered in fully-deuterated tolane[136] (diphenylacetylene with all 10 hydrogens replaced with deuterium atoms). The transition occurs at 313 K as indicated by differential scanning calorimetry with no equivalent transition showing up in

hydrogenated tolane. The crystal structure of tolane belongs to the monoclinic space group $P2_1/c$ ($Z = 2$) and the phase transition in deuterated tolane is of first-order and occurs without a change of symmetry. This is the first known compound with a deuterium-induced phase transition that is observed above room temperature. A reasonable explanation for this phenomenon is still pending.

Another example is the occurrence of a phase transition in thallium dideuterium phosphate at 127 K as determined by the technique of differential thermal analysis.[137] This transition has not yet been studied in any great detail.

Finally, a deuterium-induced phase transition occurs in sodium deuteroxide[138] (NaOD) at a temperature of 153.2 K that does not occur in sodium hydroxide[139,140] (NaOH) at atmospheric pressure at least above 6 K. All of the research work in this thesis concerns the NaOH/NaOD compound pair, and is directed toward a single focused purpose: through the detailed study and measurement of some of the thermal properties of sodium hydroxide, to provide an explanation for the lack of a phase transition analogous to that observed in NaOD. The story begins with a literature survey of the relevant properties of the alkali-metal hydroxides and deuteroxides.

Chapter 3: Anomalous Behaviour of Sodium Hydroxide

3.1 Polymorphism in Alkali-Metal Hydroxides and Deuteroxides

Polymorphism in the alkali-metal hydroxides and deuteroxides is extensive especially above room temperature.[141,142,143,144,145] These substances belong to the family of compounds with general formula $M^+ XY^-$, where M^+ is a monovalent metal cation (usually an alkali metal), and XY^- is a diatomic anion of charge -1. Besides the hydroxides, members of this family include the alkali-metal cyanides (XY = CN), and hydrogensulfides (XY = SH).[146,147] Characteristic of all of these compounds is the existence of a high-temperature cubic phase just below the melting point in which the XY^- anions are dynamically disordered among several orientations;[147,148,149] in some cases the reorientational motion approaches free rotation. As the temperature is lowered, polymorphic phase transitions take place to different solid structures of lower symmetry[141,142,143,144,145,146] where the XY^- ions become progressively more ordered as required by the third law of thermodynamics.

A list of all the polymorphic phase transitions known to occur for the alkali-metal hydroxides and deuteroxides is provided in Table 3.1 along with their corresponding transition temperatures and the melting temperatures of each compound (if known). Excellent reviews of the thermodynamic properties of the alkali-metal hydroxides can be found in the literature.[150,151] Note that at high temperatures all of these substances (with the exception of LiOH and LiOD) exist in a highly symmetrical cubic phase. The

Table 3.1. Polymorphic phase transition temperatures for the alkali-metal hydroxides and deuteroxides. Where available, the transition temperatures obtained from calorimetry were chosen over those obtained from diffraction experiments and differential thermal analysis.

Compound / Transition	Temperature / K	Reference
LiOH		
tetragonal → liquid	746	142
NaOH		
orthorhombic → monoclinic	514	141
monoclinic → cubic	566	141
cubic → liquid	594	142
NaOD		
monoclinic I → orthorhombic	153.2	152
orthorhombic → monoclinic II	500	141
monoclinic II → cubic	561	141
cubic → liquid	593	141
KOH		
monoclinic I → monoclinic II	226.7	153
monoclinic II → cubic	517	142
cubic → liquid	677	142

Continued...

Table 3.1. (continued).

Compound / Transition	Temperature / K	Reference
KOD		
monoclinic I → monoclinic II	253.1	153
monoclinic II → cubic	523	143
cubic → liquid	646	143
RbOH		
orthorhombic → monoclinic I	265	144
monoclinic I → monoclinic II	367	144
monoclinic II → cubic	511	144
cubic → liquid	653	142
RbOD		
orthorhombic → monoclinic I	300	144
monoclinic I → monoclinic II	369	144
monoclinic II → cubic	513	144
cubic → liquid	?	
CsOH		
orthorhombic I → orthorhombic II	234.0	154
orthorhombic II → cubic	498	145
cubic → liquid	619	142
CsOD		
orthorhombic I → orthorhombic II	247	155
orthorhombic II → cubic	460	155
cubic → liquid	?	

OH^- ions in the cubic phases undergo rapid reorientation.[143,144,145,148] For the case of NaOH, incoherent inelastic neutron scattering revealed that the OH^- ions rotate among the eight possible body diagonal [1,1,1] directions of the cube.[148] Phase transitions to structures of lower symmetry take place with decreasing temperature. A brief overview of the phase transitions in each compound will now be presented.

Lithium hydroxide is unique among the alkali-metal hydroxides in that it does not have a high-temperature cubic phase. In fact, unlike all of the other compounds in this group, LiOH exhibits no known polymorphism at atmospheric pressure. The lone solid phase is tetragonal with space group *P4/nmm* ($Z = 2$) as determined by X-ray[156] and neutron diffraction.[157]

Sodium hydroxide and sodium deuteroxide have three high-temperature phases in common.[141] At high temperatures they form an NaCl-type structure of space group *Fm3m* ($Z = 4$) with rapidly reorienting OH^- (OD^-) ions. In NaOH, as the temperature is lowered to 566 K, the OH^- ions become localized in a monoclinic structure with space group $P2_1/m$ ($Z = 2$), and when the temperature is lowered to 514 K, a further transition to an orthorhombic structure takes place. The orthorhombic structure has space group *Bmmb* ($Z = 4$) and this phase is the one which exists at room temperature and below. The corresponding transition temperatures for NaOD are 561 K (monoclinic to cubic) and 500 K (orthorhombic to monoclinic). These phases have been studied by X-ray diffraction[141,158,159] and neutron diffraction.[160] For sodium deuteroxide, a low-temperature phase transition occurs[152] at 153.2 K to a monoclinic phase[138,161] (space group $P2_1/a$ ($Z = 4$)). All of the NaOH/NaOD structures will be discussed in more detail

in the next section.

The sequence of phase transitions for potassium hydroxide and potassium deuteroxide is similar to that of sodium deuteroxide except that KOH and KOD skip the orthorhombic phase.[143] The room-temperature form of KOH is monoclinic with space group $P2_1/m$ ($Z = 2$)[162] which transforms to the orientationally disordered cubic phase $Fm3m$ ($Z = 4$)[143] at 517 K.[142] A transformation from the room-temperature phase to a low-temperature monoclinic phase occurs[153] at 226.7 K (space group $P2_1/n$ ($Z = 4$)).[143] The high-temperature[143] and low-temperature[153] phase transition temperatures for KOD are 523 K and 253.1 K, respectively. The structures of the different phases in both substances were determined by X-ray[162,163] and neutron diffraction.[143]

Rubidium hydroxide appears to be the least-studied of all the alkali-metal hydroxides. Nevertheless, its polymorphic behaviour has been characterized by X-ray[144,162] and neutron diffraction.[144] At high temperatures, the common rock-salt cubic modification is the stable phase. When the temperature is lowered to 511 K, a transformation to a monoclinic phase results.[144] This room-temperature monoclinic phase is isomorphous with the room-temperature phase of KOH. A further decrease in temperature leads to a second monoclinic phase at 367 K which is isomorphous with the room-temperature structure. A transition to a low-temperature phase occurs at 265 K. Unlike the low-temperature phases in NaOD and KOH/KOD, the low-temperature modification of RbOH is orthorhombic (space group $Cmc2_1$ ($Z = 4$)).[144] The deuterated form, RbOD, exhibits corresponding phases with different transition temperatures[144] (see Table 3.1).

The room-temperature phase of cesium hydroxide is orthorhombic with the same space group as that for sodium hydroxide.[145,164] The transition to the orientationally disordered cubic modification takes place[145] at 498 K. A polymorphic phase transition to a low-temperature orthorhombic phase occurs[154] at 234.0 K with space group $P2_12_12_1$ (Z = 4).[145,155] For cesium deuteroxide, the transition to the cubic phase occurs at 460 K while the low-temperature modification exists below 247 K.[145]

From the survey just presented, it is clear that LiOH and LiOD are very different from the rest of the alkali-metal hydroxides and deuteroxides. Only one solid phase exists for these compounds throughout the entire temperature range below the melting point, in contrast to the three or four solid phases that exist for the other members of this group. Furthermore, solid LiOH has a tetragonal structure which has no analogue amongst the many polymorphic phases of the other compounds. When comparing transitions and transition temperatures, it seems clear that LiOH/LiOD should be excluded from the analysis as its polymorphic behaviour does not fit the pattern observed in all of the other alkali-metal hydroxides.

Excluding LiOH and LiOD, the low-temperature polymorphic phase-transition temperatures for all of the other alkali-metal hydroxides and deuteroxides are presented in Table 3.2. One obvious anomaly stands out from this list, *i.e.*, all of the hydroxides and deuteroxides undergo a low-temperature phase transition to a more ordered structure with the exception of NaOH. This fact is even more remarkable when it is realized that deuteration of NaOH results in a low-temperature phase transition at 153 K. Clearly, NaOH and NaOD show deuterium-induced phase-transition behaviour similar to what was

Table 3.2. Low-temperature polymorphic phase transition temperatures for the alkali-metal hydroxides and deuteroxides.

Compound	Temperature / K	Reference(s)
NaOH	——	139, 140
NaOD	153.2	138, 152
KOH	226.7	153
KOD	253.1	153
RbOH	265	144
RbOD	300	144
CsOH	234.0	154
CsOD	247	155

described in detail for several compounds in Chapter 2. A look at some of the properties of NaOH and NaOD should provide some insight into the phase-transition discrepancy exhibited by these compounds.

3.2 Comparison of NaOH and NaOD

As mentioned in the previous section, both sodium hydroxide and deuteroxide show similar polymorphic behaviour above room temperature.[141] Figure 3.1(a) shows the three polymorphic phases that are observed for both compounds at room temperature and above. The phase which exists just below the melting point is the high-temperature cubic phase where the ions are arranged in a rocksalt (NaCl) type structure. The OH^- (OD^-) ions in this phase undergo rapid reorientation, which is expected in order to be consistent with the cubic symmetry. The dynamics of the OH^- ions in cubic NaOH have been examined using quasielastic neutron scattering.[148]

As the temperature is lowered to 566 K (561 K for NaOD), the free (or nearly so) reorientational motion of the hydroxide (deuteroxide) ions ceases and the protons (deuterons) become localized in a monoclinic structure. This structure forms as the repulsion between the sodium cations and the protons (deuterons) becomes important resulting in the formation of metal-oxygen double layers[160] as shown in Figure 3.1(a). Note that the sodium-oxygen layers in the cubic structure have separated from their neighbouring layers along with gliding in the *a*-direction to form the monoclinic

Figure 3.1. (a) High-temperature polymorphic phases in NaOH and NaOD along with the corresponding transition temperatures; from reference (141). (b) Room-temperature orthorhombic structure of NaOH and NaOD; from reference (165). (c) Zig-zag arrangement of OH^- ions parallel to the *bc*-plane which bound the gap between any two layers in the orthorhombic structure of NaOH when viewed along the *a*-direction.

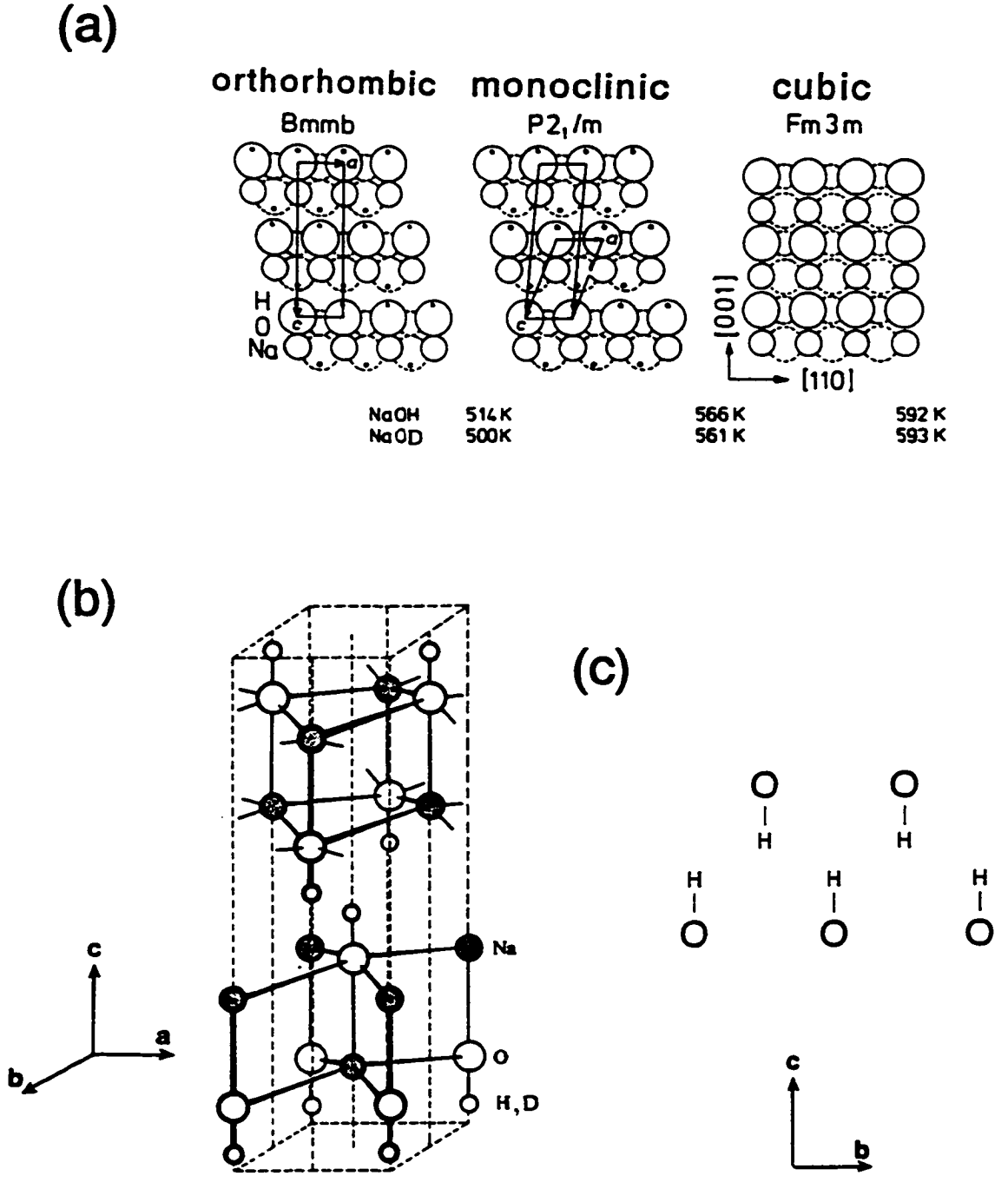

structure. The monoclinic to cubic phase transition is a first-order transition with high enthalpy and entropy changes,[166] reflecting the onset of disorder in the cubic phase.[141]

The layers in the monoclinic phase continue to glide past each other as the temperature is lowered until each layer is displaced by one-half of an *a*-lattice spacing from its neighbours at which time the gliding stops. At this point the structure is orthorhombic which is the form that exists for both compounds at room temperature. Due to the seemingly continuous nature of the orthorhombic to monoclinic transition, a second-order transition might be suspected. However, a detailed analysis of X-ray scattering data revealed that the onset of the shearing of the layers in the orthorhombic form is discontinuous.[141] Furthermore, an anomaly indicative of a small enthalpy change ($\sim$ 20 J·mol^{-1}) has been observed in the heat capacity curve of NaOH at T = 514 K.[141] Thus, the transition is first-order, although it is often referred to as "slightly first-order."

A different perspective of the room-temperature orthorhombic structure of NaOH (and NaOD) is provided in Figure 3.1(b).[160,165] This structure was first determined by X−ray diffraction with some speculation about the positions of the hydrogen atoms,[158] which were later determined by neutron diffraction.[160] Strictly speaking, an orthorhombic unit cell consists of a rectangular prism ($\alpha = \beta = \gamma = 90°$) with different lengths for the *a*, *b*, and *c* principal unit-cell axes. In NaOH, it was found from neutron diffraction[160] that $a = b = 3.399 \pm 0.001$ Å which would normally be thought of as a tetragonal unit cell. However, as can be seen from Figure 3.1(b), the positions of the atoms in the NaOH orthorhombic structure lack the four-fold axis necessary for true tetragonal symmetry. Thus, this structure is often referred to as "pseudo-tetragonal." It is also

known as the yellow TlI structure.[165]

The orthorhombic structure is made up of collinear Na-O-H entities where the hydrogen atoms have been located by neutron diffraction[160] at a distance of 0.918 ± 0.008 Å from their parent oxygen atoms. Each sodium cation is surrounded by five nearest neighbour oxygen atoms that are in an octahedral arrangement with one octahedral position unoccupied. When viewing the structure parallel to the *a*-direction along one of the gaps between any two layers, it is evident that the gap is bounded by a planar zig-zag chain of OH^- ions as shown in Figure 3.1(c). The closest distance between two oxygen atoms across the gap is 3.488 ± 0.008 Å, and the analogous hydrogen-hydrogen distance is 2.087 ± 0.008 Å.[160]

As mentioned in the previous section, with a lowering of the temperature, the orthorhombic modification of NaOD undergoes a further polymorphic phase transition at low-temperature to a monoclinic phase. Surprisingly, this phase does not exist in NaOH as it is known that the room-temperature orthorhombic modification of NaOH is maintained at least down to a temperature of 6 K.[140] The difference in the low-temperature behaviour of the two compounds was first suspected from early infrared data for NaOH and NaOD.[167] When the infrared absorption due to the O-H (O-D) stretching mode was monitored for the two compounds at room temperature and at liquid nitrogen temperature, the NaOH band showed only a slight increase in the absorption frequency. By contrast, the NaOD band was observed to split into three components at low-temperature which prompted the authors to suggest that possibly a phase change had occurred in NaOD in the observed temperature region "which has a much lower

transition temperature in NaOH."[167] Soon after, however, an adiabatic calorimetry study of NaOH was reported in the literature which showed no evidence for a low-temperature phase transition in NaOH above 12 K.[139]

The existence of the low-temperature phase transition in NaOD was confirmed by thermal studies involving the technique of differential thermal analysis (DTA) which gave an estimate of the transition temperature and the transition enthalpy.[138] The same experiment performed on NaOH showed no transition in the temperature region studied (above 110 K).[168] This was followed by a host of experiments on the two compounds including NMR and NQR studies (which are summarized in Section 3.3), adiabatic calorimetry studies, dielectric measurements, X-ray/neutron diffraction, and vibrational spectroscopy (IR/Raman). The low-temperature phase transition in NaOD was found to be first-order and the X-ray/neutron diffraction experiments revealed the space-group symmetry of the low-temperature phase ($P2_1/a$).[140] A detailed analysis of the X-ray reflections of NaOH showed no evidence for a phase transition down to 6 K at ambient pressure.[140]

The results of an adiabatic calorimetry study of NaOD are presented in Figure 3.2 where the results from analogous measurements of NaOH described in the literature are also shown.[139,152] The transition in NaOD is easily visible in its heat capacity curve as the anomaly near $T = 150$ K, but the corresponding transition is clearly absent in the calorimetric data for NaOH. Through an analysis of the sodium deuteroxide heat capacity data, the transition temperature was found to be $T = 153.2 \pm 0.1$ K, and the entropy change during the transition was determined to be $\Delta_{trs}S = 0.864 \pm 0.005$ J·K^{-1}·mol^{-1}.

Figure 3.2. Heat capacity curves of NaOH[139] and NaOD.[152]

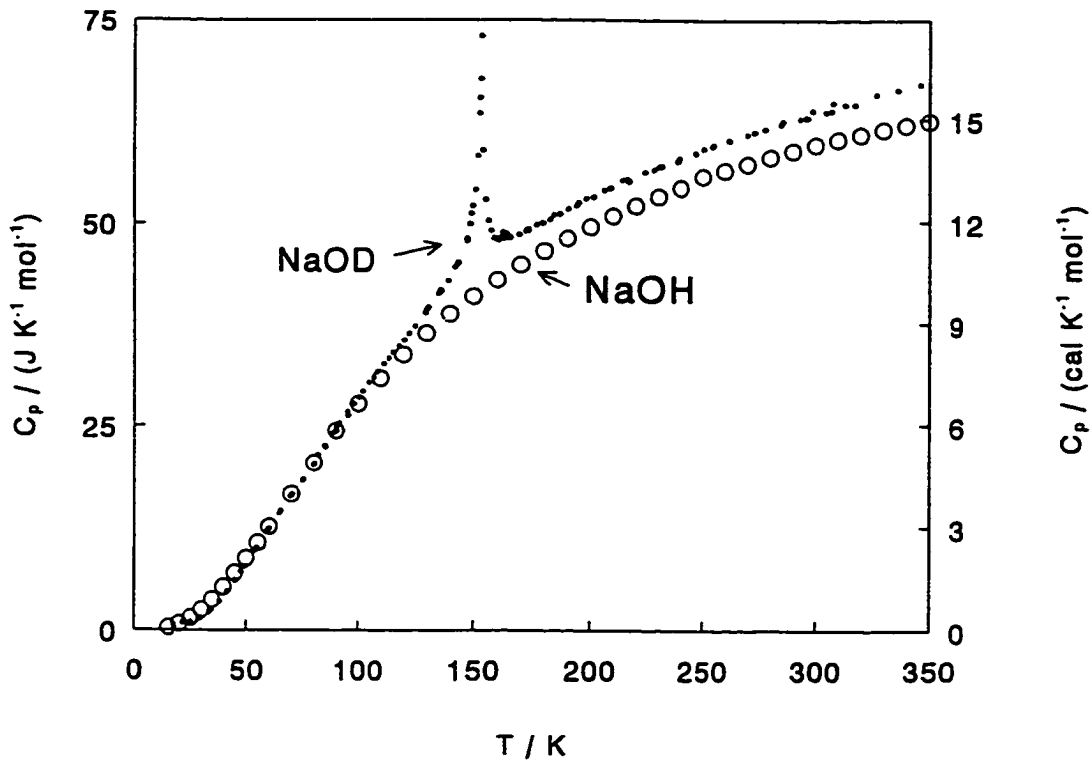

The low-temperature phase transitions in KOH and KOD also have been studied by adiabatic calorimetry and the resulting transition temperatures are listed in Table 3.2.[153,169] These transitions were found to involve entropy changes of 1.01 ± 0.02 $J \cdot K^{-1} \cdot mol^{-1}$ and 1.046 ± 0.006 $J \cdot K^{-1} \cdot mol^{-1}$ for KOH and KOD, respectively, which are comparable to the corresponding value for NaOD. These entropy changes are too small to substantiate an order-disorder mechanism for the low-temperature phase transitions in these compounds. Due to the substantial increase in the transition temperature for KOD over KOH (and also for RbOD *vs.* RbOH, and CsOD *vs.* CsOH; see Table 3.2), tunnelling of the hydrogen (or deuterium) atoms is suspected to play an important role in the low-temperature phase transitions of the alkali-metal hydroxides and deuteroxides.

Dielectric studies also show the appearance of the phase transition in NaOD, and the lack of one in NaOH.[140] Figure 3.3 shows a plot of the temperature dependence of the dielectric constant for both compounds. The NaOH dielectric constant curve shows very little dependence of the dielectric constant with temperature, while the NaOD curve shows a definite anomaly at the phase transition temperature. No extensive analysis of the dielectric data was reported in this study, and, unfortunately, the electric-field frequency at which the dielectric measurements were taken was also not reported. As will become apparent in Chapter 4, dielectric constants are very often dependent on the electric-field frequency, and thus, it is essential to provide this information.

The distinctive shape of the dielectric anomaly in the curve for NaOD is characteristic of a phase transition to an antiferroelectric phase.[140] High-resolution neutron

Figure 3.3. Low-temperature dielectric behaviour of NaOH and NaOD; from reference (140).

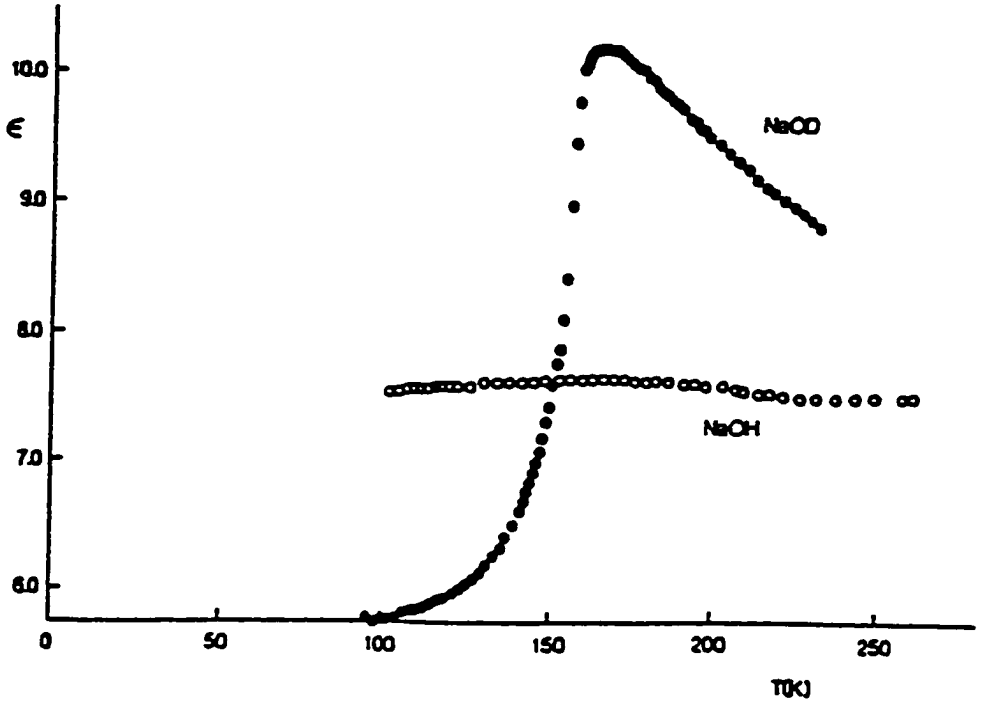

diffraction experiments confirm antiferroelectric ordering of the deuteroxide ions in the low-temperature phase of NaOD.[140] Similar dielectric and neutron diffraction measurements on the low-temperature phases of KOH,[170] KOD,[143,170] CsOH,[145,171] and CsOD[145,171] show that these phases also contain antiferroelectrically ordered hydroxide (deuteroxide) ions. By contrast, the ions in the low-temperature phases of RbOH and RbOD have been found to be ferroelectrically ordered.[144]

Raman spectra for NaOH and NaOD have also been reported at several temperatures under ambient pressure conditions.[172] Figure 3.4(a) shows the Raman spectra for both compounds in the region of the high-frequency O-H (O-D) stretching vibrations at room temperature (293 K) and at 110 K. The only change in the room temperature spectrum of NaOH upon lowering the temperature to 110 K is a slight shift of the absorption to higher wavenumbers. Clearly, this is not the case for NaOD, where the single O-D stretching band at the higher temperature is split at the lower temperature due to the transformation to its low-temperature monoclinic phase at T = 153 K. The Raman spectra in the low-frequency region for both compounds show similar behaviour as indicated in Figure 3.4(b).

Neutron diffraction experiments on the room-temperature phases of KOH, KOD, RbOH, RbOD, CsOH, and CsOD reveal that, despite the differences in space group symmetry in some cases, all of these compounds show similar zig-zag arrangements of hydroxide (deuteroxide) anions as shown in Figure 3.1(c) for the room-temperature structures of NaOH and NaOD. Furthermore, NMR and NQR measurements of these compounds indicate that in some of them, there is dynamical disorder of the protons

Figure 3.4. (a) Raman spectra of NaOH and NaOD in the high-frequency O-H (O-D) stretching region at temperatures of 293 K and 110 K at ambient pressure. (b) Raman spectra of both compounds in the low-frequency region at 293 K and 110 K; from reference (172).

(a)

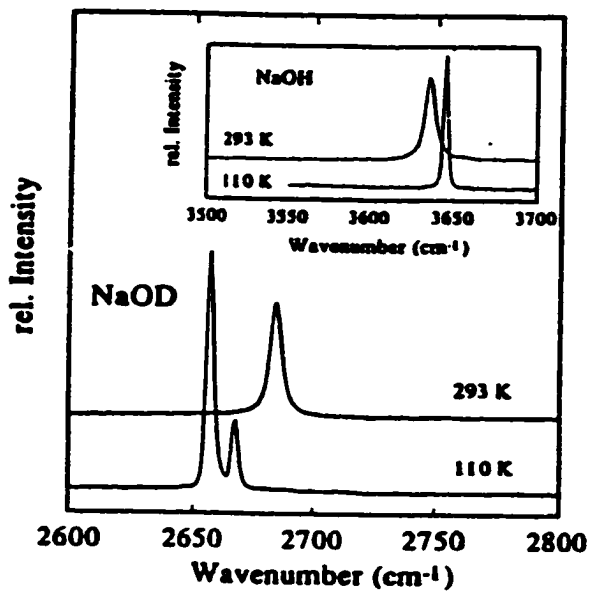

(b)

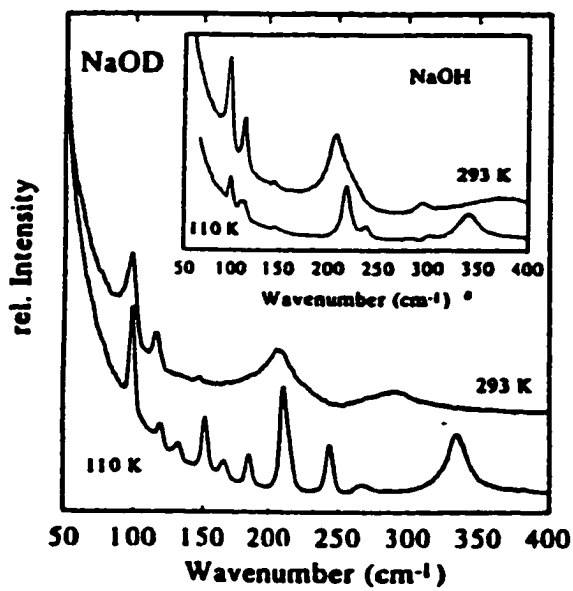

(deuterons) in the room-temperature phase. A survey of the NMR and NQR measurements reported for the alkali-metal hydroxides and deuteroxides is provided in the next section.

3.3 NMR and NQR Studies

All of the alkali-metal hydroxides have been studied by solid-state proton NMR performed on powdered samples.[168,173] With the exception of LiOH, the resulting resonance for each compound shows some structure, *i.e.*, a close doublet with a width and splitting that is noticeably smaller than that for a characteristic Pake doublet. The proton NMR spectrum of LiOH shows only a broad hump with no discernible structure.

The structure of a proton resonance is dependent upon the anisotropy of the dipolar interaction with nearby magnetically active nuclear spins. As mentioned in the previous section, the hydrogen atoms in NaOH are involved in a planar zig-zag chain between two adjacent layers in the solid-state structure, where each hydrogen atom has two neighbouring protons at a distance of 2.09 Å. It is the interaction with these protons that will contribute most to the anisotropy of the dipolar interaction for a particular proton resonance. The nearest-neighbour oxygen atoms are magnetically inactive (I = 0) and will not influence the NMR spectrum.

To account for the observed line shapes in the observed proton NMR spectra, a four-spin planar zig-zag chain model was proposed where only dipolar interactions with

the two nearest hydrogen atoms were directly taken into account.[173] Since the dipolar interaction diminishes with distance, the interactions with more distant atoms would be less significant and these were taken into account through the use of a Gaussian broadening function. The energies calculated from this model (using only the Zeeman term and the first dipolar term in the Hamiltonian) and the resulting calculated spectra revealed a doublet pattern very similar to what is observed experimentally in all of the alkali-metal hydroxides except for LiOH.

Thus, the results obtained from this model indicate that the doublet structure evident in the proton NMR line shapes of the alkali-metal hydroxides is a natural consequence of the zig-zag arrangement of the hydroxide ions in the solid structures of these compounds. Furthermore, lithium hydroxide has a tetrahedral structure that is markedly different from the other members of the group. Each hydrogen atom in LiOH has four symmetrically arranged neighbouring protons which causes a more isotropic dipolar coupling than for the protons in the other alkali-metal hydroxides. This is consistent with the experimental observation that no structure is found in the proton NMR resonance for LiOH.[173]

The majority of the other resonance-type experiments that have been performed on the alkali-metal hydroxides focus on the quadrupolar nuclei in these compounds. Quadrupolar nuclei are those with spin quantum numbers greater than ½. A quadrupolar nucleus interacts with the electric field gradient in its environment giving rise to a set of energy levels. The technique used to probe transitions between these energy levels is known as nuclear quadrupole resonance (NQR). Quadrupolar nuclei can be studied in the

presence of a magnetic field as well. When the quadrupolar interaction dominates the interaction due to the applied magnetic field (Zeeman interaction), the technique is called Zeeman nuclear quadrupole resonance. In the opposite case, *i.e.*, when the Zeeman interaction dominates, the technique is known as quadrupolar perturbed or quadrupolar coupled NMR.

The resonance powder patterns obtained in both of these experiments can be used to obtain two parameters: the nuclear quadrupolar coupling constant (χ), and the asymmetry parameter (η). Both of these quantities are related to the principal components of the electric field gradient tensor. If the nucleus in question is located at a site of axial symmetry (the electric field gradient has axial symmetry), then the asymmetry parameter will be equal to zero. If the nucleus of interest is at a site of tetrahedral, octahedral, cubic, or spherical symmetry, it will have a zero value for the nuclear quadrupole coupling constant as well, which means that the spectrum will not be broadened due to the quadrupolar interaction, and, in principle, sharp lines will be observed. Powdered samples of the alkali-metal hydroxides are generally used in these experiments because of the difficulty in obtaining good-quality single crystals of these compounds.

Several studies have been done involving the ^{23}Na (I = 3/2) nucleus in NaOH. One study obtained values of $\chi = 3.46 \pm 0.02$ MHz and $\eta = 0.40 \pm 0.10$ for the ^{23}Na nucleus at 293 K using a double quadrupole resonance experiment.[174] A similar experiment performed at 77 K yielded $\chi = 3.73 \pm 0.01$ MHz and $\eta = 0.4 \pm 0.1$.[175] These values for the asymmetry parameter were later contradicted by the results from other experiments. A ^{23}Na quadrupolar-coupled NMR experiment of NaOH gave a

powder pattern that was characteristic of a zero asymmetry parameter.[176] Taking into account uncertainties in the experiment, a value of $\eta < 0.05$ was reported at $T = 293$ K with $\chi = 3.54 \pm 0.08$ MHz. This low value for the asymmetry parameter for the ^{23}Na nucleus in NaOH was supported by another determination using Zeeman NQR.[177] Though the discrepancy has yet to be fully resolved, the full scope of evidence and analysis seems to support the near-zero value for η.[168]

A zero (or near-zero) asymmetry parameter for the ^{23}Na nucleus in NaOH might be unexpected since only a two-fold axis of symmetry exists at the sodium site in the NaOH structure and thus, the electric-field gradient is not axially symmetric. However, this can be rationalized as follows.[176] When considering a sodium atom in a single layer of the NaOH structure, it is surrounded by a square array of inverted nearest-neighbour dipoles. Thus, the local symmetry of a sodium atom in a single layer is quite high, with an axially symmetric four-fold rotation axis. The adjacent layer in the structure is 6 Å distant so that the electric field gradient at a sodium site will be dominated by contributions from the atoms within its layer and to a much lesser extent by atoms in neighbouring layers. Thus, the local environment will approximate an axially symmetric electric field gradient giving rise to a near-zero value of η.

The high-temperature polymorphic phase transitions which occur in NaOH are evident in measurements of the ^{23}Na quadrupolar coupling constant as a function of temperature determined by NMR.[178,179] The quadrupolar coupling constant decreases with an increase in temperature throughout the orthorhombic phase, shows a sharper decrease in the monoclinic phase, and suddenly becomes zero at the onset of the cubic

phase. The change of slope at the orthorhombic-monoclinic transition is related to changes in the lattice constants associated with the transition.[141] The sudden drop in the value of χ to zero reflects the structural change to cubic site symmetry for the sodium atoms in the cubic phase.

Measurements of the ^{23}Na NQR frequency in NaOH as a function of temperature show a slight discontinuity at the orthorhombic to monoclinic phase transition as shown in Figure 3.5.[178] The magnitude of the discontinuity was estimated to be 6 $\pm$ 2 kHz. This result is consistent with the "slightly" first-order nature of this phase transition.

High-temperature ^{23}Na NMR and NQR measurements have been performed for NaOD as well,[168,179] and the results are almost identical to those obtained for NaOH reflecting the similarities in the two solids above room temperature. The low-temperature results are very different, however. Measurements of NaOD by ^{23}Na NQR show a sudden drop and a sharp minimum in the NQR frequency at the low-temperature phase transition.[161] The quadrupolar-perturbed ^{23}Na NMR spectrum of NaOD at a temperature of 177 K is indicative of $\eta = 0$ as for NaOH, but a spectrum taken at $T = 77$ K is dramatically different with $\eta = 0.82$, reflecting a definite structural change at low temperature.[161]

Deuterium NMR experiments have also been performed for NaOD. The deuterium quadrupole coupling parameters determined from a spectrum obtained at room temperature are $\chi = 248.1 \pm 1.0$ kHz and $\eta = 0.046 \pm 0.008$.[178,179] The quadrupolar coupling constant decreases with an increase in temperature and drops to zero when the transition to the cubic phase is reached. The dominant contribution to the electric field

Figure 3.5. Temperature dependence of the ^{23}Na NQR frequency in NaOH. The inset shows a magnified view at the temperature of the orthorhombic to monoclinic phase transition where there is a slight discontinuity of 6 $\pm$ 2 kHz; from reference (178).

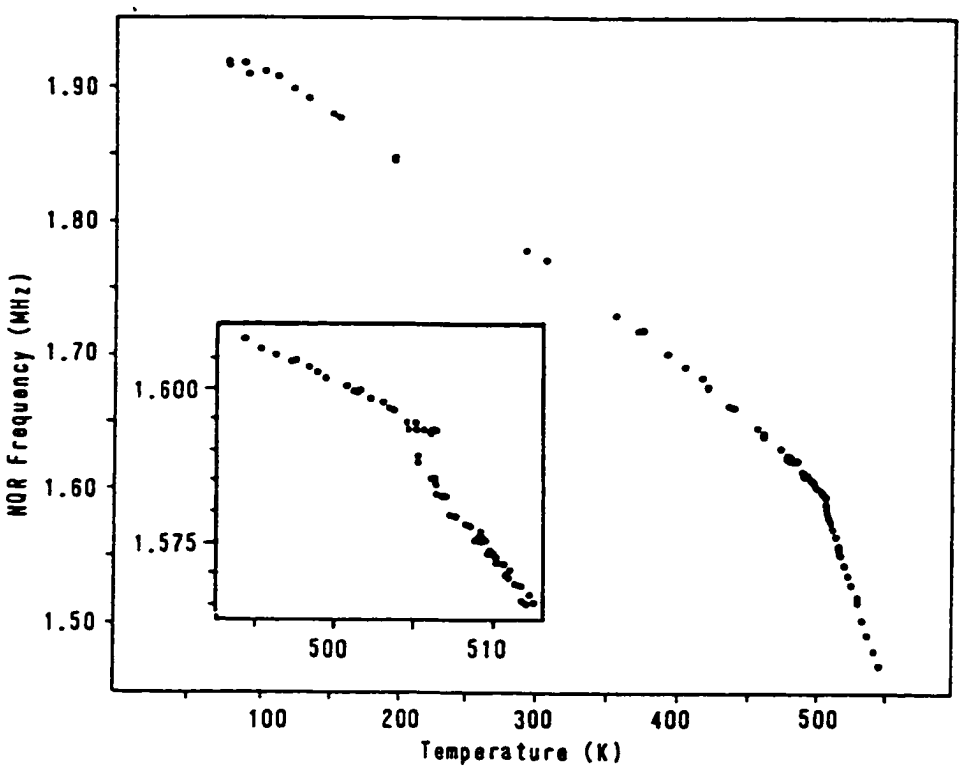

gradient for a deuterium atom in NaOD is the axially symmetric electron distribution in the O-D bond which is reflected in the low value for the asymmetry parameter measured experimentally. The sudden drop in the quadrupole coupling constant at the phase transition to the cubic phase is due to the rapid isotropic reorientational motion of the OD^- ion in the cubic phase.[168]

Deuterium NMR has been used to probe the OD^- ion dynamics in CsOD through the determination of the quadrupolar coupling parameters as a function of temperature.[180] The powder patterns obtained are characteristic of a large value for the asymmetry parameter which rises with decreasing temperature from 0.25 at the cubic phase transition to 1.0 at the low-temperature phase transition at 247 K, with $\eta \sim 0$ in the low-temperature phase. Furthermore, the deuterium quadrupolar coupling constant undergoes a sharp change at the low-temperature phase transition, doubling in value below 247 K compared to the value above the transition temperature.

If the electric field gradient at the deuterium atom in the OD^- ion is determined primarily by the electron distribution of the oxygen atom and the O-D bond, then a deuterium atom that is stationary (relative to the NMR timescale) will have a zero asymmetry parameter as observed for NaOD at room temperature. However, a deuterium atom that is flipping rapidly between two orientations relative to its parent oxygen atom, as shown in Figure 3.6, will show a high η value, due to angular averaging of the electric field gradient tensor. Calculations based on a two-fold flipping model successfully account for the observed behaviour of the deuterium quadrupole coupling parameters observed for CsOD.[180] Thus, the deuterium NMR measurements indicate that

Figure 3.6. Reorientational motion between two symmetry-related orientations of the OD^- ion in the room-temperature orthorhombic phase of CsOD as indicated by ^2H-NMR measurements. This flipping motion can be characterized by the flip angle θ.

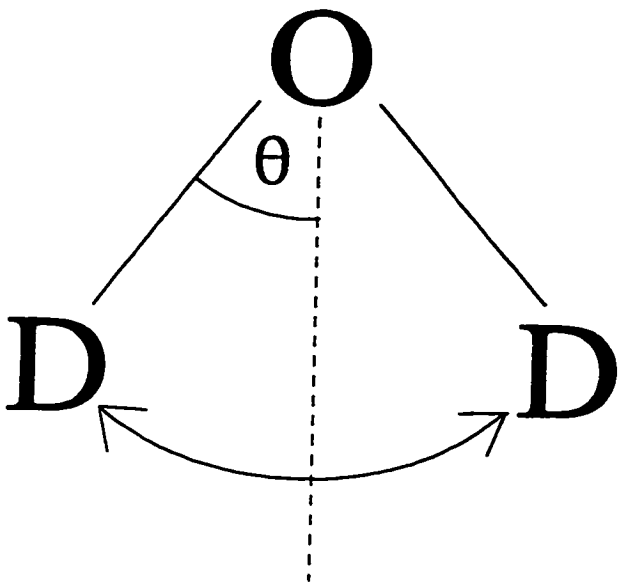

the OD^- ion is reorienting rapidly between two different sites in the room temperature orthorhombic phase. In fact, calculations using the room-temperature $\eta = 0.68$ value suggest a flip angle of 31° for this reorientational motion at room temperature.[180] The drop in the asymmetry parameter to zero indicates an absence of this reorientational motion in the low-temperature phase.

Potassium hydroxide and deuteroxide have also been the subject of NMR investigations, specifically ^{39}K and ^2H NMR, in the temperature region of the low-temperature antiferroelectric phase transition.[181] The ^2H NMR results for KOD are especially interesting since the temperature behaviour of the quadrupolar coupling constant and the asymmetry parameter are very similar to that observed for CsOD. The value of χ shows a sharp increase upon crossing the phase transition temperature of 253 K from the high-temperature side to the low-temperature side. The ^2H asymmetry parameter is $\sim$ 0.4 at room temperature, rises to a value of $\sim$ 0.6 as the temperature is lowered to 253 K, then drops to near zero below the transition temperature. The explanation used to account for the CsOD ^2H NMR data can be applied here as well, *i.e.*, the OD^- ions in KOD are undergoing rapid reorientational motion between two symmetrically related sites in the room temperature phase, but this flipping motion ceases in the low-temperature phase.[181]

Overall, measurements of the alkali-metal hydroxides and deuteroxides by NMR and NQR reveal the versatility of these two techniques. Data obtained from both techniques are able to detect the various phase transitions which occur in the alkali-metal hydroxides and deuteroxides. These resonance methods are also useful for gaining some

structural information, as well as probing the reorientational dynamics of the hydroxide (deuteroxide) ions in the solid-state phases of these compounds.

3.4 High-Pressure Studies

The NMR studies described in the previous section indicate dynamic reorientation of the OH^- (OD^-) ions in the room-temperature phases of KOH(D) and CsOH(D). Structural studies by X-ray/neutron diffraction[143,144,145] and also infrared/Raman studies[182,183] support this conclusion and also show that the same type of reorientational disorder occurs in the room-temperature phase of RbOH(D). The same studies show that in the low-temperature phases of these compounds, the hydrogen (deuterium) atoms become localized through the formation of weak hydrogen bonds with neighbouring oxygen atoms to give hydrogen-bonded zigzag chains. This occurs despite the long R_{oo} distances, greater than 3.2 Å in all cases.[143,144,145] In KOH(D) and CsOH(D), the net dipole moments of adjacent zigzag chains are arranged antiparallel to each other and thus, the low-temperature structures are antiferroelectric.[143,145,170,171] The opposite behaviour is observed for RbOH(D), where adjacent chains have parallel dipole moments, and the low-temperature orthorhombic structure is ferroelectric.[144]

It is thought[184] that repulsion between the sodium cations and the protons in NaOH is strong enough to keep neighbouring layers in the structure sufficiently distant to prevent hydrogen bonds from forming. Yet, in NaOD, the formation of hydrogen

bonds characterize its deuterium-induced low-temperature monoclinic phase,[140,172] which consists of hydrogen-bonded zigzag chains similar to those found in the heavier alkali-metal hydroxides and deuteroxides. The ordering of the chains in this phase of NaOD is antiferroelectric as for KOH(D) and CsOH(D). The capacity for hydrogen bonds to form in NaOD which seem unable to form in NaOH is certainly puzzling, especially considering the virtually identical behaviour of the two compounds at higher temperatures.[141] It should be noted that no evidence for hydrogen bonding exists for either lithium hydroxide[157,185] or lithium deuteroxide[186] in their ambient pressure tetragonal phases.

It is interesting that evidence from infrared studies of KOH(D),[187] and IR and Raman studies of RbOH(D) and CsOH(D), as well as isotopic mixtures of the hydrogenated and deuterated forms of these compounds,[182,183] support the conclusion that the hydrogen bonds in the deuteroxides are stronger than the corresponding hydrogen bonds in the hydroxide compounds. This implies that some slight differences must exist in the structural parameters of the deuterated forms *versus* their hydrogenated counterparts, most importantly, a slightly smaller O-O hydrogen-bond distance (R_{OO}) for the deuterated compound. X-ray diffraction measurements of these compounds confirm this.[143,144,145] For the case of NaOH compared to NaOD, it is known that the distance between the layers in NaOD is smaller than in NaOH by 0.3% to 0.6%.[141]

Hydrogen-bonded modifications exist at low temperature for KOH(D), RbOH(D), and CsOH(D), but not for the lightest member of this family, LiOH(D). For NaOH and NaOD, a low-temperature hydrogen-bonded modification exists for NaOD but not for

NaOH. It seems possible that the potential hydrogen-bond distance (R_{OO}) in NaOH (3.488 ± 0.008 Å at room temperature) is very close to a threshold value below which hydrogen bonds will form, but above which hydrogen bonds will not form. For NaOH, the hydrogen-bond distance could be just above the threshold value which prohibits the formation of a hydrogen-bonded structure and thus, no phase transition to a low-temperature hydrogen-bonded phase would occur. The slightly smaller hydrogen-bond distance in NaOD could place it at just below this threshold value so that a hydrogen-bonded modification can form at low temperature.

Since the interlayer distance (and thus, R_{OO}) in NaOH would decrease upon the application of pressure, a method to test this postulate would be to study the polymorphic behaviour of NaOH under pressure and look for any evidence indicating a phase transition to a hydrogen-bonded phase. Several high-pressure studies of NaOH have been reported in the literature, a summary of which will now be presented.

An initial high-pressure study of NaOH was carried out at temperatures between 0°C and the melting point for pressures up to 40 kbar.[188] The technique of differential thermal analysis (DTA) was used to detect any phase transitions. Three high-pressure phases were found, two of which were found to exist only at temperatures greater than 250°C. The stability regime of the third high-pressure phase was studied only at temperatures greater than 0°C. The atmospheric-pressure orthorhombic phase of NaOH transforms into this high-pressure phase at a pressure of about 8 kbar at T = 0°C. Although no low-temperature experiments were performed in this study, it is evident that the phase boundary between these two phases will extend to temperatures below 0°C.

The structures of the high-pressure phases were not determined.

A further high-pressure study found a high-pressure phase which exists at temperatures greater than 70°C and pressures greater than 13 kbar.[189,190] The low-temperature high-pressure phase detected in the previous study was also observed. The structures of both high-pressure phases discovered in this experiment were determined by X-ray diffraction. The high-temperature phase was found to have the cubic NaCl structure which is postulated to have static disorder. The low-temperature phase is orthorhombic with space group *Pbcm* ($Z = 4$). Since only X-ray diffraction was used, the positions of the hydrogen atoms could not be determined in this structure. This high-pressure study covered the temperature range from 0°C to approximately 150°C and the pressure range from 0 - 50 kbar.

The high-pressure polymorphic behaviour of both sodium hydroxide and sodium deuteroxide at low temperatures has been examined using Raman spectroscopy.[172] The absorptions in the Raman spectra for both compounds were monitored as a function of pressure for several different temperatures. The disappearance of one set of Raman bands with the appearance of new bands is direct evidence for a phase transition to a different solid structure. A representative example of these high-pressure Raman measurements is given in Figure 3.7, where the pressure dependence of the O-H (O-D) stretch modes for NaOH and NaOD are shown for a temperature of 200 K. Two phase transitions are evident in both compounds from the data shown in these spectra. The atmospheric-pressure orthorhombic phase converts to an intermediate-pressure phase characterized by a splitting of the stretch mode. A further increase in pressure results in a high-pressure

Figure 3.7. Pressure dependence of the O-H (O-D) stretch modes for (a) NaOD, and (b) NaOH, as measured by Raman spectroscopy at $T = 200$ K. Phase transitions from phase III to phase IV and from phase IV to phase V occur at roughly 0.9 GPa (9 kbar) and 8 GPa (80 kbar), respectively, for NaOH, and at 0.5 GPa (5 kbar) and 7 GPa (70 kbar), respectively, for NaOD; from reference (172).

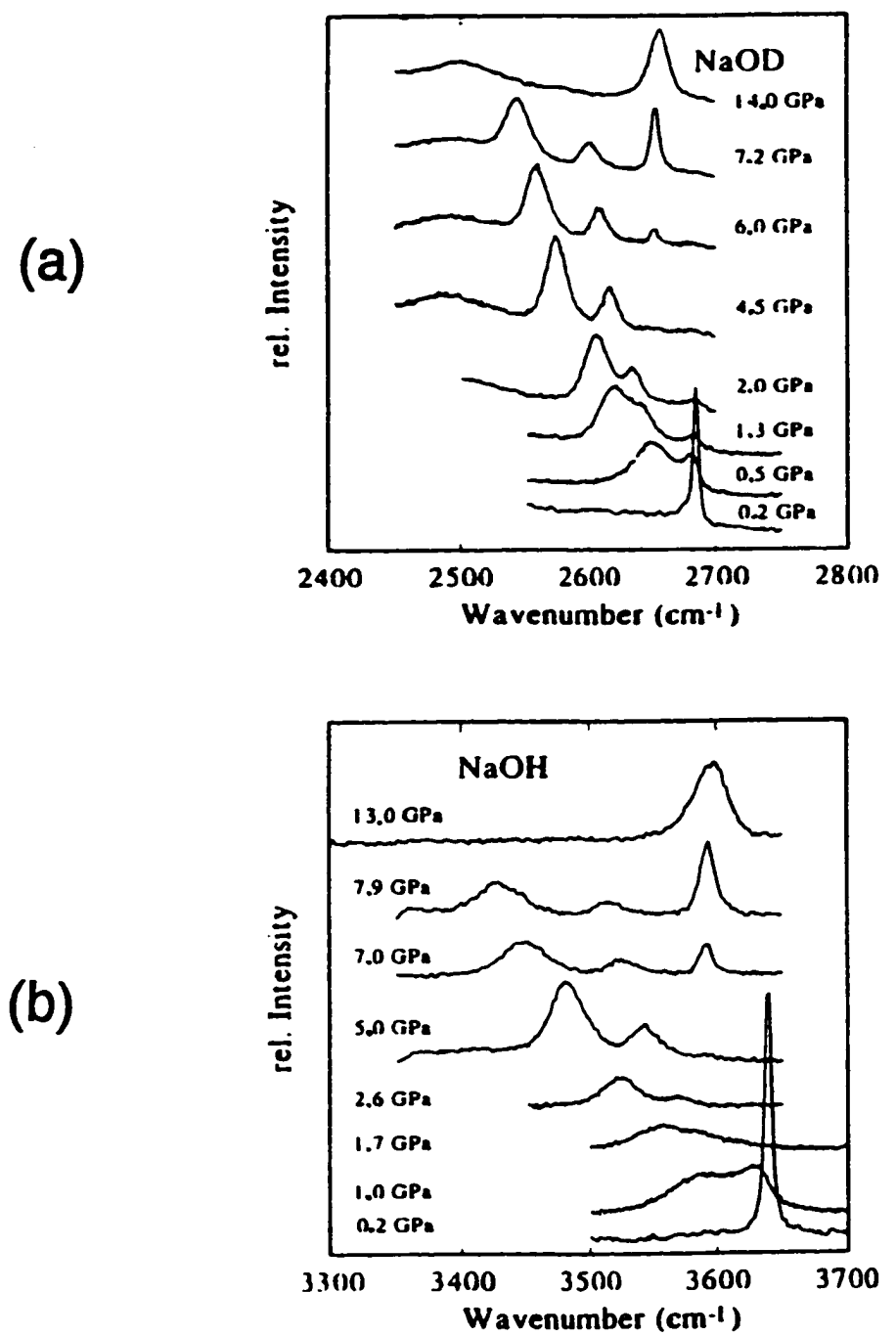

phase with only one O-H (O-D) stretch absorption. The transition pressures are slightly lower for NaOD compared to those for NaOH. The intermediate-pressure and high-pressure phases have been named phase IV and phase V, respectively.

An interesting point to note from the Raman spectra is that the frequencies of the two stretch-mode absorptions in phase IV decrease strongly with an increase in pressure. Such pressure-dependent behaviour of O-H (O-D) stretch modes is commonly accepted as a good indication that hydrogen bonding is present.[191] Furthermore, the splitting of the atmospheric-pressure orthorhombic-phase stretch mode at the orthorhombic/phase IV phase transition is characteristic of the low-temperature hydrogen-bonded monoclinic phase observed for NaOD at atmospheric pressure (see Figure 3.4(a)). Thus, it seems likely that phase IV which is observed at intermediate pressures for both NaOH and NaOD at 200 K, corresponds to the monoclinic phase observed for NaOD observed at temperatures below 153 K at atmospheric pressure. This has been confirmed by pressure-dependent Raman-spectral measurements taken at different temperatures.[172]

By combining all of the Raman-spectral data obtained at various pressures and temperatures, approximate phase diagrams for NaOH and NaOD were derived for the low-temperature region.[172] These are shown in Figure 3.8. The application of pressure is needed to induce the hydrogen-bonded monoclinic phase (phase IV) in NaOH which exists for NaOD at atmospheric pressure. A comparison of the diagrams for the two compounds indicates that if the temperature axis of the NaOH phase diagram were shifted by less than 10 kbar to higher pressures, the two phase diagrams would be virtually identical. Thus, deuteration of NaOH seems to correspond to an increase in pressure.

Figure 3.8. Phase diagrams derived for (a) NaOH, and (b) NaOD, from Raman spectroscopy measurements taken at various temperatures and pressures; styled after reference (172).

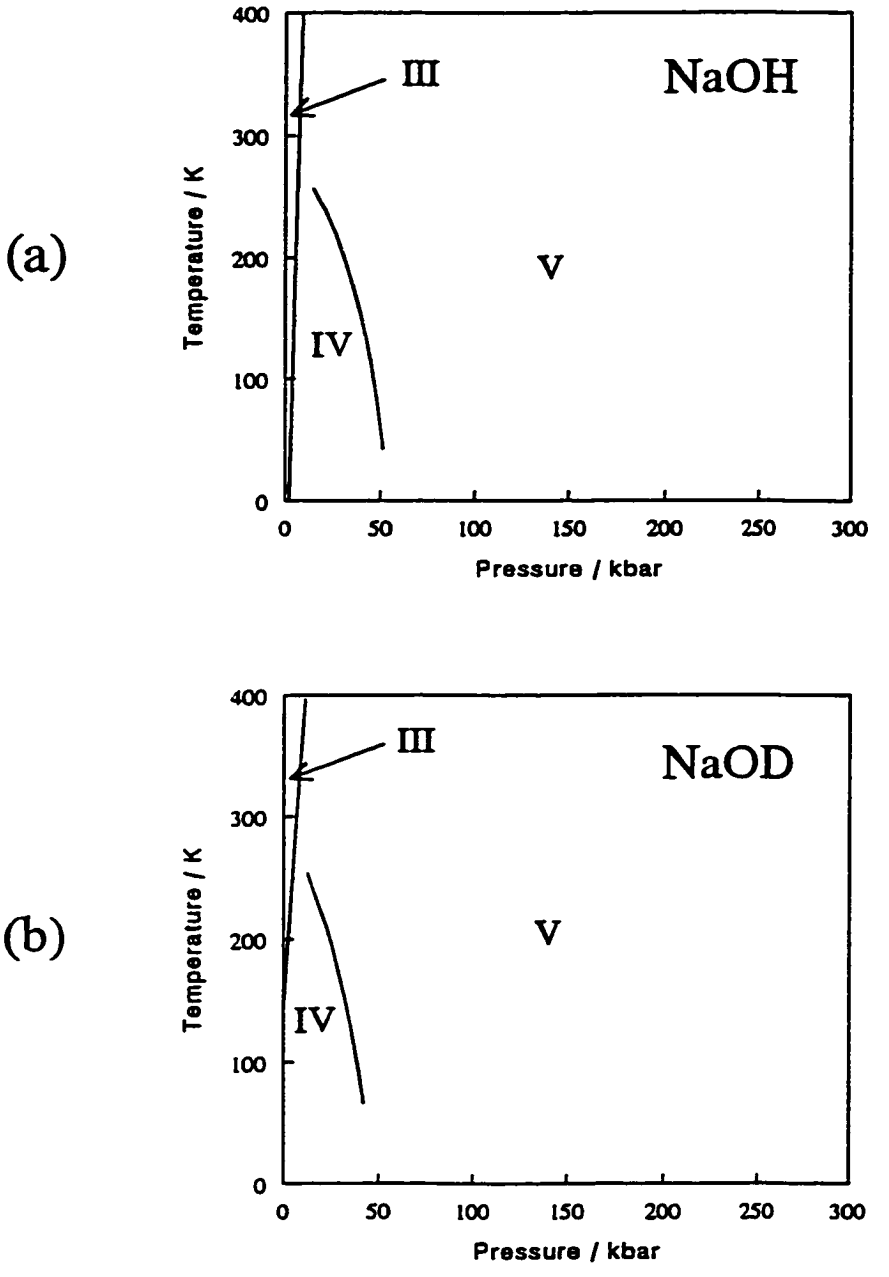

This phenomenon was also observed for $(NH_4)_3H(SO_4)_2$ as described back in Section 2.3.1.[56]

Phase V, observed for NaOH and NaOD at high pressures, is the common high-pressure phase that was found for NaOH in the high-temperature high-pressure studies described previously. The O-H (O-D) stretching frequency for this phase shows almost no pressure dependence as determined by the Raman spectra.[172] This behaviour indicates the absence of linear (or nearly linear) hydrogen bonds for phase V. However, bent or bifurcated hydrogen bonds typically show very weak pressure dependences, and therefore cannot be ruled out. More information about the structure of phase V was gained from a powder neutron-diffraction study of this high-pressure phase in NaOD.[192] The space group was confirmed to be *Pbcm*, and the presence of bent hydrogen bonds was inferred from the positions determined for the deuterium atoms.

The high-pressure behaviour of all the other alkali-metal hydroxides and deuteroxides has been examined by X-ray powder diffraction[184] and vibrational spectroscopy.[193] For KOH(D), RbOH(D), and CsOH(D), the O-H (O-D) stretching absorption as measured by Raman spectroscopy is very broad with a large halfwidth at room temperature and atmospheric pressure. This is interpreted as being a consequence of the dynamic disorder of the hydroxide (deuteroxide) ions in the room-temperature atmospheric-pressure phases of these compounds. The room-temperature Raman spectra for KOH(D) and RbOH(D) show pressure-dependent behaviour very similar to those for NaOH and NaOD at 200 K, *i.e.*, two pressure-induced phase transitions are observed. The same measurements performed on CsOH(D), however, show only one phase

transition.

The structures of all of these pressure-induced phases have been determined by X-ray diffraction.[184] The intermediate-pressure phases in KOH(D) and RbOH(D), as well as the pressure-induced phase in CsOH(D) were found to correspond to the low-temperature phases observed for these compounds at atmospheric pressure. The X-ray diffraction data for the high-pressure phases in KOH(D) and RbOH(D) could be satisfactorily fitted to the orthorhombic *Pbcm* space group, just as for NaOH and NaOD. In contrast to the high-pressure structures for NaOH and NaOD, the high pressure forms of KOH(D) and RbOH(D) exhibit strong hydrogen bonding as indicated by a strong decrease of the O-H (O-D) stretching-mode frequencies with pressure.[193] High-pressure infrared studies of CsOH(D) show no indication of a phase transition to the *Pbcm* phase at pressures up to 250 kbar.

Lithium hydroxide and its corresponding deuterated form have also been studied by high-pressure vibrational spectroscopy.[185,186] A transition to a high-pressure phase was found in both compounds by monitoring pressure-induced changes in the O-H (O-D) stretching region of the infrared and Raman spectra. A slightly negative pressure dependence was observed for the O-H (O-D) stretching frequencies in the high-pressure phase indicating the presence of weak hydrogen bonds. A powder neutron diffraction study of the LiOD high-pressure phase revealed that it has a monoclinic structure with space group $P2_1/a$ ($Z = 4$) and likely bifurcated hydrogen bonds.[186]

3.5 Possible Explanations

The high-pressure studies of the alkali-metal hydroxides and deuteroxides show that the extensive polymorphism observed for these compounds at ambient pressure continues into the high-pressure regime. More importantly, the high-pressure studies of NaOH seem to indicate that the phase transition to the low-temperature monoclinic phase (phase IV) observable in NaOD at atmospheric pressure, does occur in NaOH at higher pressures. Strictly speaking, though, the structure of phase IV of NaOH has not yet been directly determined from diffraction experiments. However, evidence seems to point to an analogy between the ambient-pressure low-temperature monoclinic phase of NaOD and the intermediate-pressure phase IV of NaOH. Phase IV of NaOH and the low-temperature monoclinic phase of NaOD occupy similarly placed positions in the phase diagrams derived for the two compounds from Raman spectroscopy (Figure 3.8). The two phases both have similar Raman spectra and, furthermore, analysis of the Raman-spectral data indicates that both phases consist of hydrogen-bonded OH^- (OD^-) ions. Thus, it seems almost certain that pressure induces the polymorphic phase transition in NaOH that exists at atmospheric pressure only in NaOD.

However, there are still some problems or questions that have to be addressed related to the behaviour of NaOH at atmospheric pressure; specifically, concerns about the proton disorder in NaOH. The orthorhombic room-temperature structures of NaOH and NaOD are provided in Figure 3.9(a).[140,152,194] At atmospheric pressure, NaOD undergoes a low-temperature phase transition at $T = 153$ K to a monoclinic form which

Figure 3.9. (a) Room-temperature orthorhombic structure of NaOH and NaOD. (b) Monoclinic structure of NaOD at T = 77 K; from references (152) and (194).

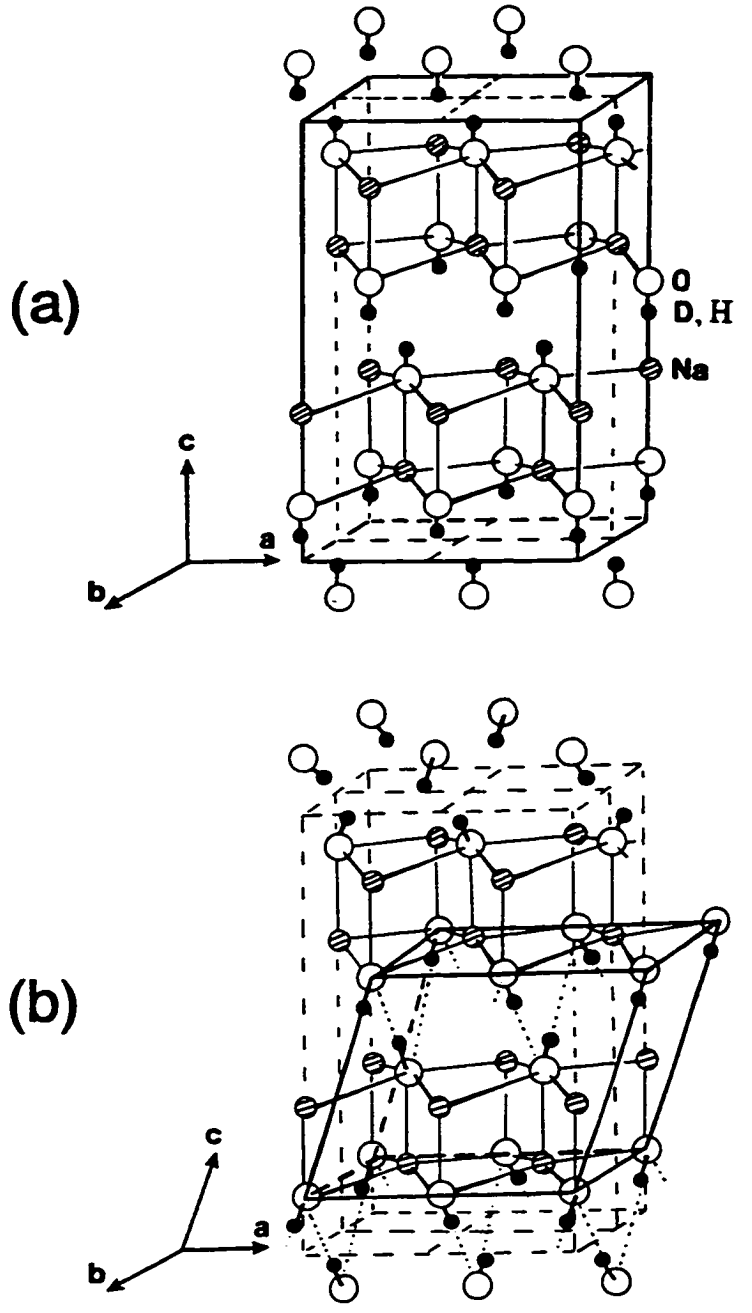

is shown in Figure 3.9(b). This phase transition is deuterium-induced at ambient pressure, *i.e.*, the analogous transition is absent for NaOH unless significant pressure is applied. An examination of Figure 3.9(b) shows that in the monoclinic form of NaOD, each deuterium atom is tilted toward an oxygen atom in a neighbouring layer to form a hydrogen bond. This occurs in the low-temperature forms of the heavier alkali-metal hydroxides and deuteroxides as well.[143,144,145] Looking at the orthorhombic form, it is evident that each deuterium atom has two equidistant oxygen atoms in its neighbouring layer from which to choose for formation of a hydrogen bond. To form the monoclinic phase, it seems equally likely that the deuterium atoms could tilt toward one of their neighbouring oxygen atoms or the other. Thus, this situation could be described by a double-well potential.

Measurements by NMR show that in the room-temperature phases of CsOD and KOD, the deuterium atoms do move rapidly back and forth between two symmetry-related orientations with respect to their parent oxygen atoms.[180,181] Measurement of the asymmetry parameter of the deuterium atoms at room temperature for NaOD give a value slightly above zero.[178] This is indicative of a stationary deuterium atom, with the term "stationary" being interpreted as slow relative to the NMR timescale. However, no such studies have been reported concerning the protons in NaOH, presumably because of the difficulties inherent in solid-state proton NMR. Sodium hydroxide and its deuterated counterpart are clearly different at low temperatures as shown by their different polymorphic behaviour and thus, blindly assuming that results for NaOD will apply equally for NaOH would be inappropriate.

A quick glance at the phase transition temperatures listed in Table 3.2 reveals that for the heavier alkali-metal hydroxides, deuteration increases the low-temperature phase transition temperature by 13 K - 35 K. This is consistent with tunnelling of the hydrogen (deuterium) atoms between the two minima of a double-well potential being involved in the mechanism of this transition. A double-well potential seems inherent in the low-temperature monoclinic structure of NaOD and possibly exists in the orthorhombic forms of NaOD and NaOH as well, just as it does for the room-temperature structures of the heavier members of this group of compounds.

Regardless, the phase transition which occurs in NaOD at $T = 153$ K involves an entropy change[152] of 0.864 $J \cdot K^{-1} \cdot mol^{-1}$. A comparison of the orthorhombic and monoclinic structures of NaOD by neutron diffraction show that the positions of the sodium atoms and the oxygen atoms in the monoclinic structure are changed only slightly from their room temperature values.[140] Thus, the entropy change during this transition is virtually totally due to a change in the disorder of the deuterium atoms.

Since the polymorphic behaviours of NaOH and NaOD are so similar at high temperatures, it would be expected that the hydrogen atoms in NaOH and the deuterium atoms in NaOD would have similar amounts of disorder associated with their structural location in their orthorhombic phases (not considering the difference in entropy as a result of the different internal vibrational frequencies of the more massive NaOD *versus* NaOH). Yet, the low-temperature phase transition in NaOD removes 0.864 $J \cdot K^{-1} \cdot mol^{-1}$ of disorder associated with the deuterium atoms. For NaOH to be in accordance with the third law of thermodynamics, it should remove an analogous amount of disorder

associated with its hydrogen atoms. One possible mechanism by which this could occur is through a phase transition similar to the one that is observed for NaOD. However, at atmospheric pressure at least, this does not happen.

A possible explanation that would resolve this discrepancy is that this extra disorder of the hydrogen atoms in NaOH does not get removed but persists down to a temperature of absolute zero. This gives rise to what is known as residual entropy or frozen-in disorder. Such a phenomenon is exhibited by several substances, and as the quest for residual entropy plays an important role in the research work in this thesis, the concept itself warrants a more detailed description.

Chapter 4: Residual Entropy and Glassy Crystals

4.1 Residual Entropy

4.1.1 Introduction

Entropy is one of the fundamental concepts in thermodynamics which, by its most precise definition, is defined by the following equation:

$$dS \equiv \frac{dq_{rev}}{T}, \tag{4.1}$$

where dS is an infinitesimal entropy change between two states of a system, dq_{rev} is the infinitesimal change in heat between the two states of a system linked by a reversible process, and T is the absolute temperature. Entropy forms the basis of the second law of thermodynamics which states in a very general form the criterion necessary for a process to be spontaneous: the process must result in the increase of the total entropy of the universe.

Entropy can also be described on a quantum-mechanical level through the use of the statistical mechanical Boltzmann equation

$$S = k_B \ln \Omega, \tag{4.2}$$

where S is the entropy of the system per particle, k_B is the Boltzmann constant, and Ω is the total number of quantum states accessible by the system under the prevailing conditions. Equation (4.2) can also be written as

$$S_m = R\ln\Omega\,, \tag{4.3}$$

where R is the gas constant, and now the entropy (S_m) is the entropy per mole of particles. The important point to realize concerning the Boltzmann equation is that the entropy increases if more quantum states become available to the system. Since a more disordered system will generally have more quantum states available to it compared to a more ordered one, this naturally leads to the familiar connection between entropy and the disorder of a system. If the disorder of a system increases, the entropy of the system must increase as well.

Entropy is also very strongly associated with the third law of thermodynamics, which says that the entropy of all substances in thermodynamic equilibrium will approach zero as the temperature approaches absolute zero. Considering this statement in light of the Boltzmann equation, the third law implies that all equilibrated systems are completely ordered at $T = 0$ K since zero entropy implies that only one quantum state is available to the system ($\Omega = 1$) by equation (4.3). However, there are certain systems that have been found to possess a non-zero entropy at $T = 0$ K and are thus disordered at absolute zero in apparent contradiction of the third law of thermodynamics. This leads to the concept of residual entropy.

Residual entropy can be defined as the entropy that a system possesses at a temperature of absolute zero. One might consider residual entropy to be a purely theoretical concept since a temperature of absolute zero is unattainable. However, it can be calculated from extrapolated experimental data relatively easily without actually having to reach absolute zero.

To calculate the residual entropy of a substance, two independent values for the molar entropy of the compound at a specified temperature and pressure are needed. One of these values must be determined from calorimetric measurements and is denoted as *S(cal)*. This quantity is the entropy of the substance relative to the entropy at $T = 0$ K and is given by the following equation:

$$S(cal) = S_m - S_0 = \int_0^T \frac{C_p'}{T} dT + \sum_{trans.} \left[\frac{\Delta_{trs}H}{T_{trs}} \right], \qquad (4.4)$$

where S_m is the entropy at the specified temperature and pressure, S_0 is the entropy of the substance at absolute zero, C_p' is the smooth-curve heat capacity (excluding phase transitions), $\Delta_{trs}H$ is the enthalpy change due to a phase transition, and T_{trs} is the temperature of the phase transition. The second term on the right-hand side of equation (4.4) represents the contribution of entropy changes due to any phase transitions which occur between $T = 0$ K and the temperature of interest.

The second independent value for the molar entropy of the compound can be found by several methods.[195] For a gas, this value can be accurately determined using spectroscopic data and the appropriate statistical mechanical equation (*S(spec)*). For an ionic substance, the entropy obtained from the study of a suitable equilibrium involving the compound is required (*S(eq)*). Both *S(spec)* and *S(eq)* give the absolute entropy of the substance at the desired temperature and pressure. Once *S(cal)* and *S(spec)* or *S(eq)* are known, the residual entropy (*S(res)*) is simply calculated as

$$S(res) = S_0 = S(eq) - S(cal) = S(spec) - S(cal), \qquad (4.5)$$

giving directly the entropy (disorder) of the substance at $T = 0$ K. For most substances, $S(res) = 0$ in accordance with the third law of thermodynamics. However, there are many common substances which have a non-zero residual entropy,[31] including ice[20,21] ($S(res) = 3.45$ J·K^{-1}·mol^{-1}) and carbon monoxide[196] ($S(res) = 4.69$ J·K^{-1}·mol^{-1}).

4.1.2 Molecular Interpretation of Residual Entropy

In general, it can be said that there are two factors which determine the stability of a particular system under a given set of conditions: thermodynamic factors and kinetic factors. These two factors are constantly at battle with each other, with the victor deciding which form of a substance is stable at a particular temperature and pressure, and also which products will form in a particular reaction. This fact is a common tool of synthetic chemists, who through the suitable manipulation of reaction conditions can tip the balance in favour of kinetic products or thermodynamic products being formed in the reaction. The existence of diamonds under everyday conditions is an example where kinetic factors win out over thermodynamics. Graphite is the more thermodynamically stable form of carbon, but the kinetic barrier for the graphite-to-diamond conversion process is so large that the conversion does not take place to any significant extent over the course of a human lifetime. In thermodynamic terms, at room temperature and pressure, diamond would be called a metastable form of carbon because it represents a

local minimum in the Gibbs energy, but cannot reach the global minimum (graphite) because it is stabilized kinetically.

The existence of residual entropy is another case where kinetics is the victor over thermodynamics. In order to explain in detail the cause of residual entropy in some substances on a molecular level, it is best to consider a specific example. The system that will be used for this purpose is carbon monoxide (CO).

Carbon monoxide is a linear molecule with a very small dipole moment,[11] 0.112 D with the negative end on carbon. In the solid state, each CO molecule can have one of two orientations: either with its dipole aligned with respect to its neighbours (lower energy orientation) or not aligned (higher energy orientation) as shown in Figure 4.1. This type of disorder is known as head-to-tail disorder.

Due to the small dipole moment of carbon monoxide, the energy difference between these two orientations is very small. In fact, this energy difference has been estimated[197] to be only 18.9 $J \cdot mol^{-1}$. This value can be used to consider the equilibrium ratio of the populations of molecules in the two different orientations using the Boltzmann distribution equation

$$\frac{N_2}{N_1} = e^{-\Delta E/RT}, \qquad (4.6)$$

where N_2 and N_1 are the numbers of molecules in the higher energy and lower energy orientations, respectively, and ΔE is the energy difference between the two orientations. For an amount of thermal energy, RT, much greater than ΔE, the equilibrium population ratio will be very nearly equal to one, according to equation (4.6), implying equal

Figure 4.1. Head-to-tail disorder of carbon monoxide. Each CO molecule can arrange itself in two orientations: (a) with dipole aligned (lower energy), or (b) with dipole not aligned (higher energy) with respect to its neighbours.

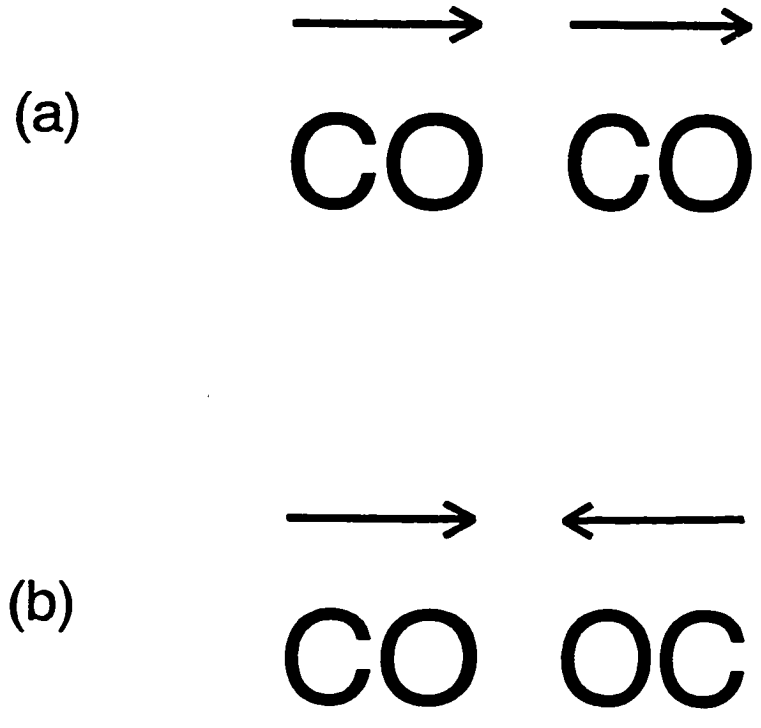

numbers of molecules in the higher energy and lower energy orientations at high temperatures.

As the temperature is lowered, more and more molecules will gradually favour the lower energy orientation, but a significant decrease in the population ratio will not occur until the thermal energy, RT, is of the order of ΔE. For $\Delta E = 18.9\ \text{J·mol}^{-1}$, this will be at a temperature of ~ 2 - 3 K. As the temperature approaches absolute zero, all of the molecules will be in the lower energy orientation with all dipoles aligned, since

$$\lim_{T\to 0^+} (N_2 / N_1) = \lim_{T\to 0^+} e^{-\Delta E/RT} = 0 . \qquad (4.7)$$

Thus, at $T = 0$ K, one would expect the molecules to have only one available orientation (quantum state), so $\Omega = 1$, and according to equation (4.3), $S = R\ln\Omega = 0$ at $T = 0$ K in accord with the third law. However, this is not observed. Carbon monoxide has a residual entropy[196] of $4.69\ \text{J·K}^{-1}\text{·mol}^{-1}$.

The reason for this discrepancy is that, so far, only the thermodynamics of the system has been considered. The situation is not simply two energy levels (orientations) with an energy difference (ΔE) between them. In reality, there is a kinetic barrier between the two orientations which must be overcome before reorientation can take place. The height of this kinetic barrier is the activation energy (E_a) for reorientation. In general, thermodynamics describes only the beginning and the end of a process, while kinetics describes what happens in-between.

As mentioned previously, for carbon monoxide at high temperatures, there will be about equal numbers of molecules in each orientation. When the temperature is

lowered to about 10 K and below, a significant number of molecules will tend to reorient to the thermodynamically favoured lower-energy orientation with aligned dipoles. However, the kinetically controlled rate of reorientation at such low temperatures will be negligible if the activation energy for reorientation is relatively large as shown by the Arrhenius equation,

$$k_T = Ae^{-E_a/RT}, \tag{4.8}$$

where k_T is the rate constant at a given temperature, and A is the pre-exponential factor. According to equation (4.8), a large activation energy and a lowering of the temperature result in a decrease in the rate of reorientation.

For the case of carbon monoxide, the activation energy for the reorientational motion has been determined using dielectric relaxation measurements[198] and found to be 6.13 $kJ \cdot mol^{-1}$. Using this value of E_a along with a temperature of 5 K to calculate the exponential part of equation (4.8) results in a value of 9×10^{-65}, a very small number. Thus, the rate of reorientation of the molecules in CO will be insignificantly small at the low temperatures where dipolar ordering is expected to take place. At low temperatures, molecules do not have enough thermal energy to overcome the kinetic barrier so they become "stuck" in one orientation or the other. This frozen-in disorder persists down to absolute zero and gives rise to the observed residual entropy.

The value of the residual entropy can be estimated knowing the number of frozen-in orientations and using the Boltzmann equation (equation (4.3)). For CO there are two possible frozen-in orientations ($\Omega = 2$) and therefore, if there was complete disorder at $T = 0$ K (50% of the molecules in one orientation and 50% in the other), the residual

entropy would be expected to be $S(res) = R\ln 2 = 5.76\ J{\cdot}K^{-1}{\cdot}mol^{-1}$. The observed residual entropy for CO is less than this, an indication that the disorder is not complete, *i.e.*, there are more molecules in the lower-energy orientation than in the higher-energy one.

To generalize the argument presented for carbon monoxide, substances which have residual entropy are disordered at high temperatures. Such substances would favour becoming more ordered at lower temperatures but are unable to undergo the ordering transition due to a large kinetic barrier which renders the rate of reorientation at low temperatures to be negligible; thus the disorder becomes frozen-in. Since there is no mechanism by which it can be removed, this frozen-in disorder persists down to absolute zero and gives rise to residual entropy. The amount of residual entropy can usually be estimated using the Boltzmann equation with Ω as the number of frozen-in orientations. The existence of residual entropy in a substance will be favoured if the substance is disordered among two or more orientations at high temperatures with a small energy difference and a large kinetic barrier between the orientations.

4.1.3 Residual Entropy and the Third Law

At this point it would be pertinent to discuss in more detail the apparent discrepancy between residual entropy and the third law of thermodynamics. The third law has been stated precisely by Lewis and Randall as follows:[199]

"If the entropy of each element in some crystalline state be taken as zero at the absolute zero of temperature, every substance has a finite positive entropy; but at the absolute zero of temperature the entropy may become zero, and does so become in the case of perfect crystalline substances."

It is the phrase "perfect crystalline substances" in the above statement which saves the validity of the third law as applied to substances with residual entropy. The implication is that for the third law to be valid, the substance must be in its thermodynamically most-stable state at low temperatures. However, this is not the case for compounds which show residual entropy since thermodynamic equilibrium is unattainable at low temperatures because of the lack of thermal energy to overcome a kinetic barrier. Thus, the entropy need not be zero at absolute zero for compounds with frozen-in disorder. The existence of residual entropy does not contradict the third law of thermodynamics as stated above with the qualification "perfect crystalline substances."

4.1.4 NaOH Residual Entropy Calculation

In Section 3.5, residual entropy was postulated for sodium hydroxide to explain the difference in its low-temperature behaviour as compared to sodium deuteroxide. A logical way to test this postulate would be to perform a residual entropy calculation for NaOH. If there is frozen-in disorder in NaOH at low temperatures, a residual entropy

calculation should yield a positive value.

A residual entropy calculation for NaOH has been reported.[200] One entropy value for NaOH (*S(eq)*) used in this calculation was determined based upon a literature study at $T = 623$ K of the equilibrium reaction[201]

$$2\ NaOH\ (\ell) \rightleftarrows H_2O\ (g) + Na_2O\ (s)\,, \qquad (4.9)$$

and a chemical thermodynamic analysis. The value of *S(eq)* obtained was 145.0 ± 1.3 $J \cdot K^{-1} \cdot mol^{-1}$. The calorimetric entropy (*S(cal)*) was calculated at the same temperature using calorimetric data available for NaOH in the literature[202] and found to be 139.8 $J \cdot K^{-1} \cdot mol^{-1}$. As shown by equation (4.5), the difference between these two entropy values gives the residual entropy, which for this calculation is $S(res) = 5.2 \pm 1.3$ $J \cdot K^{-1} \cdot mol^{-1}$. Further details of this calculation can be found elsewhere.[200]

This residual entropy calculation supports the postulate concerning the anomalous behaviour of NaOH. The residual entropy of 5.2 $J \cdot K^{-1} \cdot mol^{-1}$ is slightly less than $R\ln 2$ (= 5.76 $J \cdot K^{-1} \cdot mol^{-1}$), suggesting that the frozen-in disorder of the protons in NaOH involves two orientations. However, it must be stressed that since the residual entropy calculation for sodium hydroxide was based upon a single equilibrium constant from a single reaction in the literature; further information must be obtained through other studies that will either confirm or reject the apparent residual entropy in NaOH. A survey of the theory of glassy crystals will point the way to the appropriate studies that should be done.

4.2 Glassy Crystals

4.2.1 Introduction

It is well known that for certain substances the liquid phase can be readily supercooled below the melting point to form a metastable phase. A popular example of this is liquid glycerol.[203] The heat capacity curve of glycerol is shown in Figure 4.2.[204] At its melting point of 291 K, liquid glycerol will transform to a crystalline solid; the heat capacity of the solid is curve (a) of Figure 4.2. In addition, a metastable supercooled phase can be easily obtained and its heat capacity is curve (b) of Figure 4.2. In the region just below the melting point, the supercooled phase of glycerol has disorder characteristic of the liquid phase. However, an abrupt drop in the heat capacity of the supercooled liquid to a value that is just above that of the crystalline solid occurs at a temperature of approximately 183 K. This heat capacity drop occurs when the time required for the system to relax to its new equilibrium state is comparable to the time of the experiment. It corresponds to a freezing-in of the disorder of the liquid to form a non-crystalline substance.

This non-crystalline form of glycerol is called a rigid glass, and the temperature at which the heat capacity drop occurs is called the glass transition temperature (T_g). It should be noted that T_g is dependent on the experimental conditions, especially the cooling rate since a slower rate of cooling will allow more time for the system to relax to equilibrium and shift T_g to a slightly lower temperature.

Figure 4.2. Heat capacity curve of glycerol showing crystalline (curve(a)) and supercooled phases (curve (b)); from reference (204).

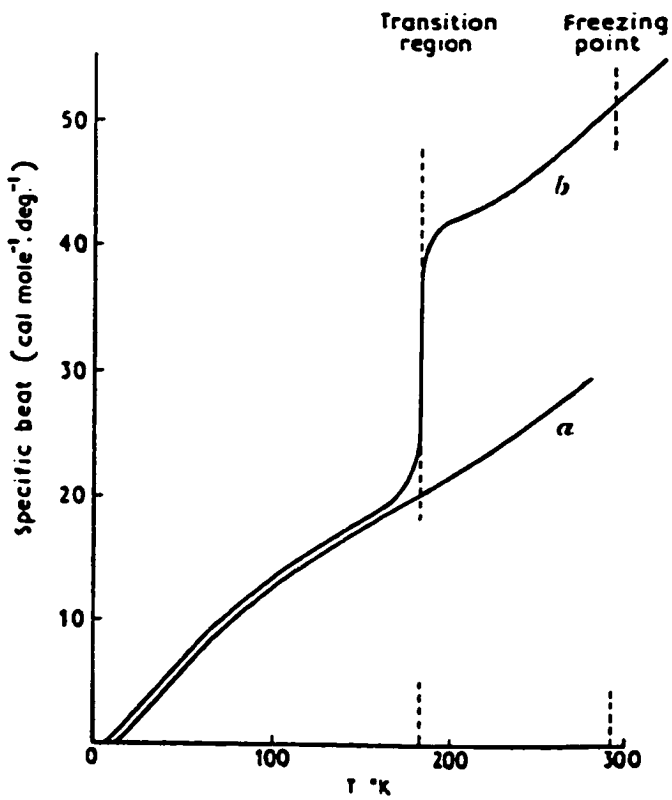

Since in the case of glycerol the glass is formed as a result of supercooling a liquid, the glassy form of glycerol is an example of a glassy liquid. However, the liquid phase of a substance is not the only phase which can be supercooled. For solids which exhibit polymorphism, supercooling below a polymorphic phase transition provides the possibility for another type of glassy substance, a glassy crystal.

The heat capacity of solid cyclohexanol has been studied in detail by calorimetry[205,206] and the measured heat capacity curve[18] is given as Figure 4.3. The melting point (T_{fus}) is evident at 299 K and a polymorphic phase transition is clearly visible at 265 K (T_{trs}). The high-temperature disordered solid phase is designated crystal I (Figure 4.3, curve (a)) while the more-ordered, low-temperature solid phase is referred to as crystal II (Figure 4.3, curve (b)). Note, however, that it is possible to supercool crystal I below the ordering polymorphic transition (Figure 4.3, curve (c)) in an analogous fashion to the supercooling of liquid glycerol below its freezing transition.

Eventually, as the temperature is lowered, a point is reached where the supercooled crystal I molecules cannot relax to their new equilibrium state in the time allowed by the experiment, and a sharp drop is observed in the heat capacity at $T = 150$ K. This drop is characteristic of a glassy phase transition. The glass transition corresponds to the freezing-in of the crystal I disorder to form a substance with a heat capacity curve slightly greater than that of crystal II. Thus, the substance below the glass transition temperature (T_g) has molecular motion similar to crystal II but with extra entropy due to the frozen-in crystal I disorder, and this phase is referred to as a glassy crystal.

Figure 4.3. Heat capacity curve of cyclohexanol showing the crystal I (curve (a)), crystal II (curve (b)), and supercooled crystal I phases (curve (c)). T_g, T_{trs}, and T_{fus} are the glass transition temperature, polymorphic phase transition temperature, and the melting temperature, respectively; from reference (18).

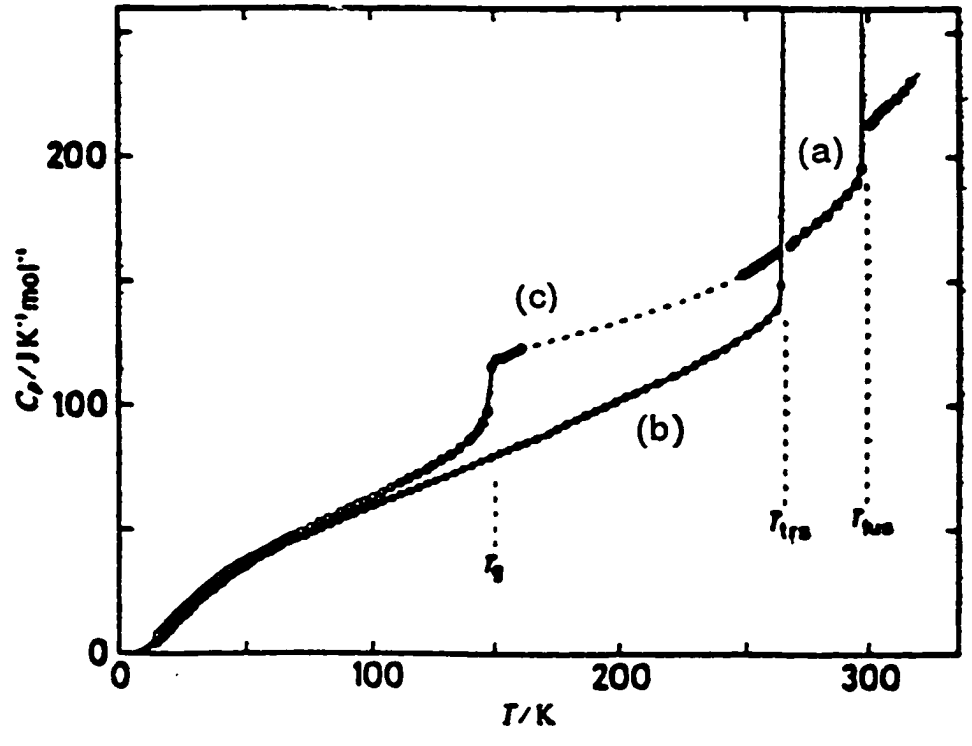

There are now known to be several solids which show glassy-crystalline behaviour and a representative list of these is given in Table 4.1.[207] Note that ice ($H_2O(s)$) is included in this list. However, ice does not form a glassy crystal in the same way as cyclohexanol. Ice provides an example of a second type of glassy crystal, the characteristics of which will now be described.

The heat capacity curve of ice[208] is shown in Figure 4.4. At P = 1 atm, the heat capacity curve has no polymorphic phase transition at all, which is different from the cyclohexanol example. A (subtle) glassy phase transition in ice is evident near 100 K. In this case it is the stable crystalline form of ice, not a supercooled form, that undergoes the glass transition upon cooling. To explain this behaviour, it can be postulated that at high temperatures the ice molecules are disordered and there is a thermodynamic driving force to remove this disorder by way of a polymorphic phase transition at a lower temperature. However, this disorder becomes frozen-in at the glass transition temperature before the phase transition can take place. Below T_g, ice is in a glassy-crystalline form.

This postulate has been confirmed from studies of ice doped with a small amount of an alkali-metal hydroxide (MOH, where M = Na, K, or Rb)[209,210]. Figure 4.5 shows the heat capacity curve[210] of ice doped with 0.01 mol·L^{-1} KOH in which a new ordering phase transition is observed at 72 K. Most of the residual entropy of ice is removed through this transition. The temperature of the transition is independent of the specific alkali-metal hydroxide used as the doping agent and is also independent of the concentration of the dopant. Because of this, the transition is thought to be a true

Table 4.1. A list of some glassy crystals with their corresponding glass transition temperatures.[207] The first column lists substances which show a glassy phase transition in a metastable supercooled phase, while the second column lists substances which are known to exhibit a glassy phase transition upon cooling the stable phase.

Supercooled Phase	T_g / K	Stable Phase	T_g / K
thiophene	37	thiophene	42
2,3-dimethylbutane	76	C_{60}	87
ethanol	90	CO	18
cyclohexene I	92	RbCN	30
cyclohexene III	93	$CsNO_2$	42
cycloheptane I	100	$TlNO_2$	60
cycloheptane II	100	H_2O (hex)	105
cycloheptane III	93	H_2O (cub)	140
cycloheptatriene	106	D_2O (hex)	115
cycloheptanol	135	pinacol·$6H_2O$	155
cyclohexanol	150	H_3BO_3	290

Figure 4.4. Heat capacity curve of ice[208] showing glassy phase transition at T_g. The anomaly in the heat capacity indicating this transition is very subtle, and is best observed by looking along the curve in the plane of the paper.

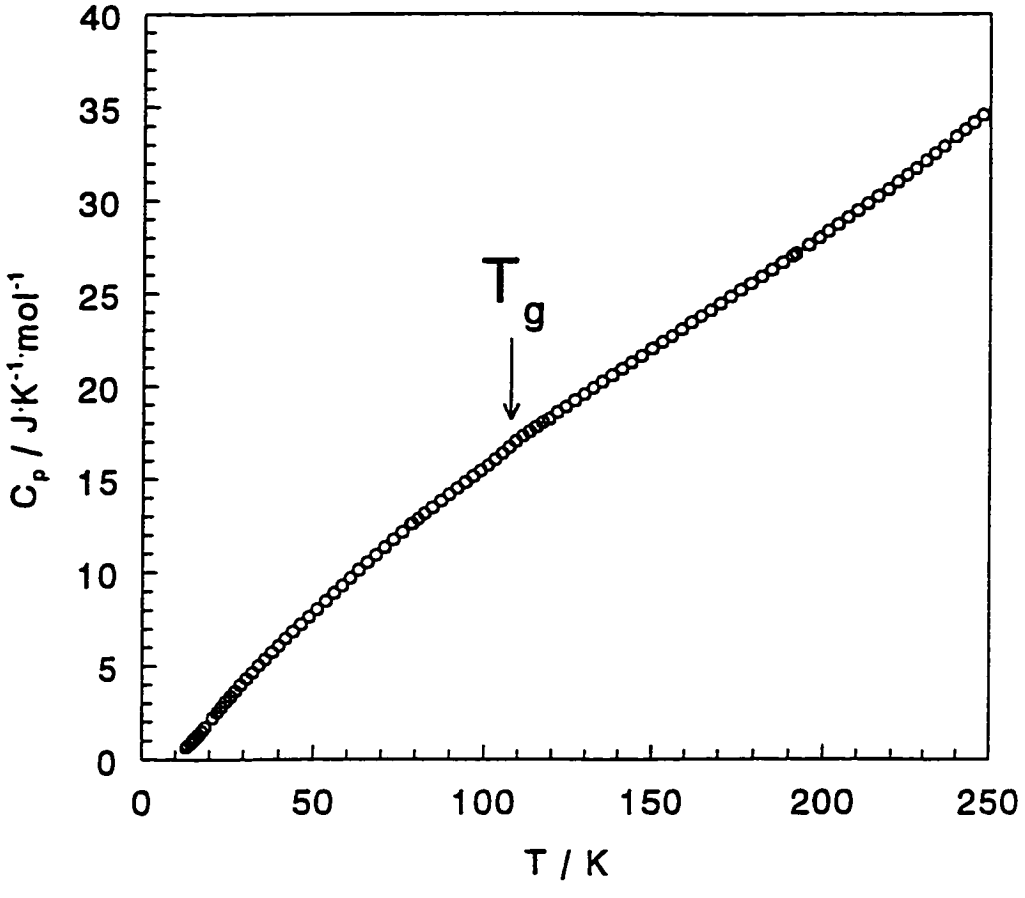

Figure 4.5. Heat capacity curve of ice doped with 0.01 M KOH. The presence of a small amount of KOH catalyzes the reorientational motion of the ice molecules so that a new ordering phase transition can take place at $T = 72$ K. The phase of ice below this transition is known as phase XI; from reference (210).

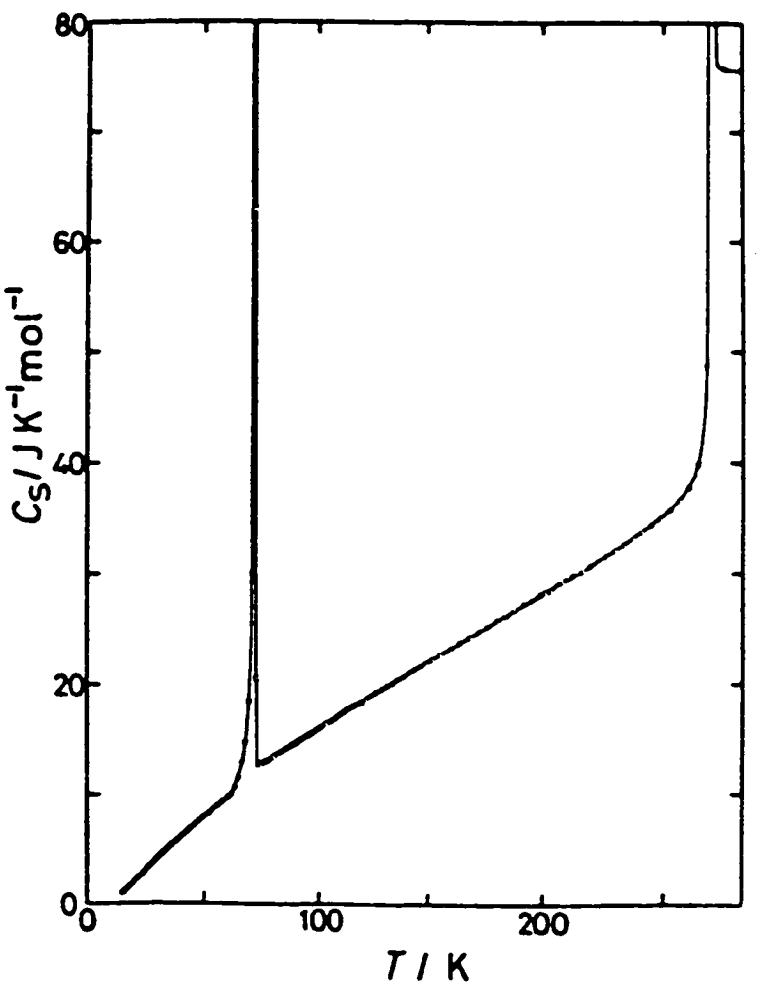

intrinsic property of ice which is observed because the presence of the alkali-metal hydroxide catalyzes the motion of the ice molecules so that the transition can take place before frozen-in disorder occurs.

Thus, there are two types of glassy crystals. In the first type, frozen-in disorder occurs in a metastable phase that has bypassed an ordering phase transition by supercooling (*e.g.*, cyclohexanol). In the second type, frozen-in disorder occurs in a stable phase before a hypothetical ordering solid-solid phase transition can take place (*e.g.*, ice). The main distinction is the relation between T_g and T_{trs}; in the former, $T_g < T_{trs}$, whereas in the latter $T_g > T_{trs}$.

4.2.2 Glassy Crystals and Residual Entropy

A very strong connection exists between glassy-crystalline behaviour and residual entropy. As explained earlier, residual entropy occurs in substances where disorder becomes frozen-in at low temperatures and is thus maintained down to absolute zero. But as just described for glassy crystals, the onset of frozen-in disorder in a solid manifests itself as a glassy phase transition in its heat capacity curve. Furthermore, glassy substances are not in thermodynamic equilibrium and therefore would not be expected to obey the third law of thermodynamics. Thus, because they are victims of frozen-in disorder at low temperatures, all glassy crystals will have residual entropy.

For the first type of glassy crystal ($T_g < T_{trs}$, *e.g.*, cyclohexanol), both the

crystalline and glassy-crystalline forms can be observed. The glassy-crystalline form will possess residual entropy whereas the crystalline form will not. For the second type of glassy crystal ($T_g > T_{trs}$, *e.g.*, ice), only the glassy-crystalline form can normally be observed at low temperatures. All substances which show glassy-crystalline behaviour of the second type will have residual entropy.

Most importantly, if a substance is known to have residual entropy, then it must have frozen-in disorder at low temperatures and the onset of this frozen-in disorder will appear as a glassy phase transition in the heat capacity curve. Thus, all compounds with residual entropy must exhibit glassy behaviour at low temperatures.

4.2.3 Detecting a Glassy Phase Transition

In Section 3.5, residual entropy was postulated for sodium hydroxide, which was supported by a residual entropy calculation in Section 4.1.4. However, since this calculation was based upon a single equilibrium study involving NaOH from the literature, further experimental studies are needed before anything definite can be said concerning residual entropy in NaOH. The theory just presented on glassy crystals suggests what studies need to be done. If sodium hydroxide truly does have residual entropy, then the onset of frozen-in disorder will show up as a glassy phase transition in its heat capacity curve. Testing for residual entropy experimentally is simply a matter of being able to detect a glassy phase transition. For example, carbon monoxide has residual

entropy and has been found to undergo a glassy phase transition[211] at $T = 18$ K.

If sodium hydroxide does show glassy-crystalline behaviour, it would be a glassy crystal of the second type, *i.e.*, one for which the frozen-in disorder occurs before a solid-solid phase transition can take place. However, glassy phase transitions of the second type are often very subtle. Illustrative examples are given by the heat capacity curves for ice[208] (Figure 4.4) and for Buckminsterfullerene[212] (C_{60}) as shown in Figure 4.6. In Figure 4.6, the glassy transition appears as a slight step at approximately 87 K. In fact, the transition is so slight that it is difficult to tell if it is a true glassy phase transition or if it is simply due to a slight error in one or two heat capacity measurements. Fortunately, there are several other methods which can be used to confirm the existence of a glassy phase transition. The first method is very simple and involves plotting the heat capacity data as C_p/T *vs.* T rather than the conventional plot of C_p *vs.* T. The quantity C_p/T is known, although uncommonly, as the encraty,[18] and as is readily seen from equation (4.4), the area under an encraty plot yields the calorimetric entropy. An encraty plot will show an enlarged anomaly at the temperature of the transition for a true glassy phase transition. Figure 4.7(a) shows some encraty plots of ice near the glass transition temperature for various thermal treatments.[208] Since the temperature of a glassy phase transition is dependent upon the thermal treatment of the sample, so is the temperature and magnitude of the encraty anomaly indicating a glass transition.

When a quenched (rapidly cooled) glassy substance is heated to a temperature near its glassy phase transition temperature, it will slowly relax to its equilibrium state

Figure 4.6. (a) Heat capacity curve of C_{60}. (b) Enlarged heat capacity plot in the region of the glassy phase transition at 87 K; from reference (212).

(a)

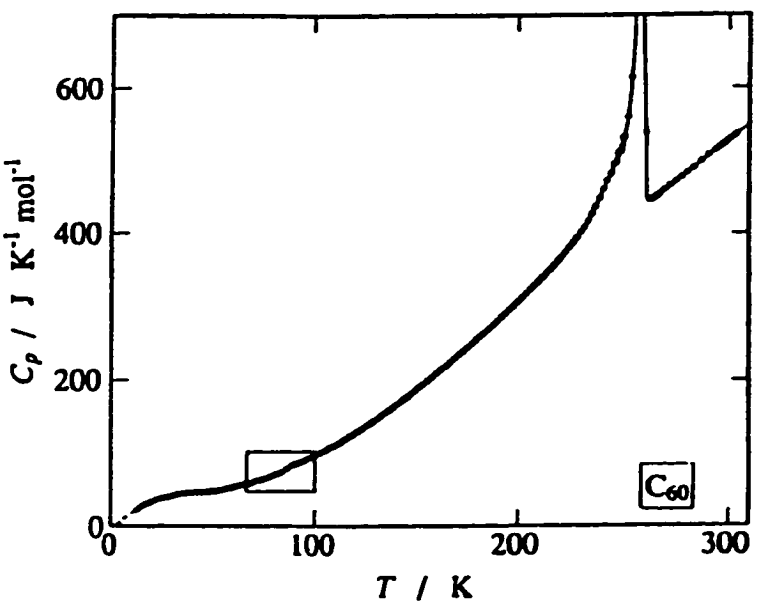

(b)

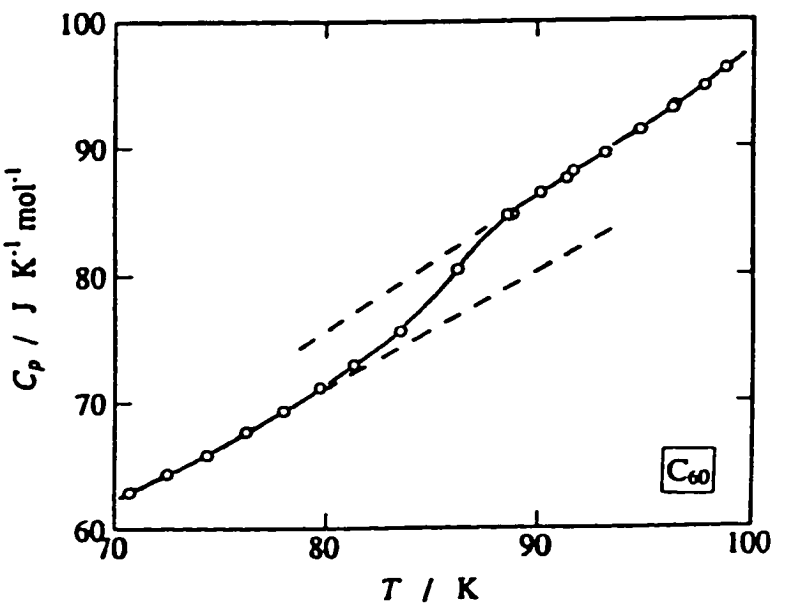

Figure 4.7. Detecting a subtle glassy phase transition. (a) Encraty plots (C_p/T *vs.* T) for ice near the glassy phase transition temperature. The different curves correspond to different thermal treatments of the sample with the largest anomalies occurring for annealed samples; from reference (208). (b) Characteristic temperature drift pattern near a glassy phase transition; from reference (18).

(a)

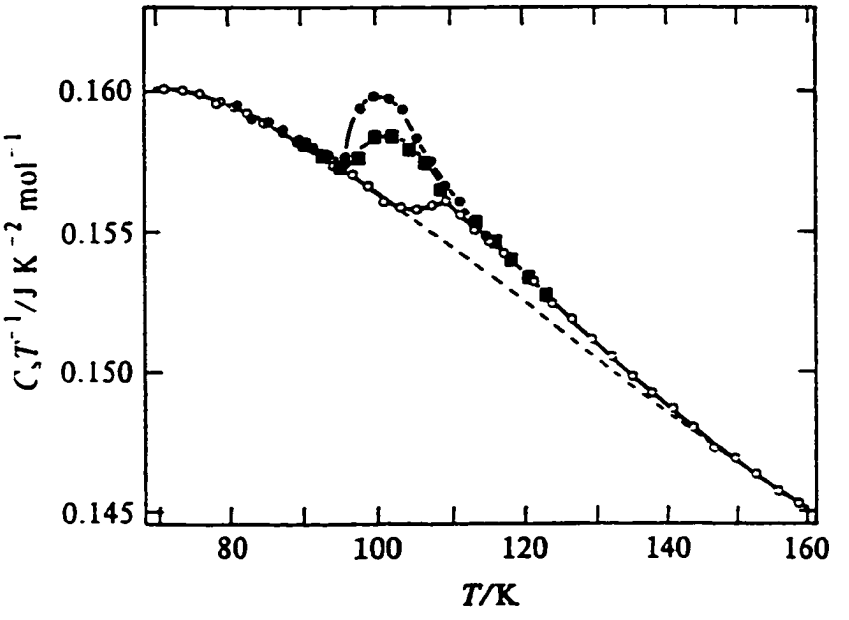

(b)

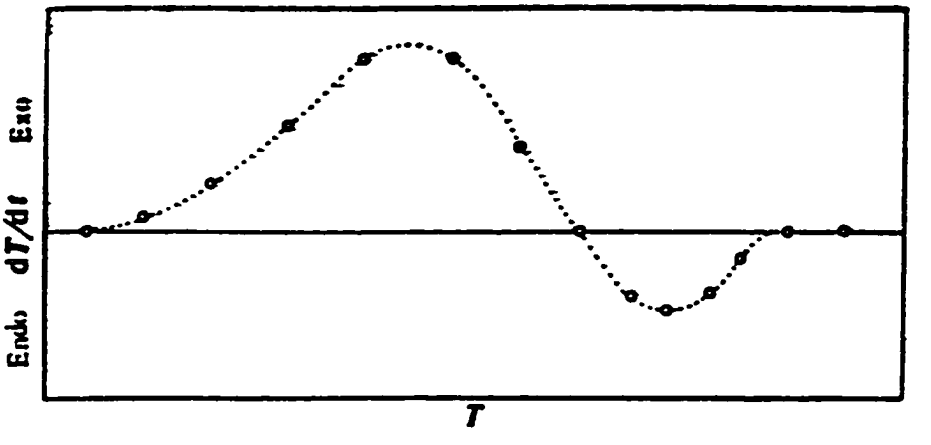

by giving off heat. A similar experiment with a glass that has been annealed will result in an absorption of heat. Thus, due to the enthalpy relaxation effects of a substance near the temperature of the transition, the calorimeter used to measure the heat capacity will show an anomalous temperature drift at temperatures near the transition.[213] This drift may be endothermic or exothermic depending on the thermal treatment of the sample and the proximity to the glassy phase transition temperature. A characteristic temperature drift pattern[18] is shown in Figure 4.7(b). However, the observed drift pattern will depend on the thermal treatment of the sample and the exact geometry of the calorimeter used.

These enthalpy relaxation effects associated with the slow approach to equilibrium of a substance near its glass transition temperature can be characterized by a relaxation time, τ. The magnitude of this relaxation time is typically of the order of 10^2 to 10^5s,[214] and thus, an adiabatic calorimeter can be used to study molecular motion with long relaxation times. It is for this reason that an adiabatic calorimeter can be thought of as an ultra-low frequency spectrometer,[214,215] and the technique of using an adiabatic calorimeter for this purpose is called calorimetric spectroscopy.[214,216] By determining the relaxation times at several temperatures near a glassy phase transition, activation parameters for the particular motion can be determined from an Arrhenius-type plot. As mentioned previously, the glass transition temperature for a substance depends slightly on the thermal treatment of the sample. However, if the activation parameters have been determined, T_g is typically reported as the calculated temperature where the relaxation time is equal to 1000 s,[18] which is roughly the timescale allowed by the calorimetric experiment.

A third, very powerful method for detecting a glassy phase transition is the technique of dielectric relaxation. Dielectric measurements give quantitative information concerning the rate of reorientational motion in solids as a function of temperature, and thus provide clear evidence for the onset of frozen-in disorder. This technique is described in great detail in the next section.

4.3 Dielectric Relaxation

4.3.1 Introduction

In general, the term relaxation describes the process by which a system reaches a new state of equilibrium after an abrupt change in one or more conditions to which the system is subjected. For the case of dielectrics, the relaxation process that is commonly studied is the rise or decay of polarization in the dielectric upon a change in an applied electric field. There can be several sources of polarization in a dielectric substance which are related to various processes occurring at an atomic or molecular level. Dielectric relaxation experiments provide a probe of the rate of reorientational motion in solids and parameters characterizing this motion. Dielectric measurements are also useful for detecting volume changes as well as changes in the order/disorder of molecules associated with certain polymorphic phase transitions in solids. However, before examining in detail the theory and methods of analysis underlying this powerful

technique, some of the necessary background concepts in electronics and electrostatics will be discussed.

4.3.2 Fundamental Concepts and Theories

Before engaging in a full discussion of concepts in electrostatic theory, a brief mention will be made of the two systems of units commonly used in electrostatics. The first of these is the familiar SI system of units in which the metre, kilogram, and second are the basic units of length, mass, and time, respectively. The second unit system is the Gaussian unit system which employs the less commonly used centimetre, gram, and second for length, mass, and time. Also, the Gaussian system makes some assumptions concerning certain fundamental constants in electrostatics. For the purposes of this discussion, the most important consequence of these assumptions is that the fundamental constant known as the permittivity of free space (ϵ_o) is equal to $(4\pi)^{-1}$ (in Gaussian units). Thus, many electrostatic equations in Gaussian units contain a seemingly anomalous 4π factor. In this thesis, all equations will be presented using the SI system. However, it is still common to see equations in either system in electrostatic textbooks.

To fully understand dielectrics, one must first realize the fundamental difference between a conductor and an insulator. A conductor is a substance which allows for long-range movement of charged particles in an electric field. On the other hand, in an insulating substance, there is no long-range migration of charges in an electric field. In

general, any substance which is an electrical insulator is called a dielectric.

Dielectrics are almost always associated with capacitors. In qualitative terms, a capacitor is an electronic component which stores charge. The most familiar type of capacitor is the parallel plate capacitor which consists of two conducting plates separated by an insulator. When a potential difference (V) is applied between the plates, a positive charge (Q) will develop on one plate of the capacitor and a negative charge of equal magnitude ($-Q$) will develop on the other plate. If the potential difference between the plates is varied, and the effect on Q is observed, one will find that Q is proportional to V, *i.e.*,

$$Q = CV, \tag{4.10}$$

where the proportionality constant C is called the capacitance of the capacitor. The unit of capacitance is the farad (F) which is equivalent to one coulomb per volt (1 F = 1 $C \cdot V^{-1}$). However, one farad is an extremely large capacitance, so it is common to see capacitances quoted in microfarads (μF), nanofarads (nF), or even picofarads (pF).

When the plates of the capacitor are separated by a vacuum, the capacitance of the capacitor (C_o) is given by

$$C_o = \frac{\epsilon_o A}{d}, \tag{4.11}$$

where ϵ_o is the permittivity of free space (= 8.8542 x 10^{-12} $C^2 \cdot N^{-1} \cdot m^{-2}$), A is the area of one of the plates, and d is the separation distance between the plates. If a dielectric (insulator) is placed between the plates of the capacitor, the capacitance (C) will change by a factor ϵ, *i.e.*,

$$C = \frac{\epsilon \epsilon_o A}{d}. \tag{4.12}$$

A comparison of equation (4.12) with equation (4.11) yields

$$\frac{C}{C_o} = \epsilon. \tag{4.13}$$

The constant ϵ is called the dielectric constant of the insulator, and since ϵ is always greater than unity ($\epsilon > 1$), the conclusion is that the presence of the dielectric increases the capacitance of a capacitor relative to that in a vacuum. The quantity $\epsilon\epsilon_o$ is called the permittivity of the dielectric. Thus, the dielectric constant is the permittivity of the insulator relative to that of a vacuum (free space). For this reason, the dielectric constant is also known as the relative permittivity of the insulator.

In practice, dielectrics are important in obtaining capacitors with very large capacitances. To fully understand how dielectrics work, one must be familiar with the concept of polarization. On a microscopic scale, a molecule is said to be polarized if the centre of negative charge of the molecule is displaced from the centre of positive charge. In general, there are three common sources of polarization[217] in a molecule in an applied electric field. The first of these is an electronic contribution which arises because the electron cloud surrounding an atom in a molecule will displace itself relative to the positively charged nucleus in an electric field, thus giving rise to an induced dipole moment. This contribution occurs in all dielectric solids, and for some solids, such as diamond, represents the only contribution to the polarization. A second source of polarization arises due to a slight displacement of atomic nuclei (especially ions) relative

to one another when placed in an electric field. This polarization mechanism is called the atomic polarization and is particularly important for ionic solids. The third possible contribution to polarization is the most important for the purposes of this research. It occurs in molecules which have a permanent dipole moment (*e.g.*, H_2O, CO) and is therefore known as the dipolar contribution.

Because there is an applied potential difference (V) between the capacitor plates, there must also be an electric field (E) between the plates, the magnitude of which is given by the equation

$$|E| = \frac{V}{d}, \tag{4.14}$$

where d is the plate separation. When a dielectric is placed between the plates of the capacitor, the molecules in the dielectric will become polarized,[218] either due to possession of a permanent dipole moment or due to a dipole moment induced by the electric field of the capacitor. The forces acting on the dipole when placed in an electric field create a net torque which tends to rotate the dipole such that it will align with the field.

This tendency to align the dipoles with the electric field is greatly opposed by thermal agitations, so that generally the alignment is far from complete.[219] With the electric field strengths that are normally used in dielectric measurements, the departure of the dipoles from random orientations is usually only moderate. They will, however, be arranged in such a way that a total net component of the dipole moments will be aligned with the electric field. For permanent dipoles reorienting in an electric field, the

average dipole moment per dipole ($\overline{\mu}$) in the direction of the field is given by the equation

$$\overline{\mu} = \frac{\mu^2 E}{3k_B T}, \tag{4.15}$$

where μ is the permanent dipole moment. Equation (4.15) shows that alignment of the dipoles with the field will improve with an increase in the electric field strength and a decrease in the temperature.

When the component dipoles in a dielectric are aligned with the electric field, they create their own electric field which opposes the applied field between the capacitor plates. Therefore, with the dielectric present, the net electric field ($|E|$) is lower than the applied electric field ($|E_o|$). This means that the voltage between the capacitor plates is less than the applied voltage since

$$V = |E|\, d. \tag{4.16}$$

But, by rearranging equation (4.10)

$$C = \frac{Q}{V}, \tag{4.17}$$

it is apparent that if the voltage decreases, the capacitance will increase. This explains why the presence of a dielectric increases the capacitance of a capacitor.

Including all of the possible mechanisms of polarization for a molecule that is placed in an electric field, the total average induced dipole moment per molecule ($\overline{\mu}_{avg}$) is given by

$$\bar{\mu}_{avg} = \alpha E_{loc}, \tag{4.18}$$

where α is the polarizability of the molecule, and E_{loc} is the local electric field acting on a molecule in the dielectric. The total polarizability, α, can be written as a sum of component polarizabilities for the various mechanisms giving rise to the total polarization as follows:

$$\alpha = \alpha_{elec} + \alpha_{at} + \alpha_{dip}, \tag{4.19}$$

where α_{elec}, α_{at}, and α_{dip} are the electronic, atomic, and dipolar polarizabilities, respectively, and their values reflect the relative importance of each mechanism to the total polarization of the dielectric. A look at equation (4.15) reveals that the dipolar polarizability is

$$\alpha_{dip} = \frac{\mu^2}{3k_B T}. \tag{4.20}$$

The quantitative definition of polarization states that it is the net dipole moment of the dielectric per unit volume. If there are N_v molecules per unit volume, the polarization (P) of the dielectric can be written in terms of microscopic quantities as

$$P = N_v \bar{\mu}_{avg} = N_v \alpha E_{loc}. \tag{4.21}$$

The polarization is given in terms of macroscopic quantities by the following equation:

$$P = \epsilon_o(\epsilon - 1)E. \tag{4.22}$$

The local electric field (E_{loc}) affecting a particular molecule is generally different from the applied field (E) due to the influence of the surrounding molecules in the dielectric.

Lorentz[220] derived an expression for E_{loc} by considering a portion of the dielectric being enclosed in a sphere whose radius is large compared to molecular dimensions but small compared to the dimensions of the capacitor. The local electric field is the sum of three contributions: (1) the applied field (E), (2) the field due to polarization charges on the surface of the sphere due to the molecules outside the sphere, and (3) the field due to the molecules inside the sphere. Lorentz considered the third factor to be equal to zero, and subsequently derived the following expression for the local field:

$$E_{loc} = E + \frac{P}{3\epsilon_o} = \frac{(\epsilon + 2)}{3} E, \tag{4.23}$$

where the far right-hand side of equation (4.23) was obtained by substituting equation (4.22) for P. Substitution of equations (4.19), (4.20), (4.22), and (4.23) into equation (4.21) yields

$$\frac{\epsilon - 1}{\epsilon + 2} = \frac{N_v}{3\epsilon_o} \left[\alpha_{elec} + \alpha_{at} + \frac{\mu^2}{3k_B T} \right]. \tag{4.24}$$

Equation (4.24) is called the Debye-Langevin equation[221] and it links the macroscopic world with the microscopic world. This equation is suitable to describe gases and dilute solutions of polar solutes in nonpolar solvents. It can also be used to qualitatively describe solids as well. For nonpolar substances, the dipolar polarizability term is equal to zero and the resulting equation is known as the Clausius-Mosotti relation.[222,223]

Onsager took the theory a step further by taking at least some component of the intermolecular interactions into account.[224] The assumptions made in this theory are that the molecule in the dielectric occupies a spherical cavity of molecular dimensions,

its polarizability is isotropic, and that the short-range interaction energy is negligible. The equation derived using these assumptions is the following:

$$\frac{(\epsilon - \epsilon(\infty))(2\epsilon + \epsilon(\infty))}{\epsilon(\epsilon(\infty) + 2)^2} = \frac{N_v\mu^2}{9\epsilon_o k_B T}, \qquad (4.25)$$

where $\epsilon(\infty)$ is the dielectric constant due to the polarization contributions other than the dipolar mechanism. Equation (4.25) is appropriately called the Onsager equation and is suitable for describing nonassociated polar liquids, and also for some dynamically disordered phases of certain solids. The parameter $\epsilon(\infty)$ will be discussed in more detail in Section 4.3.4. Further theories which take better account of the short-range forces between molecules have been developed by Kirkwood[225] and Fröhlich.[226]

4.3.3 Dielectric Constants and Phase Transitions

Measurement of the dielectric constant of a substance as a function of temperature is a useful way to detect phase transitions. A change in the dielectric constant at a phase transition can occur for several reasons, the most important of which are the following. Equations (4.24) and (4.25) give the dependence of the dielectric constant on the density of the substance. During a first-order phase transition, a volume change occurs which directly affects the density and leads to a sudden change in the dielectric constant. Furthermore, in the solid state, the mobility of the molecules in a substance is usually restricted compared to the liquid. This denies molecules with permanent dipole moments

the ability to reorient for the purpose of aligning with an electric field. When this occurs, the dipole contribution to the total electric polarization falls to zero (or near-zero) and the dielectric constant shows a sudden, often discontinuous, drop to a value characteristic of the atomic and electronic polarization mechanisms only.

An example of this is shown in Figure 4.8, which gives the temperature dependence of the dielectric constant of nitromethane[227] measured at a frequency of 70 kHz. When liquid nitromethane freezes at $T = 244.6$ K, the dielectric constant drops from 45.5 to 3.93, reflecting the ordering and restricted mobility of the nitromethane molecules in the solid state compared to the liquid. For a nonpolar substance with no permanent dipole moment, only electronic and atomic polarizations can contribute to the dielectric constant, so that freezing a nonpolar liquid generally results in an increase of the dielectric constant due to the density increase in the solid state.

In many polar substances, molecular reorientation is not severely restricted in the solid state and the dipolar polarization still contributes to the overall observed dielectric constant. Figure 4.9 shows the dielectric constant of hydrogen sulfide[228] (H_2S) as a function of temperature at 5 kHz. Liquid hydrogen sulfide freezes at 187.6 K to a face-centred cubic phase (phase I). Two polymorphic phase transitions[229] also occur; one at 126.2 K to a primitive cubic phase (phase II), and the other at 103.5 K to a less-symmetric tetragonal phase (phase III).

All of these phase transitions show up as discontinuities in the dielectric constant curve. When the liquid is cooled to the freezing point, the dielectric constant increases due to the higher density of the solid relative to the liquid. The fact that the dielectric

Figure 4.8. Dielectric constant of nitromethane as a function of temperature at an electric field frequency of 70 kHz; from reference (227).

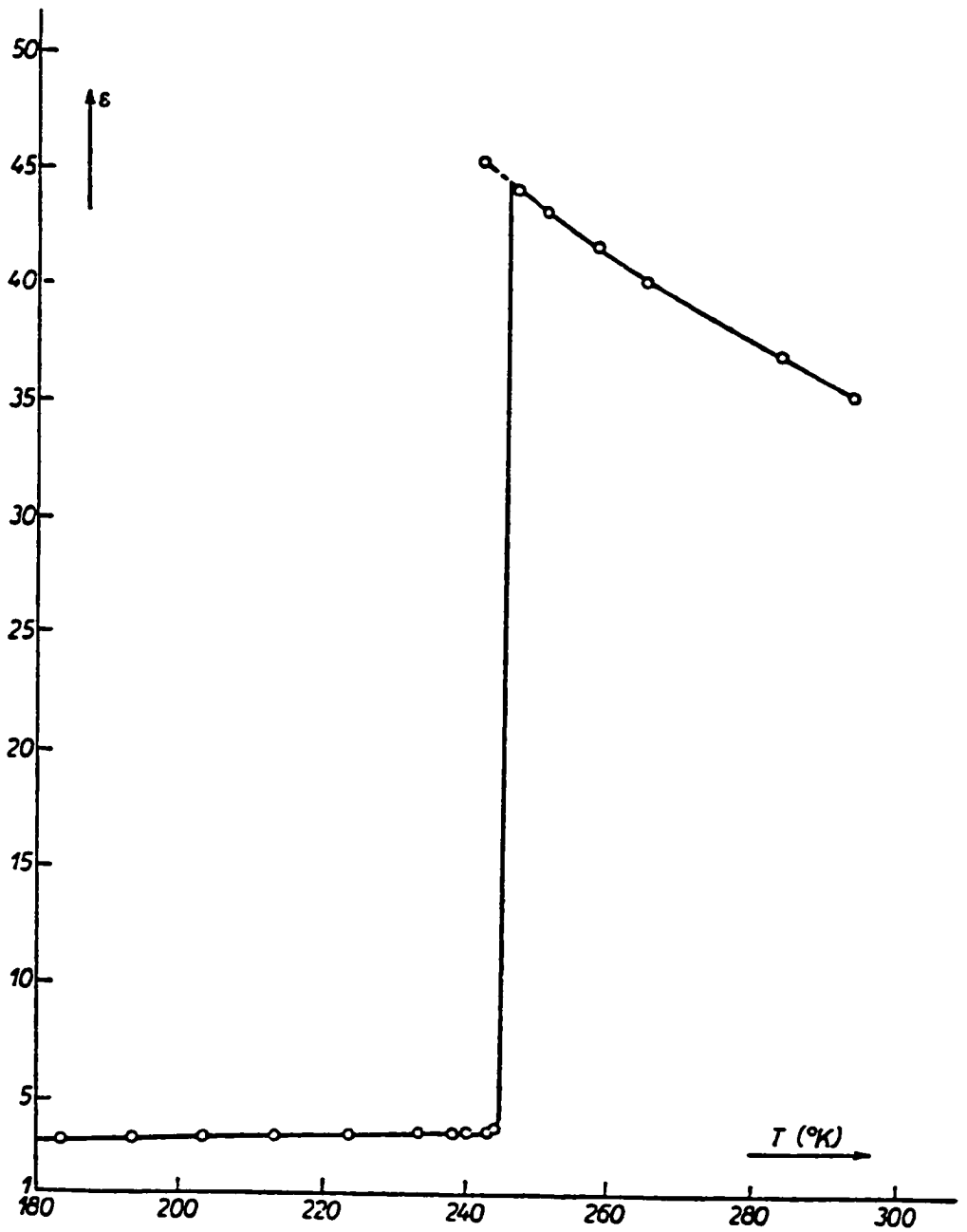

Figure 4.9. Dielectric constant of hydrogen sulfide as a function of temperature at a frequency of 5 kHz; from reference (228).

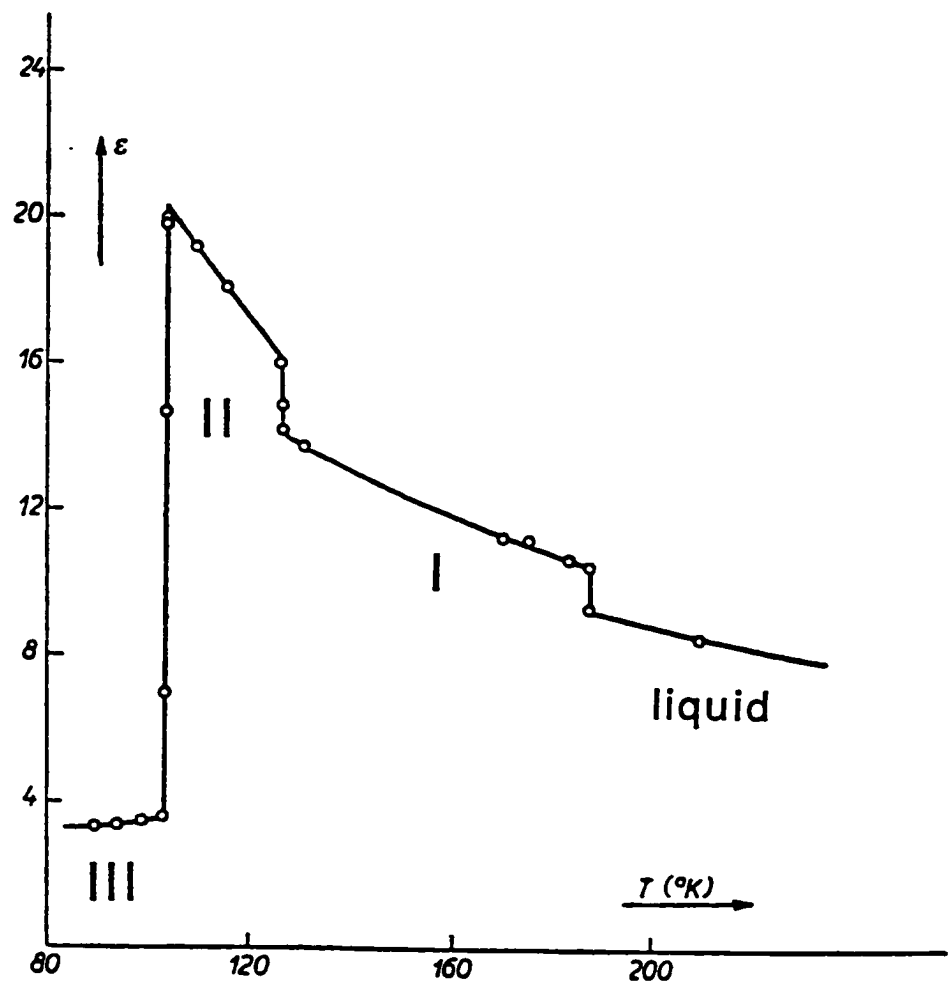

constant does not decrease as H_2S is cooled through the freezing point indicates that sufficient dynamic disorder exists in the solid for the molecular dipoles to maintain their alignment with the applied electric field. Another sudden increase in the dielectric constant is evident at the polymorphic phase transition at T = 126.2 K due to the increase in density of phase II compared to phase I. Since there is no drop in the dielectric constant upon lowering the temperature through the I-II phase transition, it can be concluded that molecular mobility still exists in phase II. At the II-III polymorphic phase transition (103.5 K), the dielectric constant shows a discontinuous drop from about ϵ = 20 to a value below 4. This reflects the order of the molecules in the low-temperature phase III compared to the other solid phases and the resulting disappearance of the dipolar polarization. However, the dielectric data do not exclude the possibility of rotation about the polar C_2 axis of the H_2S molecules in phase III which would not change the dipole direction. Experimental evidence by proton NMR suggests that this type of reorientation does indeed occur.[230,231]

In certain substances, a polymorphic phase transition occurs at low temperature whereby individual dipoles in the solid order themselves in such a way that they are aligned parallel to each other or antiparallel to each other. For parallel alignment the phase is referred to as ferroelectric; for antiparallel alignment, the phase is called antiferroelectric. A phase transition to a ferroelectric or an antiferroelectric phase gives rise to an anomaly in the dielectric constant curve with a very characteristic shape. For substances which undergo a phase transition to a ferroelectric phase (*e.g.*, KH_2PO_4 and $BaTiO_3$),[232,233] the dielectric constant will sharply increase near the transition to peak

at a value of typically several thousand at the transition temperature. The dielectric constant peak indicative of an antiferroelectric phase transition is usually more flattened with a much smaller peak dielectric constant value compared to the ferroelectric transition. An example of an antiferroelectric dielectric constant curve anomaly is shown by the dielectric curve of $Rb_3D(SeO_4)_2$ in Figure 2.4 of Section 2.3.1.[62] Another example of an antiferroelectric dielectric anomaly is the low-temperature phase transition in NaOD to its antiferroelectric phase (Figure 3.3 in Section 3.2).[140] Because of the characteristic dielectric constant anomalies exhibited by phase transitions to ferroelectric and antiferroelectric phases, they are sometimes referred to as dielectric phase transitions.

Thus, observation of abrupt changes in the dielectric constant of a substance as a function of temperature is direct evidence for the occurrence of a phase transition. Another example of this is provided by the dielectric constant curve of $(NH_4)_3H(SO_4)_2$ as shown by Figure 2.1 in Section 2.3.1.[48] Characteristic peaks in the dielectric constant curves at a phase transition can indicate the transition to a ferroelectric or antiferroelectric phase reflecting specific types of dipolar ordering. Furthermore, dielectric measurements provide qualitative information concerning the extent of the disorder of molecules in various solid-state phases. Quantitative information concerning reorientational kinetics in solids can be obtained through dielectric measurements as a function of the frequency of the applied electric field.

4.3.4 Dielectrics in an Alternating Electric Field

Useful information concerning molecular motion in a dielectric solid can be obtained by measuring its dielectric constant in an alternating electric field. However, before proceeding with the theory describing the behaviour of a dielectric in an alternating electric field, the concept of dielectric loss[234] must first be understood.

Consider a parallel plate capacitor in a vacuum connected to an alternating voltage source

$$V(t) = V_o e^{j\omega t}, \tag{4.26}$$

where,

$$j = \sqrt{-1}\ ,\ \omega = 2\pi f, \tag{4.27}$$

$V(t)$ is the voltage at time t, V_o is the peak voltage, and f is the frequency of the alternating voltage. From equation (4.14), the alternating electric field between the capacitor plates is given by the equation

$$E(t) = \frac{V(t)}{d} = \frac{V_o}{d} e^{j\omega t} = E_o e^{j\omega t}. \tag{4.28}$$

Since $Q = C_o V$, the current charging the capacitor (I_c) is

$$I_c = \frac{dQ}{dt} = C_o \frac{dV}{dt} = j\omega C_o V(t) = I_o e^{j(\omega t + \pi/2)}. \tag{4.29}$$

Thus, the current leads the voltage by a phase angle of $\pi/2$ radians or 90° (see Figure 4.10(a)).

Figure 4.10. (a) Current-voltage relationship in an ideal capacitor. (b) Representation of a real capacitor as an ideal capacitor connected in parallel to a resistor. (c) Current-voltage relationship in a real capacitor. The phase angle (θ) is less than 90° due to the loss current (I_t).

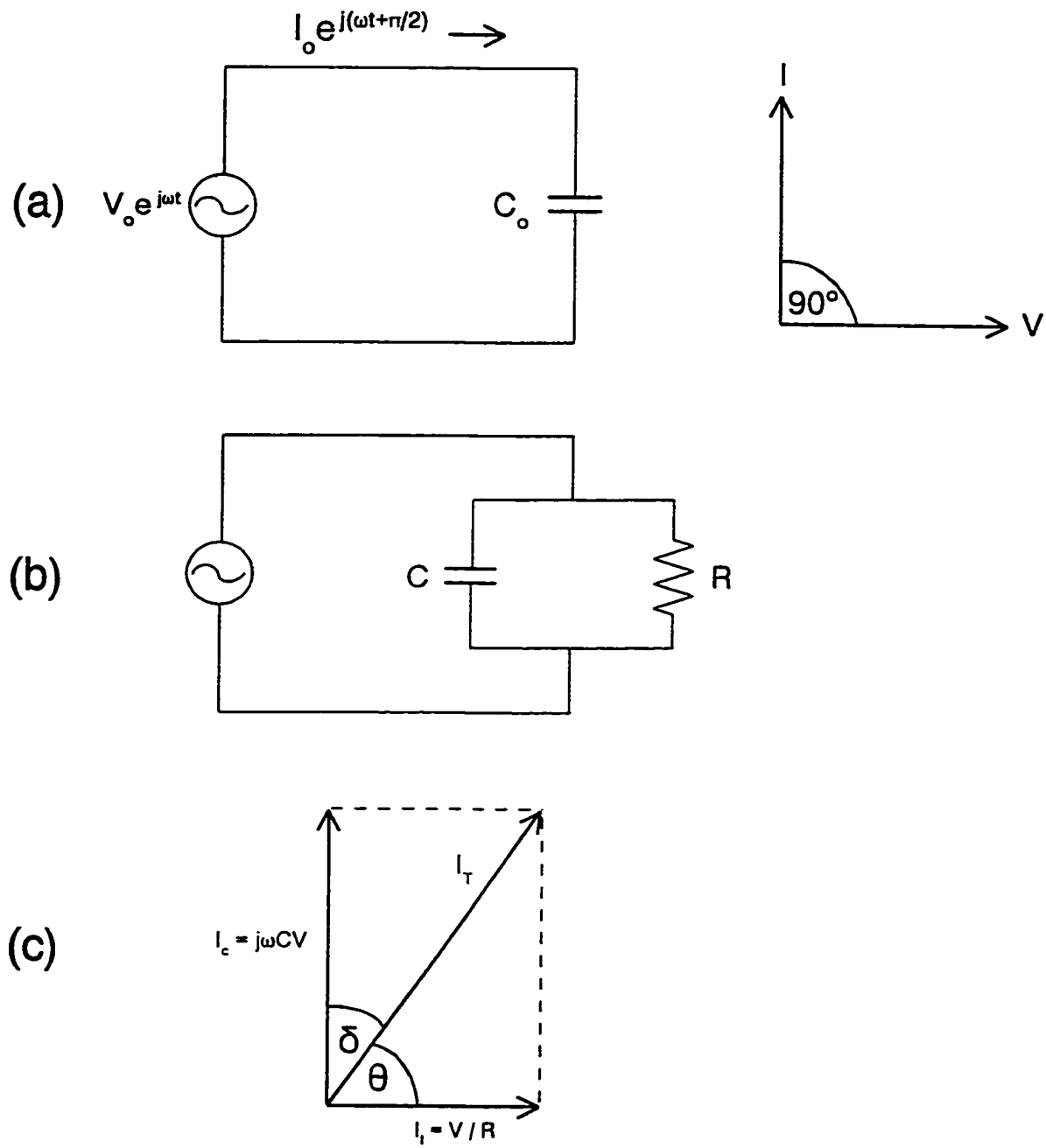

Now consider the capacitor with a dielectric between the plates. If the system were ideal, one would expect the resistance between the capacitor plates to be infinite. However, no capacitor is ideal. The dielectric will always have some finite resistance (R) associated with it, and the situation is best represented as an ideal capacitor connected in parallel to a resistor (see Figure 4.10(b)). There will thus be a current flowing through the resistor (I_ℓ) which can be calculated from Ohm's law, *i.e.*,

$$I_\ell = \frac{V}{R}. \tag{4.30}$$

This current will be in phase with the applied voltage and represents a loss of energy of the system because of the resulting heat dissipation. The current I_ℓ is therefore referred to as the loss current.

The total current passing through the system, I_T, is given by

$$I_T = I_c + I_\ell = \left[j\omega C + \frac{1}{R} \right] V, \tag{4.31}$$

where $C = \epsilon C_o$. The phase angle between the total current and the applied voltage can be determined by adding the two currents in a complex plane diagram as shown in Figure 4.10(c). From this diagram it is apparent that the presence of the loss current causes the phase angle to be less than the ideal 90°. In fact, the phase angle is (90°- δ) where tanδ, known as the loss tangent, can be found from the equation

$$\tan\delta = \frac{I_\ell}{|I_c|} = \frac{1}{\omega RC}. \tag{4.32}$$

Alternating currents and voltages in electronics are usually expressed using

complex notation as in equation (4.26). Because of this, and since the loss current is due to the properties of the dielectric, it is customary to take it into account by introducing a complex dielectric constant, ϵ^*, defined by

$$\epsilon^* \equiv \epsilon' - j\epsilon'', \tag{4.33}$$

where ϵ' is the actual dielectric constant and ϵ'' is called the dielectric loss. If the charging current is written as

$$I_c = j\omega\epsilon' C_o V, \tag{4.34}$$

and the loss current is written in an analogous fashion as

$$I_l = \omega\epsilon'' C_o V, \tag{4.35}$$

then the total current in equation (4.31) can be written

$$I_T = j\omega C_o V(\epsilon' - j\epsilon'') = j\omega\epsilon^* C_o V. \tag{4.36}$$

Thus, the loss tangent can be given as

$$\tan\delta = \frac{\epsilon''}{\epsilon'}. \tag{4.37}$$

By equating equations (4.30) and (4.35), a quantitative definition of the dielectric loss (ϵ'') is given by

$$\epsilon'' = \frac{1}{\omega C_o R}. \tag{4.38}$$

If the system is ideal and the resistance of the dielectric is infinite, the dielectric loss is

$$\lim_{R\to\infty} \epsilon'' = \lim_{R\to\infty} \frac{1}{\omega C_o R} = 0. \qquad (4.39)$$

But, as mentioned earlier, no system is ideal and every dielectric will have a finite resistance giving rise to a positive, non-zero dielectric loss. In most cases, the dielectric loss of a capacitor system is negligibly small. However, under certain conditions, the dielectric loss will become significant, as illustrated in the following situation.

Consider a dielectric that is subjected to an alternating electric field with frequency f (angular frequency $\omega = 2\pi f$). As was mentioned in Section 4.3.2, dipoles in an electric field will feel a net torque that will tend to cause them to align with the field. In an alternating electric field, the dipoles in the dielectric will still want to align with the field even as it is alternating, but they can only do this if they have sufficient motional freedom in the solid. Assuming the dipoles in the dielectric do have some form of reorientational freedom, if the frequency of the alternating electric field is low enough, the reorientational motion of the molecules will allow them to stay aligned with the field, and the dielectric constant (ϵ') can be measured. As the frequency of the field is gradually increased, eventually a frequency will be reached where the dipoles are unable to keep aligned with the field because their reorientational motion is not fast enough. In order for the dielectric constant to be maximum, the dipoles must be able to align with the field. Thus, if the frequency of the field is too high, the dipoles cannot keep up with the alternations of the electric field and the dielectric constant drops. At this point dielectric losses become significant as well, in that the dielectric begins to act as a conductor with an effective finite resistance.

Typical plots of the dielectric constant (ϵ') and the dielectric loss (ϵ'') as a function of the frequency of the applied alternating electric field at a given temperature are shown in Figure 4.11. The curves in Figure 4.11 are commonly known as dielectric dispersion or dielectric relaxation curves and can be described by the following equation:[231]

$$\epsilon^* = \epsilon(\infty) + \frac{(\epsilon(0) - \epsilon(\infty))}{1 + j\omega\tau} = \epsilon(\infty) + \frac{\epsilon(0) - \epsilon(\infty)}{1 + \omega^2\tau^2} - j\frac{(\epsilon(0) - \epsilon(\infty))\omega\tau}{1 + \omega^2\tau^2}. \quad (4.40)$$

Equating the respective real and imaginary parts of equations (4.33) and (4.40) results in the following two equations:

$$\epsilon' = \epsilon(\infty) + \frac{\epsilon(0) - \epsilon(\infty)}{1 + \omega^2\tau^2}, \quad (4.41)$$

and

$$\epsilon'' = \frac{(\epsilon(0) - \epsilon(\infty))\omega\tau}{1 + \omega^2\tau^2}, \quad (4.42)$$

for the dielectric constant and dielectric loss, respectively. These equations describe the curves in Figure 4.11 and are commonly known as the Debye equations[221] or the Pellat-Debye equations. The parameters $\epsilon(0)$ and $\epsilon(\infty)$ are the limiting low-frequency (static) and high-frequency dielectric constants, respectively, and τ is a relaxation time for the reorientational motion of the dipoles in the dielectric and is thus related to the rate of reorientation. This relaxation time can be easily obtained from the maximum in the dielectric loss curve since, at the maximum,

Figure 4.11. Typical plots of the dielectric constant (ϵ') and dielectric loss (ϵ'') as a function of the frequency of the applied electric field at constant temperature.

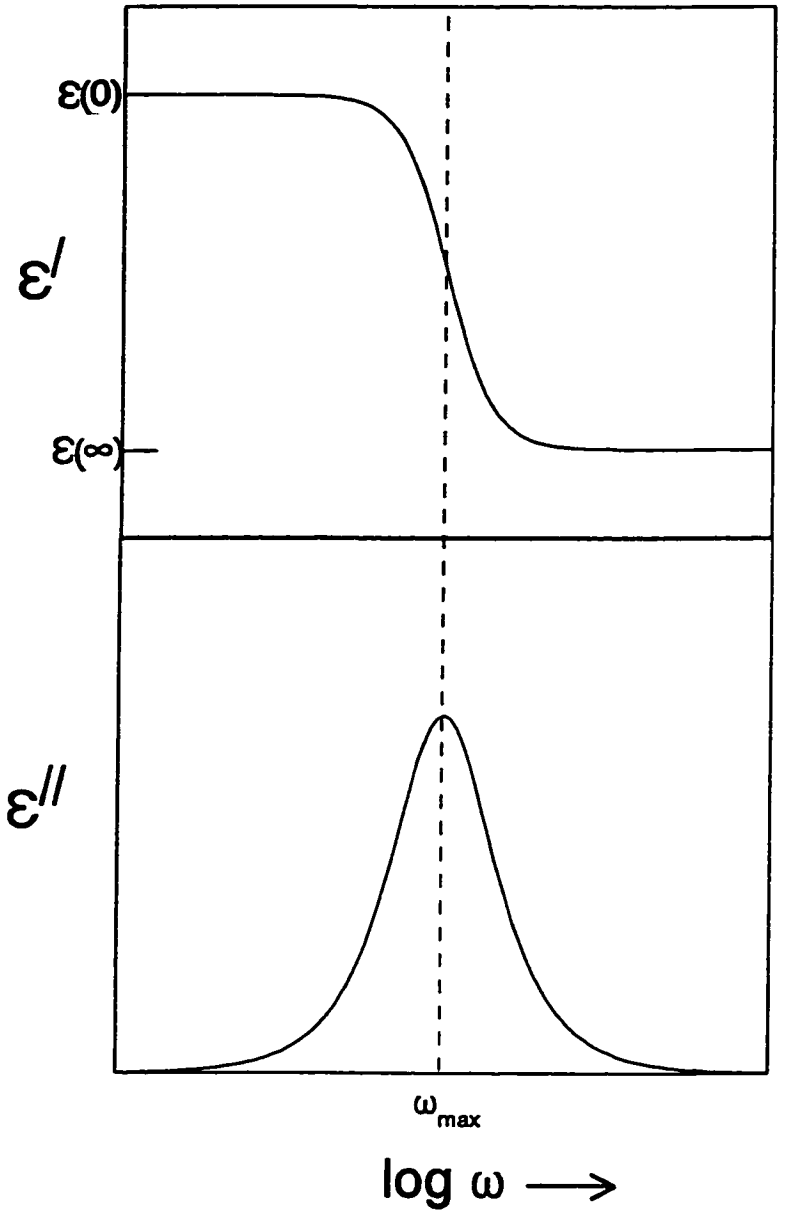

$$\omega_{max}\tau = 1 . \tag{4.43}$$

The Debye equations are derived assuming that the reorientational process giving rise to the dispersion can be characterized by a single relaxation time, and also that the polarization decays or rises with a change in the electric field in an exponential fashion.

If one solves equation (4.41) for the parameter ω and substitutes the resulting expression into equation (4.42), an equation is obtained involving only the dielectric constant and dielectric loss, *i.e.*,

$$\left[\epsilon' - \frac{\epsilon(0) + \epsilon(\infty)}{2}\right]^2 + (\epsilon'')^2 = \left[\frac{\epsilon(0) - \epsilon(\infty)}{2}\right]^2 . \tag{4.44}$$

Thus, a plot of the dielectric loss *vs.* the dielectric constant will be a circle with

$$centre = \left[\frac{\epsilon(0) + \epsilon(\infty)}{2}, 0\right] , \tag{4.45}$$

and

$$radius = \frac{\epsilon(0) - \epsilon(\infty)}{2} . \tag{4.46}$$

Such a plot is called a Cole-Cole plot and consists only of an upper-half plane semicircle since, in practice, dielectric losses are always positive. A typical Cole-Cole plot is shown in Figure 4.12. If, for a set of experimental dielectric data, the Cole-Cole plot is a perfect semicircle whose centre is on the ϵ'-axis, then it can be concluded that the system being studied can be characterized by a single Debye relaxation time.

If the dielectric constant and dielectric loss of a solid are measured as a function

Figure 4.12. Typical Cole-Cole complex plane plot for a dielectric reorientational process characterized by a single relaxation time.

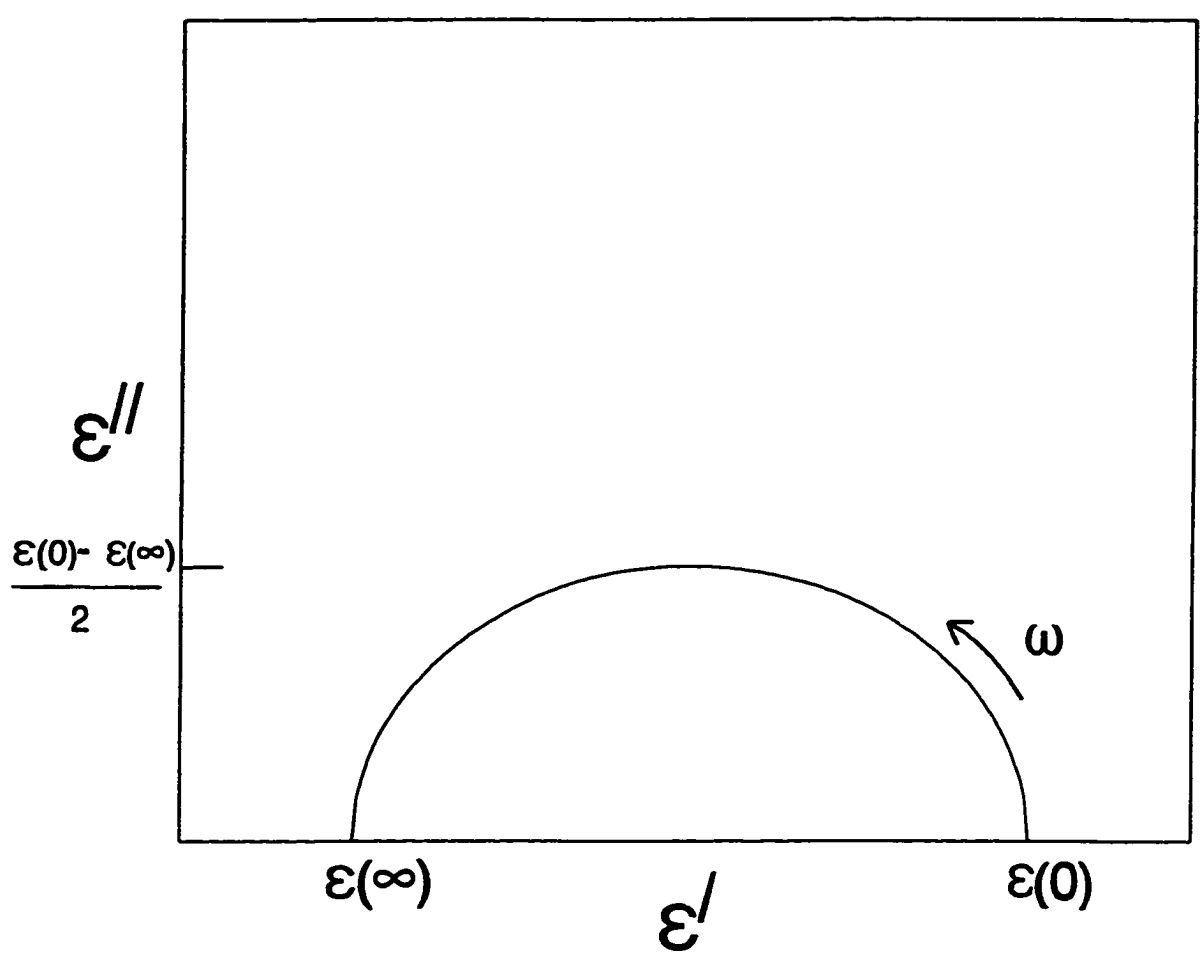

of frequency at several temperatures, a value for the relaxation time τ for the reorientational motion of the molecules in the dielectric can be obtained for each temperature using the dielectric loss curves and equation (4.43). The relaxation time τ is related to the rate of reorientation by the following equation:

$$\tau = \frac{1}{k_T}, \tag{4.47}$$

where k_T is the rate constant for reorientation at the particular temperature. Thus, if the temperature dependence of the relaxation time obeys the Arrhenius equation, it can be expressed as

$$\frac{1}{\tau} = Ae^{-E_a/RT}, \tag{4.48}$$

where A is a pre-exponential factor and E_a is the activation energy for the reorientational motion of the molecules in the dielectric. According to equation (4.48), a plot of the logarithm of the relaxation time ($\ln \tau$) *vs.* the reciprocal of the absolute temperature ($1/T$) will be linear and the activation energy can be calculated from the slope of the plot.

Since the relaxation time as a function of temperature is given by equation (4.48), this equation can be substituted into the Debye equations to obtain equations for the dielectric constant and dielectric loss as a function of temperature. Thus, another approach in measuring the dielectric properties of a substance is to keep the frequency of the field (ω) constant and to measure the dielectric constant and dielectric loss as a function of temperature. This is the approach usually seen in the literature for reporting dielectric measurements. A typical plot of ϵ' *vs.* T at a constant field frequency will look

similar to Figure 4.13 and can be rationalized as follows. At high temperatures, the motion of the molecules in the dielectric will be relatively fast and the dipoles can align with the alternating electric field giving a large dielectric constant. As the temperature is lowered, the reorientational motion of the molecules will slow down. Eventually, as the temperature is lowered, a temperature will be reached where the dipoles can no longer keep up with the oscillations of the electric field and a sharp drop in the dielectric constant occurs, along with dielectric losses. A typical dielectric loss curve as a function of temperature will have a similar shape to the curve in Figure 4.11, and a relaxation time can be obtained from the maximum in the curve using equation (4.43), where τ will be for the temperature of the maximum dielectric loss. Once τ is determined for various temperatures, the activation energy for the motion can be found using equation (4.48). Thus, dielectric measurements provide quantitative information concerning the rate of reorientational motion in solids, including the activation energy for the motion.

4.3.5 Distribution of Relaxation Times

Experimentally, it has been found that for many solids (and some liquids) which show dielectric dispersion effects, the data do not conform satisfactorily with the Debye curves described by equations (4.41) and (4.42). Typically, an experimental dielectric constant curve is flatter than the Debye curve, and the dielectric loss curve is broader than the Debye curve with a smaller maximum. Furthermore, the Cole-Cole plot of such

Figure 4.13. Typical dielectric constant *vs.* temperature plot at a constant frequency of the alternating electric field.

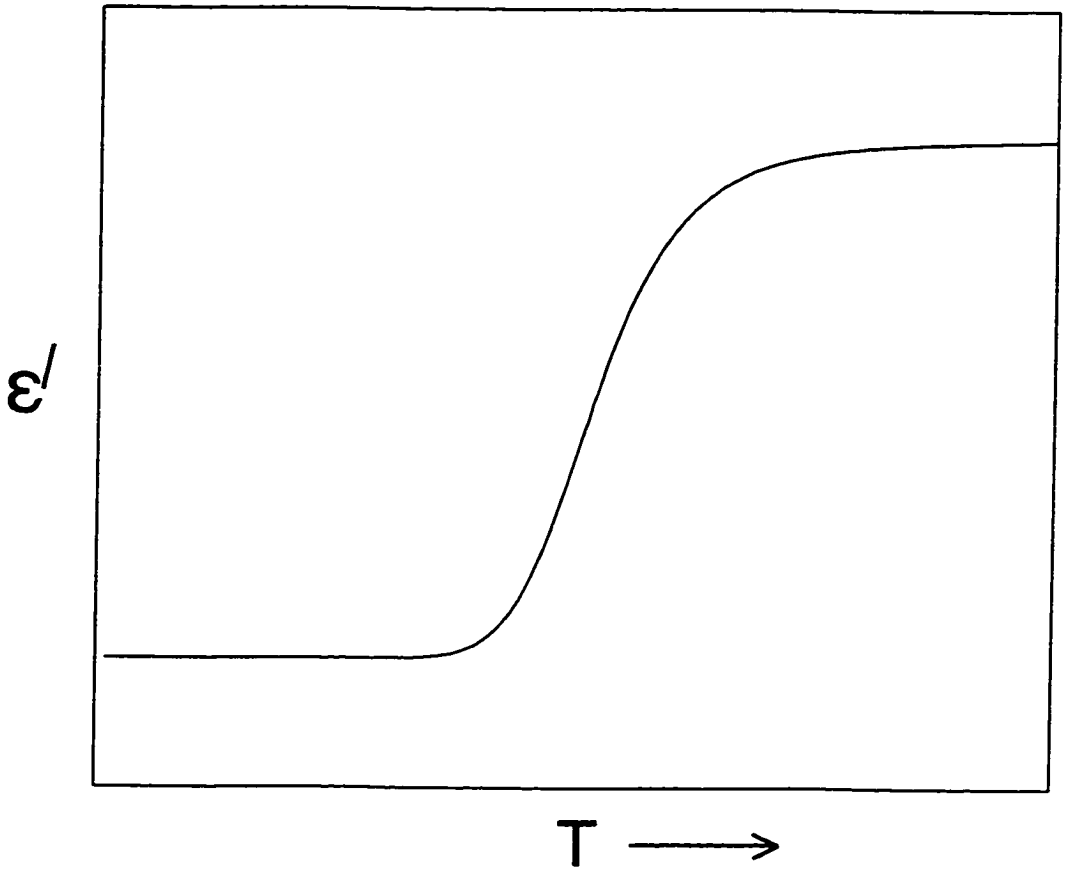

data is a circular arc with centre below the ϵ'-axis. The Debye equations are useful for a dispersion process which can be characterized by a single relaxation time. Deviations from the Debye curves can occur when a single relaxation time is not suitable to describe the process giving rise to the relaxation. It has been found that a theory based on a distribution of relaxation times is helpful to model experimental data which show deviations from the Debye curves. The reason such a distribution of relaxation times exists in condensed phases is related to the varying interaction forces and thermal influences that each dipole in a condensed phase experiences in different locations and at different times.[219] There are several empirical methods which have been developed to analyze data that are best represented by a model based on a distribution of relaxation times.[232]

Cole and Cole[233] reported the following empirical formula which can be used to describe a dispersion process showing deviations from Debye behaviour:

$$\epsilon^* - \epsilon(\infty) = \frac{(\epsilon(0) - \epsilon(\infty))}{1 + (j\omega\tau_o)^{1-\alpha_{cc}}}. \qquad (4.49)$$

The parameter α_{cc} can take on values between 0 and 1, and takes into account the relaxation time distribution. When $\alpha_{cc} = 0$, equation (4.49) is the same as the Debye equation (4.40) characterized by only a single relaxation time. The larger the value of α_{cc}, the greater is the extent of the relaxation time distribution. The parameter τ_o is an average relaxation time about which the distribution is symmetrically spread.

Solving equation (4.49) for the real (ϵ') and imaginary (ϵ'') parts of the complex dielectric constant (ϵ^*) gives[237]

$$\epsilon' - \epsilon(\infty) = \frac{(\epsilon(0) - \epsilon(\infty))[1 + (\omega\tau_o)^{1-\alpha_{cc}} \sin\frac{1}{2}\alpha_{cc}\pi]}{1 + 2(\omega\tau_o)^{1-\alpha_{cc}} \sin\frac{1}{2}\alpha_{cc}\pi + (\omega\tau_o)^{2(1-\alpha_{cc})}}, \qquad (4.50)$$

and

$$\epsilon'' = \frac{(\epsilon(0) - \epsilon(\infty))(\omega\tau_o)^{1-\alpha_{cc}} \cos\frac{1}{2}\alpha_{cc}\pi}{1 + 2(\omega\tau_o)^{1-\alpha_{cc}} \sin\frac{1}{2}\alpha_{cc}\pi + (\omega\tau_o)^{2(1-\alpha_{cc})}}. \qquad (4.51)$$

These equations are analogous to the Debye equations (4.41) and (4.42). The analogous Cole-Cole plot-type equation is obtained by eliminating $\omega\tau_o$ from equations (4.50) and (4.51) to yield

$$\left[\epsilon' - \frac{\epsilon(0) + \epsilon(\infty)}{2}\right]^2 + \left[\epsilon'' + \frac{\epsilon(0) - \epsilon(\infty)}{2}\cot\frac{(1-\alpha_{cc})\pi}{2}\right]^2 = \left[\frac{\epsilon(0) - \epsilon(\infty)}{2}\csc\frac{(1-\alpha_{cc})\pi}{2}\right]^2. \qquad (4.52)$$

which is the equation of a circle whose centre lies below the ϵ' axis. A representative plot of such a circular arc is shown in Figure 4.14. The parameter α_{cc} can be found from this Cole-Cole plot geometrically since, as can be derived from equation (4.52), the angle between a radius vector drawn from $(\epsilon(\infty),0)$ to the centre of the circle and the ϵ'-axis is equal to $\alpha_{cc}\pi/2$. The parameter τ_o can be determined by selecting any point on the circular arc and finding the length of segments u and v for this point as defined in Figure 4.14. The ratio of these two lengths is related to τ_o by the following equation:

Figure 4.14. Schematic Cole-Cole plot for a dielectric dispersion that is best represented by a symmetrical distribution of relaxation times. Note that the centre of the circular arc lies below the ϵ'-axis. The parameter α_{cc} can be found from the angle between the radius vector and the ϵ'-axis as shown. The relaxation parameter τ_o can be determined from the ratio of the distances v and u as described in the text.

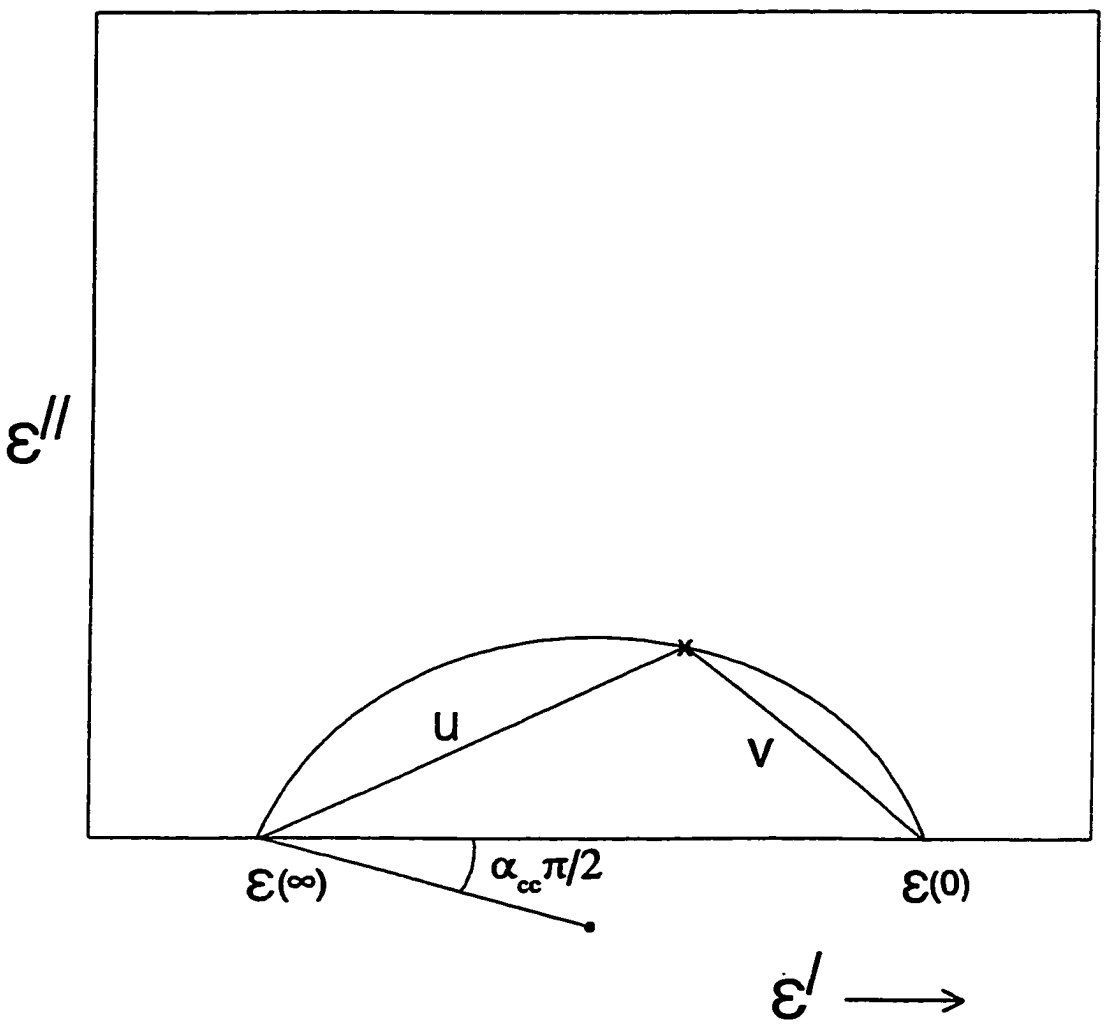

$$\frac{v}{u} = (\omega\tau_o)^{1-\alpha_{cc}} . \tag{4.53}$$

A better value of τ_o could be obtained by choosing several points on the circle and determining u and v for each point. As shown by equation (4.53), a plot of $\ln(v/u)$ *versus* $\ln\omega$ would be a straight line with slope $1-\alpha_{cc}$ and intercept $(1-\alpha_{cc})\ln\tau_o$.

Another empirical relation that was formulated by Fuoss and Kirkwood[238] is the following equation:

$$\epsilon'' = \epsilon''_m \, sech\left[\beta \ln\left[\frac{\omega}{\omega_m}\right]\right] , \tag{4.54}$$

where ω_m is the angular frequency corresponding to the maximum in the dielectric loss curve ϵ_m'', sech is the hyperbolic secant function, and β is a parameter describing the distribution of relaxation times. The value of β can range from 0 to 1, where a value of 1 corresponds to a single relaxation time, and progressively lower values represent a wider distribution of relaxation times. To a good approximation, the parameter β in the Fuoss-Kirkwood equation is related to the parameter α_{cc} in the Cole-Cole equation by[219]

$$\beta\sqrt{2} = \frac{1-\alpha_{cc}}{\cos\left[\frac{(1-\alpha_{cc})\pi}{4}\right]} . \tag{4.55}$$

Both the Cole-Cole equation and the Fuoss-Kirkwood relation assume a symmetrical distribution of relaxation times. A further empirical relation was brought forth by Cole and Davidson[239,240] to describe a system that is best represented by an unsymmetrical distribution,

$$\epsilon^* - \epsilon(\infty) = \frac{\epsilon(0) - \epsilon(\infty)}{(1 + j\omega\tau_{DC})^{\alpha_{DC}}}, \qquad (4.56)$$

where α_{DC} is an empirical parameter between 0 and 1, and τ_{DC} is the Davidson-Cole relaxation time. This relation results in a Cole-Cole plot that is not a circular arc but a skewed arc. An example of a substance for which such an arc is necessary to describe the experimental data is the dielectric relaxation behaviour of supercooled liquid glycerol[239,240] at $T = 223$ K.

4.3.6 Examples of Dielectric Measurements

As stated earlier, dielectric relaxation measurements are especially useful for studying motion in solids and for obtaining the activation energy for this motion. There are many examples of dielectric relaxation measurements of solids in the literature. A representative survey of some examples will now be presented.

A substance that has been extensively studied by this technique is ice. As discussed in Section 4.2.1, at relatively high temperatures the water molecules in ice are orientationally disordered, but ice does not undergo an ordering phase transition at lower temperatures because the reorientational motion in ice is slow at low temperatures and eventually freezes-in at a glassy phase transition temperature above where the ordering transition would normally take place.[208] Evidence of the slow reorientational motion in ice can be seen from dielectric relaxation measurements of ice.[237,238] Figure 4.15(a)

Figure 4.15. (a) Dielectric constant behaviour of ice as a function of temperature (○, measured ‖ to *c*-axis, ●, measured ⊥ to *c*-axis). (b) Dielectric loss curves for ice as a function of temperature (measured ‖ to *c*-axis). (c) Dielectric Cole-Cole plots for ice at three different temperatures (from data measured ⊥ to *c*-axis); from reference (242).

(a)

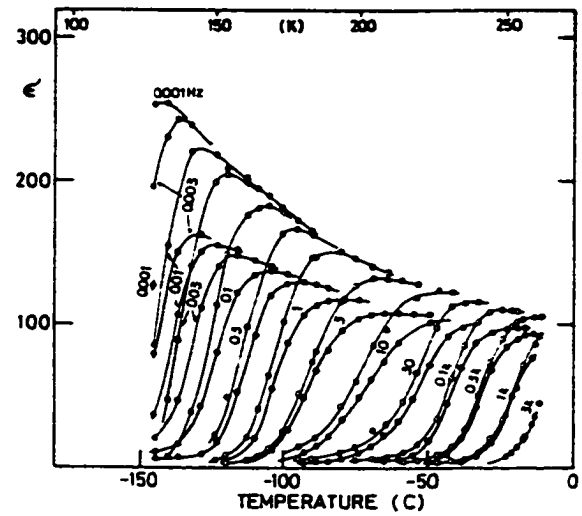

(b)

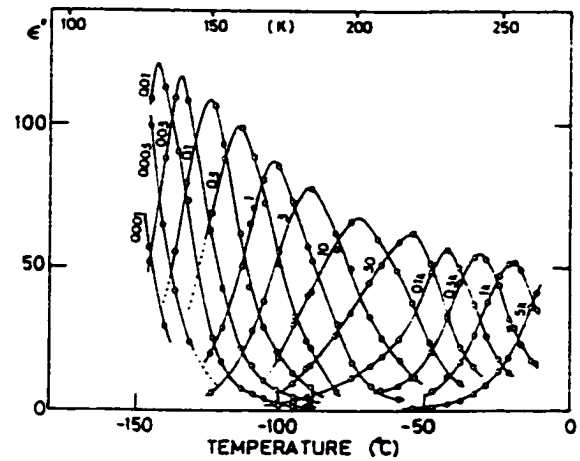

(c)

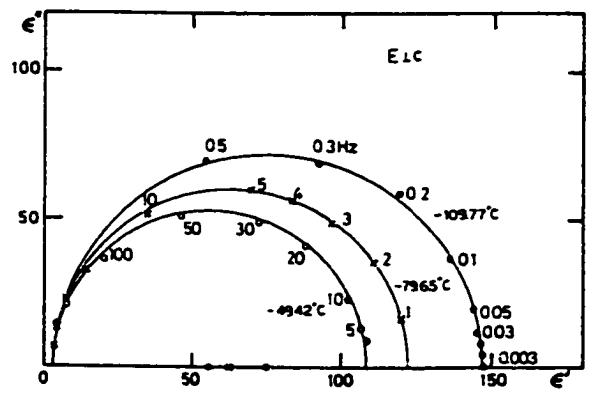

shows the dielectric constant of ice as a function of temperature for several field frequencies.[242] There are two sets of curves shown. In one set the measurements were taken parallel to the *c*-axis in the ice crystal; in the other set the measurements were taken perpendicular to the *c*-axis. The corresponding dielectric loss curves are given in Figure 4.15(b) and some Cole-Cole plots are shown in Figure 4.15(c). These plots are consistent with a relaxation that can be described by a single relaxation time. The lowest temperature studied in this experiment is ~ -150°C (123 K) which is ~ 15 K above the glassy phase transition temperature of ice. Note that at T = -150°C the motion of the ice molecules cannot keep up with a field that is alternating at a frequency of only 0.003 Hz. Thus, these measurements confirm that the reorientational motion of ice is slow at the low temperatures just above the glassy phase transition.

Recall, however, that by doping ice with a small amount of KOH, a new phase transition[209,210] is observed at T = 72 K which can occur because the presence of KOH catalyzes the motion of the ice molecules. Evidence for the catalytic effect of the KOH on the motion of the ice molecules should be observed in measurements of the dielectric properties of KOH-doped ice. The dispersion curves are shown in Figure 4.16(a) along with Cole-Cole plots for two temperatures (Figure 4.16(b)).[243,244] The Cole-Cole plots are circular arcs with centres below the ϵ'-axis which is consistent with a relaxation time distribution which, in the Cole-Cole model (equation (4.49)), corresponds with an α_{cc} value of 0.2. Recall that in pure ice, the molecules had trouble keeping up with a 0.003 Hz field at T = 123 K, but note that in the KOH-doped ice, significant relaxation does not occur in a 1.0 Hz field until the temperature is lowered to 75 K. Thus, these

Figure 4.16. (a) Dielectric constant behaviour of KOH-doped ice. (b) KOH-doped ice Cole-Cole plots at two different temperatures; from reference (243).

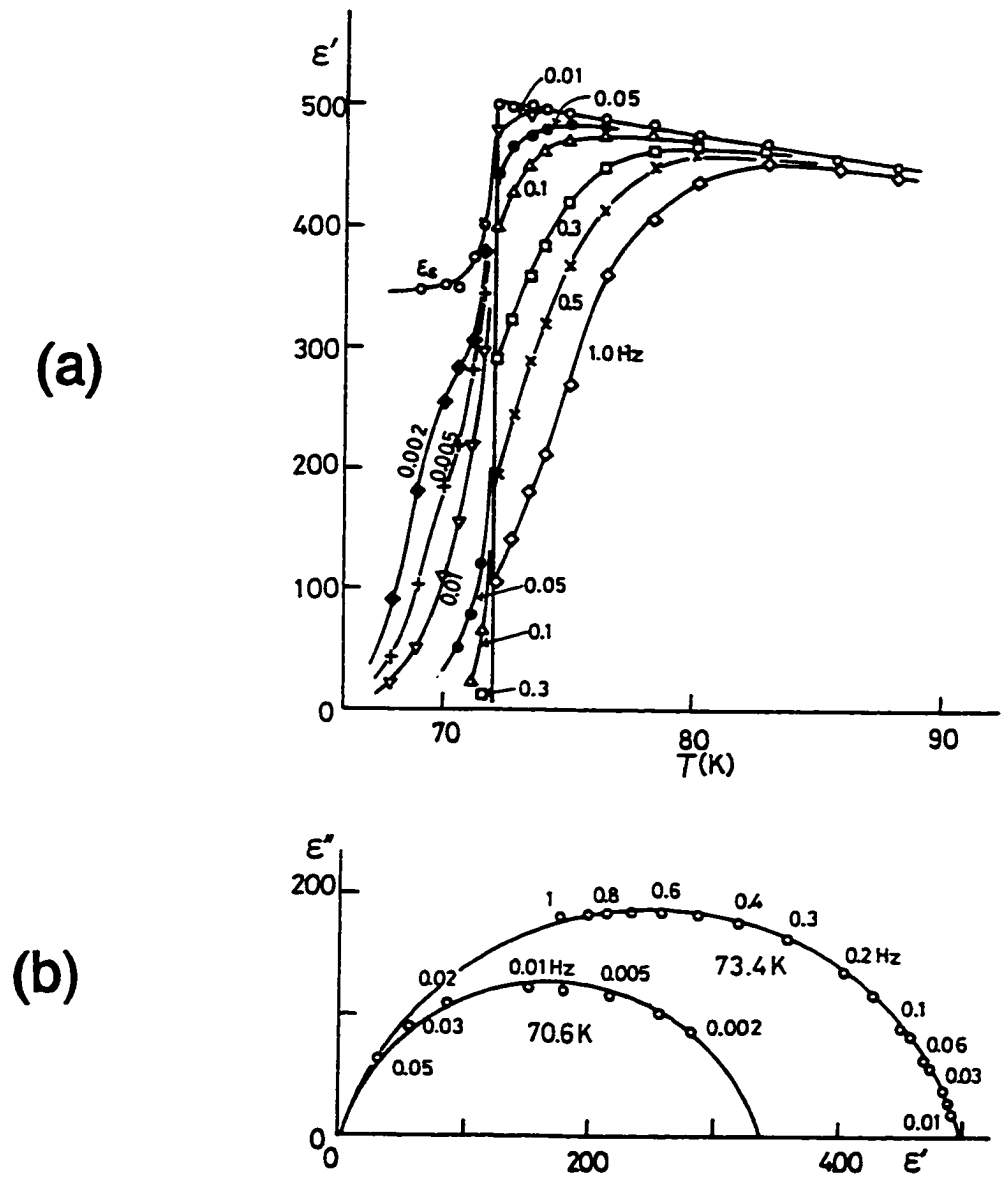

measurements show that the KOH impurity does indeed catalyze the reorientational motion in ice.

This conclusion also can be reached by calculating the activation energy for the reorientational motion of pure ice and KOH-doped ice. This can be done by determining the dielectric relaxation times at various temperatures from the maxima in the dielectric loss curves, and calculating the slope of an Arrhenius plot of the relaxation data. The resulting activation energies[243] are 14.6 $kJ \cdot mol^{-1}$ for the KOH-doped ice and 55.2 $kJ \cdot mol^{-1}$ for the pure ice.

Another system that has been extensively studied by the dielectric relaxation technique is carbon monoxide. Recall that a dipolar ordering transition for CO is expected at a temperature of $\sim$ 5 K but cannot occur because the rate of reorientation of CO at low temperatures is negligible leading to frozen-in disorder[211] in CO and residual entropy.[196] Dielectric measurements[198] of solid CO give an activation energy of 6.13 $kJ \cdot mol^{-1}$ for the motion of carbon monoxide and a pre-exponential factor of $A = 4.9 \times 10^{14}\ s^{-1}$. Using these parameters, the rate of reorientation for CO at low temperatures can be extrapolated. Such a calculation yields rate constants (k_T) of 1 h^{-1} at $T = 17.5$ K and $(10\ h)^{-1}$ at 16.6 K which is very slow compared to the laboratory time-scale. Thus, these measurements prove that the disorder (motion) in carbon monoxide is frozen-in at temperatures above the temperature of the predicted dipolar ordering transition.

Another system that will be mentioned due to its similarity to the alkali-metal hydroxides is rubidium cyanide. The alkali-metal cyanides are similar to the alkali-metal

hydroxides in that they consist of dumbbell-shaped anions that are dynamically disordered in cubic phases at high temperatures. As the temperature is lowered these compounds undergo phase transitions where the cyanide ions become more ordered. A transition from the high-temperature cubic phase I to phase II occurs at T = 288 K, 168 K, and 132 K for NaCN,[245] KCN,[246] and RbCN,[247] respectively. In phase II much of the cyanide ion disorder is removed, although head-to-tail disorder of the cyanide ions in this phase is suggested by the entropy change of the I-II transition. It would be expected that this disorder would be removed through another phase transition driven by electrostatic interactions between the CN^- dipoles. This does indeed occur for NaCN[245] and KCN[246] at temperatures of 172 K and 83 K, respectively, where in the low-temperature phases the cyanide ions are fully ordered in an antipolar arrangement.[248]

The expected ordering transition is not observed for RbCN.[247,249] It is likely that the reorientational motion of the cyanide ions in RbCN becomes frozen-in before the phase transition can take place. This has been confirmed through the observation of thermal relaxation effects in RbCN at a temperature of 30 K indicating a glassy phase transition and the onset of frozen-in disorder.[247] Dielectric relaxation measurements have also been performed on RbCN.[250,251] Dielectric dispersion is observed between 40 - 70 K due to the reorientational motion of the cyanide ions. The relaxation times that were obtained from these measurements exhibited Arrhenius Law behaviour with temperature resulting in an activation energy of 9.65 $kJ \cdot mol^{-1}$ and a pre-exponential factor of 8.33 $\times$ 10^{13} s^{-1}. Extrapolating using these kinetic parameters, the rate constant for reorientation is 1 h^{-1} at $T \sim$ 28.8 K and $(10\ h)^{-1}$ at $T \sim$ 27.3 K. These results along

with the observation of the glassy phase transition at $T = 30$ K indicate that the disorder of the cyanide ions in RbCN becomes frozen-in before an ordering transition can take place.

4.4 Research Objectives

A deuterium-induced phase transition to a low-temperature monoclinic phase occurs in NaOD at a temperature of 153 K which does not occur in NaOH at atmospheric pressure. A postulate of residual entropy in NaOH was made to explain the differing low-temperature behaviour of NaOH compared to NaOD. The source of the proposed residual entropy in NaOH would be a freezing-in of the disorder of the hydrogen atoms before a phase transition could take place. This residual entropy postulate has been tested through a residual entropy calculation of NaOH based upon a single equilibrium study involving NaOH that was found in the literature. The result of this calculation suggested that NaOH has a residual entropy of 5.2 ± 1.3 $J \cdot K^{-1} \cdot mol^{-1}$.

More direct evidence for residual entropy in NaOH is needed before any definite conclusions concerning the residual entropy postulate can be made. Since the onset of frozen-in disorder manifests itself as a glassy phase transition in the heat capacity curve, this evidence could come from the detection of a glassy phase transition in NaOH. Glassy phase transitions in solids are often subtle, but they can be detected by a couple of methods. One method is to look for thermal relaxation effects by calorimetry. Another

method is to obtain information concerning the kinetics of reorientation of the molecules in the solid by the technique of dielectric relaxation, and thereby determining at what temperature the motion of the molecules in the solid becomes too slow compared to the laboratory timescale. It should be noted that even if these studies disproved the existence of residual entropy in NaOH, valuable insight would be still be gained through calorimetric and dielectric studies into the source of the anomalous behaviour in NaOH.

Thus, the major purpose of this research was to confirm or reject the postulate of residual entropy in sodium hydroxide through a detailed search for a glassy phase transition in NaOH. The first study that was done with this aim in mind was an examination of NaOH by adiabatic calorimetry to look for thermal relaxation effects. Secondly, it was desired to study sodium hydroxide using the dielectric relaxation method to look for evidence of dielectric dispersion. However, no apparatus for measuring the dielectric relaxation properties of solids existed in the laboratory. Thus, a major focus of this research project was the design and construction of an experimental apparatus suitable for measuring dielectric relaxation in solid samples. Once the apparatus was designed, built, and suitably tested, it was used to measure the dielectric properties of NaOH and NaOD.

Chapter 5: Calorimetric Measurements

5.1 Basic Principles and Concepts

5.1.1 Theory of Heat Capacity

Calorimetry is an experimental technique associated with the measurement of the heat content and/or heat capacity of a substance. The heat capacity is a necessary quantity for the accurate determination of the fundamental thermodynamic functions of enthalpy, entropy, and Gibbs energy. Furthermore, as described in Section 1.5, the heat capacity as a function of temperature shows very characteristic behaviour at a phase transition. For a first-order phase transition, the heat capacity will increase to very high values over a narrow temperature range (ideally, if the transition is truly isothermal, the heat capacity should go to infinity at the transition temperature). For a phase transition of second-order, the anomaly in the heat capacity is usually more gradual, with a small finite jump discontinuity in the heat capacity curve at the transition temperature. Thus, measurement of the heat capacity curve as a function of temperature is a powerful method for detection of phase transitions, especially polymorphic phase transitions, and whether they are first- or second-order.

By a qualitative definition, the heat capacity (C) is the amount of heat (q) required to increase the temperature of a given amount of a substance per kelvin of temperature rise. This can be expressed more quantitatively as

$$C \equiv \frac{dq}{dT}. \tag{5.1}$$

During a first-order phase transition, the heat applied to a substance is used to rearrange its molecular structure, rather than directly increase its temperature, so that a large amount of applied heat results in a very small (ideally zero) temperature change of the sample which results in an abrupt increase in the heat capacity by equation (5.1). This explains the heat capacity anomaly that is observed in the heat capacity curve of a substance at a phase transition.

Heat, in general, is not a thermodynamic state function[252] (*i.e.*, dq is an inexact differential), which means that the heat capacity as stated by the definition in equation (5.1) is dependent on the path taken to increase the temperature of the sample from one temperature to another. Meaningful, reproducible heat capacity data for a substance can only be reported if the thermodynamic path between the two states is unambiguously specified. There are two popular constraints that are imposed on the path for the heat capacity measurement: constant volume (isochoric) and constant pressure (isobaric). Heat applied to a system under constant volume conditions is equal to the change in internal energy (dU) of the system, while heat at constant pressure is equal to the change in enthalpy (dH). Both the internal energy and the enthalpy are state functions. Therefore, a heat capacity under constant volume conditions (C_v) can be defined as

$$C_v \equiv \frac{dq_v}{dT} \equiv \left[\frac{\partial U}{\partial T}\right]_v, \tag{5.2}$$

and a heat capacity at constant pressure (C_p) can be defined as

$$C_p \equiv \frac{dq_p}{dT} \equiv \left[\frac{\partial H}{\partial T}\right]_p, \tag{5.3}$$

both of which are state functions. Thus, suitable measurement of C_v or C_p will result in meaningful quantities that can be uniquely specified for each state of the system.

Typically, heat capacity measurements are made under constant pressure conditions (to be more precise, at the saturated vapour pressure of the sample, C_{sat}, to be discussed later), so it is common to see values of C_p quoted for substances in the literature. If a material is isotropic, values of C_p can be converted to C_v by the expression[253]

$$C_p - C_V = \frac{\alpha^2 VT}{\beta_T}, \tag{5.4}$$

where α is the coefficient of thermal expansion defined by equation (1.16), and β_T is the isothermal compressibility defined by

$$\beta_T \equiv -\frac{1}{V}\left[\frac{\partial V}{\partial P}\right]_T. \tag{5.5}$$

For anisotropic materials, the conversion of C_p to C_v is more complicated, requiring knowledge of the elastic constant and thermal expansion tensors for the material.

Once the heat capacity (C_p) is known, the enthalpy, entropy and Gibbs energy can immediately follow. An expression for the enthalpy can be obtained by direct integration of equation (5.3), *i.e.*,

$$H - H_o = \int_0^T C_p dT, \tag{5.6}$$

where H_o is the absolute enthalpy at a temperature of absolute zero. The heat capacity can be related to the entropy using the differential relation

$$dH_p = TdS, \tag{5.7}$$

which, when substituted into equation (5.3) gives

$$C_p = T\left[\frac{\partial S}{\partial T}\right]_p. \tag{5.8}$$

Integration of equation (5.8) yields the following expression for the entropy:

$$S - S_o = \int_0^T \frac{C_P}{T} dT, \tag{5.9}$$

where S_o is the residual entropy. Note that equation (5.9) represents the calorimetric entropy (*S(cal)*). Once H and S are known, the Gibbs energy (relative to G at absolute zero) can be obtained from its definition,

$$G \equiv H - TS. \tag{5.10}$$

The enthalpy change ($\Delta_{trs}H$) during a phase transition can be determined by integration of the anomalous heat capacity and subtraction of the smoothed baseline heat capacity that would exist in the absence of the phase transition. The entropy change ($\Delta_{trs}S$) can be found in a similar fashion by integration of the anomalous C_p/T contribution. Evaluation of $\Delta_{trs}S$ is very important towards understanding the nature of the order/disorder, dynamical changes, and the mechanism of a transition.

On a microscopic level, the heat capacity of a sample arises due to excitations of the various degrees of freedom in the sample, which basically involves transitions

between quantum-mechanical energy levels. For solids, the most important degree of freedom is vibrational in nature, although rotation also can contribute if rotation is possible in the solid state. For the most part though, measurement of the heat capacity of solids probes transitions between the vibrational energy levels of the material, including both intramolecular and intermolecular (lattice) vibrations. Thus, heat capacity measurements can provide direct information concerning the density of states and molecular dynamics in the solid state.

There are two main statistical-mechanical models that have been developed to describe the heat capacity of solids.[254] The first of these is the Einstein model[255] which treats a solid as a collection of independent three-dimensional harmonic oscillators all of which vibrate at the same frequency, ν. Applying the principles of statistical mechanics and thermodynamics to this model yields the following equation for C_v:

$$C_v = 3R\left[\frac{h\nu}{k_B T}\right]^2 \frac{e^{h\nu/k_B T}}{(e^{h\nu/k_B T} - 1)^2}. \qquad (5.11)$$

The Einstein model for the heat capacity performs well at high temperatures, but the Einstein heat capacity decreases much more rapidly at low temperatures than the T^3 dependence of C_v that is observed experimentally.

The experimentally observed low-temperature heat capacity is much better described by the Debye heat capacity model[256] which takes into account the fact that atoms (molecules) in a solid vibrate with a distribution of frequencies rather than just a single frequency. The Debye model assumes that the low-frequency (long wavelength) vibrations are the important contributors to the heat capacity, and considers all

frequencies up to a cut-off frequency (ν_D). The cut-off frequency is chosen so that the total number of vibrations employed in the Debye model (which uses a density of states distribution that is proportional to the square of the frequency) is equal to the total number of vibrational modes in the solid. Again, using the harmonic oscillator approximation and the principles of statistical mechanics, the Debye model gives the following equation for C_v:

$$C_v = 9R\left[\frac{T}{\Theta_D}\right]^3 \int_0^{\Theta_D/T} \frac{x^4 e^x}{(e^x - 1)^2} dx , \tag{5.12}$$

where Θ_D, defined as

$$\Theta_D = \frac{h\nu_D}{k_B} , \tag{5.13}$$

is called the Debye temperature. In the limit of low temperatures, the Debye equation reduces to

$$C_v = \frac{12}{5}\pi^4 R\left[\frac{T}{\Theta_D}\right]^3 , \tag{5.14}$$

which is in accordance with the observed T^3-dependence of the heat capacity of solids at low temperatures. The Debye model provides a good description for lattice vibrations whereas the Einstein model more accurately describes intramolecular vibrations.

As mentioned previously, the heat capacity at constant pressure (C_p) is generally the quantity that is measured experimentally, and is useful for deriving H, S, and G. However, it is the heat capacity at constant volume that is more useful theoretically as

can be seen from the Einstein and Debye heat capacity equations that are derived for C_v. The advantage of C_v over C_p in a theoretical sense stems from the fact that theoretical models are concerned with the calculation of the internal energy of a system which is directly related to C_v. If the experimental C_p heat capacity data are to be theoretically analyzed in terms of solid-state dynamics, density of states, or decomposition into component vibrational contributions using the Einstein and/or Debye heat capacity models (or other models of solid-state properties), then it is desirable to convert the C_p values to C_v values. This can be done for an isotropic material using equation (5.4) provided the thermal expansion coefficient and isothermal compressibility of the substance are known as a function of temperature. In the absence of these data, a C_p - C_v correction term of the form

$$C_p - C_v \sim A C_v^2 T \sim A C_p^2 T \tag{5.15}$$

can be used, where A, given by

$$A = \frac{V\alpha^2}{\beta_T C_p^2}, \tag{5.16}$$

is assumed to be temperature independent.[257,258,259] Equation (5.15) is known as the Nernst-Lindemann relation.[260]

5.1.2 Measurement Techniques

5.1.2.1 Thermal Analysis Methods

The various types of experimental apparatus that can be used to explore the thermodynamic functions of a substance can be divided into two groups: thermal analysis and calorimetry.[261] Thermal analysis methods are commonly scanning methods, which means that measurements are taken without allowing for the establishment of equilibrium. Two common examples of thermal analysis methods are differential scanning calorimetry (DSC) and differential thermal analysis (DTA). As the names imply, these are differential techniques, meaning that the measurements taken are not absolute, but are measured relative to a reference. The big advantages of thermal analysis methods over absolute calorimetry are the ability to use small sample sizes (typically 10 mg or less), the fast data collection time, and the commercial availability of instruments. The disadvantages are less accuracy, non-equilibrium and relative measurements, and the inability to attain temperatures below 100 K.

Differential scanning calorimetry[261] involves mounting a sample ($\sim$ 10 mg) in a sample pan that is placed on a sample platform. Next to this is a reference platform which contains the reference (which is usually an empty pan). The reference and sample platforms have separate heaters, and the temperature difference (ΔT) between the sample and the reference, and the difference in power supplied to the sample *versus* the reference (ΔP) can be monitored. The actual DSC experiment involves heating (or cooling) the

sample and reference at a constant rate (the scanning rate) and determining the difference in power between the sample and the reference required to maintain $\Delta T = 0$ at all temperatures during the scan.

The output of the DSC experiment is a plot of ΔP *versus* time (or temperature, since both temperature and time are related by the controlled scanning rate). When the sample undergoes a thermal event such as a phase transition, a peak will appear in the DSC output curve. For an endothermic event, the peak will be in one direction (more power required to increase the temperature of the sample relative to the reference when the sample undergoes an endothermic process). Conversely, when the sample exhibits an exothermic event, the peak in the ΔP *versus* time curve will be in the other direction.

Since the area under a curve of power *versus* time is equal to energy, the area under a peak associated with a thermal event will be related to the enthalpy change which occurs during the event. Furthermore, the temperature at which the event occurs (called the onset temperature, T_{onset}) can be determined from the peak. This illustrates the major use of DSC: it enables the quick determination of the temperature at which a phase transition occurs in a substance and the enthalpy change during the transition. In order to obtain $\Delta_{trs}H$ values, the DSC must be calibrated with at least one standard substance that has a well-characterized phase transition. The substance that is often chosen for this purpose is indium (melting phase transition at $T = 429.8$ K).

The signal in a DSC experiment is actually proportional to the difference between the heat capacity of the sample and the heat capacity of the reference material. Thus, DSC can be used to measure the heat capacity of the sample. Again, suitable calibration

with a standard sample of well-known heat capacity is essential for accurate measurements. With suitable precautions, especially concerning thermal contact, heat capacities can be obtained from DSC that are accurate to within $\pm$ 3%.[262,263]

Differential thermal analysis[261] (DTA) is another thermal analysis technique which is similar to DSC in many ways. Both are scanning, non-equilibrium techniques that involve measurements relative to a reference. However, in DTA, both the sample and the reference are heated with the same heater, and the temperature difference between them ($\Delta T = T_{ref} - T_{sample}$) is monitored as a function of temperature. Since phase transitions take place more or less isothermally, when the sample undergoes a phase transition a peak will occur in the DTA output curve. During an endothermic phase transition, the temperature of the sample will lag behind that of the reference ($\Delta T > 0$), so that a peak will result in the DTA curve. For an exothermic phase transition, a peak in the opposite direction will be observed.

Thermal analysis methods are particularly useful in the determination of phase diagrams, especially binary phase diagrams. The speed at which data can be obtained using DSC and DTA means that runs can be done for several binary compositions. All of the thermal events associated with binary systems can be detected and characterized, *e.g.*, eutectics, peritectics, polymorphic phase transitions, and compound formation.

5.1.2.2 Adiabatic Calorimetry

The term adiabatic calorimetry[261,264,265,266] is associated with a method that will accurately determine the heat capacity (and subsequently, the thermodynamic functions) of a given sample. Whereas DSC and DTA can scan an entire temperature range in several minutes, the measurement of one heat capacity value using adiabatic calorimetry can take over an hour. The benefits, though, are the very accurate and reproducible results that are obtained. Furthermore, since measurements are taken relatively slowly, in most cases the resulting values are equilibrium values. No reference is needed in adiabatic calorimetry, as the technique gives absolute heat capacities. Besides being a slow method, the disadvantages of adiabatic calorimetry are that large samples are required for measurement (can be as low as 1 g, but usually much more), and the required equipment is not available commercially, and therefore must be home-built.

An adiabatic calorimeter is a device that determines the heat capacity of a sample under adiabatic conditions, *i.e.*, there is no exchange of heat between the system and the surroundings. Ideally, the heat capacity measured with an adiabatic calorimeter is due solely to thermal changes within the sample without complications due to heat exchange with the surroundings. In practice, it is impossible to have perfect adiabatic conditions, *i.e.*, to completely thermally isolate a system from its surroundings. However, near adiabatic conditions can be established through the use of a high vacuum to minimize thermal conduction by gases, an adiabatic shield to minimize the temperature gradient between the system and the surroundings, and the use of fine wires as electrical leads and

a heat sink to minimize heat exchange with the surroundings.

The heat capacity of a sample is usually measured by adiabatic calorimetry using a heat pulse method. By this method, a known amount of heat (q) is applied to the sample and the temperature before (T_i) and after (T_f) the heat pulse are measured so that the temperature difference is known ($\Delta T = T_f - T_i$). The heat capacity is then calculated as

$$C_p = \frac{q}{\Delta T}, \tag{5.17}$$

where the determined heat capacity is for the average of T_i and T_f.

The heat capacity calculated by equation (5.17) represents the total heat capacity of the calorimeter vessel and its contents, which includes the calorimeter vessel itself, the sample, the heater for the vessel, the thermometer, and any other materials which receive heat from the vessel heater. The heat capacity contributions from all of the components exclusive of the sample must be known and subtracted from the total heat capacity in order to obtain the heat capacity of the sample only.

A note should be made about the type of heat capacity that is measured in an adiabatic calorimeter. The conditions under which the measurements are taken are not strictly constant pressure conditions since the sample may have a significant vapour pressure which will change with temperature. Strictly speaking, the heat capacity measured is the heat capacity at the saturated vapour pressure of the sample, C_{sat}. The heat capacity at constant pressure (C_p) can be calculated from C_{sat} using the relation[267]

$$C_p - C_{sat} = \alpha V T \left(\frac{\partial P}{\partial T} \right)_{sat} . \qquad (5.18)$$

For the usual case of nonvolatile solids, the difference between C_p and C_{sat} is negligible. Thus, for all practical purposes involving solids, $C_p \simeq C_{sat}$, and it is common to see heat capacity data for solids obtained from adiabatic calorimetry reported as either C_p or C_{sat}.

A very important component of an adiabatic calorimeter is the thermometer since temperatures need to be measured to a very high degree of accuracy. Resistance thermometers[268] can provide the required accuracy and reproducibility, provided that they are properly calibrated. Resistance thermometers made from various materials are available commercially. The useful temperature range over which a resistance thermometer can be used depends on the material from which it is made. A thermometer that is commonly used in adiabatic calorimetry is the platinum resistance thermometer, which has good sensitivity from about 20 K to above room temperature.

Older adiabatic calorimeters required sample masses of the order of 50 - 100 g or more to obtain meaningful data. Today, calorimeters which can take measurements of smaller samples in the 5 - 10 g mass range are fairly common.[269,270,271] With the passage of time, designs of adiabatic calorimeters have become more and more innovative. Adiabatic calorimeters have been designed that can take measurements on samples with masses less than 0.5 g;[272,273] others can take measurements at high pressures.[274,275]

Accurate equilibrium heat capacity data from calorimetry are necessary for the precise determination and characterization of phase transitions.[261] Along with a

discontinuous anomaly in the heat capacity curve, a polymorphic phase transition often consists of a gradual, non-isothermal component that can only be detected by equilibrium methods. Adiabatic calorimetry can be used to determine the heat capacity over a very wide temperature range, so that for a phase transition, a baseline heat capacity can be accurately interpolated. This means that the anomalous portion of the heat capacity during a phase transition can be separated from the normal baseline component which is necessary for the accurate determination of the thermodynamic parameters of the transition, such as the enthalpy and entropy changes. The temperature at which a phase transition occurs (T_{trs}) can be obtained by taking many heat capacity measurements with small q in the region of the transition, where T_{trs} is the temperature at which the peak heat capacity value occurs.

Data from adiabatic calorimetry are important for the determination of the chemical thermodynamic parameters of a substance as a function of temperature. These include the enthalpy, entropy, and Gibbs energy, the calculation of which requires accurate knowledge of the heat capacity. These parameters allow for the comparison of relative thermodynamic stabilities of substances, and also an understanding of the thermodynamic driving forces for chemical reactions. As described in Section 4.1, calculation of the residual entropy of a substance requires the use of the entropy determined from calorimetric data.

Low-temperature heat capacity data under equilibrium conditions are necessary in order to decompose the experimental values into components due to the various degrees of freedom which give rise to the heat capacity. The most important

contributions are vibrational, but effects due to rotational, electronic, magnetic, and tunnelling degrees of freedom can also be observed.

It is only through very precise calorimetric measurements that the subtle effects indicating a glassy phase transition can be detected as discussed in Section 4.2. A glassy phase transition in solids gives rise to a slight step in the heat capacity curve (*e.g.*, in ice,[208] Figure 4.4) which can be resolved through adiabatic calorimetry. The ability to maintain adiabatic conditions over a long period of time (several hours) allows for the observation of enthalpy relaxation effects near the glassy phase transition temperature. These effects are characterized by relaxation times of the order of 10^2 to 10^5 s. In this way, an adiabatic calorimeter acts as an ultra-low frequency spectrometer.[214,215]

5.2 Experimental Apparatus

5.2.1 Description of Adiabatic Calorimeter

The adiabatic calorimeter that was used in this research work[269,276] was home-built and obtained heat capacity data by use of the heat-pulse method. A schematic diagram of the adiabatic calorimeter is shown in Figure 5.1. A more detailed look at the sample cell and the heater/thermometer assembly is provided in Figure 5.2. The sample cell was made of gold-plated copper (volume ~ 5 mL) into which was placed the sample to be measured. The vessel had a lid which was also made of gold-plated copper that was

Figure 5.1. Schematic diagram of the adiabatic calorimeter; styled after reference (276).

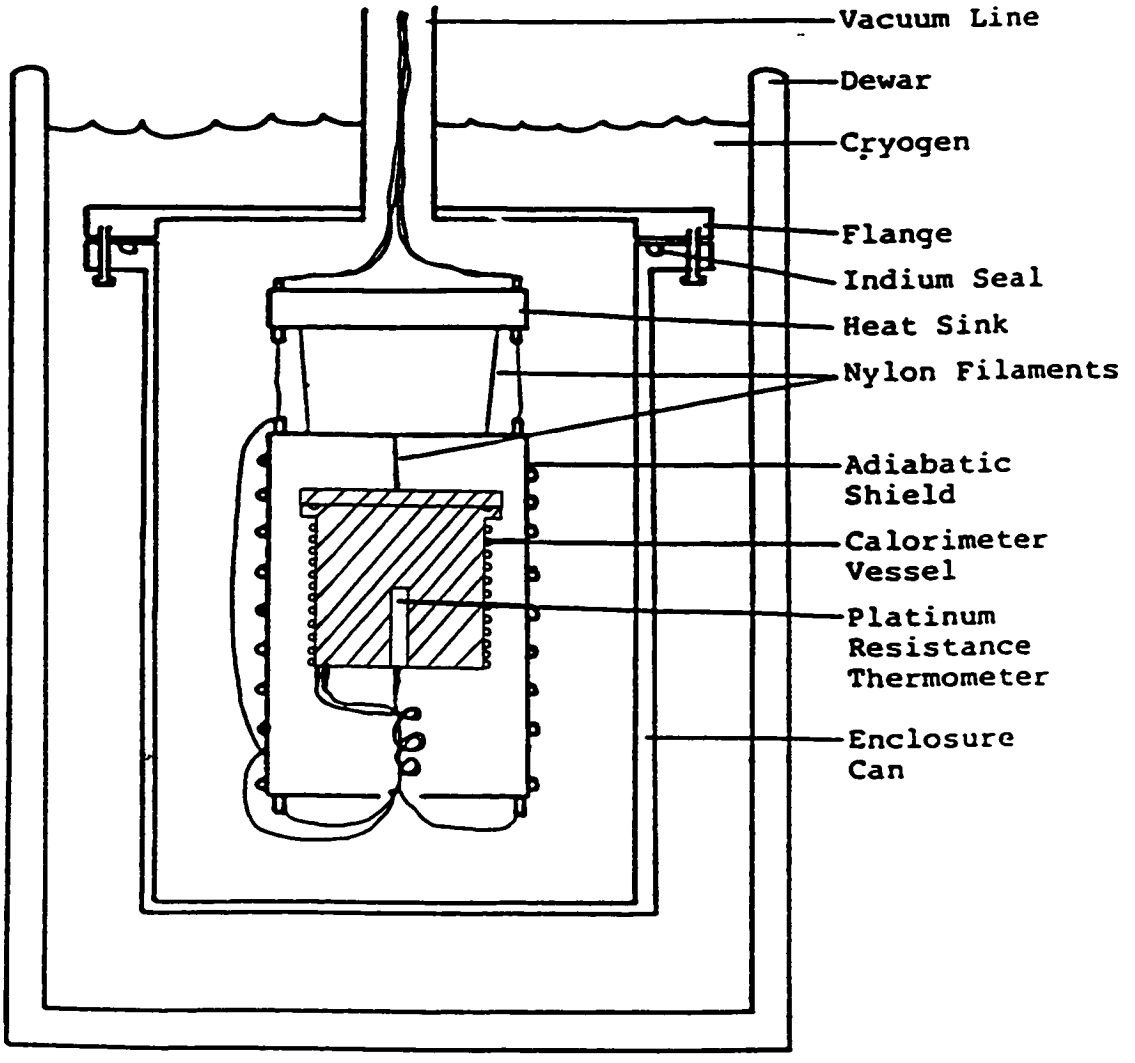

Figure 5.2. The sample vessel and heater/thermometer assembly of the adiabatic calorimeter; from reference (276).

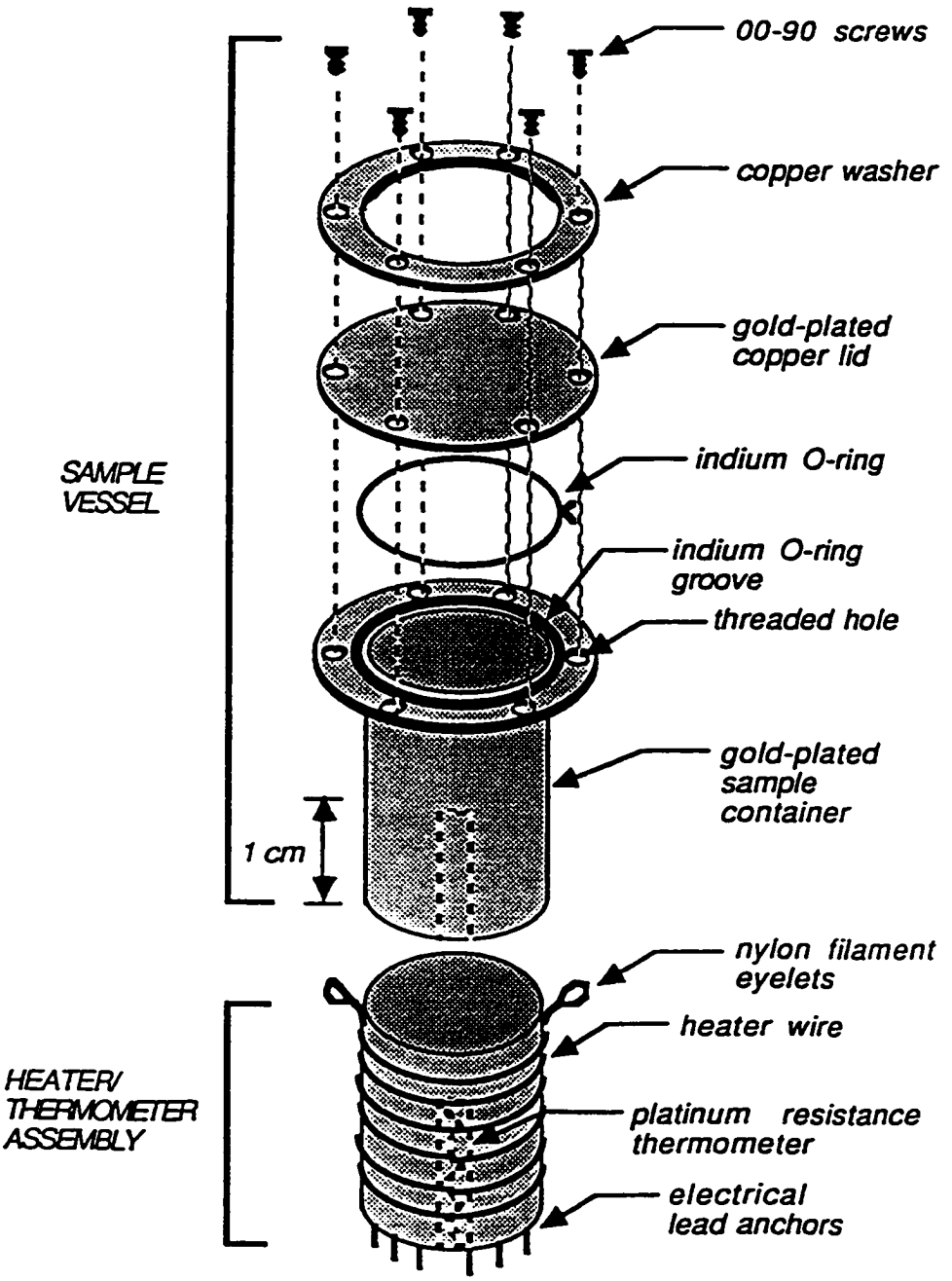

attached to the vessel with 8 screws. The junction between the vessel and the lid was sealed with a ring of 0.5 mm diameter indium wire. Indium is a soft metal which forms a good seal with applied pressure from the screws and lid.

The sample cell fit snugly into a heater/thermometer assembly consisting of thin-walled copper with a narrow, cylindrical, centrally located thermometer well. Thermal contact between the sample vessel and the assembly was facilitated with the application of a small amount ($\sim$ 5 mg) of Apiezon T grease (Apiezon Products Ltd., sold by Fisher Scientific). The heater was an electrical resistance heater made up of approximately 2.6 m of double silk-wound Karma wire bifilarly wound around the heater/thermometer assembly. The heater resistance was approximately 550 Ω at room temperature.

All temperature measurements were obtained using a platinum resistance thermometer (Lake Shore Cryotronics model Pt-103; $R \sim 100\ \Omega$ at $T = 273$ K) placed inside the thermometer well of the heater/thermometer assembly. This thermometer well fit into a matching centrally located cylindrical hole at the bottom of the sample vessel. The thermometer was calibrated from 4 K to 380 K by the supplier with a reported calibration accuracy of $\pm$ 10 mK above $T = 27$ K, and $\pm$ 15 mK below 27 K.

The sample cell and the heater/thermometer assembly were suspended inside an adiabatic shield by a nylon filament attached to the assembly and placed onto a hook at the top of the shield. The shield itself was made of thin-walled copper and completely surrounded the cell and assembly. Approximately 15 m of manganin wire were bifilarly wound around the shield to serve as the shield heater. The resistance of the shield heater was approximately 100 Ω. A copper-constantan thermocouple monitored the temperature

difference between the shield and the calorimetric vessel. The thermocouple was connected to an Artronix 5301-E shield controller which was the power supply for the shield heater. The controller worked in conjunction with the thermocouples and an appropriate set point to apply the amount of power necessary to the shield in order to maintain acceptable adiabatic conditions, which were such that the calorimetric vessel exhibited a temperature drift within $\pm$ 1 mK / min.

The adiabatic shield was suspended from a copper heat sink by three nylon filaments. All electrical leads entered the cryostat through a hermetic electrical feedthrough. Copper is a good electrical conductor, but it is also an excellent thermal conductor which means that thermal conduction from the surroundings into the cryostat along the leads had to be minimized. This was accomplished by wrapping the leads several times around the heat sink which acted as a thermal anchor. The entire setup was placed into an enclosure can that was tightly fastened to a flange with screws and hermetically sealed with a ring of 1.0 mm diameter indium wire. The whole system was vacuum tight, with an oil diffusion pump backed by a roughing pump providing a pressure of less than 10^{-5} Torr. This high vacuum was necessary to maintain adiabatic conditions.

The enclosure can was immersed in a Dewar containing a cryogenic fluid. For measurements at temperatures above ~ 80 K, liquid nitrogen was used as the cryogen. Liquid helium was the cryogenic fluid of choice to maintain temperatures between ~ 30 K and ~ 100 K (30 K was the lowest practical operating temperature of this calorimeter). With liquid helium, two Dewars were used, stacked one inside the other.

The inner Dewar was filled with liquid helium while the outer Dewar contained liquid nitrogen. This arrangement served to keep the very volatile (and much more expensive) helium from boiling away too fast.

A block diagram of the entire setup of the adiabatic calorimeter including electronic components is provided in Figure 5.3. The cell heater had its own power supply with a manually controlled voltage. The heater voltage, heater resistance, and temperature measurements were made with a HP 3456A digital voltmeter. Data collection by the adiabatic calorimeter was fully automated by interfacing the voltmeter to a Hewlett-Packard 87A personal computer with an IEEE488 interface card.

The accurate measurement of temperature is essential for the determination of accurate heat capacity data. To maximize sensitivity, the platinum resistance thermometer (PRT) was connected in series with a standard resistor of known resistance (100 Ω) and the ratio of the voltage drop across the PRT and the 100 Ω standard resistor was measured by the HP 3456A digital voltmeter. This measurement was made by passing a constant current of 1 mA to the temperature measuring circuit. A current of 1 mA was found to give reasonable sensitivity while minimizing Joule heating of the thermometer. Since the current was the same through both the PRT and the standard resistor, the voltage ratio was equal to the resistance ratio. Connections between two dissimilar metals gives rise to thermal emfs (thermocouples). To correct for this, resistance ratio measurements were taken with the current in the forward direction and with the current in the reverse direction.

From the known resistance of the standard resistor and the resistance calibration

Figure 5.3. A schematic block diagram of the automated adiabatic calorimeter, where V is the constant voltage power supply for the heater, i is the constant current supply, R is the 100 Ω standard resistor, i↓ ↑ is the computer-controlled relay which switches the direction of the current, H/T represents the heater/thermometer relays, and DVM is the HP 3456A digital voltmeter; from reference (276).

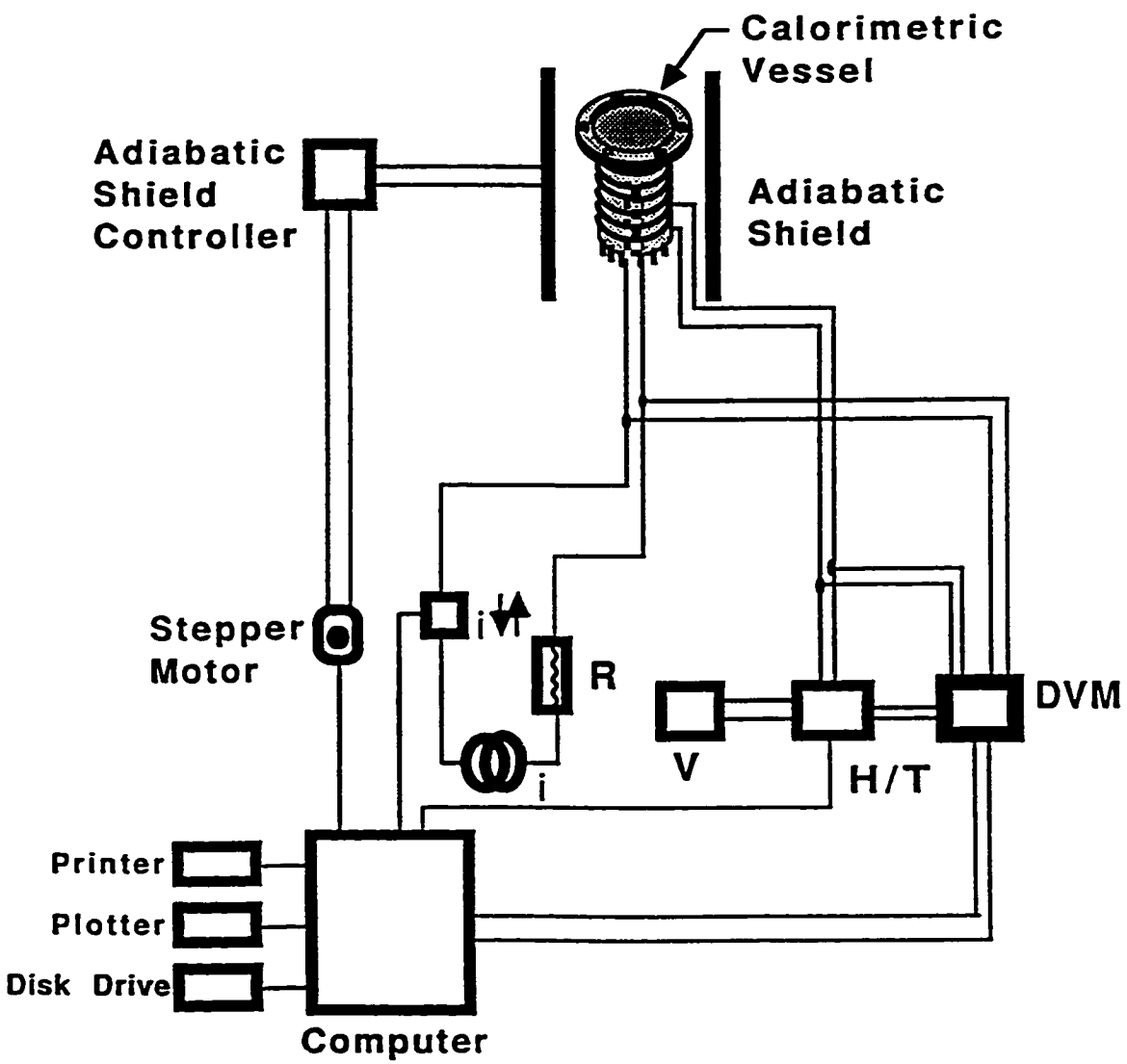

of the PRT, the measured resistance ratio could be converted to temperature. For the purpose of interpolation between calibrated points, the calibration data were fitted by a spline fitting procedure.[277,278,279] This involved fitting each successive pair of points to its own cubic polynomial subject to the conditions that the cubic polynomials on either side of a particular point had to be continuous through that point, had to have a continuous first derivative at that point, and a continuous second derivative at that point. By also requiring that the second derivatives at the first and last points in the series be zero, there were a sufficient number of constraints to determine the spline interpolation parameters for a particular series of points. Algorithms that enable a computer to perform a spline fitting procedure are readily available.[280] Once the resistance ratio was measured, it was converted to temperature using the fitted spline interpolation parameters.

The accuracy of the calorimeter had been tested by measuring the heat capacity of Calorimetry Conference (NBS-49) benzoic acid as a function of temperature.[276] The experimental results were within 0.5% of the literature values. Further details of this adiabatic calorimeter can be found in the literature.[269,276]

5.2.2 Sample Loading and Measurement Procedure

The sample loading procedure involved placing a known amount of the sample to be studied (in the form of a solid powder or a liquid) into the calorimetric vessel in

a dry helium atmosphere and tightly sealing the vessel by fastening the lid over a known mass of indium wire on the rim of the vessel. The presence of helium gas inside the sealed vessel served to promote thermal equilibrium among the cell and its contents without significantly contributing to the total heat capacity. The calorimetric vessel was then placed inside the heater/thermometer assembly with a known mass of Apiezon T grease. The indium seal was then tested by evacuating the cell in a vacuum desiccator followed by a measurement of its mass. A leak-free seal for a volatile sample was indicated if the mass remained constant after several evacuation/measurement cycles.

The cell and assembly were suspended inside the adiabatic shield and the wires associated with the cell heater, thermometer, and thermocouple were soldered to their appropriate ceramic posts at the bottom of the shield. Each post at the bottom of the shield had a matching member at the top of the shield. The shield was suspended from the heat sink by nylon filaments and electrical leads from the heat sink were soldered to their corresponding ceramic posts on top of the shield. These leads travelled out of the vacuum system through a hermetic feedthrough and were attached to their appropriate instrumentation. All soldering was done using thermal-free solder (Leeds and Northrup, the solder is an alloy composed of 70.44% Cd and 29.56% Sn[281]). The enclosure can was attached and sealed with indium and the system was evacuated. It could take a couple of days for the system to achieve a satisfactory vacuum ($P < 10^{-5}$ Torr).

Once the system was evacuated, it was cooled to the desired temperature by immersing the enclosure can in a Dewar containing a cryogenic fluid, *e.g.*, liquid nitrogen or liquid helium. Efficient thermal contact between the cryogenic fluid and the

sample cell was provided by introducing a small amount of helium exchange gas into the enclosure can which was pumped away once the sample had been cooled to the desired temperature. The power supply to the adiabatic shield was then turned on, and the power to the shield was manually adjusted with a set point controller until adiabatic conditions were established within allowable tolerance, *i.e.*, a calorimeter temperature drift rate within $\pm$ 1 mK·min^{-1}.

At this point data acquisition commenced and could be automated with the use of suitably programmed computer software. Acquisition of heat capacity data using this calorimeter was accomplished in the following manner: Initial temperature (resistance ratio) readings of the sample were taken for a period of time (preheating period, usually $\sim$ 1 - 3 hours), after which the sample was heated by a desired temperature increment (heating period), and final temperature readings were taken (postheating period, again for 1 - 3 hours). During the sample heating period, the heater voltage was measured (the heater resistance was measured just before and just after the sample heating period), and the heat to the shield was increased to compensate for the rising temperature of the sample. The temperature data during the preheating period were extrapolated forward, and the data during the postheating period were extrapolated backward, both to the time of the middle of the heating period, to obtain the initial (T_i) and final (T_f) temperatures. The temperature difference during the heat (ΔT) was then calculated as

$$\Delta T = T_f - T_i . \tag{5.19}$$

The amount of Joule heat (q) supplied to the sample during the heating period was determined by the following equation:

$$q = \frac{V^2}{R} t, \tag{5.20}$$

where V is the heater voltage, R is the resistance of the heater, and t is the duration of the heating period. The time was measured by the internal clock of the computer. Once q and ΔT were known, the total heat capacity, $(C_p)_{total}$, could be found from the equation

$$(C_p)_{total} = \frac{q}{\Delta T}. \tag{5.21}$$

The heat capacity calculated from equation (5.21) consisted of the heat capacity of the sample ($(C_p)_{sample}$), plus the heat capacity contribution from the sample vessel ($(C_p)_{vessel}$), as well as contributions from the indium seal ($(C_p)_{ind}$) and the Apiezon T grease ($(C_p)_{ApT}$). The heat capacity of the empty sample vessel had been measured separately as a function of temperature and the data were fitted by the spline fitting procedure.[276] Furthermore, heat capacity data for indium[282,283,284] and Apiezon T grease[285] are available in the literature and have been subjected to spline fitting. All of these spline parameters were contained in the software that automates the calorimeter, and thus, the heat capacity contributions from the empty sample vessel, the indium seal, and the Apiezon T grease could be suitably interpolated to the temperature of the total heat capacity measurement.

To obtain only the heat capacity of the sample, the heat capacity contributions from the addenda had to be subtracted from the total, *i.e.*,

$$(C_p)_{sample} = (C_p)_{total} - (C_p)_{vessel} - (C_p)_{ind} - (C_p)_{ApT}. \tag{5.22}$$

The molar heat capacity ($C_{p,m}$) was then found by dividing the measured sample heat

capacity by the number of moles of sample (n) in the calorimeter vessel, *i.e.*,

$$C_{p,m} = \frac{(C_p)_{sample}}{n}. \qquad (5.23)$$

The temperature at which a particular heat capacity value was reported was taken to be the average of the initial and final temperatures obtained by extrapolating the preheating and postheating temperatures to the midpoint of the heating period. The postheating period temperature measurements for one heat capacity point could be used as the preheating period for the next point. Thus, data acquisition over a full temperature range involved successive cycles of a 1 - 3 hour temperature measuring period followed by a heating period, all of which was fully automated by the data acquisition software.

5.3 Thermal Relaxation Studies of Ice

Experimental evidence of frozen-in disorder in a substance can come from the observation of a glassy phase transition in its heat capacity curve. A detailed low-temperature adiabatic calorimetric study of NaOH to search for such a transition would determine whether or not NaOH possesses residual entropy at low temperatures. As explained in Section 4.2.3, glassy phase transitions in the heat capacity curves of many solids are very subtle. However, the enthalpy relaxation effects of a substance near a glassy phase transition will lead to the observation of anomalous temperature drifts by the calorimeter. As these effects will depend on the exact configuration of the calorimeter

used, a better understanding of the temperature drifts and their appearance would be obtained by first performing calorimetric measurements on a solid that has a well-characterized glassy phase transition. The solid that was chosen for this purpose was ice, which has a glass transition temperature[208] of ~ 100 K.

The ice sample for these experiments was prepared by degassing a quantity of nanopure water by a series of freeze-pump-thaw cycles. A 3.5960 g portion of this sample was then loaded in liquid form into the adiabatic calorimeter using the sample loading procedure described in Section 5.2.2.

The exact thermal treatment of the sample was the following: The water sample was frozen (at T = 273 K) and cooled to a temperature of 268 K where it was left for 24 hours. This was followed by cooling to liquid nitrogen temperature (~ 80 K) at a rate of 0.5 - 1.0 $K \cdot min^{-1}$. The sample was then annealed for 24 hours at this temperature after which calorimetric data were obtained from T = 80 - 125 K. A plot of the experimental heat capacity results obtained for ice for several runs in this temperature range is shown in Figure 5.4 along with results reported in the literature.[208] There is fairly good agreement between the literature and experimental values with the maximum deviation being 3.8%.

The step in the heat capacity curve betraying the presence of the glassy phase transition in ice is visible in the literature data just below 100 K. It is easily seen by looking along the literature curve in the plane of the paper. However, arriving at the same conclusion by a similar examination of the present experimental results is doubtful at best. Although the scatter in the data is slight, it appears to be sufficient to prevent the

Figure 5.4. Experimental heat capacity curve for ice (○) along with the corresponding literature values (●).[208]

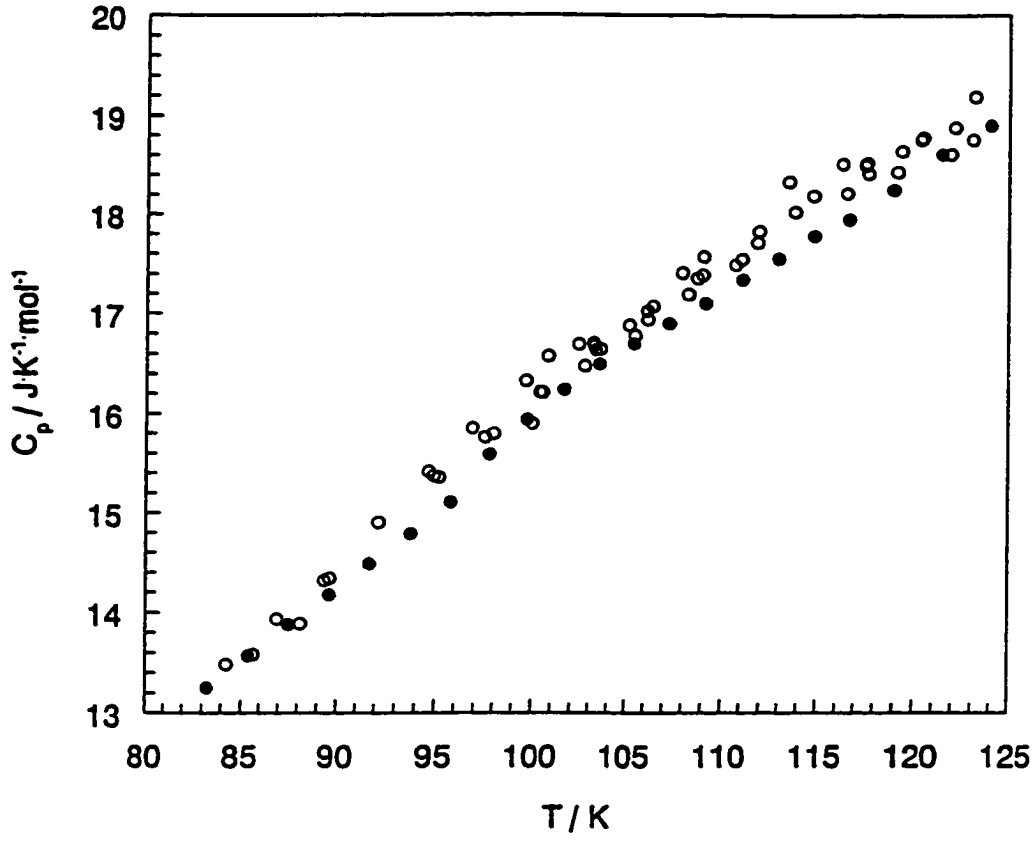

subtle step in the heat capacity curve from being resolved.

However, evidence for the occurrence of the glassy phase transition in ice is clearly seen from temperature drift data. After each heating of the sample during a calorimetric run, a temperature *versus* time profile was obtained for a period of two hours after the heat. Above $T = 105$ K, these profiles were straight lines as would be expected for a thermally well-behaved sample. From $T \sim 82$ K to 105 K, anomalous temperature drifts were observed, an example of which is shown in Figure 5.5. This plot was obtained after subtraction of the background temperature drift of the calorimeter due to incomplete adiabaticity. The observation of this type of temperature *versus* time profile is clear evidence that enthalpy relaxation is taking place.

The anomalous temperature drifts observed in this temperature region are presented as a plot of the drift rate (*dT/dt*) *versus* temperature in Figure 5.6. The plotted temperature drift values were all corrected for the baseline temperature drift of the calorimeter, and were calculated at a time of 30 minutes after heating. The uncertainty in the temperature drift values is estimated to be $\pm$ 0.1 $mK \cdot min^{-1}$ based upon the scatter in the temperature *versus* time data. Such a temperature drift profile is confirmation of the presence of the glassy phase transition in ice and is similar to the drifts reported in the literature for ice.[208]

Figure 5.5. Temperature *versus* time profile for ice showing enthalpy relaxation indicating a glassy phase transition.

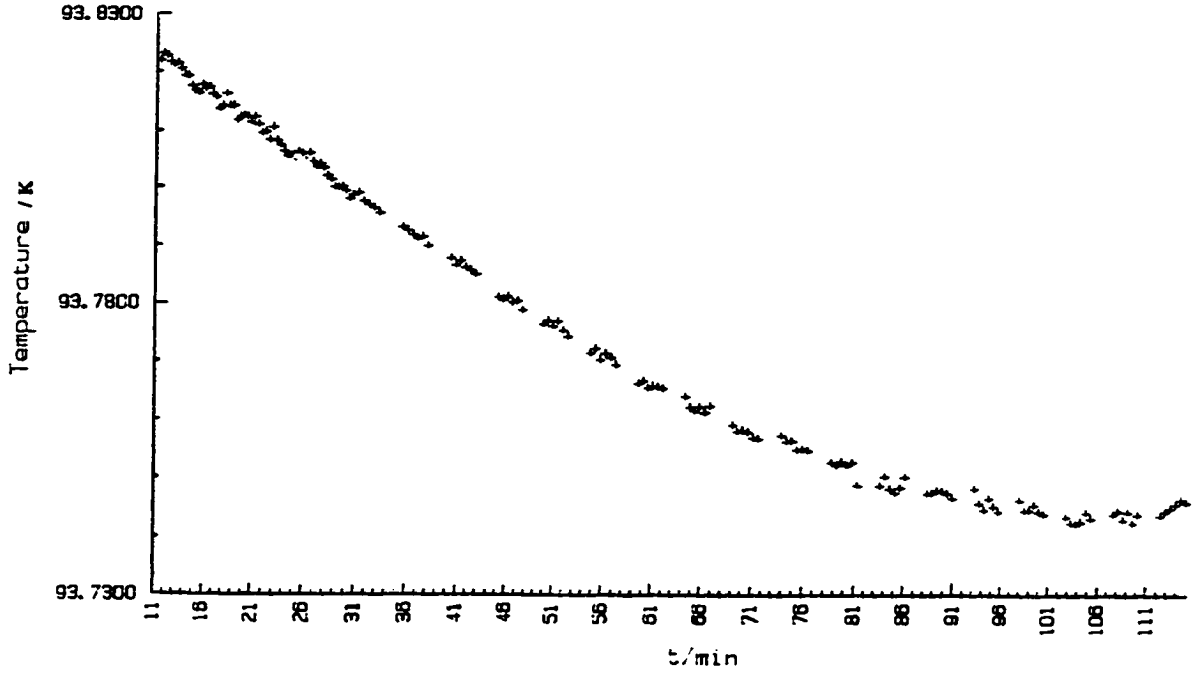

Figure 5.6. Measured temperature drift pattern for ice near the glassy phase transition. All drift values were corrected for the baseline temperature drift due to the incomplete adiabaticity of the calorimeter, and were determined 30 minutes after heating.

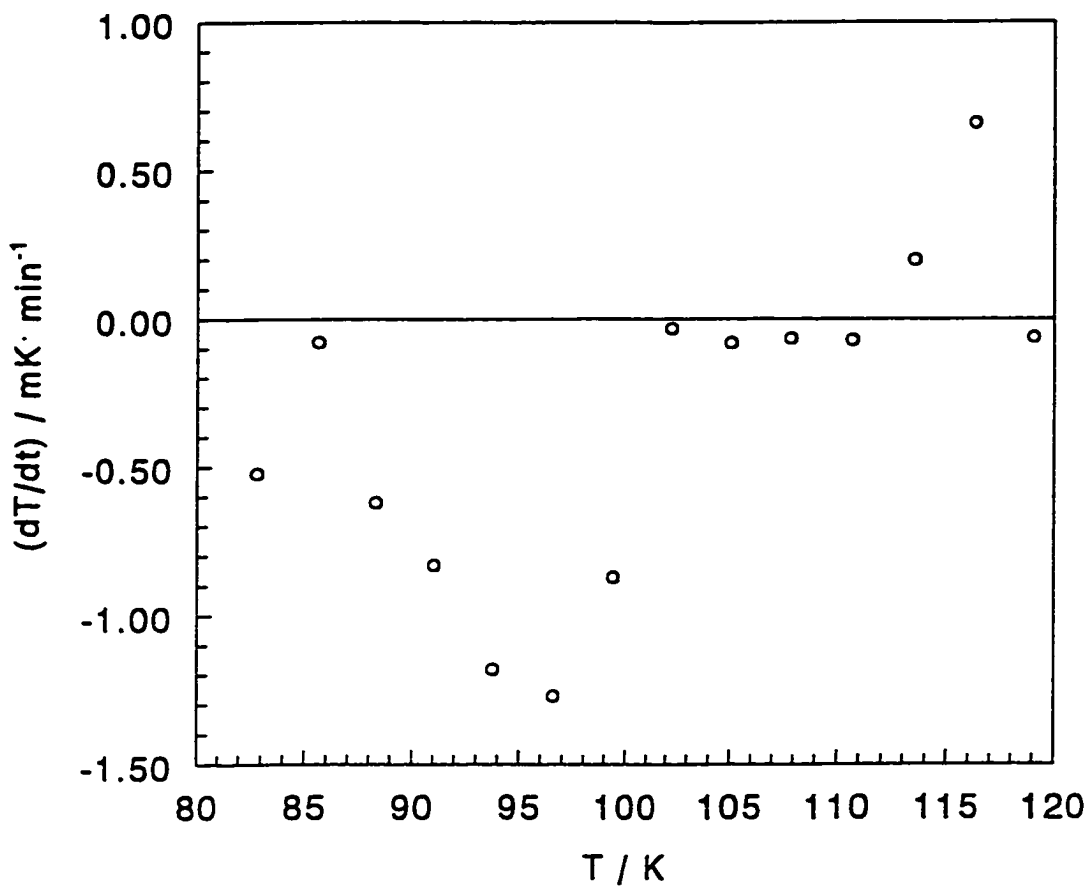

5.4 NaOH Calorimetric Measurements

5.4.1 Sample Preparation and Purity

The results in the previous section show that the adiabatic calorimeter used is fully capable of detecting glassy phase transitions in solids. For the purpose of looking for such a transition in sodium hydroxide to test the postulate of residual entropy, a sample of NaOH was prepared and loaded into the calorimeter.

The alkali metal hydroxides and deuteroxides are difficult compounds to deal with, due to their highly corrosive nature, and their ability to readily absorb moisture and CO_2 from the air. Therefore, special precautions and care must be taken in the preparation of a sample to preserve its purity. The sodium hydroxide sample was prepared using 99.99% pure NaOH pellets purchased from the Aldrich Chemical Co. A quantity of these pellets was crushed into a fine powder with a mortar and pestle in a dry nitrogen glove bag. The glove bag was flushed four times with dry nitrogen before use. The powdered sample was placed in a zirconium crucible which was subsequently placed in a sublimator apparatus. The sample was dried by heating the sublimator apparatus to a temperature of $\sim$ 160°C for 24 hours under vacuum.

The dried sample was characterized using differential scanning calorimetry (DSC). As described in Section 5.1.2.1, this technique is a quick method for determining the enthalpies of transitions with reasonable accuracy. The DSC apparatus was calibrated against the melting transition of indium which has a known enthalpy of fusion[286] ($\Delta_{fus}H$)

of 28.45 $J \cdot g^{-1}$.

The water content of the prepared NaOH sample was estimated using DSC by determination of the enthalpy of the NaOH/$NaOH \cdot H_2O$ eutectic transition which occurs at a temperature of approximately 335 K. The enthalpy of fusion of the pure monohydrate[287] is $\Delta_{fus}H$ = 3570 $J \cdot mol^{-1}$ = 61.54 $J \cdot g^{-1}$. A comparison of the enthalpy of the monohydrate eutectic of the sample with the enthalpy of fusion of the pure monohydrate yields the percent of $NaOH \cdot H_2O$ in the sample, which enables the calculation of the percentage of water in the sample.

Furthermore, the extent of CO_2 contamination of NaOH can also be determined using DSC. Sodium hydroxide readily reacts with CO_2 in the air to form sodium carbonate (Na_2CO_3). A mixture of NaOH and Na_2CO_3 shows a eutectic transition at a temperature[141] of ~ 559 K. The enthalpy of fusion of pure Na_2CO_3 is $\Delta_{fus}H$ = 29.6 $kJ \cdot mol^{-1}$ = 279.3 $J \cdot g^{-1}$. Thus, a comparison of the enthalpy of the carbonate eutectic of the sample as measured by DSC with the enthalpy of fusion of the pure carbonate yields the percent of Na_2CO_3 in the sample.

Several DSC samples of the dried NaOH sample were prepared in the following manner: Preweighed and dried sample vials were placed in a dry nitrogen glove bag. Each DSC sample was prepared and put into a separate sample vial that was sealed with a lid and a piece of parafilm. Measurements using a Perkin-Elmer DSC-1 apparatus or a Perkin-Elmer Pyris-1 DSC apparatus were obtained for each sample.

The eutectic enthalpies were measured for all the samples. The enthalpies of the eutectics varied among the samples due to the varying amounts of contamination during

the preparation of the DSC samples. The sample which gave the best (*i.e.*, smallest) monohydrate eutectic enthalpy is shown in Figure 5.7 where the eutectic transition is the peak at $T \sim 337$ K. For this run, a eutectic enthalpy of 1.4 $J \cdot g^{-1}$ was obtained by determining the area under the peak. Using this enthalpy value, the water content of the sample was calculated to be 0.69% by mass.

One sample was subjected to a DSC run covering the whole temperature range from 50°C to 310°C using the Pyris-1 DSC. The resulting DSC scan for this run is shown in Figure 5.8. Peak A can be assigned to the monohydrate eutectic with an onset temperature (T_{onset}) of 64.3°C (337.4 K). The orthorhombic to monoclinic polymorphic phase transition in NaOH is revealed by peak B, with T_{onset} = 240.7°C (513.8 K). Peak C is the carbonate eutectic with a measured onset temperature of 285.4°C (558.6 K), and the large peak at the end of the scan (peak D) can be assigned to the first-order monoclinic to cubic polymorphic phase transition in NaOH, with T_{onset} = 292.4°C (565.6 K). The enthalpies of the orthorhombic to monoclinic and monoclinic to cubic phase transitions were determined by integration of the areas under their respective peaks to be 22.7 $J \cdot mol^{-1}$ and 6350 $J \cdot mol^{-1}$, respectively. The small enthalpy change during the orthorhombic to monoclinic transition reflects the slight first-order nature of this transition as discussed in Section 3.2. The uncertainty in the enthalpy values is no better than $\pm$ 10 %, although they are almost identical to the values reported in the literature.[141] The processes giving rise to the two small anomalies between 100°C and 150°C in Figure 5.8 are unknown.

There is some slight overlap between the peaks due to the carbonate eutectic and

Figure 5.7. DSC scan of prepared NaOH sample showing the NaOH/NaOH·H_2O eutectic. The enthalpy was determined from the area under the peak and the water content was calculated to be 0.69% by mass.

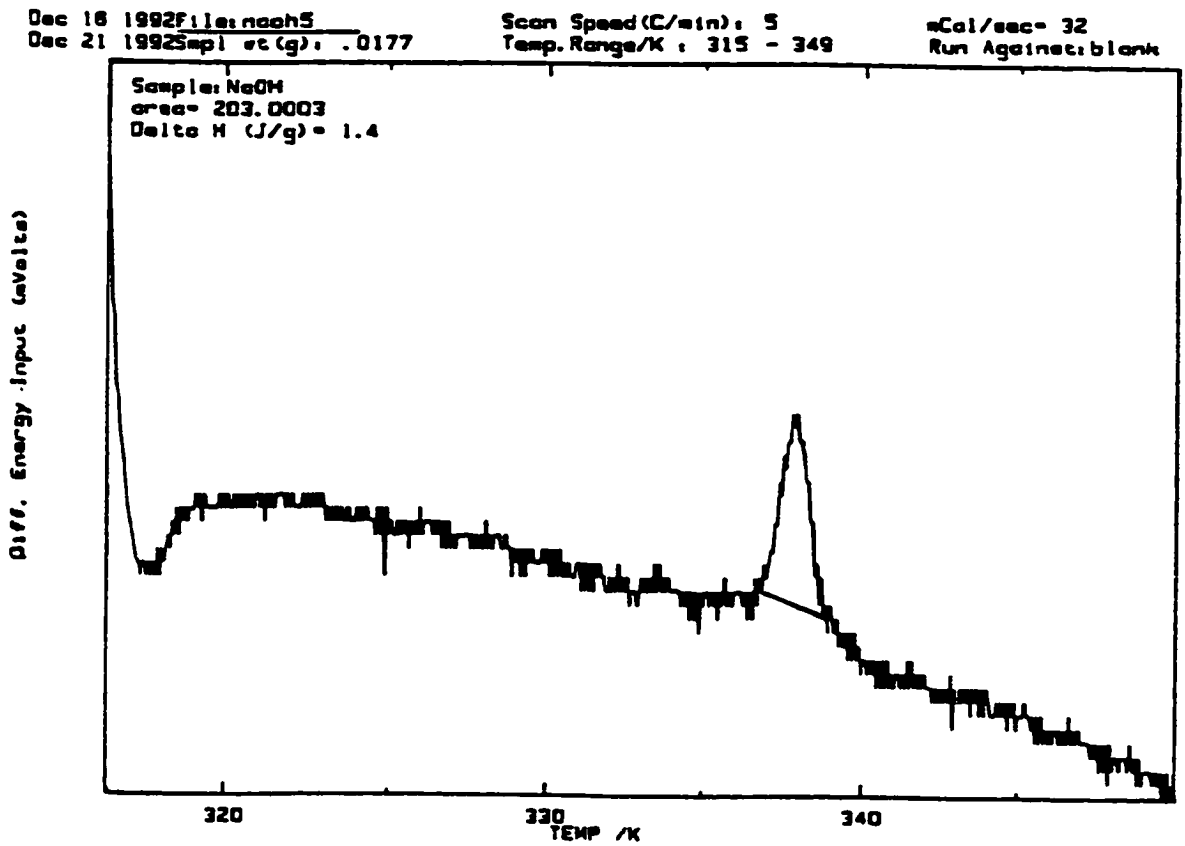

Figure 5.8. DSC scan of NaOH from 50°C to 310°C showing the NaOH/NaOH·H_2O eutectic (peak A), the NaOH orthorhombic to monoclinic phase transition (peak B), the NaOH/Na_2CO_3 eutectic (peak C), and the NaOH monoclinic to cubic phase transition (peak D). The processes giving rise to the anomalies between 100°C and 150°C are unknown.

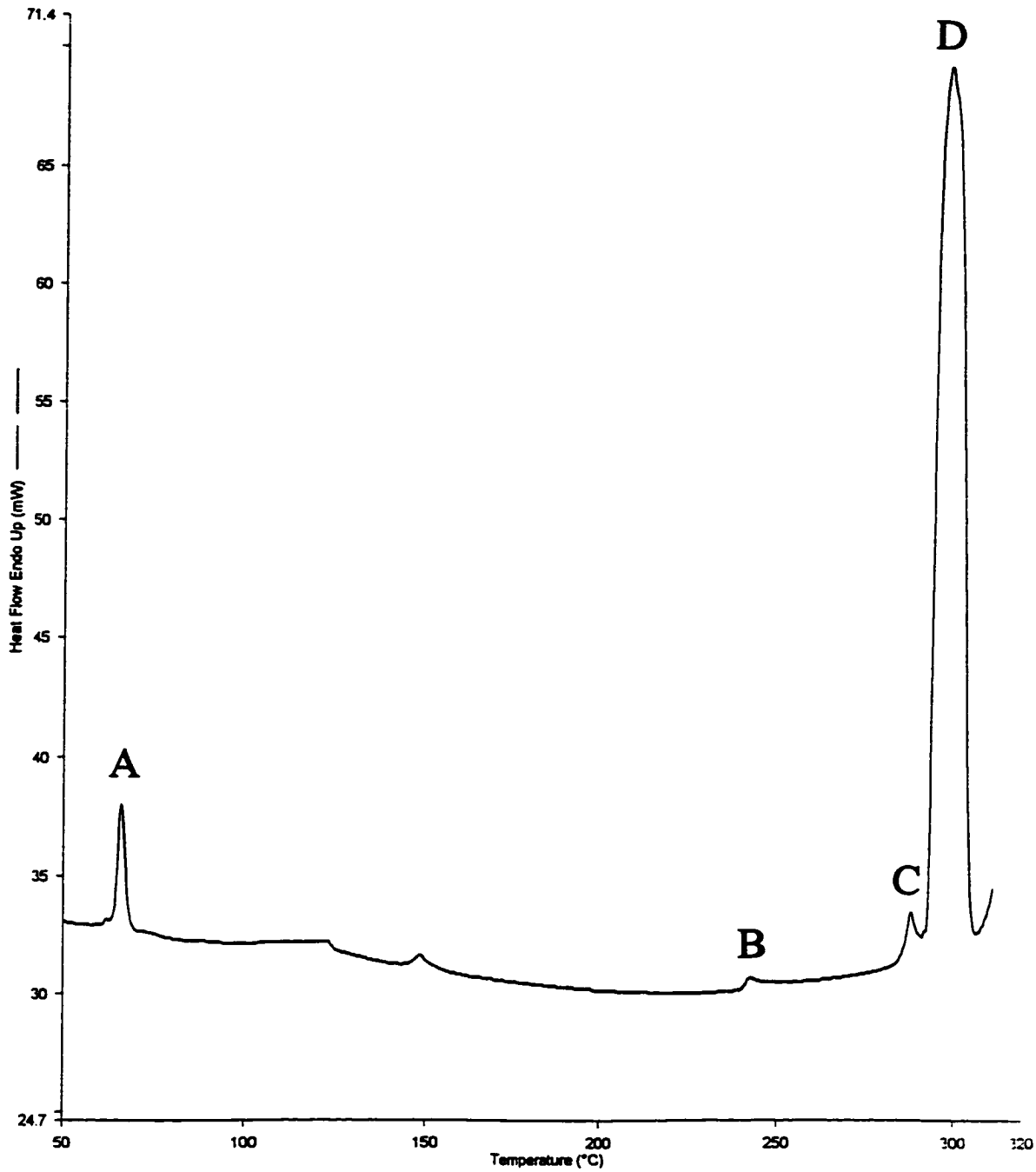

the monoclinic to cubic phase transition, however, a reasonable estimate of the eutectic enthalpy could still be obtained. The enthalpy was determined to be $\Delta H = 2.1\ J \cdot g^{-1}$ which corresponds to a sodium carbonate content of the sample of 0.75% by mass.

This determined water composition of 0.69% and the sodium carbonate composition of 0.75% are actually upper limits to the true impurity contents of the original prepared sample. The DSC apparatus was not in a dry atmosphere, so the DSC samples were partially exposed to the air for a short period of time before being placed in the DSC, and would undoubtedly pick up some moisture and CO_2 from the air. Also, the DSC pans were metallic and thus there was the opportunity for contamination by adsorbed water. The water and carbonate contents of the DSC samples would therefore be greater than the corresponding impurity compositions of the original sample.

Since the water and carbonate compositions of the prepared sample were found to be very small (less than 0.69% and 0.75% by mass, respectively), it was considered to be pure enough to be loaded into the calorimeter. A mass of 4.1710 g of the powdered NaOH sample was carefully placed into the calorimeter vessel in a glove box under a dry nitrogen atmosphere. The vessel was then placed in the heater/thermometer assembly and all the wiring was connected. The system was then evacuated to a reasonable vacuum ($< 10^{-5}$ Torr) before the start of the heat capacity measurements.

5.4.2 Results and Discussion

When the glass transition in ice was being observed in the calorimeter, it was already known beforehand at what temperature the glass transition would occur since the ice system has been well-studied.[208] The situation with sodium hydroxide was different, however, because if NaOH did have a glassy phase transition, the temperature at which it would be observed was completely unknown. Thus, the search for a glass transition in NaOH was a very slow process since several calorimetric runs had to be done covering a large temperature range. Furthermore, in ice it was possible to anneal the proton disorder by melting the sample *in situ*, but this was not possible for NaOH so thermal treatment had to be carried out in a careful manner so as not to quench the sample unrecoverably.

The first heat capacity measurements were taken in the relatively high-temperature range (200 K to room temperature) and subsequent runs covered progressively lower and lower temperatures down to ~ 80 K using liquid nitrogen as the cryogenic fluid. Two runs were also performed with liquid helium between 35 K and 130 K. The heat capacity results from all of the measurements are plotted as a function of temperature in Figure 5.9 along with results reported in the literature.[139] Above 60 K, these values are within 3% of the literature values for NaOH,[139] with most of them being within 1.5%. Below 60 K, the deviations are greater than 3% with the greatest deviation being 11% at the lowest temperature measured (T = 38 K).

During the heat capacity measurements, temperature *versus* time curves were

Figure 5.9. Experimental heat capacity results for NaOH (○) along with the corresponding literature values (●).[139]

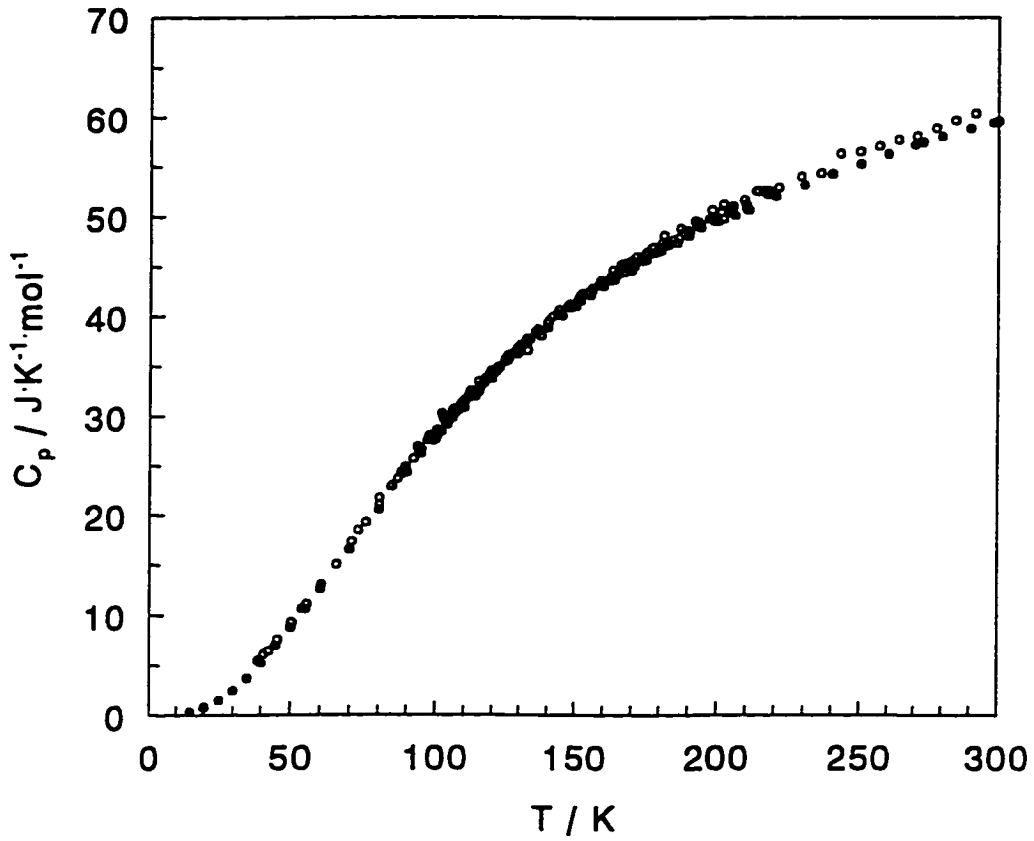

obtained after each heating period. This was done for various thermal treatments of the sample. In all runs, the sample was first kept at room temperature for at least 24 hours, after which it was cooled down to the initial temperature of the run and held there for 24 hours before beginning the run. The cooling rates during this process varied from -3 $K \cdot min^{-1}$ to -0.1 $K \cdot min^{-1}$ and were controlled through the introduction of helium exchange gas into the vacuum chamber.

Initially, the temperature was monitored for a period of 3 hours after heating and no anomalous temperature *vs.* time behaviour was observed between 100 K and 300 K. Between 79 K and 100 K, anomalous temperature drifts were evident during measurements with liquid nitrogen. These were further examined by performing runs in this temperature range where the temperature was monitored for 5 hours, 10 hours, and 24 hours after heating. These anomalies consisted of two distinct types. In the temperature range from 85 K to 100 K, the temperature *vs.* time curve started off linearly, which is normal for a thermally well-behaved sample, but then underwent an abrupt rise through a distinct inflection point before reaching a peak and becoming linear again. An example is provided in Figure 5.10(a).

The second type of anomaly always occurred in the temperature region from 79 K to 85 K and an example is shown in Figure 5.10(b). After the heat input was complete, the temperature rose monotonically with time but never in a linear fashion. After an initial period of about three hours, the temperature rose at a decreasing rate.

Both of these anomalies can be reasonably explained as being caused by factors other than enthalpy relaxation of the sample. Effects due to enthalpy relaxation should

Figure 5.10. Examples of two types of thermal anomalies observed in the temperature *vs.* time curves for NaOH, (a) in the temperature range from 85 K - 100 K, and (b), in the 79 - 85 K temperature range.

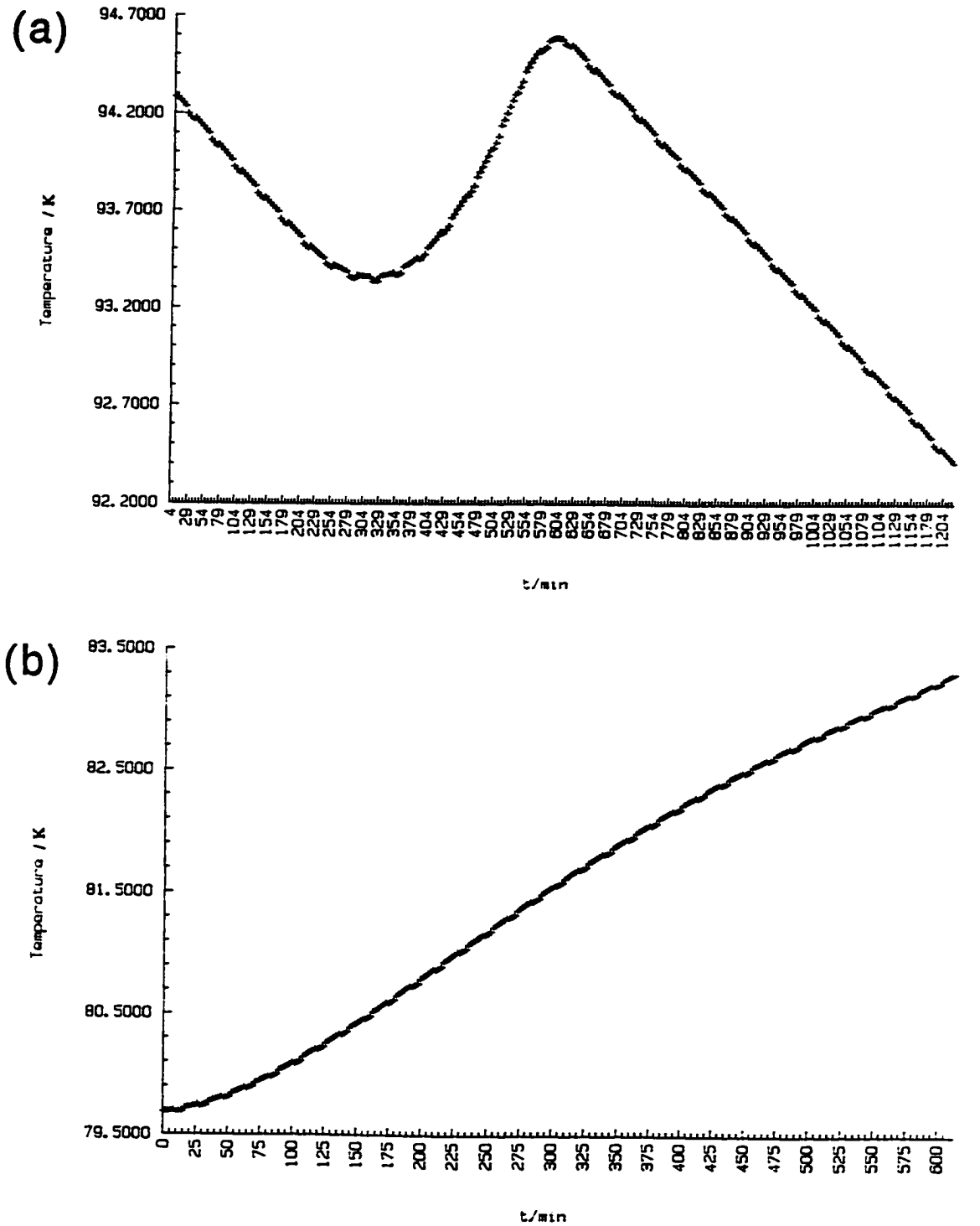

be evident in the temperature *vs.* time curve soon after the heating period is over. However, the data in Figure 5.10(a) do not show any anomalous behaviour until 4 hours after the heat so clearly enthalpy relaxation cannot be involved. An effect due to the long monitoring period is likely responsible. Since the conditions were not completely adiabatic, the sample temperature drifted downward after the heat. It is possible that after several hours when the temperature had dropped below a threshold level, the shield controller adjusted the power to the shield to compensate, causing the sudden temperature rise.

The anomaly shown in Figure 5.10(b) is characteristic of a sample showing anomalous exothermic temperature drifts due to enthalpy relaxation. However, suspicion was raised when it was realized that this anomaly was observed only at the lowest temperatures that could be attained with the calorimeter using liquid nitrogen. With the sample heater turned off, there are two factors which conspire to change the temperature of the sample (besides the adiabatic shield). One of these is due to the temperature of the calorimetric system being greater than the liquid nitrogen in which it is immersed, tending to cause a downward temperature drift. This can be described by Newton's Law of Cooling which states that the approach to thermal equilibrium of two bodies in thermal contact with each other is proportional to the temperature difference between them. A factor tending to increase the temperature of the sample arises due to heat leaks along the electrical leads which run from the electronic instrumentation outside of the calorimeter (*i.e.*, at room temperature) through hermetic feedthroughs into the vacuum system and eventually to the calorimeter cell. These heat leaks are minimized through the use of very

fine electrical wires and a copper heat sink, yet they exist nonetheless.

Normally the tendency for the sample to drop in temperature to that of the cryogenic fluid so greatly overwhelms the effects due to heat leaks along the leads that the heat leak effects are not observable in the temperature *vs.* time profiles. However, at sample temperatures very close to that of liquid nitrogen (*i.e.*, 79 K - 85 K), the tendency for the sample temperature to drop further is very small, and it is possible to observe electrical-lead heat leak effects, which are likely the source of the anomalies seen in this temperature region, such as that shown in Figure 5.10(b). This was confirmed by measurements using liquid helium as the cryogenic fluid, since no abnormal behaviour similar to that shown in Figure 5.10(b) was observed in the 79 K - 85 K temperature range during the liquid helium runs. The anomalous temperature drifts observed for ice in Section 5.3 were endothermic, and mostly occurred outside of this temperature range, so the abnormal behaviour in this case was due to the ice sample itself.

During the NaOH calorimetric liquid helium runs, the temperature was monitored for 5 - 8 hours after the heating period was over. In several cases, the temperature drifts were linear for a time followed by a gradual upward or downward change in slope. However, these anomalies could be correlated to the level of liquid helium in the Dewar. The thermal conductivity of the copper enclosure can is low at liquid helium temperatures,[288] so the temperature drift of the sample was very sensitive to how much of the enclosure can was immersed in the liquid helium at a particular time. Right after the Dewar was filled with helium, the sample temperature drift rate was observed to drop. When the helium in the Dewar had evaporated so that its level was below a certain

point on the enclosure can, a gradual increase was observed in the temperature drift. Thus, it does not appear that the sample was responsible for these anomalies.

An encraty plot (C_p/T *vs.* T) for the heat capacity data collected during these experiments is shown in Figure 5.11. The scatter in the data is minimal, and shows no dependence on thermal treatment (*cf.* ice data in Figure 4.7). Thus, no anomalous behaviour is evident that would be due to a glassy phase transition.

Considering all of the data collected during the adiabatic calorimetry measurements of sodium hydroxide, it seems that there is no conclusive evidence for the existence of a glassy phase transition in NaOH. The assessment of the results of a dielectric relaxation study of sodium hydroxide will provide further insight into this problem upon which a more definite conclusion can be based.

Figure 5.11. Encraty plot for NaOH obtained from the experimental heat capacity results of Figure 5.9.

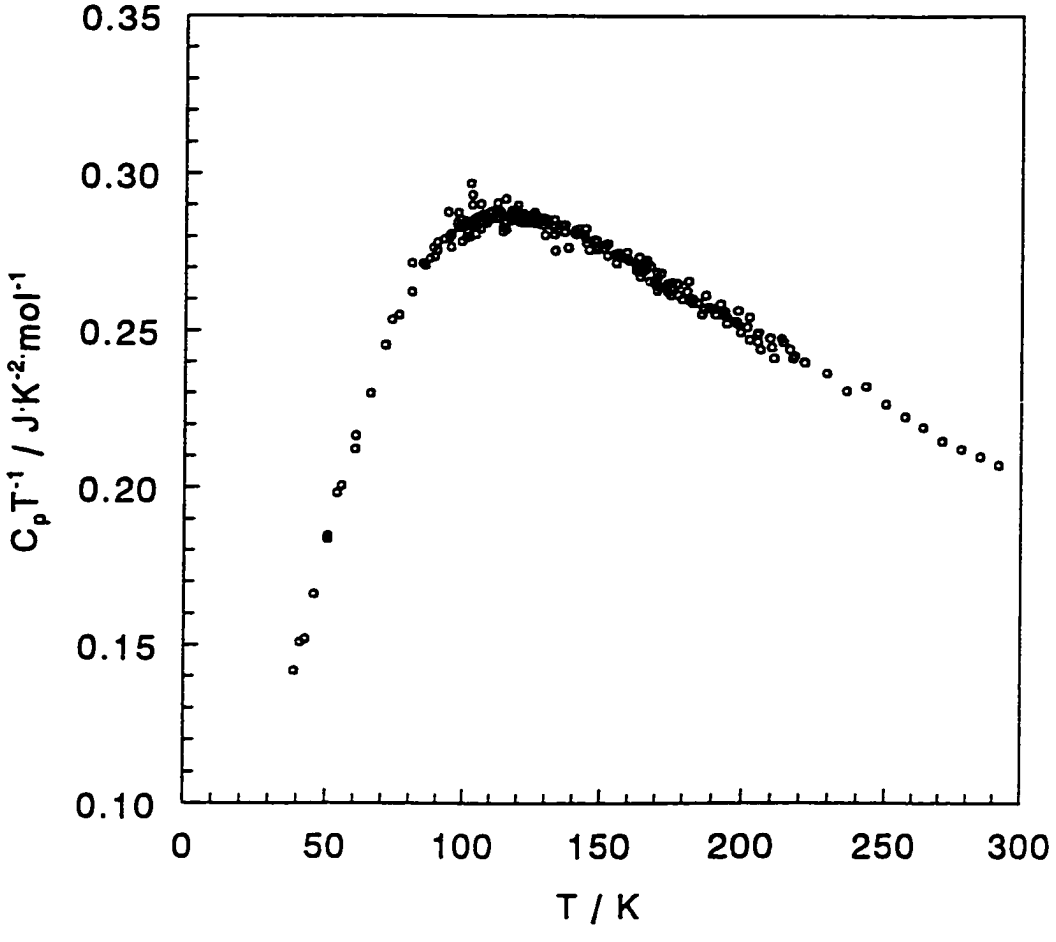

Chapter 6: Dielectric Relaxation Apparatus

6.1 Introduction

Dielectric relaxation measurements of NaOH and NaOD should provide some insight into the phase behaviour for these compounds at low temperature. The results of these experiments would provide more conclusive evidence for or against the existence of low-temperature glassy behaviour in NaOH, and thus provide a basis for a firm judgement concerning the postulate of frozen-in order and residual entropy in NaOH.

However, the facilities did not exist in our lab for measuring the dielectric properties of solid samples, nor is such a piece of equipment available commercially. A major aim of this research project was therefore the construction and development of an apparatus for dielectric measurements of solid samples as a function of temperature. Since it is very difficult to obtain single crystals of NaOH and NaOD, this apparatus had to be able to take measurements on powdered samples, and the equipment had to be able to perform at cryogenic temperatures. Moreover, it was highly desirable to automate the data acquisition and analysis as much as possible, so that only a minimum of attention was required by the operator. All of these factors had to be taken into account in the design of the apparatus.

When considering the design of a new piece of equipment, the first logical step is to extensively search the literature to survey similar equipment that others have designed and made. These designs can then be critically evaluated in terms of the

characteristics that are desired in the apparatus to be built, *i.e.*, ease of construction and measurement, powdered samples, reasonable accuracy, cryogenic temperatures, potential for automation, and overall good performance. The next section provides a summary of some of the fundamental concepts involved in the experimental determination of dielectric properties as well as a review of some of the design features of dielectric relaxation equipment described in the literature.

6.2 Literature Survey

6.2.1 Measuring Techniques

In determining the dielectric constant of an insulator, the method that is most often used employs the definition of the dielectric constant, *i.e.*,

$$\epsilon = \frac{C}{C_o}, \tag{6.1}$$

where C is the capacitance of a capacitor containing the dielectric, and C_o is the capacitance of the capacitor in a vacuum (*i.e.*, no dielectric). The type of capacitor that is usually employed in solid-state measurements is a capacitor consisting of two parallel conducting plates separated by an insulator. The vacuum capacitance of a parallel-plate capacitor can be calculated from the geometrical parameters of the capacitor using the following equation:

$$C_o = \frac{\epsilon_o A}{d}, \tag{6.2}$$

where ϵ_o is the permittivity of free space (= 8.8542 x 10^{-12} $C^2 \cdot N^{-1} \cdot m^{-2}$), A is the area of one of the parallel plates, and d is the distance between the two plates. Once the capacitance of the condenser containing the dielectric has been determined, the dielectric constant of the insulating material can be calculated using equation (6.1). Thus, in a fundamental sense, the problem of measuring the dielectric constant of a substance reduces simply to the problem of measuring capacitance.

There are two common ways of measuring capacitance. One of these is the bridge method where the dielectric of interest is inserted between the plates of a capacitor that forms one of the arms of a modified Wheatstone bridge.[289]

The Wheatstone bridge is commonly known in the context of measuring resistance as shown in Figure 6.1(a).[290] When measuring resistance using a Wheatstone bridge, two of the bridge arms contain constant standard resistors (R_1, R_2) of well-known resistance, a third arm contains a variable resistor (R_3) whose resistance is known, and the fourth arm contains the unknown resistor (R_4). The bridge is balanced when there is zero voltage through the detector, which occurs when the following balance condition is satisfied:

$$\frac{R_1}{R_2} = \frac{R_3}{R_4}. \tag{6.3}$$

By adjusting the variable resistor until the detector reads 0 V, the unknown resistance can be determined from equation (6.3). The situation is more complicated when the

Figure 6.1. Schematic of the (a) Wheatstone bridge for measuring resistance,[290] and (b) the Schering impedance bridge for measuring AC impedances.[291]

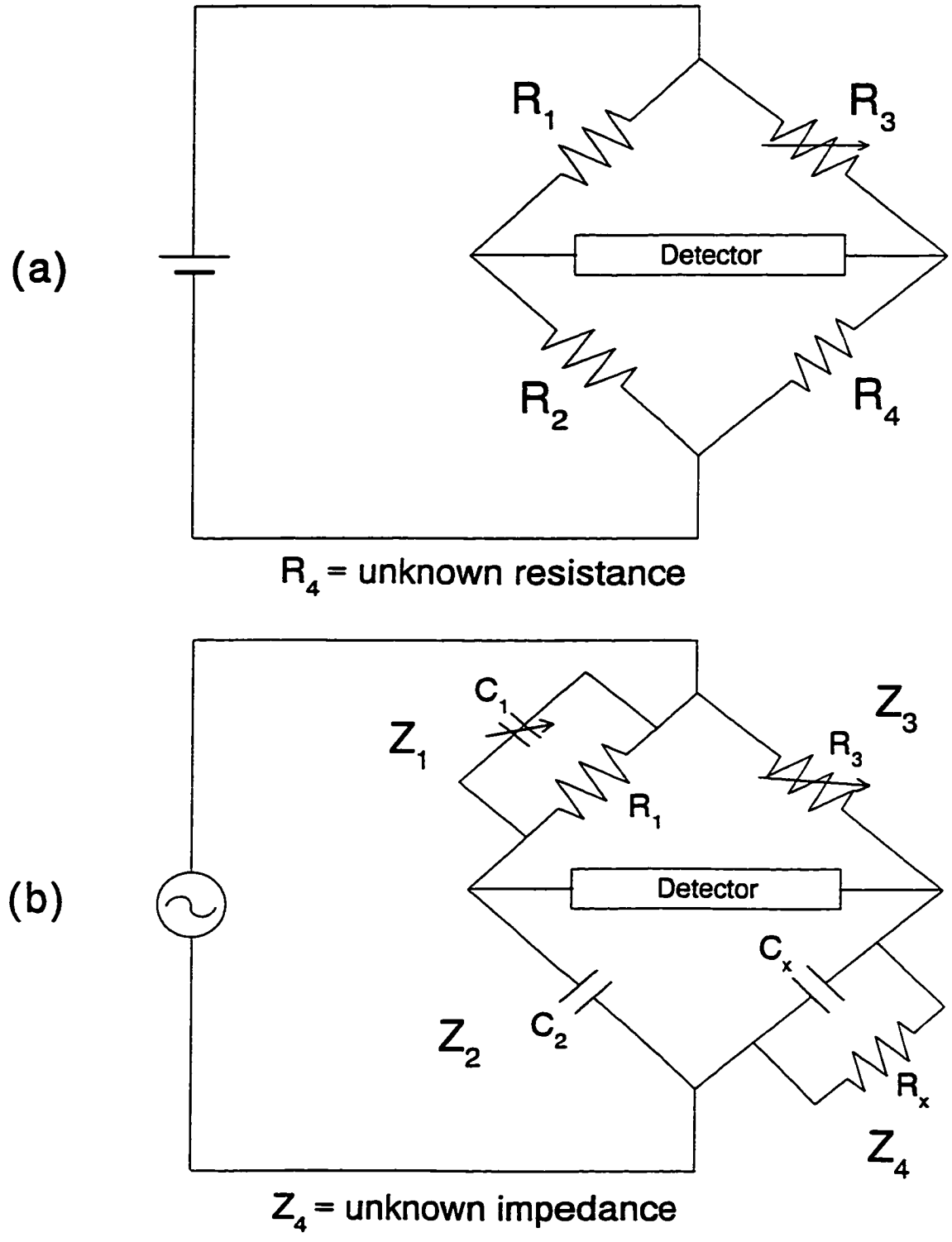

measurement of AC impedance components is desired (*i.e.* capacitance or inductance). In this case, the voltage across different arms of the bridge is described by both a magnitude and a phase angle, in contrast to the DC impedance measurement where voltage has magnitude only. In order for the bridge to be balanced, the voltage across the detector must be zero, meaning the potentials at the two detector junctions must be identical in both magnitude and phase angle. This occurs when the following two balance conditions are satisfied simultaneously:[289]

$$\frac{Z_1}{Z_2} = \frac{Z_3}{Z_4}, \tag{6.4}$$

and

$$\phi_1 - \phi_3 = \phi_2 - \phi_4, \tag{6.5}$$

where the Z's are the magnitudes of the impedances along the various bridge arms, and the ϕ's are the corresponding phase angles. In order to satisfy both balance conditions, the impedance bridge must contain two variable impedances, one to vary the magnitude to satisfy equation (6.4), and another to vary the phase angle to simultaneously satisfy equation (6.5). In the Schering bridge shown in Figure 6.1(b),[291] these two variable impedances are the variable resistor (R_3) and the variable capacitor (C_1). Using this bridge, the magnitude and phase angle of the impedance along the unknown arm of the bridge (*i.e.*, Z_4 and ϕ_4) can be determined.

Another way to measure capacitance is to place the capacitor in a resonant circuit,[292] the simplest form of which consists of a resistor, inductor, and the unknown impedance connected in series to an alternating voltage source. The unknown impedance

often consists of the unknown capacitor linked in parallel with a known variable capacitor (C_s) as shown[293] in Figure 6.2. At a given frequency the variable capacitor is adjusted until a maximum voltage gain is detected by the voltage detector. At this point, the system is said to be at resonance and the resonance condition is given by

$$\omega_{res} = \frac{1}{\sqrt{L(C_s + C_{unk})}}, \tag{6.6}$$

where ω_{res} is the angular frequency of the alternating voltage at resonance, L is the inductance, C_s is the variable capacitance, and C_{unk} is the unknown capacitance. Thus, the capacitance of the unknown capacitor can be determined.

The impedance bridge method is more accurate than the resonance method. However, a complication with the bridge technique in the measurement of AC impedances is that there are always stray inductance and capacitance along and between the leads of the bridge, the effects of which depend on the frequency. At low frequencies the residual inductances and capacitances are relatively insignificant. This is true for frequencies from 0 Hz up to about 1 MHz.[294] For frequencies greater than this, increasing stray impedances render bridge methods ineffective for measuring capacitance and the resonance method usually is used. The resonance circuit is simpler with very few branches so the stray impedances are not as significant. Furthermore, at the resonant frequency the current circulating through the circuit is at its maximum possible value, so stray currents are reduced to a minimum effect.[292] Resonance techniques give meaningful data for frequencies up to about 1 GHz.[294] For measurements at frequencies greater than this, lumped circuit methods are no longer usable, and more complicated

Figure 6.2. Schematic diagram of the resonance technique for measuring capacitance.[293]

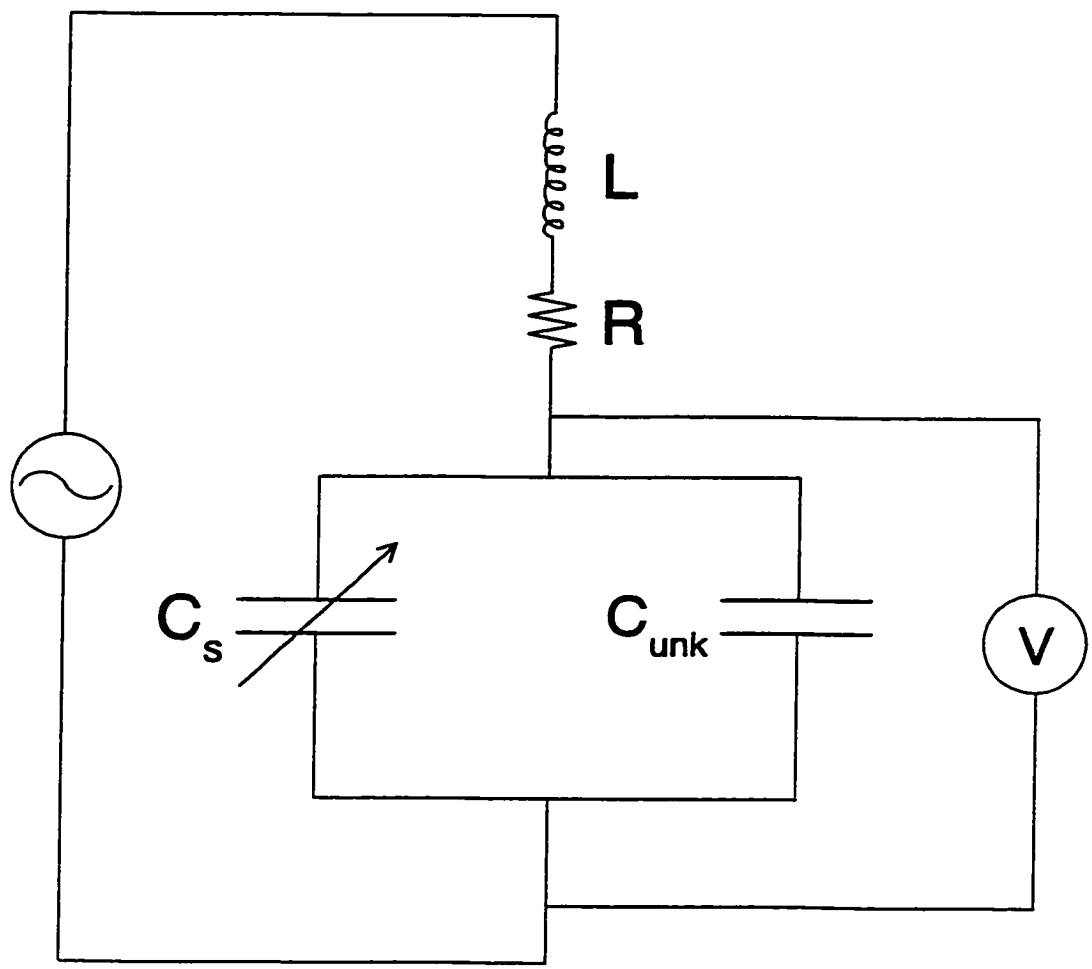

techniques must be used.[295,296] However, for the purposes of this research, *i.e.*, dielectric measurements of solids, where the frequency of measurement is almost always less than 1 MHz, some form of impedance bridge method will be the best way to measure capacitance. Meters that can measure capacitance are available commercially.

When considering dielectric relaxation measurements, the second dielectric property that is measured (besides the dielectric constant ϵ') is the dielectric loss of a substance. An ideal dielectric between capacitor plates would have infinite resistance, but this is not realized in practice. A dielectric does act as a conductor to some extent with a finite resistance, and because of this, energy is dissipated by the dielectric in the form of heat giving rise to dielectric loss (ϵ''). Dielectric loss is a property of the dielectric and it varies with a change in frequency. Dielectric losses are normally negligible except when the frequency of the alternating electric field (voltage) to which the dielectric is subjected is comparable to the frequency of the reorientational motion of the dipoles in the dielectric. At this point the dielectric loss becomes appreciable. When representing a capacitor containing a dielectric substance in a circuit, it is best to represent it as a loss-free capacitor in parallel with a resistor (R) where the resistor represents the effective resistance of the dielectric.

The dielectric loss can be measured in two ways. The impedance bridge circuit can be used to measure the effective resistance of the dielectric, from which the dielectric loss can be calculated from the following relationship:

$$\epsilon'' = \frac{1}{\omega R C_o}. \tag{6.7}$$

The phase angle between the current and the voltage of an ideal loss-free capacitor is 90° ($\pi/2$ radians). In a complex-plane plot, there would be no component of the current in the direction of the voltage (refer back to Figure 4.10(a)). When a dielectric is placed between the capacitor plates, dielectric loss gives rise to a component of the current in the direction of the potential so that the phase angle between the current and the voltage is less than 90° (Figure 4.10(c)). The angle by which the phase angle differs from 90° is called the loss angle (symbol δ) and it is related to the dielectric loss by the following equation:

$$\tan\delta = \frac{\epsilon''}{\epsilon'}, \tag{6.8}$$

where tanδ is called the loss tangent. Measurement of the phase angle between the current and the voltage of a capacitor and knowledge of the dielectric constant of the dielectric substance enables the calculation of the dielectric loss by equation (6.8). The loss tangent is also known as the dissipation factor (D).

6.2.2 Sample Cells

Once the method to measure capacitance has been decided upon, the other important component in any apparatus designed to measure dielectric properties is the cell to contain the sample. Several designs of sample cells were found from a survey of

the literature from which the following summary can be reported.

Cells for measuring the dielectric properties of liquids and solutions often consist of coaxial cylinders to form the capacitor into which the dielectric is placed.[297,298] Such an approach is not really feasible for solids, except possibly for solids that can be formed *in situ* by the freezing of the liquid or solution. For most measurements on solid dielectrics, the sample is placed between the plates of a parallel-plate capacitor. The plates of the capacitor are insulated from each other and the rest of the cell. The distance between the capacitor plates must be accurately known so that the vacuum capacitance (C_o) of the condenser can be calculated using equation (6.2), to be used in the calculation of the dielectric constant by equation (6.1). This distance is usually determined by fitting the cell with a micrometer. Figure 6.3 is a simple depiction of this type of cell.[299]

However, there is a major problem with this two-terminal dielectric cell. It is always assumed that the electric field between the capacitor plates is everywhere uniform. While this may be true at the centre of the plates, this assumption does not hold at the edges of the plates. The change in the electrode curvature at the plate boundaries gives rise to a fringing of the field as shown[300] in Figure 6.4(a). At the edge of the plates the electric field samples materials outside of the region between the plates which makes the electrodes appear to be larger than they really are. The actual measured capacitance is larger than that calculated from the geometry of the capacitor plates (equation (6.2)). This extra capacitance is called "fringing capacitance." There have been many formulas developed to account for and correct for this, but these are generally inaccurate and difficult to apply.[301] This fringing effect also causes errors in the

Figure 6.3. Diagram of a two-terminal dielectric cell; from reference (299).

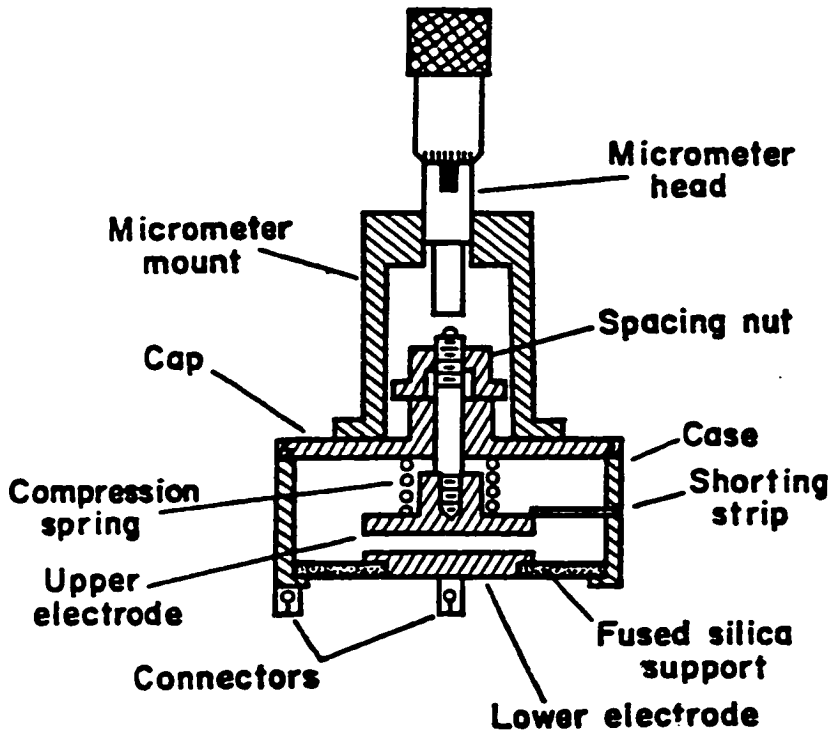

Figure 6.4. (a) Fringing of the electric field at the edge of capacitor plates; from reference (300). (b) Nearly uniform electric field lines between the plates of the capacitor with one plate surrounded by a guard ring separated by a guard gap α; from reference (302). (c) Closeup of guard gap showing that a slight fringing of the electric field still occurs even with the guard ring; from reference (302).

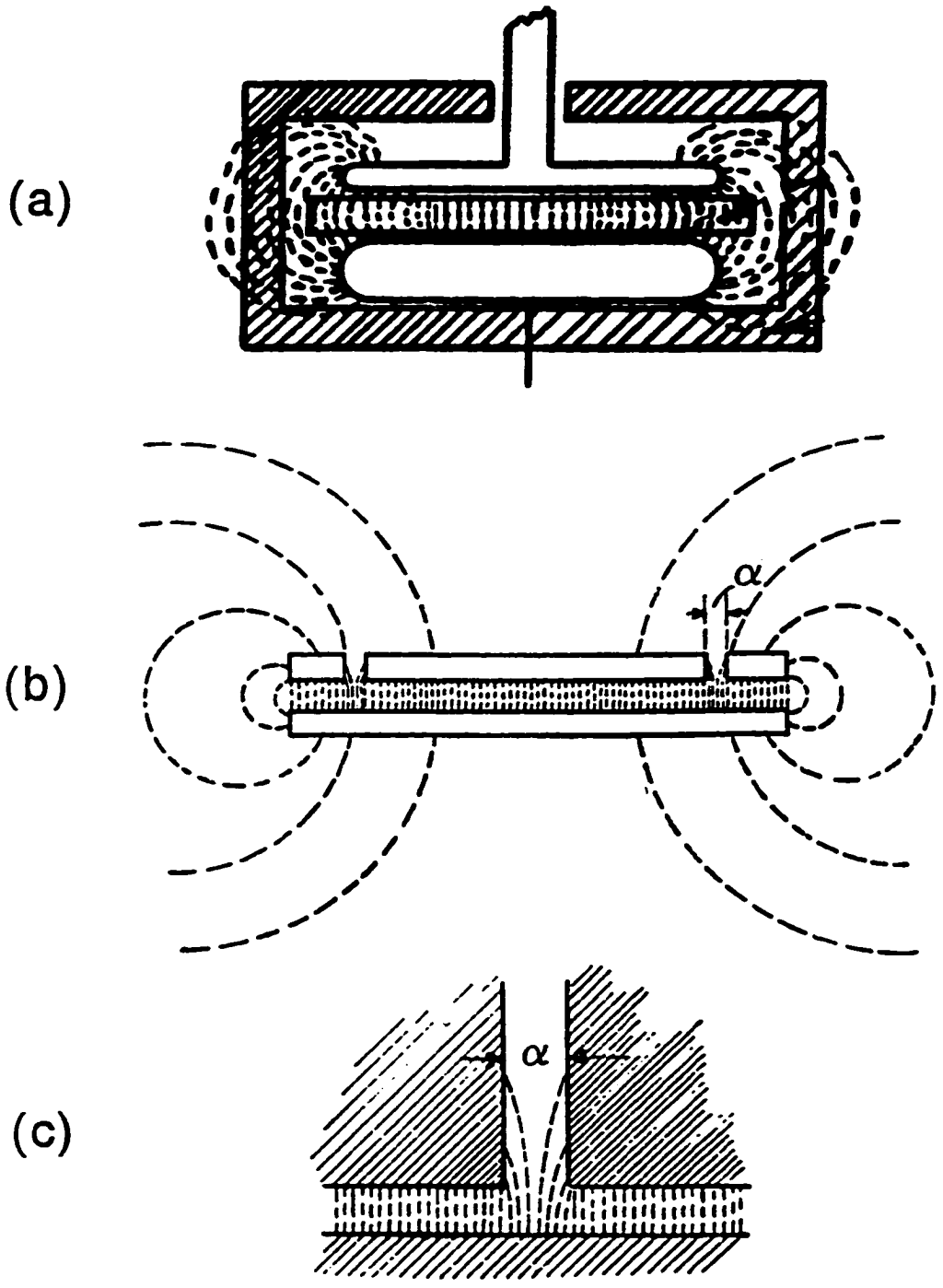

dielectric loss, since the measured loss includes the loss of materials encompassed by the fringing field.

The fringing field effect can be practically eliminated through the use of a guard electrode.[300,302] A guard electrode (also called a guard ring) completely surrounds the edge of one of the electrodes but is separated from it by a small distance α called the guard gap, which is typically of the order of 0.1 mm. The electrode that the guard ring surrounds is called the guarded electrode, and the guarded electrode is insulated from the guard ring by an insulator in the guard gap. For most of the dielectric cells in the literature using guarding techniques, this insulator is typically an epoxy resin, a ceramic ring, or another insulating substance such as teflon or mica.

If the guarded electrode and the guard ring are at the same potential when the impedance bridge is balanced, the field between the two plates of the capacitor will be very nearly uniform throughout, as shown[302] in Figure 6.4(b). Furthermore, as long as the dielectric sample is completely surrounded by the smaller of the two capacitor plates, the vacuum capacitance can be calculated based on the area of the smaller plate. However, as will be noticed[302] from Figure 6.4(c), a slight fringing of the field does still occur even with the presence of the guard ring, so the effective area of the smaller electrode must be used in calculating capacitance. The effective area is usually determined by assuming the effective radius of the circular electrode (r_{eff}) is greater than its true radius (r) by an amount equal to one-half the guard gap width (*i.e.* $r_{eff} = r + \alpha/2$),[302] although sometimes more complicated correction formulas are used.[302,303]

In practice, for the three-terminal cell (the third terminal is the guard terminal)

to be effective, the guard gap should be less than 1/4 the thickness of the sample, and the width of the guard electrode (ring) should be at least five times the sample thickness.[300] The three-terminal guarded cell is the design most often used for dielectric measurements.[304,305,306,307,308] A simple design of a three-terminal dielectric cell is shown[309] in Figure 6.5.

While some solid samples can be measured as single crystals or sheets, the measurement of powders is a bit more difficult. For the measurement of dielectric properties of powders, the powder sample must be in the form of a compressed disk formed by the application of high pressures. There are some reports in the literature describing how this can be done,[306,310,311] involving the use of a die and piston, and a hydraulic press.

The compressed disk sample must have flat, parallel faces in order to make good contact with the electrodes. Poor mechanical contact between the sample and the electrodes can lead to major errors in the dielectric measurements. Mechanical contact can be improved by attaching pieces of tinfoil to the sample with a very thin film of petroleum jelly.[312,313]

Another problem that is encountered especially in low-temperature work is that as the temperature is lowered, thermal contraction of the electrodes and the sample will occur. Most cells have a spring or a bellows assembly against one of the electrodes in order to maintain intimate sample-electrode contact at all temperatures. However, thermal expansion/contraction of the sample with changes in temperature causes a change in the interelectrode distance (d). As equation (6.2) shows, the capacitance of a parallel-plate

Figure 6.5. Diagram of a three-terminal dielectric cell; from reference (309).

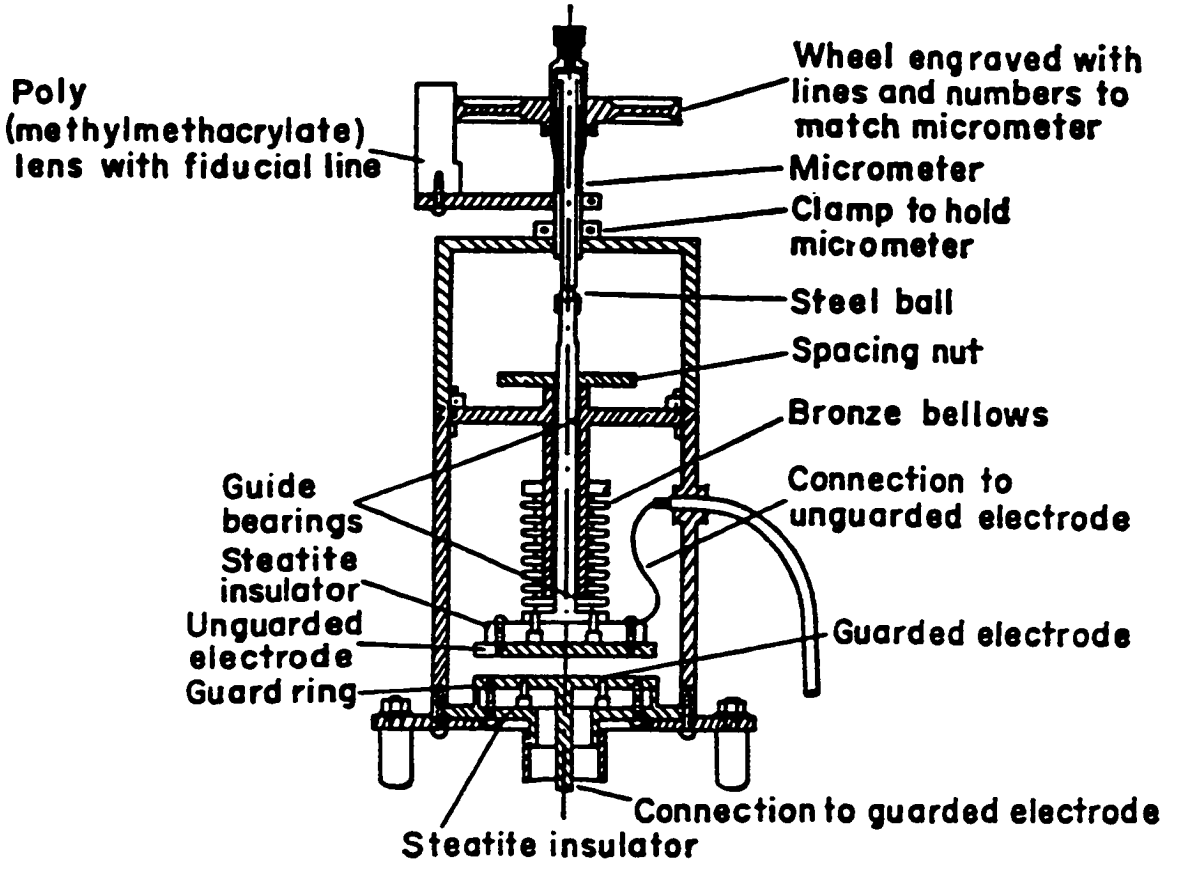

capacitor depends critically on d, and unless some method is developed to determine how d changes with temperature, serious errors in the dielectric measurements will occur. Furthermore, as indicated by equation (6.2), the capacitance depends on the area of the plates forming the parallel-plate capacitor which will also change with temperature due to the dimensional changes of the conducting substance from which they are made. This introduces further errors in the measurements. In most cases in the literature, the error due to changes in A with temperature is ignored.

There will always be some stray impedance in the electrode leads. The amount of stray capacitance can be determined by calibration with a substance that has a well-known dielectric constant. A commonly used standard substance is benzene.[308,313] Commercially available impedance meters usually have a calibration feature so that a correction can be made for stray lead impedance.

For the study of solids, most of the cells found in the literature consist of circular parallel plates made of copper or gold-plated brass. Most are of the three-terminal type, although a few two-terminal cells were found.[242,244] The distance between the two electrodes is typically of the order of 1-2 mm. In some of the literature cells one of the electrodes is movable and the distance between the electrodes is read with a micrometer.[304,307] In some cells both electrode plates are fixed, but these are used to measure the dielectric properties of solids that can be conveniently formed from the melt or from freezing a solution.[308] The plates are insulated from the rest of the cell by an insulating substance, usually teflon.

The temperature of the sample is normally measured with a thermocouple

(chromel-constantan[308] or copper-constantan[298,306]), although in some cases a resistance thermometer is used.[298,306,307] The outside of the sample area of the cell is surrounded by heating wire to heat the sample. The temperature control and measurement system does not have to be as elaborate or as stable as for adiabatic calorimetry measurements, so an adiabatic shield usually is not included. Most of the cryostat designs found in the literature survey were of the immersion type, where the system is immersed in a Dewar containing a cryogenic fluid, although one design was found using a gas flow cryostat,[307] where a continuous flow of cold gas surrounds the cell and maintains the cryogenic temperatures. The advantage of the flow cryostat is that shorter electrical leads can be used and this reduces residual impedance effects.

In general, the electrical leads that are used to connect the electrodes inside the sample cell to the appropriate capacitance measuring instrument outside of the cryostat are miniature coaxial cables. Coaxial cables consist of a two conducting layers separated by an insulating layer. The inner conductor is a thin central conducting wire. The whole wire is surrounded by an outside layer of insulation. The outer conductor acts as a screen which reduces the effects of stray capacitance between the cable and other cables or other parts of the cell.[314]

It should be noted that sample cells to measure capacitance are not exclusively designed for the purpose of determining dielectric constants. There is a strong dependence of the parallel-plate capacitance on the distance between the plates as shown by equation (6.2). Cells have been designed where the distance between the plates of a capacitor is correlated to dimensional changes of the sample, and thus, the thermal

expansion of the sample can be measured as a function of temperature.[315,316] In fact, capacitance dilatometry is the most sensitive conventional technique for measuring thermal expansion.

One design of a guarded dielectric sample cell found in the literature is worthy of further attention since it provides a unique method for determining the dielectric constant without knowledge of the sample thickness.[310] A schematic of the electrode system for this cell is shown[310] in Figure 6.6. Referring to this figure, the sample S, in the form of a pressed powder, is sandwiched between an upper electrode P and a lower disk electrode D. Outside of the disk electrode is a ring electrode R, where the ring electrode and disk electrode are fastened inside a guard block G, and insulated from it with 0.1 mm-thick mica. All of the electrodes including the guard block are made from copper. Electrical leads L connect each electrode to a capacitance bridge located outside of the cryostat.

The dielectric between the upper electrode and the disk electrode is the sample to be measured, whereas the dielectric between the upper electrode and the ring electrode is just the surrounding atmosphere (a small amount of helium exchange gas; effectively a vacuum). The disk capacitance (C_D) is therefore (*cf.* equation (6.2))

$$C_D = \frac{\epsilon \epsilon_o A_D}{d}, \tag{6.9}$$

where ϵ is the dielectric constant of the sample, A_D is the area of the disk electrode, and d is the distance between the upper electrode and the disk electrode (*i.e.*, the thickness of the sample). The ring capacitance (C_R) is

Figure 6.6. Diagram of a guarded literature dielectric cell employing an upper electrode (P), a disk electrode (D), and a ring electrode (R). The disk and ring electrodes are located in a guard block (G). The sample (S) is between the upper electrode and the disk electrode. Several leads (L) connect each electrode to a capacitance bridge; styled after reference (310).

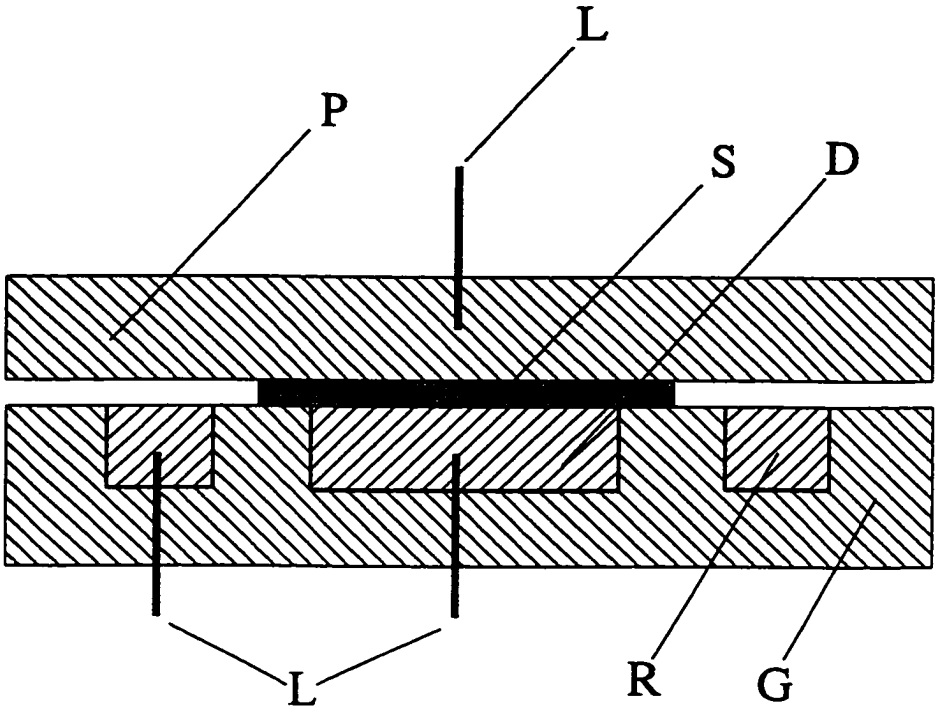

$$C_R = \frac{\epsilon_o A_R}{d}, \tag{6.10}$$

where A_R is the area of the ring electrode.

Measurement of the disk capacitance and the ring capacitance at a particular temperature and electric field frequency can be used to determine the dielectric constant of the sample from the ratio of the two capacitances,[310] *i.e.*, dividing equation (6.9) by equation (6.10),

$$\frac{C_D}{C_R} = \epsilon \times \frac{A_D}{A_R}, \tag{6.11}$$

or, solving for ϵ,

$$\epsilon = \frac{C_D}{C_R} \times \frac{A_R}{A_D}. \tag{6.12}$$

Thus, the dielectric constant is measured without knowledge of the sample thickness, and requires only the ratio of the areas of the ring electrode to the disk electrode. Thermal expansion/contraction of the sample with temperature changes should not cause error in the dielectric constant measurements made by this cell (assuming the area ratio A_R/A_D is known as a function of temperature) because the dielectric constant as determined from equation (6.12) does not depend on the sample thickness. The disk capacitance and ring capacitance are affected equally by dimensional changes in the sample, and by taking the ratio of these capacitances, the effect of changes in d cancels out. The dielectric apparatus that was constructed in this research project was designed to take dielectric relaxation measurements based upon this principle.

6.3 Design and Construction of Dielectric Apparatus

6.3.1 Sample Cell

Perhaps the most important component of any experimental apparatus is the cell which contains the sample to be measured. The cell should be designed to allow for easy loading and removal of the sample taking into account the form of the sample being considered (*e.g.*, gas, liquid, solution, powder, single crystal), and should allow for the expedient measurement of the property of interest under the desired measurement conditions. The cell that was constructed for the dielectric relaxation apparatus developed for this thesis work was designed to measure the dielectric properties of powdered solids in the range of cryogenic temperatures. Furthermore, the material from which the cell was made had to be able to resist corrosion to some extent, since the compounds which were to be measured were highly corrosive, *i.e.*, NaOH and NaOD. The ability to load samples into the cell in an inert atmosphere was crucial due to the very hygroscopic nature of sodium hydroxide and sodium deuteroxide.

The cell that was built for the dielectric relaxation apparatus combined many of the features of sample cells that were described for similar pieces of equipment from the literature as summarized in the last section, as well as some original ideas. A diagram of the sample cell that was finally decided upon and constructed is provided in Figure 6.7. The cell consisted of an upper part and a lower part, with the actual sample itself being located at the boundary where the two parts come together. Top views of the upper

Figure 6.7. Diagram of the sample cell of the constructed dielectric relaxation apparatus.

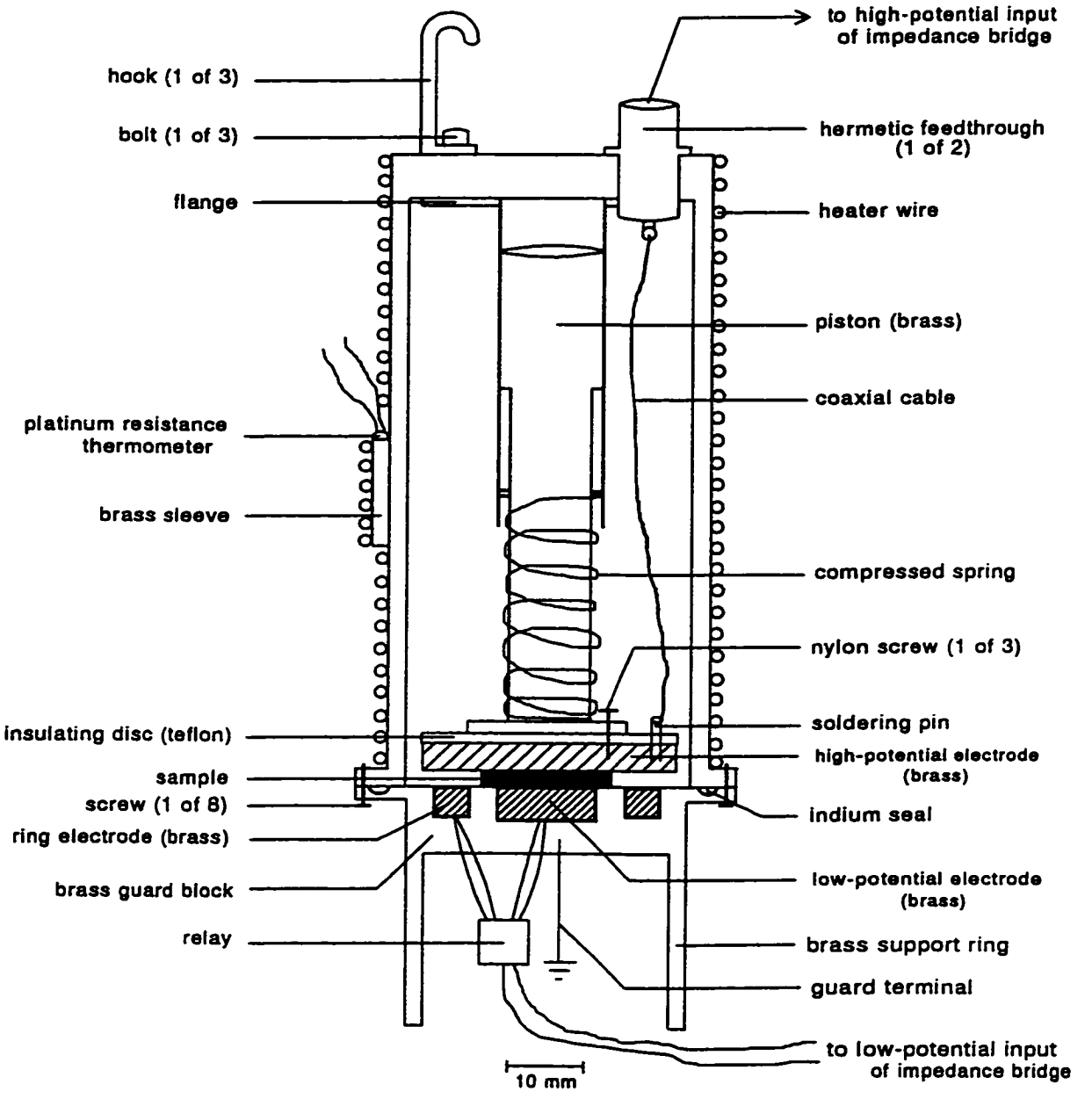

and lower parts of the cell are shown in Figure 6.8(a) and Figure 6.8(b), respectively.

The sample, in the form of a pressed powder, was squeezed between two circular parallel conducting electrodes of a capacitor: a high-potential electrode and a low-potential electrode, so-named corresponding to the inputs of the capacitance meter to which they were eventually connected. The low-potential electrode was in the form of a disk that was located in a guard block along with an annular ring electrode. Only a small pressure of helium gas existed between the high-potential electrode and the ring electrode and thus, this cell was designed to take measurements in a similar manner to the cell reported by McCammon and Work,[310] as described in the last section.

The ring electrode and disk electrode were fastened to the guard block with GE7031 varnish (also known as IMI7031 varnish) so chosen because of its adhesive properties, its ability to withstand low temperatures and temperature cycling, and its electrical insulating properties. All of the electrodes and the guard block were made of brass which does not readily corrode when exposed to alkali-metal hydroxides or deuteroxides. A guard terminal attached to the guard block was connected to ground potential. Since the disk and ring electrodes were electrically isolated from a grounded guard block, this cell was of the three-terminal type, meaning that the effects of fringing capacitance were to be greatly reduced for measurements with both the ring electrode and disk electrode. The electrical isolation of the ring and disk electrodes from the guard block (and each other) was confirmed by measuring the resistances between them with a Hewlett-Packard 34401A digital multimeter. The meter read "overload" in all cases, implying a resistance greater than 100 MΩ.

Figure 6.8. Top views of the (a) upper, and (b) lower parts of the sample cell.

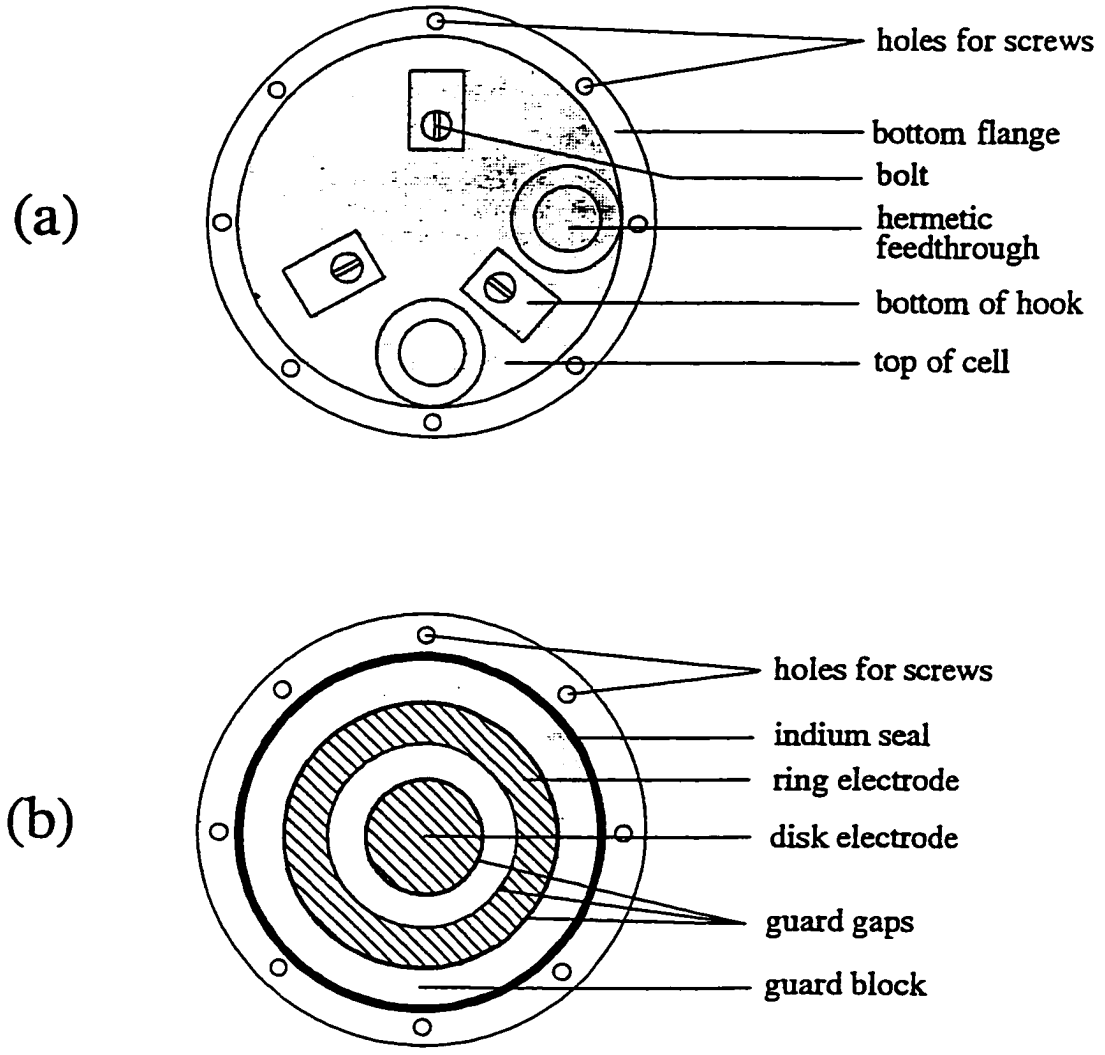

The disk electrode had a diameter of 12.48 ± 0.04 mm as measured with a vernier calliper. The inner and outer diameters of the ring electrode were measured to be 21.52 ± 0.04 mm and 28.32 ± 0.04 mm, respectively. The guard gap between the disk electrode and the guard block was determined to be 0.12 ± 0.028 mm. Similarly, the average inner and outer guard-gap widths between the ring electrode and the guard block were found to be 0.14 ± 0.03 mm and 0.09 ± 0.03 mm, respectively. The design of the cell was such that the diameter of the sample should be in the 14 mm - 20 mm range, so that the disk electrode was completely covered while the ring electrode was completely exposed to the atmosphere of the cell.

Soldering pins were connected to the ring electrodes and disk electrodes through holes in the guard block. The pins were electrically isolated from the guard block with a coating of GE7031 varnish. It was through soldering to these pins that the ring and disk electrodes were connected to a small relay (Teledyne, model 732-12, hermetically sealed) which, itself, was eventually connected to a power supply. Toggling the power supply on or off switched the capacitance measurement mode between the high-potential/disk electrodes and the high-potential/ring electrodes. It was from these two measurements that the dielectric constant of the sample was to be obtained without knowledge of the sample thickness as shown by equations (6.11) and (6.12).

The high-potential electrode was electrically isolated from the rest of the cell by an insulating support disk made from teflon. A soldering pin was attached to the high-potential electrode through a hole in the teflon disk. A brass piston lay on top of the teflon disk that was fastened to the high-potential electrode with three electrically

insulating nylon screws. The piston was free to move in the vertical direction to conform to the thickness of the sample. Intimate contact between the sample and the electrodes at all temperatures was maintained by a weak, compressed spring which surrounded the bottom portion of the piston. The upper part of the piston was confined inside a casing attached to a flange which was bolted to the top of the cell with three screws. These screws also fastened three copper hooks to the top of the cell which allowed the cell to be suspended in the cryostat. Two pieces of 3.2 mm diameter miniature coaxial cable were soldered to the soldering pin in the high-potential electrode and to two BNC hermetic feedthroughs which were screwed into two threaded holes in the top of the cell. The outer casing of the cell was made of brass.

The upper and lower parts of the cell were joined together by eight screws which, due to the nature of this cell's design, had to be administered from the bottom. The surfaces which met when the upper and lower parts of the cell were joined together (especially the electrodes) were milled as flat as possible (within 0.02 mm) to allow for good sample-electrode contact. The cell was vacuum sealed from its surroundings by a ring of 0.5 mm diameter indium wire which was placed in a groove in the guard block, and also by O-rings underneath the hermetic feedthroughs, and Apiezon T grease applied to the bolts at the top of the cell. The cell was $\sim$ 13.5 cm in height when it was fully put together and was $\sim$ 50 mm in width at its widest point. The mass of the cell was $\sim$ 700 g.

6.3.2 Heater/Thermometer

The measurement of temperature for this apparatus was performed with a platinum resistance thermometer (TRI Research, model PR-100; $R \sim 100\ \Omega$ at 273 K) that was calibrated by the manufacturer between 15 K to 300 K, with an uncertainty of $\pm$ 0.01 K. The thermometer was capsule-like, measuring approximately 9 mm in length and 1.5 mm in diameter, with two protruding leads. This thermometer fit snugly into a sleeve fashioned out of a piece of brass plate that was soldered to the outside of the upper part of the cell (see Figure 6.7). Thermal contact between the thermometer and the cell was enhanced by the application of a small amount of Apiezon T grease.

Two electrical leads consisting of double-silk wound 38 SWG copper wire were soldered to each of the two leads of the platinum resistance thermometer using thermal-free solder. These four leads eventually connected to a Hewlett-Packard 34401A digital multimeter which measured the resistance of the thermometer. The use of the four leads allowed the resistance to be measured by the four-wire ohm method, which compensated for the resistance in the leads themselves (which was $\sim 4\ \Omega$).

The resistance/temperature calibration data obtained from the manufacturer for this thermometer were subjected to a spline-fitting procedure as was described in some detail in Section 5.2.1. The resulting spline parameters were used to interpolate between the calibration data so that the measured resistance readings could be converted to temperature values.

In contrast to a heat capacity determination by calorimetry, neither temperature

nor temperature differences are directly involved in the determination of a dielectric constant. Accuracy in temperature of $\pm$ 0.1 K can be reasonably tolerated in dielectric measurements. Because of this, the sophisticated measures involved to determine the temperature extremely accurately in an adiabatic calorimetry experiment were not really required in the dielectric relaxation apparatus. Thus, absolute resistance measurements were converted directly to temperature without measuring the resistance relative to a standard resistor (resistance ratio). Also, a constant current source was not necessary with this apparatus, and the temperature did not have to be measured with current in the forward and reverse direction to correct for the relatively subtle effect of thermal emfs (the error introduced by ignoring thermal emfs is typically 0.02 - 0.045 K, depending on the temperature). This greatly simplified the temperature measurement procedure.

The cell heater consisted of $\sim$ 5 m of 32 SWG manganin wire bifilarly wound around the outside of the upper part of the cell (see Figure 6.7). The heating wire was attached to the cell with GE7031 varnish. In general, the power (P) supplied by an electrical heater of resistance R and applied voltage V (for Joule heating) is given by

$$P = \frac{V^2}{R}. \qquad (6.13)$$

The resistance of the heater was measured with a digital multimeter and found to be 35.5 Ω at room temperature. Because of the high thermal mass of the cell, this low heater resistance was necessary to supply sufficient power to increase the temperature of the system at a reasonable rate ($\sim$ 0.1 - 1.0 $K \cdot min^{-1}$). A piece of double-silk wound 38 SWG copper wire was soldered to each end of the heater wire to serve as leads to the

heater. These leads eventually connected to a power supply which provided the voltage to power the heater.

6.3.3 Cryostat

Once a sample was loaded into the sample cell, the cell was mounted in a cryostat which allowed the system to be evacuated and also allowed for the use of cryogenic temperatures. The cryostat that was built for the dielectric relaxation apparatus was of the immersion type, *i.e.*, cryogenic temperatures were maintained by immersing the system in a Dewar containing liquid nitrogen or liquid helium.

A diagram of the cryostat is shown in Figure 6.9. It consisted of a long ($\sim$ 0.5 m) stainless steel tube with two circular stainless-steel plates soldered to it near the bottom. The lower plate had three symmetrically placed threaded holes into which three hooks were located. The sample cell was suspended in the cryostat with three loops of 9-kilogram load nylon line mounted between the hooks at the bottom of the cryostat to the hooks at the top of the cell. Since the hooks at the bottom of the cryostat were in threaded holes, they could be adjusted so that the cell hung straight up and down.

The bottom of the larger stainless-steel plate was milled as flat as possible ($\pm$ 0.02 mm) and had eight drilled holes symmetrically placed near its outer perimeter. To the bottom of this plate was attached a brass enclosure can which surrounded the sample cell. The top of the enclosure can consisted of a stainless-steel annular ring which had

Figure 6.9. Diagram of the cryostat for the dielectric relaxation apparatus.

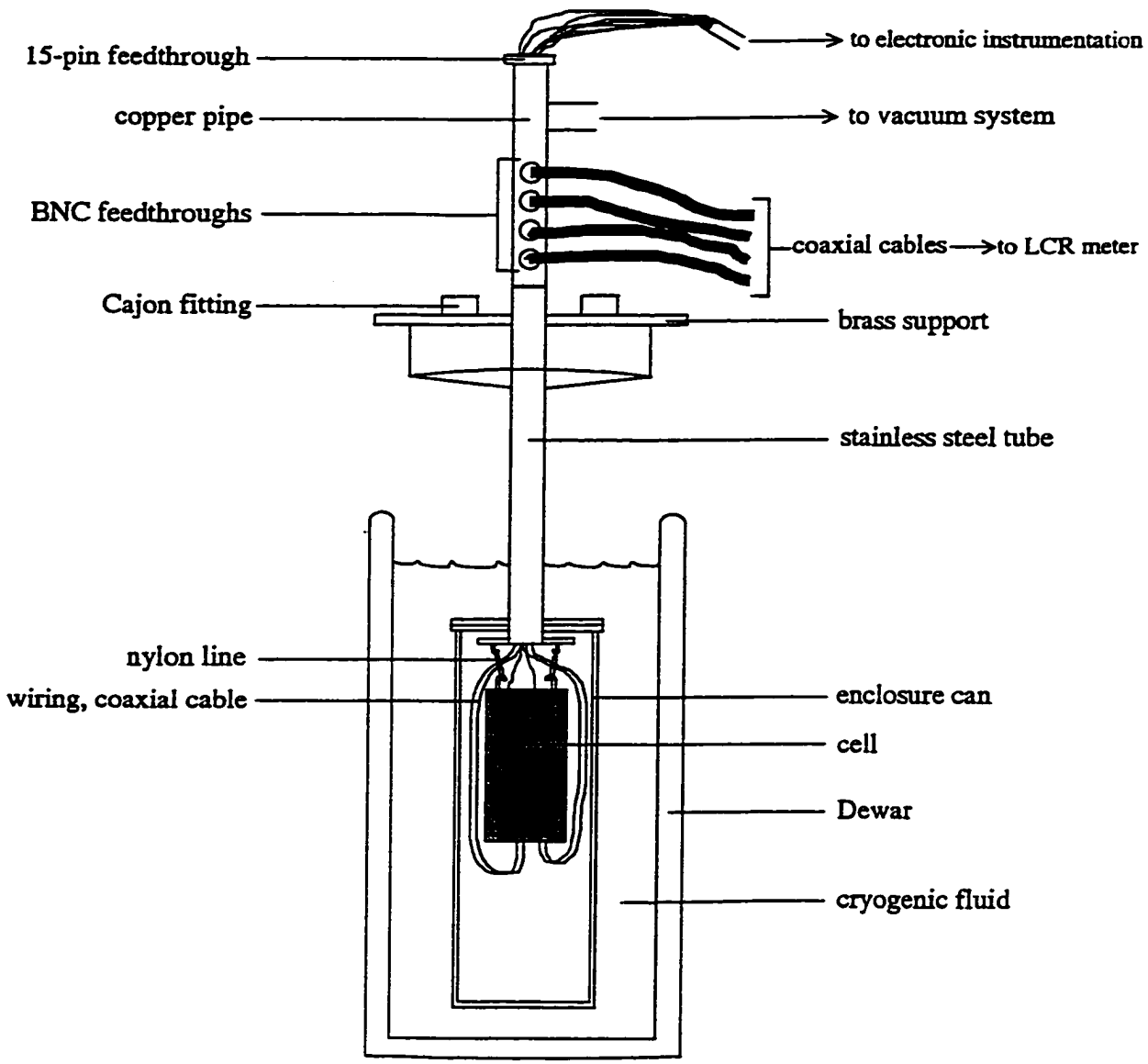

a concentrically located 1 mm-wide groove as well as eight threaded holes in its surface. The eight threaded holes corresponded to the eight holes drilled into the stainless steel plate to which it was to be attached. A suitable length of 1 mm-diameter indium wire was placed in the groove of the enclosure can which provided an excellent vacuum seal when pressed against the surface of the stainless steel plate and squeezed by the pressure of eight hexagonal-head screws.

Near the top of the stainless-steel tube was a square brass plate which allowed the cryostat to be mounted in a stand. Attached to the brass plate was a cylindrical piece of brass and two 9.5 mm (inside diameter) Cajon fittings. These accessories were necessary for experiments using liquid helium. During a liquid helium run, two Dewars were used, one inside the other, with the inner Dewar containing liquid helium while the outer Dewar contained liquid nitrogen. The inner Dewar was further insulated by attaching a suitably sized piece of rubber tubing around the cylindrical piece of brass which also fit snugly around the top of the liquid helium Dewar. One of the Cajun fittings was for a liquid helium transfer tube which was used to fill the inner Dewar with the liquid helium. To the other fitting was attached an exhaust valve which enabled the helium gas that inevitably formed above the inner Dewar to be expelled.

Silver soldered to the top of the stainless-steel tube was a $\sim$ 40 cm-long piece of copper pipe. Along the side of the pipe were four holes to which were soldered short cylinders of brass with a threaded hole in the centre. The holes were the right size for BNC feedthroughs to be administered into them. These feedthroughs formed a vacuum-tight seal against the pressure of rubber O-rings. The cell had four coaxial leads

extending from it; two from the small relay at the bottom, and two from the top of the cell. These leads were fed through to the outside world through the four BNC feedthroughs.

At the top of the copper pipe was a 15-pin hermetic feedthrough which was used to pass copper wires from inside the cryostat to the electronic instruments outside. Pressure from a threaded brass piece at the top against a rubber O-ring provided the vacuum seal. Near the top of the copper pipe along the side was an opening to which was soldered a 12.5 mm Cajon fitting. The opening in the centre of the Cajon fitting was encircled by a rubber O-ring which fit snugly around a brass piece that was connected to the vacuum system. An oil diffusion pump backed by a roughing pump could evacuate the system to a pressure on the order of 10^{-5} Torr, as determined from a pressure gauge directly attached to the vacuum system.

6.3.4 Electronics

Crucial to the success of this apparatus was the electronics system. The accuracy and precision of the eventual dielectric measurements were vitally dependent on the performance of the various electronic instruments and the proper connection of wiring between the sample cell inside the cryostat and the electronic instruments outside. A schematic showing all of the electronic instruments involved in measurements with this apparatus and the connections between these instruments is provided in Figure 6.10.

Figure 6.10. Schematic diagram of the automated dielectric relaxation apparatus showing all of the electronic instrumentation involved.

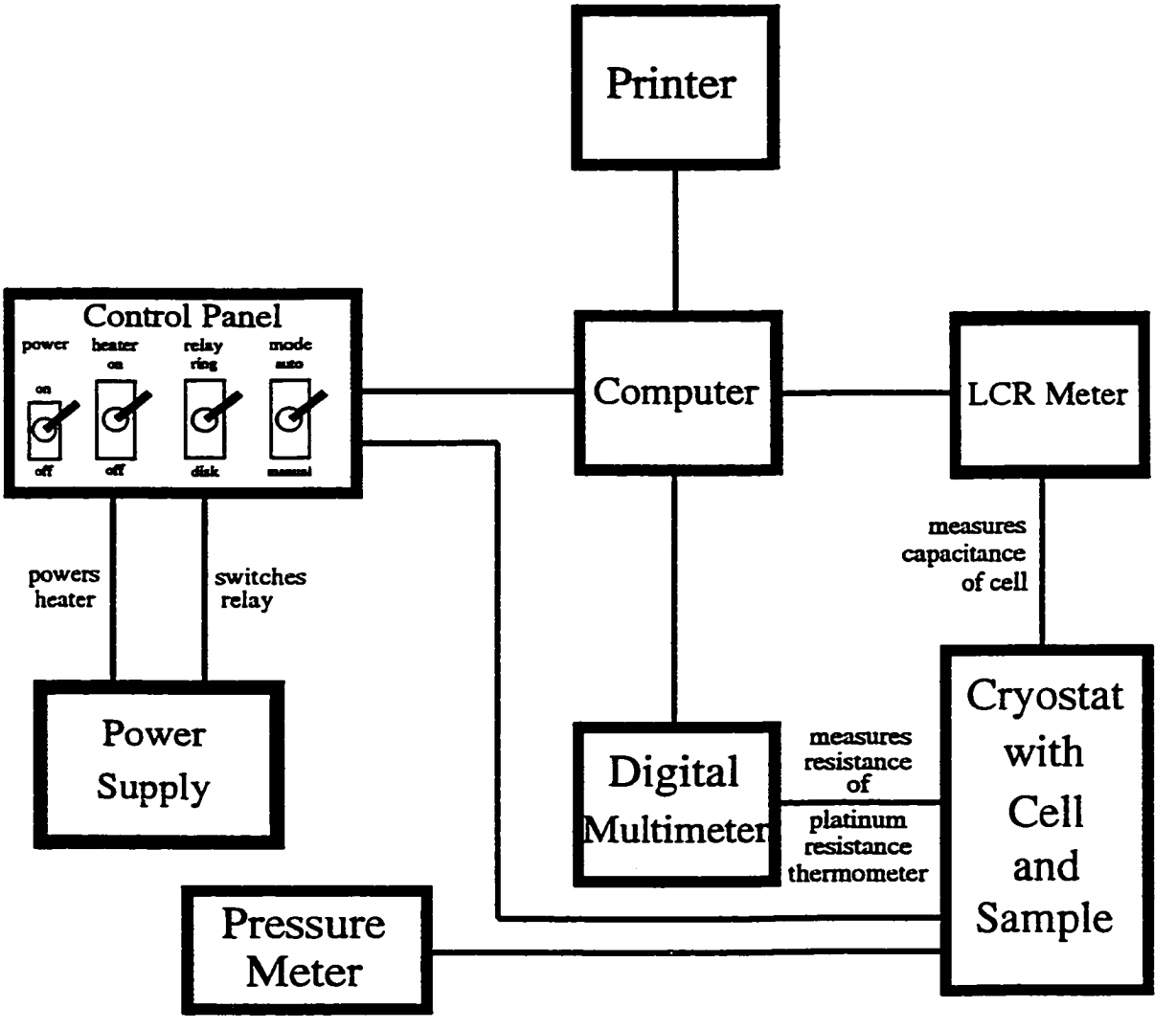

The pressure inside the vacuum system was read by a pressure meter attached to the pressure gauge. All of the leads to the sample cell had to be fed out of the cryostat while maintaining the vacuum-sealed conditions. This was accomplished by the hermetic feedthroughs. Soldered to the BNC feedthroughs inside the cryostat were four pieces of 3 mm-diameter miniature coaxial wire which hung down inside the stainless steel tube and terminated in BNC connectors. These connectors were matched to the connectors soldered to the ends of the four coaxial leads coming from the cell. Two of the cell's coaxial leads were soldered to the relay at the bottom of the cell which were connected to the disk electrode or the ring electrode depending on the status of the relay. The other two coaxial leads of the cell were connected to a soldering pin in the high-potential electrode which were soldered to two BNC hermetic feedthroughs at the top of the cell (see Figures 6.7 and 6.8).

The outer conducting layers of all four of the coaxial cables were mutually connected together. Two coaxial leads were required for each electrode because one lead was for the current and the other was for the voltage. Having independent current and voltage leads reduced the effects of mutual lead impedances.[314]

Outside of the cryostat, four BNC connectors were attached to the BNC feedthroughs. These connectors were part of a 2 m-long cable which was eventually attached to a Hewlett-Packard 4284A precision LCR meter. The meter measured impedance by an auto-balancing bridge method. It was capable of taking measurements at various frequencies ranging from 20 Hz to 1 MHz. The voltage level could be varied from 5 mV_{rms} to 2 V_{rms}. The meter could be set up to take readings in several

configurations such as impedance/phase angle, resistance/reactance, series inductance/resistance, and many more. For the purposes of these experiments, the desired parameters were the dielectric constant and the dielectric loss. A capacitor containing a dielectric can be represented as a pure capacitor in parallel with a resistor (representing the dielectric loss). However, once the dielectric constant is known from the capacitance measurement, the dielectric loss can be readily determined from a measurement of the dissipation factor ($\tan\delta$) using equation (6.8). Thus, the LCR meter was set up to take measurements in parallel capacitance/dissipation factor mode.

All of the other leads coming from the cell were silk-wound copper wires. These exited the cryostat through the 15-pin hermetic feedthrough. A sufficient length of silk-wound copper wire was soldered to each of the pins in the feedthrough and these wires hung freely inside the stainless steel tube of the cryostat so that they could be soldered to their corresponding leads coming from the cell. In total, eight leads came from the cell (seven of the wires from the feedthrough were spares). Two of these were from the sample cell heater, four were from the platinum resistance thermometer embedded outside of the cell, and the other two were connected to the relay at the bottom of the cell.

Outside of the cryostat, 15 wires from a 25-wire cable were soldered to the outside of the 15-pin hermetic feedthrough. Only eight of these wires were used at any one time, so that there were seven spares. The four wires which came from the platinum resistance thermometer were connected to a Hewlett-Packard 34401A digital multimeter which was set up to measure resistance by the 4-wire ohm method. The other four wires

(two from the cell heater, and two from the cell relay) were connected to their appropriate places on a control panel which contained a power supply. The power supply gave the necessary voltage required to switch the cell relay between its two positions, *i.e.*, between the disk electrode and the ring electrode. The power supply also provided the power for the cell heater, and the voltage could be varied from 0 V to 19.6 V. The control panel was interfaced to a computer so that switching the relay, turning the heater on or off, and changing the heater voltage could be done either manually or by suitable commands from the computer.

The HP 4284A LCR meter and the HP 34401A digital multimeter also were interfaced to the computer through an IEEE488 interface card. Thus, all of the workings of the apparatus (heater on/off, heater voltage, switching the relay, instrument settings, data acquisition and analysis) could be controlled by the computer. The automation potential of this apparatus was fully realized through the programming of suitable software (using the QBASIC language) that ran the system. Once the sample was loaded and cooled to the desired starting temperature, the program prompted the experimenter for some measurement parameters. The run would then commence and proceed under computer control with a minimum of supervision from the operator, except for the occasional refilling of the Dewar with cryogenic fluid. The data from the run were stored on disk in both raw and analyzed form. The data also were printed out on a printer connected to the computer.

6.4 Sample Preparation

The dielectric relaxation apparatus just described was designed to perform measurements on pressed powdered samples. Thus, before measurements could be taken on a desired solid, it had to first be crushed and ground into a fine powder. This could be accomplished with a mortar and pestle or with a grinding mill.

Once a fine powder had been obtained, the sample had to be pressed to form a pellet. The pellet had to be formed in such a way that its faces were both flat and parallel, so that it had a constant thickness, and that it would have good contact with the electrodes of the sample cell. The sample cell was designed to accommodate a pellet with a diameter in the 14 mm - 20 mm range and therefore, the sample pellet had to have dimensions which conformed to these restrictions. It should be noted that samples in the form of sheets could also be measured as long as they could be cut to suitable dimensions with plane, parallel faces.

To press a powdered sample into a pellet of the appropriate dimensions, a die and piston device was designed and made from steel. A diagram of the die and piston set up is shown in Figure 6.11. The faces of the pistons were ground as flat as possible. Two of these devices were obtained; one which produced 17 mm-diameter pellets, and the other for 19 mm-diameter pellets.

To obtain a pressed pellet suitable for measurement, the powdered sample was loaded into one of the die and piston devices by placing it between the two pistons such that it was well-packed and as level as possible. The die and piston was then placed in

Figure 6.11. A diagram of a die and piston device used to make pressed powdered samples for measurement by the dielectric relaxation apparatus.

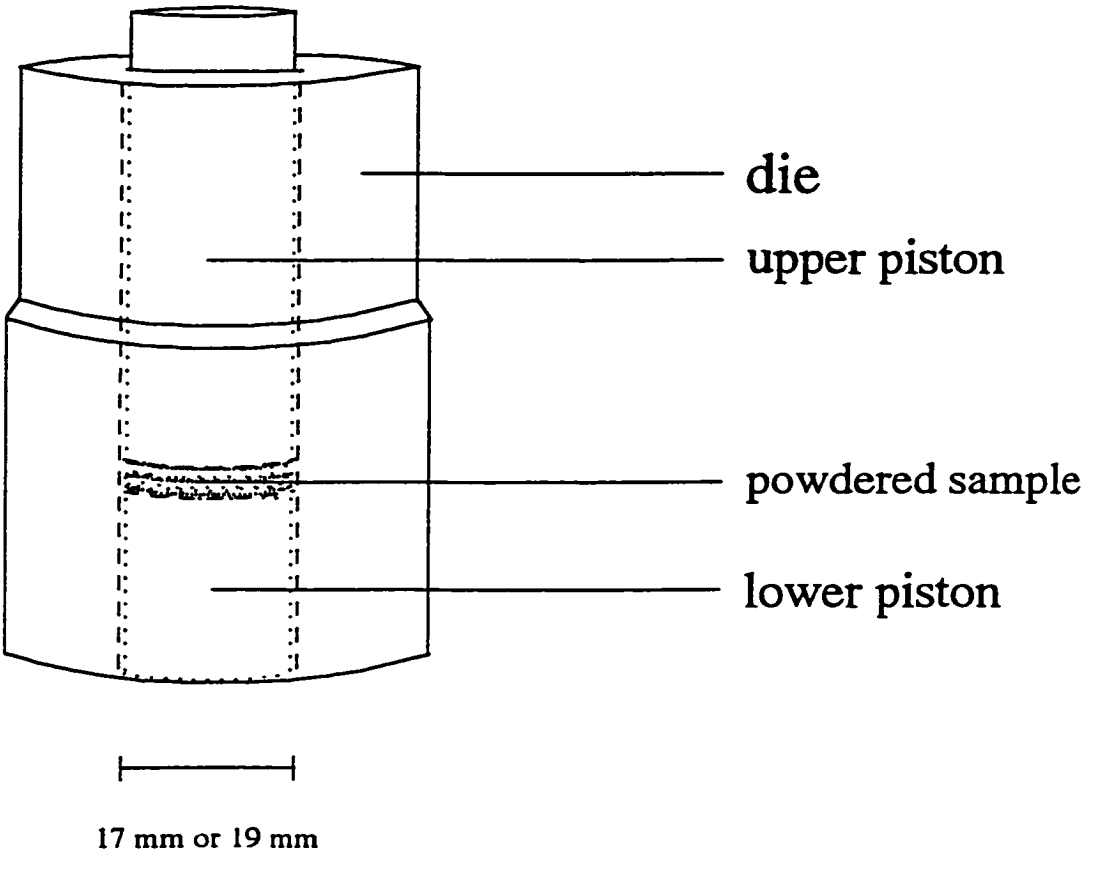

a hydraulic press to apply the pressure necessary to form the pellet. Many pellet pressing techniques were tried, and it was found that suitable pellets were obtained by the following method: First of all, a force equivalent to ~ 5 metric tonnes (5000 kg) was applied to the sample for a period of 1.5 minutes. The die was then removed from the press, rotated 180°, and placed back in the press to be pressed for another 1.5 minutes. This cycle was then repeated once more. After this procedure, the pistons were usually jammed in the die, but could be released by careful use of an Arbor press apparatus to obtain the pellet.

Pressed pellets with thicknesses in the range of 0.9 mm to 1.8 mm could be readily made by this method. The faces of the pellets were very flat, and a measurement of the thickness variation of a pellet with a vernier calliper revealed a constant thickness within the experimental uncertainty of $\pm$ 0.02 mm in most cases. Once a suitable pellet was made, it could be loaded into the sample cell for measurements by the dielectric relaxation apparatus.

6.5 Experimental Procedure

Loading a sample in the sample cell was usually done in a glove bag that was flushed several times with helium gas. This was done so that some helium would be trapped inside the cell when it was sealed, and this would help to promote thermal equilibrium during the measurements.

A ring of 0.5 mm-diameter indium wire was placed in the groove in the bottom part of the cell. The pellet sample was placed on top of the bottom portion of the cell in such a way that it completely covered the disk electrode but left the ring electrode completely exposed. The upper part of the cell was then placed on top of the bottom part with the high-potential electrode pressing firmly against the sample. This had to be done very carefully to avoid moving the sample during this procedure. The two parts of the cell were attached using the eight screws that also applied pressure to the indium to form a good vacuum seal.

The cell was then removed from the glove bag and suspended from the bottom of the cryostat from its hooks using loops of nylon line. The two coaxial cables inside the cryostat corresponding to the high-potential and high-current inputs of the LCR meter were connected to the BNC feedthroughs at the top of the cell. The low-potential and low-current coaxial leads in the cryostat were attached to the BNC connectors terminating at the ends of the two coaxial leads soldered to the relay at the bottom of the cell. The hooks threaded into the bottom of the cryostat were adjusted until the cell hung in a vertical fashion.

The remaining leads of the cell were then soldered to their corresponding silk-covered copper wires inside the cryostat. The platinum resistance thermometer was placed into its brass sleeve at the side of the cell with a small amount of Apiezon T grease for good thermal contact. The four cryostat thermometer leads were soldered to the thermometer followed by soldering of the two cryostat heater wires to the cell heater, and the two relay switching wires to the relay at the bottom of the cell. After the wires

were soldered, all of the soldering junctions were covered by a small piece of heat-shrink tubing to prevent them from shorting against the sides or top of the cell during the measurements.

The cell was then encased in the brass enclosure can which had an indium seal made from a ring of 1.0 mm-diameter indium wire. This provided a good vacuum-tight seal when the enclosure can was fastened tightly to the stainless steel plate of the cryostat with eight screws. The system was then opened to the vacuum system and evacuated to a pressure of about 10^{-5} Torr. Achieving this level of evacuation could take several hours.

When a suitable vacuum had been reached as read from the pressure meter, the enclosure can was submerged in a Dewar containing liquid nitrogen (or liquid helium), and the temperature of the system was allowed to fall. This cooling process could be facilitated by the introduction of a small pressure of helium exchange gas into the cryostat, which was pumped away when the desired starting temperature of the run had been reached. The measurement parameters for the run were input into the automation software to start the acquisition of data for this run.

The measurement parameters input into the computer included the desired frequencies at which measurements would be taken, how many measurements would be taken at each frequency, the desired heating rate (in $K \cdot min^{-1}$), and the temperature interval between each set of measurements. At the start of the run, the program turned on the cell heater which remained on for the duration of the run. The computer automatically set the heater voltage (V) at a value designed to produce the desired input

heating rate (dT/dt) as calculated from the following equation for the heater power (P):

$$P = \frac{V^2}{R_{heater}} = m_{cell} C_{cell} \frac{dT}{dt}, \tag{6.14}$$

where R_{heater} is the resistance of the cell heater, m_{cell} is the mass of the cell, and C_{cell} is the heat capacity of the cell. Solving for V yields

$$V = \sqrt{m_{cell} C_{cell} R_{heater} \frac{dT}{dt}}. \tag{6.15}$$

The heat capacity of the cell was estimated for this calculation by assuming that the cell was made entirely out of brass, and using data from the literature for the heat capacity of brass as a function of temperature.[317] The heat capacity at the cell temperature was determined by interpolation using a spline fit of the literature heat capacity data. The cell heater resistance was measured as a function of temperature in a separate experiment and the data were spline fitted so that the needed interpolated value could be obtained at any temperature. Using this data along with the known mass of the cell would give the required heater voltage to maintain the desired heating rate by equation (6.15).

The computer set the heater voltage at this calculated value at the start of the run. However, other factors affected the heating rate of the cell besides those included in equation (6.15). Most importantly, the conditions in the system were not adiabatic; there was no adiabatic shield, no heat sink for the electrical leads, nor a perfect vacuum. These factors were not accounted for by equation (6.15), so that the true heating rate was often different from the desired one. The computer program corrected for this by keeping track of the average heating rate over one-minute intervals. If the experimentally determined

rate differed from the desired rate by a certain threshold value, then the heater voltage would be adjusted by the program by an amount calculated from an empirical formula which was proportional to the difference between the actual rate and the desired rate. Since the heater voltage was thus evaluated and updated every minute, the actual heating rate was maintained within $\pm$ 10% of the desired rate at all times.

The digital multimeter constantly monitored the temperature of the cell by measuring the resistance of the platinum resistance thermometer. The computer set the LCR meter to the first frequency and the capacitance and dissipation factor between the high-potential electrode and the disk electrode were measured a pre-determined number of times (usually 5-10 times). The results were then averaged and a standard deviation was calculated. The temperature for this measurement was taken as the average of the temperatures before and after the disk electrode measurements were taken. When the disk electrode measurements were completed, the computer switched the relay at the bottom of the cell to take capacitance measurements between the high-potential electrode and the ring electrode. These measurements were taken several times and an average value and standard deviation were determined. The dielectric constant was then calculated from equation (6.12), and the dielectric loss was calculated from equation (6.8). The computer then set the LCR meter to the next frequency and the measurements were repeated, until all of the desired frequencies had been measured. It took only a couple of minutes to obtain the measurements at all of the frequencies, during which time the temperature of the cell would typically rise by about 2 K.

It should be noted that the experimental uncertainties based upon the standard

deviations of the measurements and the uncertainty in the area ratio of the ring and disk electrodes (see next section) were propagated throughout all of the calculations. Thus, an experimental uncertainty was determined for each calculated dielectric constant and dielectric loss value. The data were saved to disk and were also printed out on the printer.

Once a set of measurements had been taken at all of the desired frequencies, the temperature of the cell was monitored until it had increased by a set interval entered by the experimenter at the start of the run. When the temperature had increased by the desired amount, the capacitance measurements began again, and a dielectric constant and dielectric loss value were determined for each frequency. This process was repeated, and dielectric data were determined as a function of frequency at different temperatures until the end temperature of the run was reached, at which point the computer turned off the cell heater. The maximum voltage that could be set for the cell heater using the present configuration was ~ 19.6 V, which could maintain a cell temperature up to a maximum of ~ 360 K. Thus, there was little danger of overheating and damage to the cell or its wiring due to power fluctuations or computer problems.

When all of the data for a run had been collected, it could be plotted and analyzed using the appropriate data plotting software. The computer software for the apparatus was designed to take readings in the cooling direction as well as the heating direction, although the cooling rate of the cell was more difficult to control than the heating rate.

6.6 Calibration

Before meaningful measurements could be taken with the dielectric relaxation apparatus, certain aspects of the equipment had to be suitably calibrated.

First of all, the residuals in the leads between the LCR meter and the cell had to be taken into account. The HP 4284A LCR meter had a built-in feature which could be used to compensate for these residuals. An OPEN correction was performed whereby the ends of the high-potential/current and low-potential/current leads were left open, and the stray admittance was measured by the LCR meter at various frequencies. The other correction that was done was the SHORT correction, which involved directly connecting the ends of all the leads together and the residual impedance was measured by the LCR meter at several frequencies. The results of these compensation measurements were stored in the meter's memory to be used to correct all future measurements taken by the meter for residual effects.

Although the LCR meter was capable of obtaining data at frequencies in the range of 20 Hz to 1 MHz, only measurements at frequencies greater than about 65 Hz provided meaningful data as measured by the dielectric relaxation apparatus. The reason for this is that the impedance of a (pure) capacitor (Z_c) varies with the angular frequency ($\omega = 2\pi f$, f is the frequency) and the capacitance by the following equation:

$$|Z_c| = \frac{1}{\omega C}. \qquad \textbf{(6.16)}$$

The capacitance between the high-potential electrode and the disk electrode (or ring

electrode) of the cell was of the order of 1 pF = 1 × 10^{-12} F, which is a very small capacitance. Since the impedance of the capacitor varies inversely with the angular frequency and the capacitance, measuring a very small capacitance with a low frequency represents the measurement of a very large impedance. For example, a 1 pF capacitor measured at f = 20 Hz would have an impedance of ~ 8 GΩ. The LCR meter could apply a signal level as high as 2 V_{rms}. The magnitude of the current (I) is related to the magnitude of the voltage and the impedance by

$$|I| = \frac{|V|}{|Z|}. \tag{6.17}$$

For a voltage of 2 V and an impedance of 8 GΩ, the current through the capacitor was 0.25 nA which was very difficult for the measuring instrument to detect and balance with great accuracy. For the low capacitances which had to be measured with the dielectric relaxation apparatus, inaccurate and imprecise data were obtained at frequencies below ~ 80 Hz due to the very small currents involved.

One other important aspect of the cell that had to be determined before dielectric measurements could be taken was the value of the area ratio of the ring electrode to the disk electrode (A_R/A_D). This ratio was necessary for calculating the dielectric constant from the capacitances of the disk and ring electrodes as was shown in equation (6.12). This ratio was determined by performing capacitance measurements of the cell loaded with an annular teflon spacer. The teflon spacers used had inner diameters of ~ 14 mm and outer diameters of ~ 20 mm, with flat, parallel faces. Considering the dimensions of the disk and ring electrodes, the annular teflon ring occupied the space between the

disk and ring electrodes so that both of the electrodes were completely exposed. This meant that the space between the high-potential electrode and the disk electrode, as well as the space between the high-potential electrode and the ring electrode were occupied by a vacuum (actually ~ 1 atm of helium with $\epsilon \sim 1.000068$ at T = 298 K,[318] practically a vacuum as far as the dielectric constant is concerned). The capacitance of the ring electrode under these circumstances was therefore

$$C_R = \frac{\epsilon_o A_R}{d}, \tag{6.18}$$

while the capacitance of the disk electrode was given by

$$C_D = \frac{\epsilon_o A_D}{d}. \tag{6.19}$$

Thus, measuring both the ring capacitance and the disk capacitance under these conditions and taking the ratio of the two values yielded

$$\frac{C_R}{C_D} = \frac{A_R}{A_D}, \tag{6.20}$$

which was the area ratio that needed to be determined.

Ring and disk capacitance measurements were made with each of three different annular teflon spacers which had thicknesses of 0.98 mm, 1.41 mm, and 1.82 mm (± 0.02 mm). The measurements were made at several different frequencies at temperatures from 78 K to ~ 280 K, and an area ratio value was calculated for each ring capacitance/disk capacitance measurement pair. The heating rates during these runs ranged from 0.5 to 1 $K \cdot min^{-1}$.

Plots of the area ratio results as a function of temperature at various frequencies for the 0.98 mm, 1.41 mm, and 1.82 mm thickness teflon spacers are provided in Figure 6.12, Figure 6.13, and Figure 6.14, respectively. In all of the capacitance measurements, several readings were taken (usually 10) at each frequency, and the results were averaged and a standard deviation about the average was obtained. Uncertainties in the area ratio values were calculated from the standard deviations in the ring and disk capacitances, and these uncertainties are presented in Figures 6.12, 6.13, and 6.14 in the form of error bars. If no error bar is shown, the uncertainty is equal to or less than the size of the symbol used to represent the data point.

It is apparent from these plots that the area ratio does not change significantly with temperature (the greatest deviation over the temperature range studied for a particular frequency is less than 1%) nor is there a great dependence on the measurement frequency. All of the area ratio values are between 2.240 and 2.268 with most of them being between 2.244 and 2.260, a variation of only 0.7%. Assigning the area ratio a value of 2.252 ± 0.008 encompasses almost all of the measured values within their experimental uncertainties. Therefore, it seemed reasonable to use this value for the area ratio in all measurements with this apparatus.

If the areas of the ring and disk electrodes are calculated from their room-temperature geometric dimensions as given in Section 6.3.1, and correcting each radius value by including the effect of one-half of the guard-gap width, effective area values of 274.3 ± 1.6 mm^2 and 124.7 ± 0.7 mm^2 are obtained for the ring and disk electrodes, respectively. The ratio of these two values is 2.200 ± 0.018 which differs from the

Figure 6.12. Area ratio (A_R/A_D) measurements as a function of temperature and measuring frequency using a 0.98 mm thickness annular teflon spacer. Experimental uncertainties are represented by error bars. If no error bar is shown, the uncertainty is equal to or less than the size of the symbol used to represent the data point. + 10 kHz, ○ 100 kHz, ▲ 500 kHz.

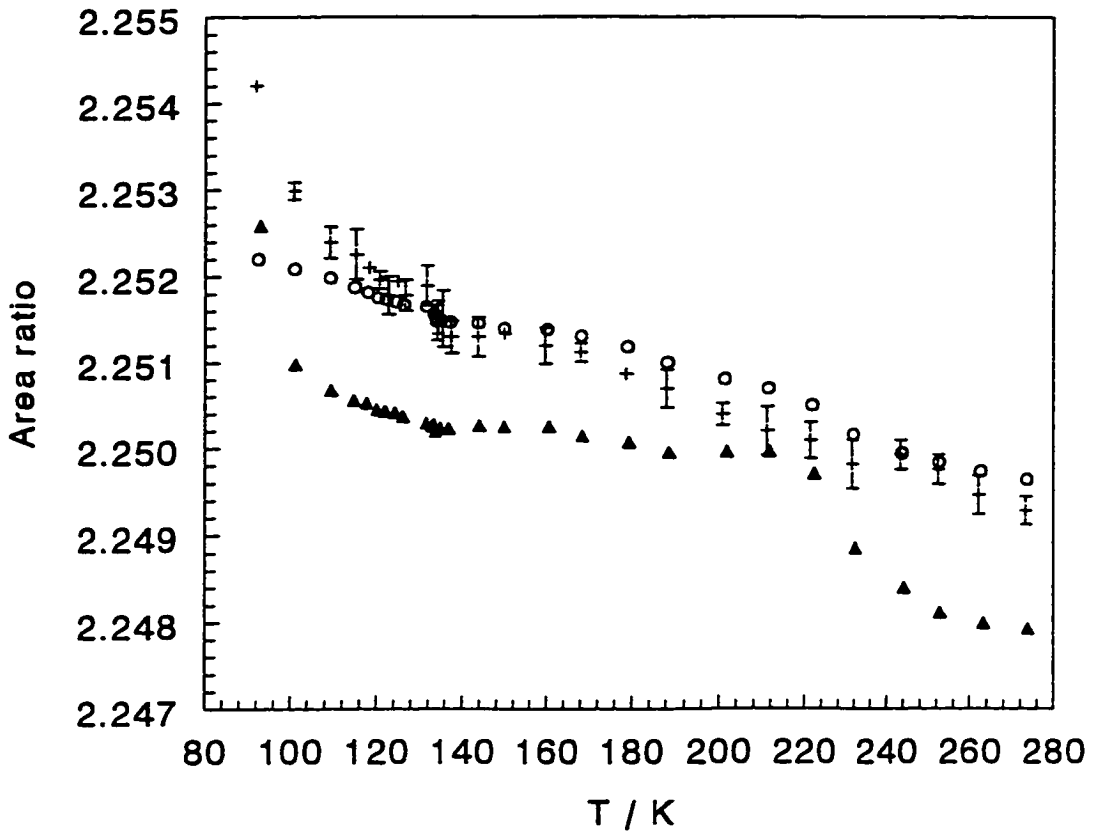

Figure 6.13. Area ratio (A_R/A_D) measurements as a function of temperature and measuring frequency using a 1.41 mm thickness annular teflon spacer. Experimental uncertainties are represented by error bars. If no error bar is shown, the uncertainty is equal to or less than the size of the symbol used to represent the data point. + 10 kHz, ○ 100 kHz, ● 300 kHz.

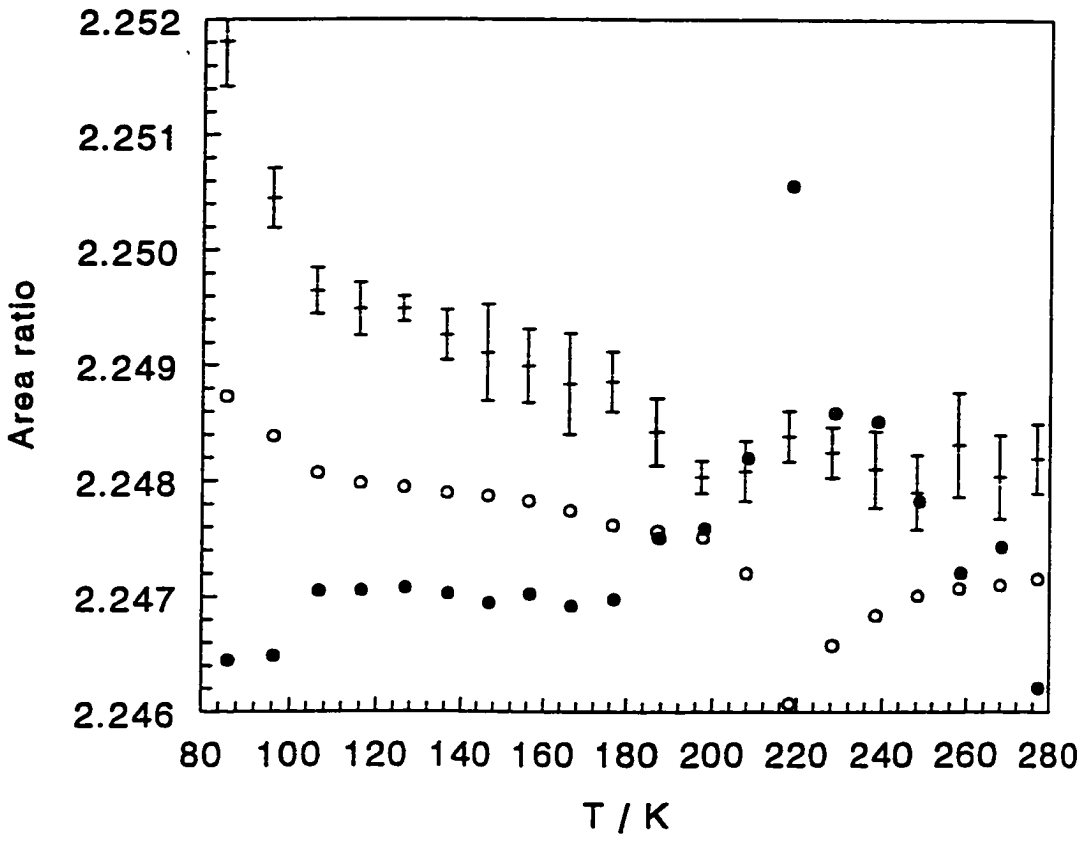

Figure 6.14. Area ratio (A_R/A_D) measurements as a function of temperature and measuring frequency using a 1.82 mm thickness annular teflon spacer. Experimental uncertainties are represented by error bars. If no error bar is shown, the uncertainty is equal to or less than the size of the symbol used to represent the data point. + 1 kHz, O 10 kHz, ▲ 100 kHz, ▽ 300 kHz.

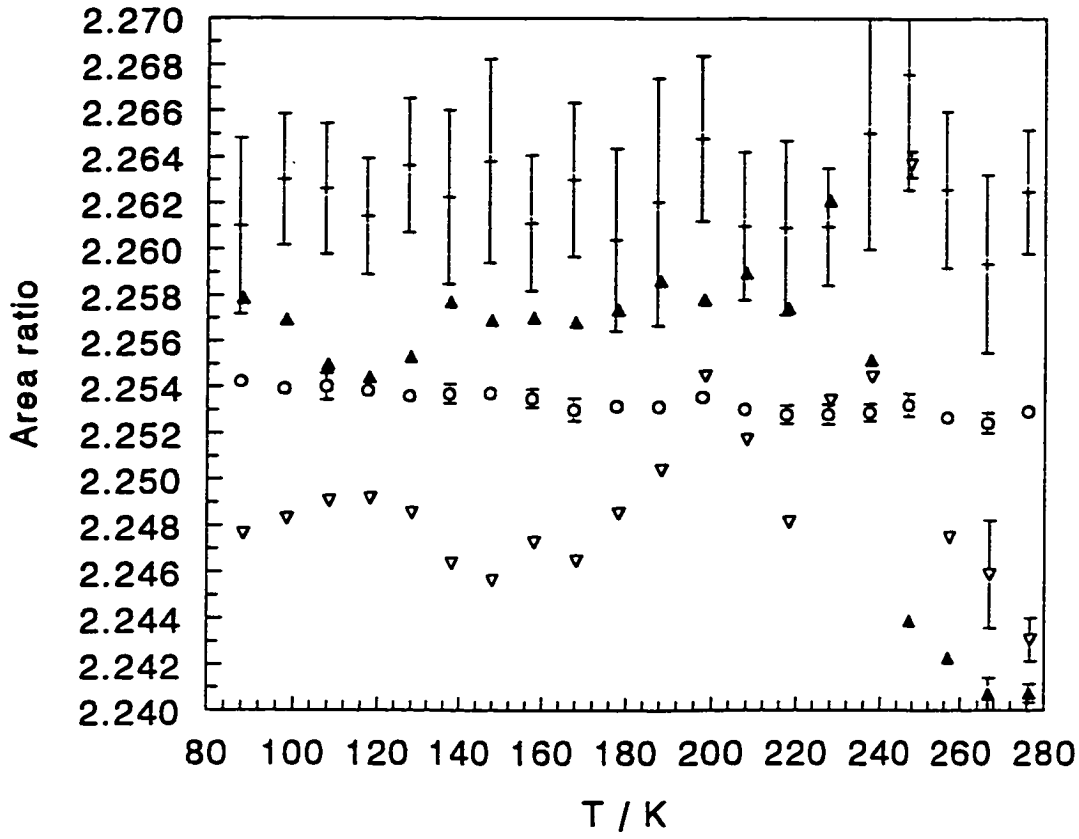

determined value of 2.252 by only 2.3%. Since the area ratio calculated geometrically is very close to that determined experimentally from capacitance measurements, it can be concluded that the guarding techniques employed in the sample cell for the capacitance measurements were successful in reducing fringing capacitance effects.

6.7 Teflon Measurements

Once the dielectric relaxation apparatus was calibrated, the next logical step was to test it with some sample for which the dielectric constant was known, to see how well the apparatus performed. An ideal substance to test would be one which does not have any unusual dielectric anomalies, whose dielectric constant is well-known in the literature, and also one that could be obtained in a machinable bulk form (*i.e.*, not a powder) in the proper dimensions for measurement.

Teflon met all of these requirements. It can be shaped to the necessary dimensions to be loaded into the sample cell and its dielectric constant is reported in the literature[319,320] to be 1.9 - 2.2. The only drawback with teflon was the difficulty in obtaining flat surfaces to maintain good contact with the electrodes. Despite this, however, a teflon disk was machined with a diameter of 17.06 $\pm$ 0.02 mm and a thickness of 1.41 $\pm$ 0.02 mm with reasonably flat surfaces. This disk was loaded into the cell and all the wiring was hooked up to take measurements. The system was evacuated and then cooled down with liquid nitrogen.

Several runs were done with the teflon disk covering various temperature ranges between ~ 80 K and 290 K. Some of the dielectric constant results obtained are shown in Figure 6.15, Figure 6.16, and Figure 6.17. Figure 6.15 shows some dielectric data for a measuring frequency of 1 kHz, while Figure 6.16 and Figure 6.17 give results for 10 kHz and 100 kHz, respectively. Error bars for each data point indicate the uncertainty in each value as calculated from the standard deviations of the capacitance measurements and the uncertainty in the ring/disk area ratio as discussed in the last section.

The dielectric data for teflon do show some scatter but overall the measurements indicate that the dielectric constant of teflon does not change appreciably (less than 2.5%) over the temperature range studied or with the frequency of measurements. Furthermore, the results are within the range given in the literature for the dielectric constant of teflon (1.9 - 2.2).[319,320] The slight scatter of the data could be attributed to the surface roughness of the faces of the teflon disk which would prevent ideal sample-electrode contact in the cell. From the results of the teflon measurements it was concluded that the dielectric relaxation apparatus gave reasonable results, and further testing could proceed.

Figure 6.15. Measured temperature dependence of the dielectric constant of the teflon disk at a frequency of 1 kHz. Error bars reflect the experimental uncertainty in each point.

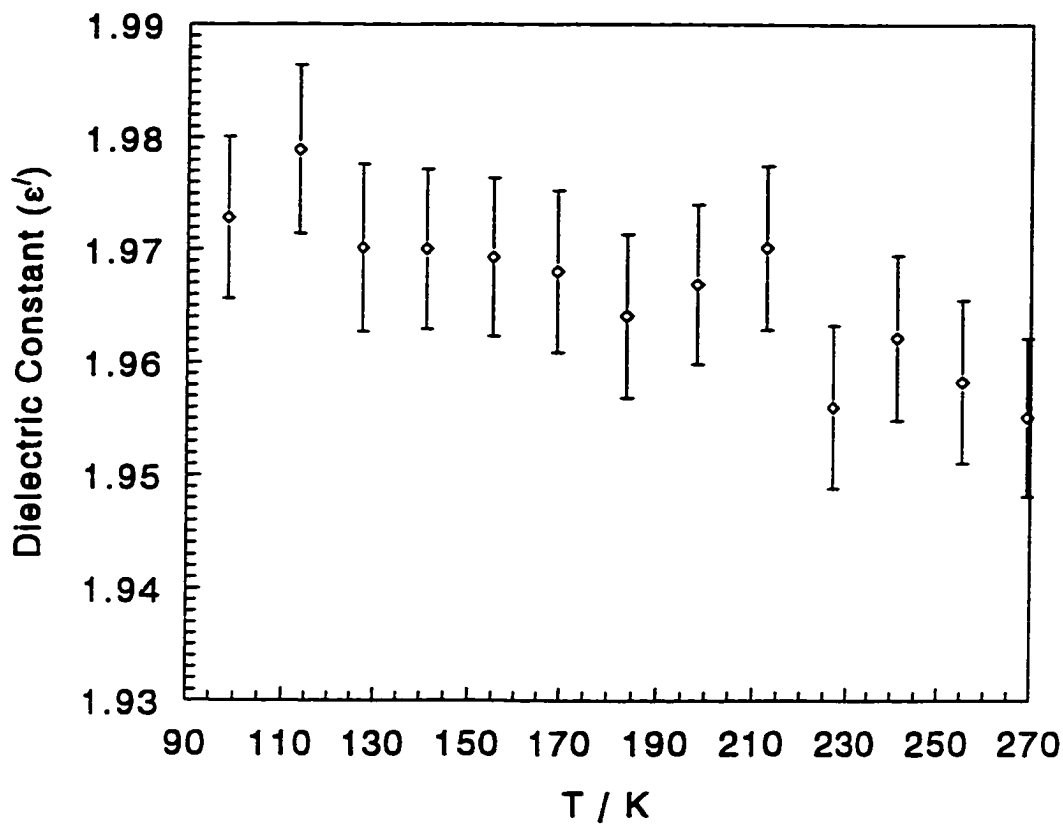

Figure 6.16. Measured temperature dependence of the dielectric constant of the teflon disk at a frequency of 10 kHz. Error bars reflect the experimental uncertainty in each point.

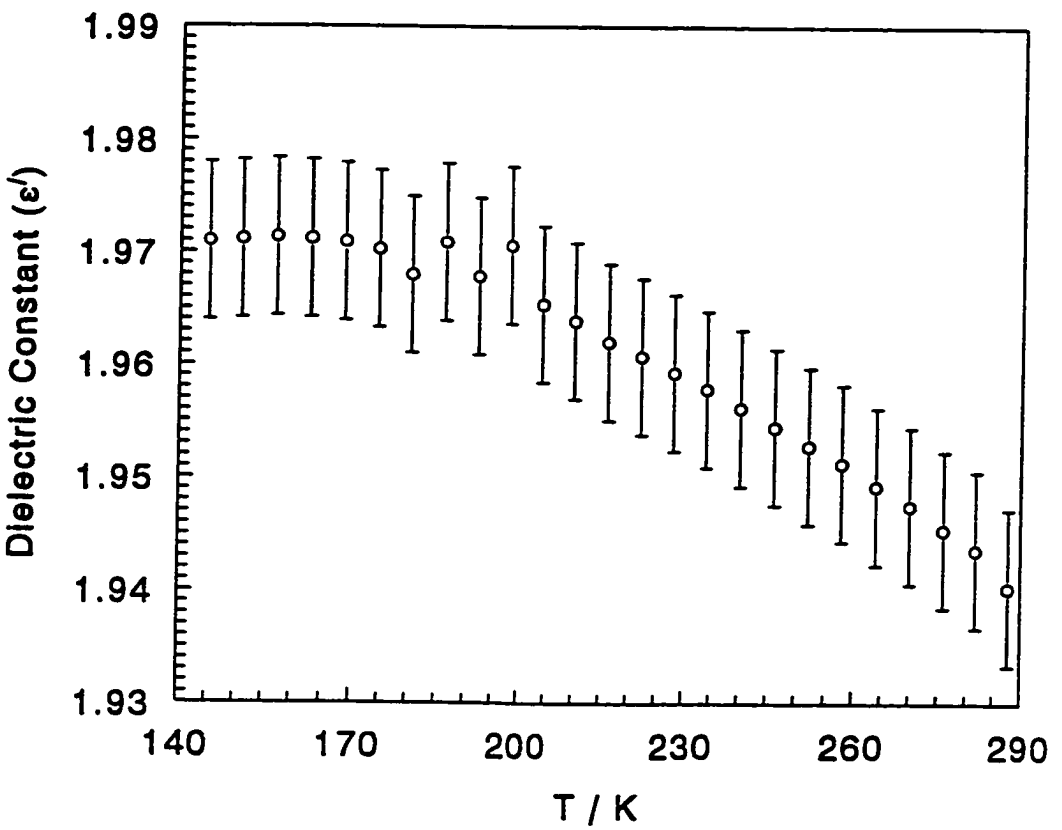

Figure 6.17. Measured temperature dependence of the dielectric constant of the teflon disk at a frequency of 100 kHz. Error bars reflect the experimental uncertainty in each point.

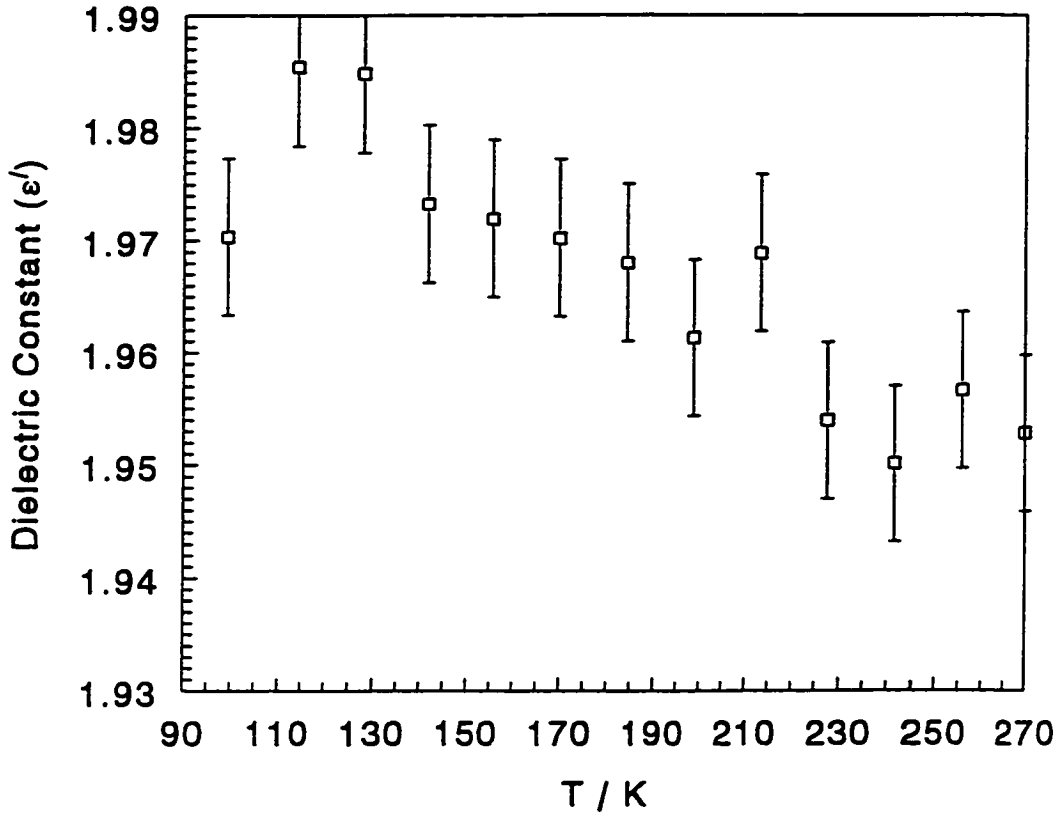

Chapter 7: Dielectric Measurements of Ionic Salts

7.1 Introduction

The main purpose for constructing the dielectric apparatus was to measure the dielectric properties of NaOH and NaOD. These compounds are very difficult to obtain in single-crystal form. It was because of this limitation that the dielectric apparatus was designed to perform measurements on powdered samples. The dielectric results for teflon obtained using the constructed apparatus were presented at the end of the previous chapter. These results showed that the dielectric relaxation apparatus gave data which agreed well with the literature value for teflon. The teflon sample, however, was in the form of a bulk solid. Furthermore, teflon is a not an ionic solid but an organic polymer. Since the ultimate goal of the apparatus was the measurement of powdered ionic samples (NaOH and NaOD), it was desirable to test the dielectric equipment by measuring some powdered ionic samples that have been well-studied and have well-known dielectric constants. Some very common ionic solids were chosen for this purpose.

The measurement of ionic powders presented some additional challenges which did not have to be considered in the teflon measurements. The sources of polarization which give rise to the observed dielectric constant of teflon are the electronic and atomic polarization mechanisms, which make constant contributions to the dielectric constant at frequencies below infrared frequencies. However, additional polarization mechanisms exist in ionic solids and these contribute to the measured dielectric constants at low

frequencies. Also, the low-frequency dielectric constant of powders is greatly affected by the presence of air-solid interfaces. Furthermore, since a powder is a heterogeneous system consisting of particles of the ionic solid mixed with air, a method had to be found which would enable the conversion of the measured dielectric constant of the powdered material to the dielectric constant of the bulk ionic solid. The next two sections look at all of these concerns in more detail.

Several compounds were chosen as representative examples of ionic solids which could be used to test the dielectric relaxation apparatus for accuracy in the measurement of the dielectric constants of powdered samples. These tests also allowed for a detailed examination of the factors which affect the low-frequency dielectric properties of powdered ionic solids. The ionic solids chosen for these tests were sodium chloride (NaCl), potassium chloride (KCl), potassium bromide (KBr), ammonium chloride (NH_4Cl), and ammonium bromide (NH_4Br). All of these substances have been extensively studied in the literature by dielectric measurements and the literature values of their dielectric constants are readily found in compilations of dielectric constants of solids.[321,322]

7.2 Sources of Electric Polarization in Powdered Ionic Salts

There are several mechanisms which contribute to the polarization of ionic solids.[217,323,324,325] One of these is the electronic polarization which is present in all

substances. As was mentioned in Section 4.3.2, the electronic polarization arises due to the displacement of the electrons relative to their parent nuclei under the influence of an applied electric field. The electronic contribution shows dielectric dispersion effects only at very high frequencies, usually in the ultraviolet or X-ray region,[217] and therefore, this contribution will always exist at the usual (much lower) frequencies for dielectric measurements.

A very important contribution to the dielectric constant, especially in the case of ionic solids, is the atomic contribution. This results from the displacement of nuclei with respect to one another in the presence of an electric field. The driving force for this is the redistribution of electronic charge which occurs when atoms of differing electronegativities combine to form compounds. It is the slight positive or negative character inherited by each atom in these polar compounds that interacts with the electric field and gives rise to the atomic polarization. This contribution does not occur in homonuclear substances such as diamond, and is present to a very small extent in nonpolar substances such as hydrocarbons.

An ionic solid can be looked upon as nearing one extreme in these atomic polarization effects, with the anion acquiring most of the valence-electron charge density from the cation. Thus, the atomic polarization mechanism is generally the principal contributor to the dielectric constant of ionic salts. It is for this reason that the atomic polarization is sometimes referred to as the ionic polarization.

The atomic polarization mechanism occurs on the timescale of molecular vibrations and therefore does not undergo dispersion until subjected to field frequencies

in the infrared region ($\sim 10^{12}$ Hz).[217] For the usual frequencies involved in dielectric measurements (especially the work in this thesis, where the electric field frequency was always $\leq$ 1 MHz) the atomic polarization maintains a mostly constant contribution to the dielectric properties of measured substances.

If the electronic and atomic mechanisms were the only contributions to the total polarization of simple ionic solids, their dielectric behaviour would be fairly constant as a function of frequency and temperature, as was observed for teflon at the end of the last chapter. However, ionic solids are not perfect insulators, and their electrical conductivity tends to increase with an increase in temperature.[326,327] The effects of this increasing conductivity greatly influence the dielectric properties of these substances at low frequencies.

In a perfect ionic solid, each lattice site would be occupied by a cation or an anion. Such a situation never occurs in nature as a true ionic solid contains defects.[326,328] These defects can be of several types. Those most relevant to this discussion are the point defects, in which only a single atom or lattice site is involved.

Two common point defects which occur in ionic solids are known as Schottky defects and Frenkel defects. A Schottky defect is a vacant cation site and a vacant anion site in the lattice, as shown in Figure 7.1(a) for NaCl. Each vacancy can be considered to have a charge. A cation vacancy has a charge of -1, since electroneutrality would be restored upon placement of a cation at that site. For a similar reason, an anion vacancy has a charge of +1. These vacancies can occur in the crystal at random, but they may also associate due to the Coulombic force of attraction between oppositely charged

Figure 7.1. Some point defects in ionic crystals. (a) Schottky defects in NaCl where a cation (Na^+) site and an anion (Cl^-) site are both vacant. (b) A Frenkel defect in AgCl where a Ag^+ ion leaves its lattice site to occupy an interstitial site.

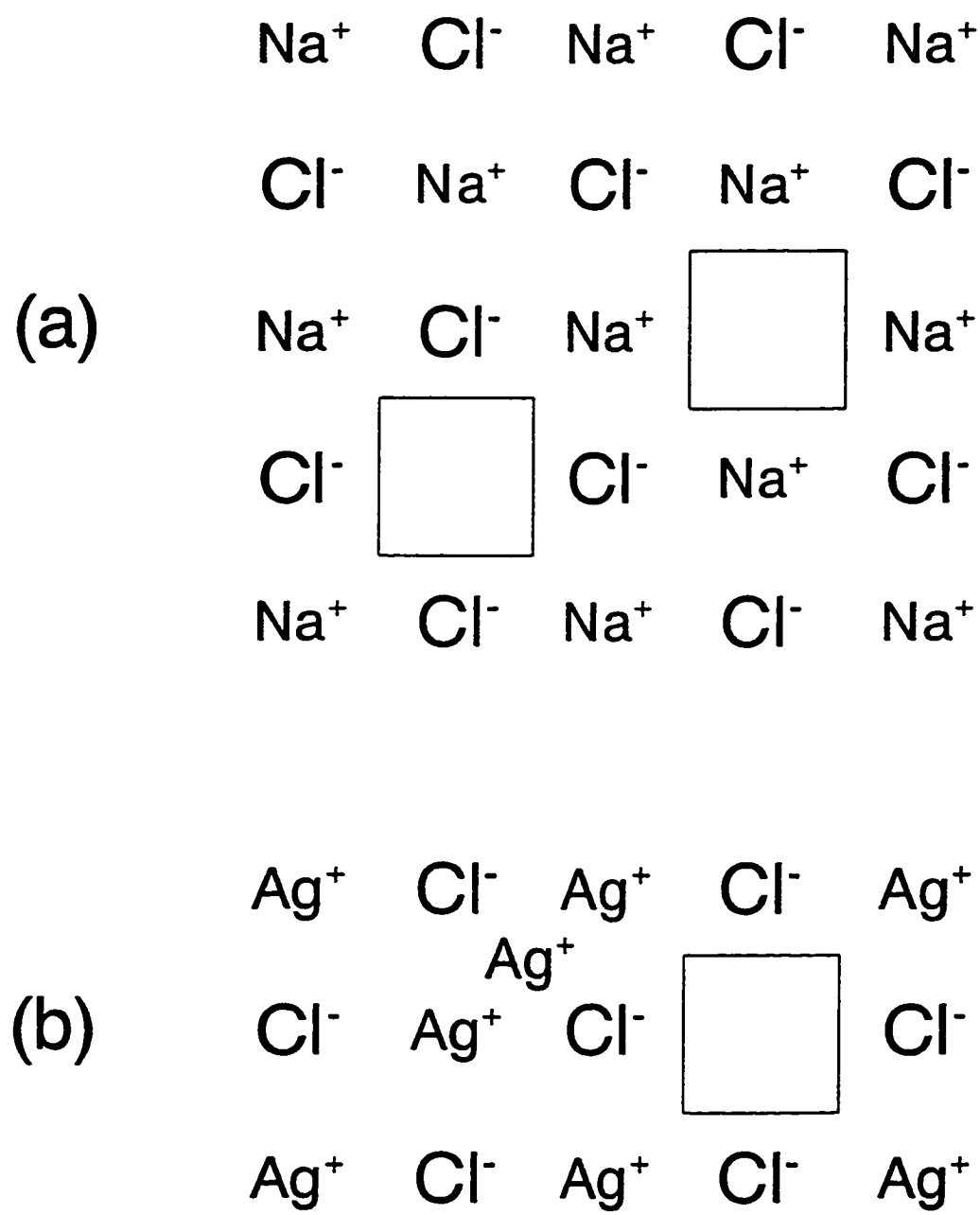

cation vacancies and anion vacancies to form cation-anion vacancy pairs. Schottky defects are prevalent among the alkali halides.

In a Frenkel defect, an ion in the crystal lattice is displaced off its lattice site into an interstitial site. An example of a substance which exhibits this type of point defect is AgCl as shown in Figure 7.1(b). The interstitial Ag^+ ion and the cation vacancy left behind are oppositely charged and may associate to form a pair. The number of Schottky defects and Frenkel defects in a particular lattice increases with an increase in temperature in an Arrhenius-type fashion.

These point defects in the lattice provide the major mechanism of electrical conductivity in many ionic solids.[326,327] For the example of NaCl with a cation vacancy in its lattice as shown in Figure 7.2, a neighbouring Na^+ ion can move into the vacancy leaving its own site vacant. Similarly, a sodium cation adjacent to this new vacancy can move out of its site to fill the void, leaving a vacancy behind, and so on. It is through this process that cation vacancies can move through the crystal lattice. Since a cation vacancy has a charge, this mechanism provides a means of charge transport through the crystal, and thus, electrical conductivity. The number of vacancies in the lattice increases with an increase in temperature, which means that the conductivity will show a similar temperature-dependent behaviour. Typically for an ionic solid such as NaCl, the number of thermally activated vacancies below room temperature is very small, and thus, the effects of the ionic conductivity are appreciable only at high temperatures. Anions are usually less mobile than cations due to the larger size of the anions, which means that cation vacancies are the main carriers of current in solids such as NaCl. Frenkel defects

Figure 7.2. The mechanism of electrical conductivity in NaCl. The cation vacancy has a charge of -1 and effectively moves throughout the lattice when other Na^+ ions occupy the void leaving a new vacancy behind.

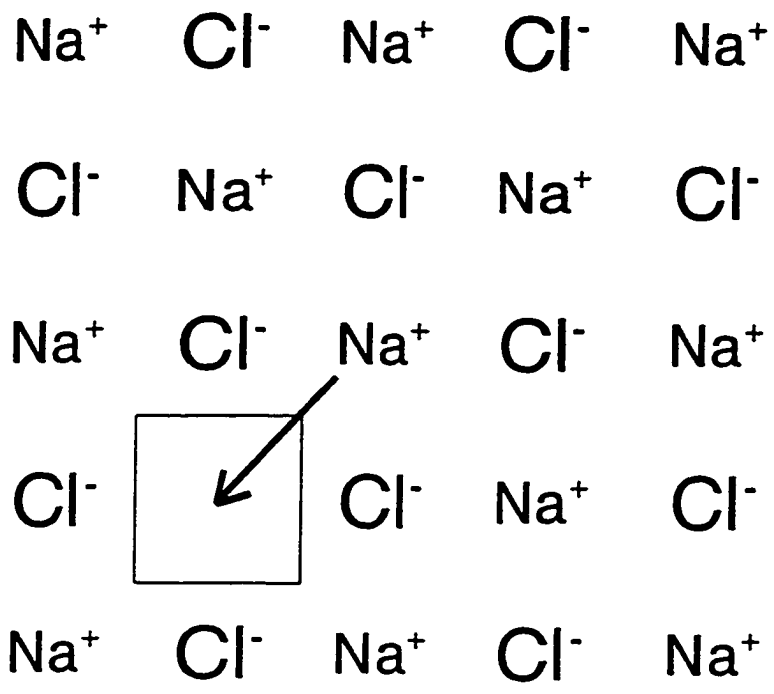

in ionic solids give rise to electrical conductivity by a similar mechanism.

Electrical conductivity in ionic solids at high temperatures will have a noticeable effect on the observed dielectric properties.[329] Conductivity (σ) and resistivity (ρ_R) are inversely related, so that a conductivity increase with an increase in temperature gives rise to a corresponding decrease in the resistance of the ionic dielectric. The dielectric loss is inversely related to the resistance of the dielectric[234] as shown by equation (6.7), which means that at high temperatures, the dielectric loss will exhibit a noticeable increase due to the electrical conductivity of the dielectric. Furthermore, equation (6.7) reveals that the dielectric loss is inversely related to the measuring frequency[234] which means that the conductivity effects will be especially important at low frequencies. High dielectric losses at high temperatures and low frequencies can mask dielectric dispersion effects due to the dipolar reorientation mechanism which may exist at these conditions.

The number of vacancies in an ionic solid can be increased by introducing a divalent impurity, such as Cd^{2+}, into a crystal lattice of monovalent ions.[326,327] When such a cation successfully occupies a lattice site in the crystal, a cation vacancy also must be created in order to maintain charge neutrality. Thus, the presence of the divalent impurity can cause a considerable enhancement of the electrical conductivity. Furthermore, the divalent cation and the cation vacancy tend to associate to form a close complex due to the electrostatic interaction between the excess positive charge of the impurity and the negative charge of the cation vacancy. This essentially forms a dipole which can reorient in an electric field through the "hopping" of an adjacent cation into the vacancy.[330,331] This changes the position of the vacancy site next to the divalent cation which redirects

the associated dipole.

Dielectric dispersion effects have been observed due to this dipole reorientation mechanism as studied by dielectric relaxation.[332,333,334,335,336] From an analysis of dielectric loss curves as a function of temperature, the activation energy for the process which relates to the kinetics of cation movement in the ionic solid can be obtained. The dielectric dispersion due to this form of dipole reorientation usually occurs at high temperatures and the associated dielectric loss curve is therefore superimposed on the loss due to electrical conductivity. Several studies of this type have been reported in the literature involving NaCl doped[331,332,333,334,336] with small amounts of either Mg^{2+}, Co^{2+}, Ni^{2+}, Sr^{2+}, Ca^{2+}, Mn^{2+}, Zn^{2+}, Cd^{2+}, Ba^{2+}, or Pb^{2+}; KCl doped[332,334,335,336] with Ca^{2+}, Sr^{2+}, Ba^{2+}, or Pb^{2+}; KBr doped[332,334,336] with Sr^{2+} or Ba^{2+}; and many other studies.[332,334,337] In most cases the dielectric dispersion results conformed very closely to the Debye curve with a single relaxation time. One study[338] claimed to have observed dielectric losses due to reorientation of the dipole due to an associated cation vacancy-anion vacancy complex in pure ionic crystals, but others were unable to reproduce these results.[333,339]

A powdered sample is a heterogeneous system consisting of solid granules of the substance to be measured mixed with air. The interfaces between the solid particles and the air can give rise to an interfacial polarization,[329,340,341,342] otherwise known as the Maxwell-Wagner effect.[343,344] Interfacial polarization arises due to the migration of charge carriers throughout the dielectric, which is different from the electronic, atomic, and dipolar polarizations. This effect occurs in any heterogeneous system when

the conductivity to dielectric constant ratio (σ/ϵ) differs for any two components making up the system. This is certainly true for the solid particles and the air which make up powdered systems.

Interfacial polarization occurs due to the accumulation of charge at the interfaces of two substances with different conductivities. The buildup of charge at the interfaces is transported to the electrode-dielectric interface through conduction currents in the heterogeneous phases of the dielectric, with positive charges migrating toward the negative electrode and negative charges moving toward the positive electrode. This type of polarization can result in very large dielectric constants being observed, as well as dielectric losses associated with the mechanism of the charge conduction process.

The mathematical treatment of the interfacial polarization mechanism can be examined through the study of a capacitor containing a two-layer dielectric as was originally done by Wagner.[344] In this treatment, the dielectric is considered to be made up of two parallel slabs each consisting of a different substance. A thorough mathematical analysis reveals that the dielectric constant and dielectric loss of this system will have frequency dependences that obey the Debye equations. There is one important difference, however. The dielectric loss from this mathematical analysis also contains an extra term for the effects due to the electrical conductivity,[341] *i.e.*,

$$\epsilon'' = \frac{1}{\omega C_o (R_1 + R_2)} + \frac{(\epsilon_o - \epsilon_\infty)\omega\tau}{1 + \omega^2\tau^2}, \qquad (7.1)$$

where R_1 and R_2 are the resistances of the two components of the dielectric (*cf.* equations (4.42) and (6.7)). The relaxation time in this case is related to the conductivities and

dielectric constants of the two components making up the heterogeneous dielectric. The relaxation time due to the interfacial polarization mechanism tends to be longer than for other polarization mechanisms and thus, interfacial dispersion usually is observed at very low frequencies. Dispersion due to the interfacial polarization can be distinguished from dispersion due to a dipolar reorientational mechanism only through observation of the effects of the electrical conductivity term in the dielectric loss. An ideal interfacial dielectric loss curve is provided in Figure 7.3. Measurement of only the dielectric constant will not distinguish between dipolar and interfacial polarization dispersions since they both exhibit the same Debye-type behaviour.

Thus, the measurement and analysis of the measured dielectric properties of ionic powders must involve consideration of the effects of ionic conductivity and interfacial polarization, which become evident at high temperatures and low frequencies. The high dielectric constants which can be observed due to interfacial polarization are considered to be spurious, since a true dielectric is an insulator, and the interfacial polarization is a result of the substance acting as a conductor. The true dielectric constant of a substance includes only those polarization mechanisms derived from charge distributions of atoms or molecules that are more or less fixed, and cannot migrate throughout the material. Dielectric constants that are reported for substances must exclude the effects of the interfacial polarization. It is perhaps a paradox, therefore, that the so-called static dielectric constants reported for ionic solids actually had to be measured at high frequencies, where the electrical conductivity and interfacial polarization are insignificant.

Figure 7.3. An ideal dielectric loss curve resulting from the interfacial polarization mechanism. The total interfacial dielectric loss is the sum of a Debye term and a conductivity term (see equation (7.1)).

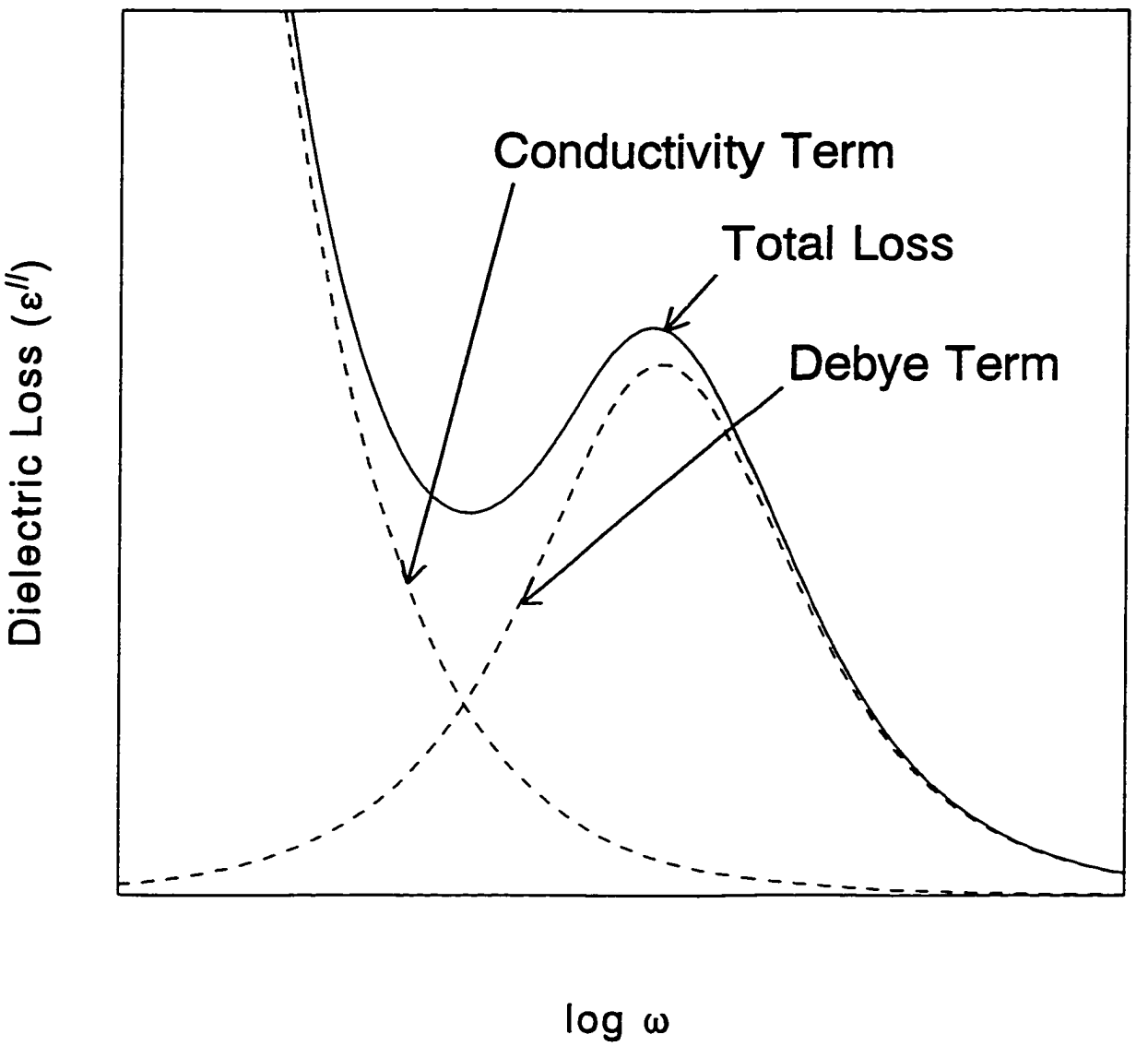

7.3 Converting Powder Dielectric Data to Bulk Values

A major consideration in the measurement of the dielectric properties of powdered samples involves the extraction of bulk dielectric data from the measured powder data. The measured dielectric constant of a powder contains contributions from the dielectric properties of the sample and from the air enclosed in the powder. The bulk dielectric properties of the solid making up the powdered sample are usually of interest, and thus, a method must be obtained for determining the bulk characteristics from measurements of the powder. Several reviews pertaining to this subject exist in the literature.[342,345,346,347,348]

The dielectric constant of a mixture of two components will depend not only on the bulk dielectric constants of the components making up the mixture (ϵ_1, ϵ_2), but also on the volume fractions of the components (δ_1, δ_2; $\delta_1 + \delta_2 = 1$), the shape of the particles in the mixture, and the polarization of the environment outside each individual particle. Polder and Van Santen[349] derived a general formula relating the dielectric constant of a mixture of ellipsoidal-shaped particles to ϵ_1, ϵ_2, δ_2, and the average dielectric constant of the medium surrounding a particle ($\overline{\epsilon}$). Most of the formulae that appear in the literature for the dielectric constant of mixtures can be derived from Polder and Van Santen's equation by making further assumptions about $\overline{\epsilon}$ and the shape of the particles.

There are two cases which are normally considered[342,348] for the value of $\overline{\epsilon}$. For a dilute mixture of component 2 in component 1 (small δ_2), it is reasonable to assume

that the mean dielectric constant surrounding each particle is equal to the dielectric constant of component 1, *i.e.*, $\bar{\epsilon} = \epsilon_1$. The other situation is to consider a mixture where component 2 is present in a greater amount, in which case the average dielectric constant surrounding each particle is set equal to the dielectric constant of the mixture (ϵ_m). Since the mixtures whose dielectric properties were measured in this thesis consisted of homogeneous solid particles mixed with air ($\epsilon_{air} = 1.00054 \sim 1$),[350] in most of the forthcoming discussion of dielectric mixture formulae, component 1 will be air and component 2 will be the solid. Thus ϵ_1 will be set equal to 1, ϵ_2 will be ϵ_s (the dielectric constant of the bulk solid), δ_2 will just be δ (the volume fraction of the solid in the powdered sample), and ϵ_m will be denoted ϵ_p, representing the dielectric constant of the powder.

The simplest particle shape to consider is a spherical particle. Assuming a dilute mixture of spherical particles ($\bar{\epsilon} = \epsilon_1 = 1$), the following equation can be derived from the equation of Polder and Van Santen:

$$\frac{\epsilon_p - 1}{\epsilon_p + 2} = \delta \frac{\epsilon_s - 1}{\epsilon_s + 2}. \qquad (7.2)$$

This formula was first derived by Rayleigh.[347,351] It also can be readily obtained from the Clausius-Mosotti relation (see Section 4.3.2).

If a mixture consisting of a higher concentration of spherical particles is assumed ($\bar{\epsilon} = \epsilon_p$), the following equation is obtained:

$$\frac{\epsilon_p - 1}{3\epsilon_p} = \delta \frac{\epsilon_s - 1}{2\epsilon_p + \epsilon_s}. \tag{7.3}$$

This equation was derived by Böttcher[346,352] and is known as Böttcher's formula. It has been found that for reasonably low values of the dielectric constant, the influence of the shape of the particles is only of minor significance,[349] so that Böttcher's formula can often be used in situations where the particles are not spherical. For large dielectric constants, however, Böttcher's formula is valid for spherical particles only. Another formula for spherical particles was derived by Bruggeman[346,353] starting from equation (7.2) to give

$$\frac{\epsilon_s - \epsilon_p}{\epsilon_s - 1} = (1 - \delta)\sqrt[3]{\epsilon_p}. \tag{7.4}$$

A fourth expression for a mixture of spherical particles was derived by Looyenga[354] who assumed that the mixture was composed of two types of spheres that themselves were heterogeneous mixtures of the two components. The equation that was obtained is

$$\epsilon_p = (1 + \delta(\sqrt[3]{\epsilon_s} - 1))^3. \tag{7.5}$$

Polder and Van Santen's equation also can be used to derive formulas which describe dielectric mixtures consisting of non-spherical particles. Particles which are shaped in the form of cylinders, rods, or needles can be considered to be prolate spheroids, which upon application of Polder and Van Santen's theory leads to an equation derived by Niesel,[342,355]

$$\frac{\epsilon_s - \epsilon_p}{\epsilon_s - 1} = (1 - \delta)\left[\frac{\epsilon_s + 5\epsilon_p}{\epsilon_s + 5}\right]^{2/5} . \qquad (7.6)$$

An equation for oblate spheroids, suitable for describing the dielectric constant of a mixture of lamellae, disks, or flakes was formulated by Bruggeman[353] and can be obtained from Polder and Van Santen's theory by assuming that $\overline{\epsilon} = \epsilon_p$ to give

$$\frac{\epsilon_s - \epsilon_p}{\epsilon_s - 1} = (1 - \delta)\left[\frac{2\epsilon_s + \epsilon_p}{2\epsilon_s + 1}\right] . \qquad (7.7)$$

The survey of formulae just presented does not by any means exhaust the offerings of equations for the dielectric constants of mixtures that have been reported in the literature over the last century. Many others exist, several of which involve the use of empirical parameters.[345,356,357,358]

There are several studies in the literature whereby the performances of the various mixture formulae have been evaluated.[347,359,360] Most of these studies involve one or more of the four equations describing a mixture of spherical particles, *i.e.*, Rayleigh's equation (equation (7.2)), Böttcher's formula (equation (7.3)), Bruggeman's equation (equation (7.4)), and Looyenga's equation (equation (7.5)). The dielectric constant of the bulk solid as calculated from these equations using the experimentally determined dielectric constant for the powder was compared to the literature bulk value of the dielectric constant. This was done for several powders, including NaCl, NH_4Cl, NH_4Br, KCl, LiF, KBr, and CaF_2 at various volume fractions (δ). The results of these comparisons indicated that Böttcher's formula and Looyenga's equation gave significantly

and consistently better results than Rayleigh's equation and Bruggeman's equation. Both Rayleigh's and Bruggeman's equations tended to give calculated bulk dielectric constants that were larger than the experimental values, with Rayleigh's equation being the worse of the two. Böttcher's formula and Looyenga's equation performed very well, with deviations between the calculated and experimental values being less than 5% in almost all cases.[347]

All of the mixture equations can be extended to include dielectric loss by replacing ϵ_s and ϵ_p in all of the equations by their complex equivalents,[345,360] *i.e.*,

$$\epsilon_s \rightarrow \epsilon_s' - j\epsilon_s'', \tag{7.8}$$

and

$$\epsilon_p \rightarrow \epsilon_p' - j\epsilon_p''. \tag{7.9}$$

Substituting (7.8) and (7.9) into any of the mixture formulae and solving for ϵ_s' and ϵ_s'' by equating real and imaginary parts of both sides of each equation will allow for the conversion of the measured dielectric constant and the dielectric loss of the powder to the corresponding values for the bulk solid. Applying this procedure to Böttcher's formula results in the following equations relating the dielectric properties of the bulk crystal to the measured dielectric properties of the powder:

$$\epsilon_s' = \frac{(2\epsilon_p' + 3\delta - 2)[(3\delta - 1)(\epsilon_p'^2 + \epsilon_p''^2) + \epsilon_p'] - 2\epsilon_p''^2}{(3\delta - 1)^2(\epsilon_p'^2 + \epsilon_p''^2) + 2\epsilon_p'(3\delta - 1) + 1}, \tag{7.10}$$

and

$$\epsilon_s'' = \frac{2(3\delta - 1)(\epsilon_p''^3 + \epsilon_p'^2\epsilon_p'') + \epsilon_p''(3\delta - 2) + 4\epsilon_p'\epsilon_p''}{(3\delta - 1)^2(\epsilon_p'^2 + \epsilon_p''^2) + 2\epsilon_p'(3\delta - 1) + 1}. \qquad (7.11)$$

The accuracy in the determination of the dielectric loss of the bulk solid by equation (7.11) using measured data from the powder has been found not to be very high when compared to literature values for the bulk loss (generally too low, within 10% - 30%).[360] This inaccuracy may not be entirely due to problems with the formula itself, but also with the difficulty in obtaining accurate and reproducible dielectric losses for bulk solids. On the other hand, calculating the dielectric constant from powder data and equation (7.10) was found to be much more accurate, usually within 5% of the literature values.[360]

The volume fraction of the solid particles in a powder dielectric sample (δ) can be determined from the following elementary analysis. In general, the volume fraction is given by

$$\delta = \frac{V_{solid}}{V_{powder}}, \qquad (7.12)$$

where V_{solid} is the volume occupied by the solid particles in the powder, and V_{powder} is the total volume of the powder. The volume fraction can also be written in terms of the densities (ρ) and masses (m) as follows:

$$\delta = \frac{\frac{m_{solid}}{\rho_{solid}}}{\frac{m_{solid} + m_{air}}{\rho_{powder}}} = \left[\frac{\rho_{powder}}{\rho_{solid}}\right]\left[\frac{m_{solid}}{m_{solid} + m_{air}}\right]. \qquad (7.13)$$

Since the mass of the air in the powder will be much less than the mass of the solid

particles making up the powder, it can be assumed that

$$m_{solid} + m_{air} \sim m_{solid}, \tag{7.14}$$

meaning that the second factor at the right-hand side of equation (7.13) is approximately equal to one. Under this assumption, the volume fraction will be given by

$$\delta = \frac{\rho_{powder}}{\rho_{solid}}. \tag{7.15}$$

Therefore, the volume fraction of the solid particles in the powder, which is required for the use of any of the mixture equations described in this section, can be simply determined by measuring the density of the powder in the sample pellet and dividing by the known density of the bulk solid.

It is evident from the discussion presented in this section, that there are numerous equations based on various models which can be used to convert the dielectric data obtained from the measurement of a powder sample to the dielectric properties characteristic of the bulk solid alone. The powdered samples that were studied in this research were alkali halides, ammonium halides, sodium hydroxide, and sodium deuteroxide. When these compounds were crushed to a powder, the particles were approximately spherical or lamellar in shape. Four equations have been presented here to describe a powder of spherical particles, with literature evaluations of their performances seeming to favour Böttcher's formula or Looyenga's equation. Due to the simple polynomial nature of Böttcher's equation, it is much simpler to decompose to obtain expressions for both the dielectric constant and the dielectric loss as shown by equations (7.10) and (7.11). A similar decomposition of Looyenga's equation would

require taking the cube root of complex numbers which is not so straightforward. Bruggeman's equation for lamellar particles (equation (7.7)) was also available if the particles in the powder could best be described by a lamellar model. In any case, the actual equation which should be used to convert the powder data obtained from measurements by the dielectric apparatus into data relevant for the bulk solid material could not be decided upon until the apparatus was tested by measuring powders made up of well-known ionic solids. Thus, the major purpose in measuring the dielectric properties of powdered NaCl, KCl, KBr, NH_4Cl, and NH_4Br using the newly-built dielectric equipment was to determine which model was the best to use to obtain reliable and accurate bulk dielectric properties from the measurement of the corresponding powders.

7.4 Sample Preparation and Procedure

All of the ionic solids measured were purchased from the Aldrich Chemical Company and were used without additional purification. A quantity of each of NaCl (listed as 99+% pure), KCl (99+% pure), KBr (99+% pure), NH_4Cl (99.99% pure), and NH_4Br (99+% pure) were ground and crushed with a mortar and pestle until a very fine powder was obtained. Pressed pellets of each of these solids were formed by loading some powder into a die and piston device and pressing the powder with a hydraulic press following the procedure described in Section 6.4. Each pellet was loaded, in turn, into

the dielectric sample cell in a helium atmosphere inside a glove bag. The sample cell was then suspended from the cryostat and all of the necessary wiring was connected. After attachment of the enclosure can, the system was evacuated to a pressure of ~ 10^{-5} Torr. The system was immersed in liquid nitrogen and cooled down to a temperature of ~ 80 K, at which time the automated software was started and the measurements began.

Dielectric measurements were performed on one pellet each of NaCl, KCl, KBr, and NH_4Br, with measurements being done on two separate pellets of NH_4Cl. Prior to loading into the dielectric cell, the mass of each sample was determined, and the thickness and diameter were measured with a vernier calliper for the purpose of calculating the density. The calculated density of the pressed powder sample could then be used in conjunction with the literature values of the densities to calculate the volume fraction (δ) of the ionic solid in the sample. A summary of this data for each measured pellet is provided in Table 7.1. The volume fractions were required in order to convert the measured dielectric properties for the powder into values representative of the corresponding bulk ionic solid using one of the models described in the last section. The final choice for the model used in the conversion from powder data to bulk data was based upon a comparison of the results obtained by applying each relevant equation from Section 7.3 to the measured powder data and evaluating the calculated values with respect to the known literature values[322] for the bulk solid, as will be fully described in the next section.

Table 7.1. (a) The masses, diameters, and thicknesses of all the NaCl, KCl, KBr, NH_4Br, and NH_4Cl pressed powder samples measured are listed. (b) These data were used to calculate the density of each sample which, when divided by the corresponding literature density values[361] (also listed), gave the volume fraction of the solid in each sample (see equation (7.15)).

(a)

Ionic Solid	Mass / g	Diameter / mm	Thickness / mm
NaCl	0.6338 ± 0.0002	19.08 ± 0.02	1.12 ± 0.02
KCl	0.5011 ± 0.0002	19.08 ± 0.02	1.02 ± 0.02
KBr	0.6706 ± 0.0002	19.08 ± 0.02	0.90 ± 0.02
NH_4Br	0.7383 ± 0.0002	19.08 ± 0.02	1.12 ± 0.02
NH_4Cl (1)	0.4616 ± 0.0002	19.08 ± 0.02	1.12 ± 0.02
NH_4Cl (2)	0.5065 ± 0.0002	19.08 ± 0.02	1.20 ± 0.02

(b)

Ionic Solid	Powder Density / $g \cdot cm^{-3}$	Literature Density / $g \cdot cm^{-3}$	Volume Fraction
NaCl	1.979 ± 0.035	2.165	0.914 ± 0.016
KCl	1.718 ± 0.034	1.984	0.866 ± 0.017
KBr	2.606 ± 0.058	2.75	0.948 ± 0.021
NH_4Br	2.306 ± 0.041	2.429	0.949 ± 0.017
NH_4Cl (1)	1.441 ± 0.026	1.527	0.944 ± 0.017
NH_4Cl (2)	1.476 ± 0.025	1.527	0.967 ± 0.016

7.5 Results and Discussion

7.5.1 Choosing a Conversion Formula

All of the runs for the ionic salts covered the temperature range from ~ 80 K to at least 300 K, with some reaching up to about 340 K. The heating rates used varied from 0.5 to 1.0 $K \cdot min^{-1}$, and dielectric measurements were taken for at least 8 frequencies in each case, ranging from 65 Hz to 800 kHz. At least three runs were done for each sample. An example of the raw powder data obtained is shown in Figure 7.4 which gives the dielectric constant for a pressed powder sample of NaCl as a function of temperature at several different frequencies.

At the lower frequencies, some slight scatter is evident in the data shown in Figure 7.4 which, as explained in Section 6.3.4, can be understood in terms of the very high impedances involved when using low measurement frequencies. From the lowest temperatures measured to $T \sim 240$ K, the dielectric constant of NaCl increases gradually with an increase in temperature and does not vary significantly with frequency. At higher temperatures, however, the dielectric constant increases sharply as the temperature rises and there is a noticeable variation in the dielectric behaviour at the different frequencies, with the lower frequencies giving higher dielectric constant values than the higher frequencies at a particular temperature. This behaviour is evidence of dielectric relaxation due to interfacial polarization in the powder sample. As explained in Section 7.2, this mechanism is partly due to the increased conductivity of NaCl at higher temperatures and

Figure 7.4. Measured dielectric constant data for the powder NaCl sample as a function of temperature for several frequencies. The lines are simply for guiding the eye. ○ 65 Hz, ✦ 80 Hz, ▲ 100 Hz, ● 200 Hz, ▽ 500 Hz, ◇ 1 kHz, □ 5 kHz, ▼ 10 kHz, ◆ 50 kHz, ■ 100 kHz, no symbol 250 kHz, + 500 kHz, △ 800 kHz.

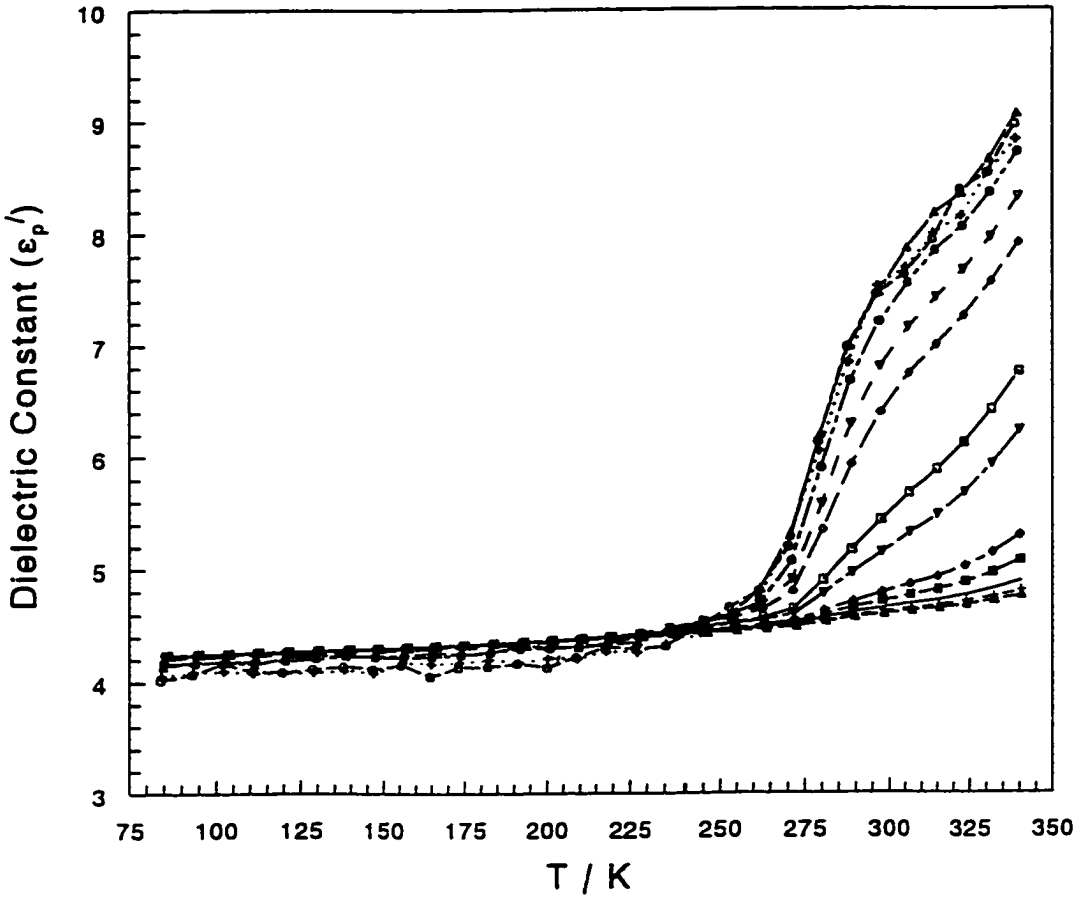

the heterogeneous nature of a powder sample.

Values of the dielectric constants reported for ionic crystals in literature compilations are typically obtained from single crystal data (bulk samples) and reported at room temperature.[321,322] The "true" dielectric constant must exclude the effects due to mechanisms associated with electrical conductivity in the sample. Thus, for comparison of the data obtained from the powder measurements made here with the results from the literature, the powder dielectric constant free from interfacial polarization at a temperature of 300 K had to be used. It is evident from the data presented in Figure 7.4 that the effects of interfacial polarization decrease with an increase in frequency at a given temperature. In fact, the data for the highest measuring frequency, 800 kHz, seem little affected at $T = 300$ K by interfacial polarization. It was necessary to decide which equation from Section 7.3 was best for converting the measured powder data to bulk dielectric data. To do this, it was decided to perform calculations using each appropriate equation from Section 7.3 to convert the measured 800 kHz powder values for each ionic salt, and assess the results from each model by comparison with the bulk literature values.

Since the particles in the powder samples could best be described as spheres or lamellae, the equations chosen to assess conversion from powder to bulk values were Böttcher's formula (equation (7.3)), Bruggeman's equation for spherical particles (equation (7.4)), Bruggeman's equation for oblate particles (equation (7.7)), and Looyenga's equation (equation (7.5)). Rayleigh's equation (equation (7.2)) was excluded from this analysis since it is theoretically appropriate only for dilute mixtures of particles

($\delta < 0.20$). The results of the calculations are shown in Table 7.2 which lists the experimentally obtained powder dielectric constant values for each ionic sample at 800 kHz and T = 300 K, the bulk results obtained from each conversion equation, and the bulk literature dielectric constant values for comparison.[322]

It is immediately apparent that the bulk dielectric values calculated for the ionic salts from measured powder data using the four conversion equations are all consistently lower than the corresponding literature values. This behaviour likely stems from several factors, including inadequacies in the models used to derive the conversion formulae, along with errors in the experimental method, such as imperfect sample-electrode contact.

It appears from the results in the table, that all four of the equations perform about equally well, although deviations from the literature values are as high as 14% in some cases. The results from Bruggeman's spherical formula and Looyenga's formula are slightly better than the other two equations, but the differences are not very significant. Furthermore, in the end, the chosen equation would have to also be used to correct the measured dielectric loss values for the powder. This would be done by applying the procedure described in Section 7.3, whereby the dielectric constants in a particular correction formula are replaced by their complex equivalents and a correction equation for the dielectric constant and dielectric loss are obtained by equating real and imaginary parts. The results of this procedure for Böttcher's formula were given in equations (7.10) and (7.11).

If this procedure were applied to Bruggeman's spherical formula or Looyenga's

Table 7.2. Conversion of the powder dielectric constants for the ionic solids to bulk values using Böttcher's formula, Bruggeman's equation for spherical particles, Bruggeman's equation for oblate particles, and Looyenga's equation. For each solid, the powder value measured at room temperature (300 K) and 800 kHz is given, along with the results from each conversion equation, and the room-temperature bulk literature values for comparison.[322]

Ionic Solid	Powder Value	Böttcher	Bruggeman (spherical)	Bruggeman (oblate)	Looyenga	Lit. Value
NaCl	4.60	5.07	5.20	5.06	5.14	5.9
KCl	3.64	4.20	4.32	4.18	4.26	4.86
KBr	4.24	4.48	4.53	4.48	4.51	4.88
NH_4Br	5.91	6.28	6.41	6.28	6.35	7.1
NH_4Cl	6.19	6.43	6.52	6.43	6.48	6.9

formula, it is evident from the nature of these equations that one would have to take the cube root of the complex dielectric constant. The cube root of a complex number can be obtained readily using De Moivre's theorem.[362] However, every complex number has three complex cube roots, meaning that three different equations would be obtained for converting the dielectric constant and for converting the dielectric loss. This would result in ambiguity that would be difficult, if not impossible, to reconcile satisfactorily.

Because of the ambiguity associated with Bruggeman's spherical formula and Looyenga's equation, it was decided to use Böttcher's formula to convert the powder dielectric data obtained using the dielectric relaxation apparatus to bulk dielectric values, since Böttcher's formula seems to perform a bit better than Bruggeman's equation for oblate particles. The equations from Böttcher's formula which could be used to correct dielectric constant and loss values were given in equations (7.10) and (7.11), respectively. From the results in Table 7.2, the deviations of Böttcher's formula from the literature values range from 6.8% for NH_4Cl to 14.1% for NaCl. All of the powder dielectric data measured using the constructed dielectric relaxation apparatus were converted to bulk values using equations (7.10) and (7.11).

7.5.2 Results and Error Analysis

The dielectric constant results for NaCl obtained after conversion by Böttcher's formula using equation (7.10) are shown in Figure 7.5. It is evident from this plot that

Figure 7.5. Dielectric constant of NaCl as a function of temperature at several frequencies obtained by converting the measured powder data to bulk data using Böttcher's formula. The lines are merely a guide to the eye. ○ 65 Hz, + 80 Hz, ▲ 100 Hz, ● 200 Hz, ▽ 500 Hz, ◇ 1 kHz, □ 5 kHz, ▼ 10 kHz, ◆ 50 kHz, ■ 100 kHz, no symbol 250 kHz, + 500 kHz, △ 800 kHz.

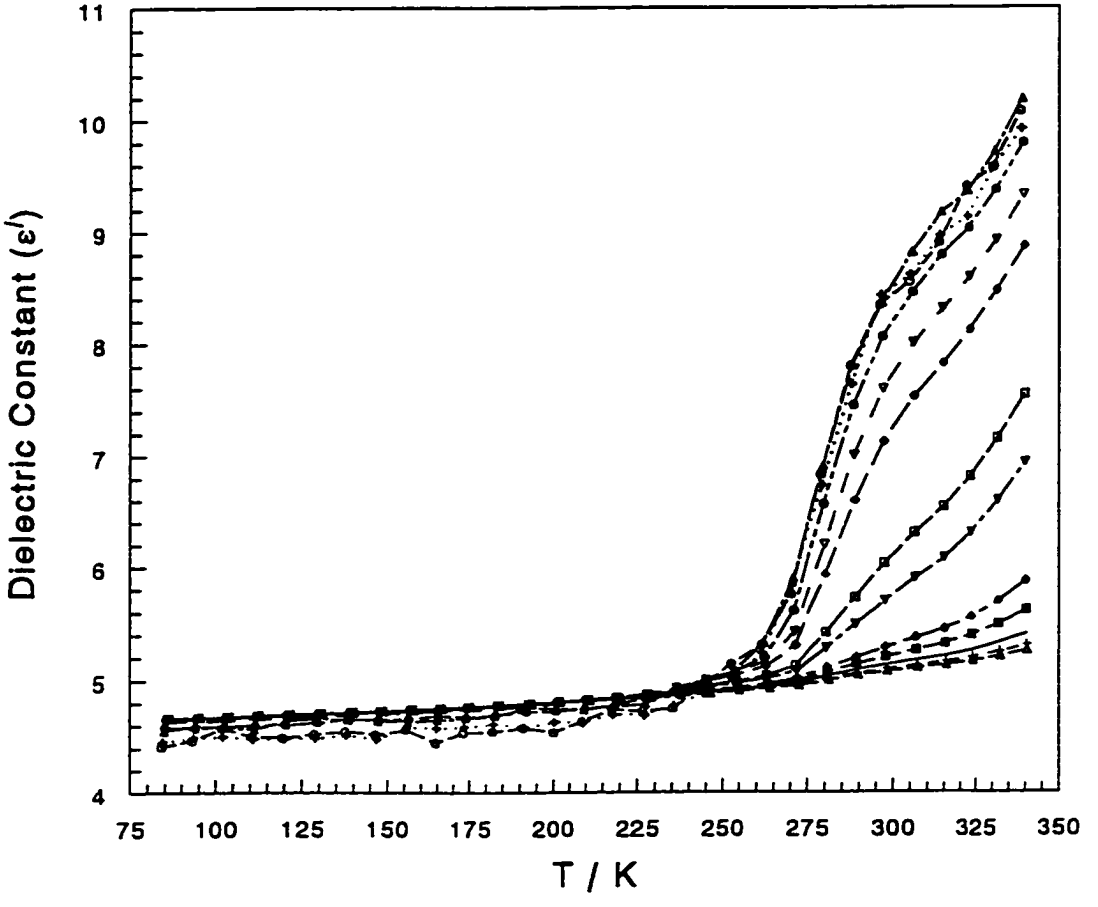

while Böttcher's formula (and all of the other conversion equations) provides a means for extracting bulk dielectric data from measurements of the heterogeneous powder system, there is nothing built into the models upon which the conversion formulae are derived to account for electrical conductivity of the sample or the effects of interfacial polarization in powders. Thus, the high dielectric constant values due to these effects at high temperatures are still present in the converted data shown in Figure 7.5.

The measured dielectric loss data for NaCl corrected by Böttcher's formula using equation (7.11) are shown in Figure 7.6. These data can be readily correlated to the dielectric constant data in Figure 7.5. At low temperatures, the dielectric loss is close to zero at most frequencies as would be expected for a well-behaved insulating dielectric substance in the absence of any dielectric relaxation. At very low frequencies the dielectric loss deviates negatively from zero at low temperatures which is likely attributable to the difficulty the LCR meter has in measuring the loss at such a high impedance. Above $T \sim 230$ K, the dielectric loss climbs to high values in a frequency- and temperature-dependent manner that is characteristic of the relaxation of some mechanism of polarization. This loss can be correlated to the dielectric constant curves shown in Figure 7.5 as arising due to the relaxation of interfacial polarization in the NaCl powder sample at high temperatures.

When capacitance and dissipation factor measurements were taken by the dielectric relaxation apparatus to determine the dielectric constant and dielectric loss of the sample at a particular temperature and frequency, each measurement was taken several times (usually ten times) with the results being averaged and a standard deviation

Figure 7.6. Dielectric loss of NaCl as a function of temperature at several frequencies obtained by converting the measured powder data to bulk data using Böttcher's formula. The lines are simple for guiding the eye. ○ 65 Hz, + 80 Hz, ▲ 100 Hz, ● 200 Hz, ▽ 500 Hz, ◇ 1 kHz, □ 5 kHz, ▼ 10 kHz, ◆ 50 kHz, ■ 100 kHz, no symbol 250 kHz, + 500 kHz, △ 800 kHz.

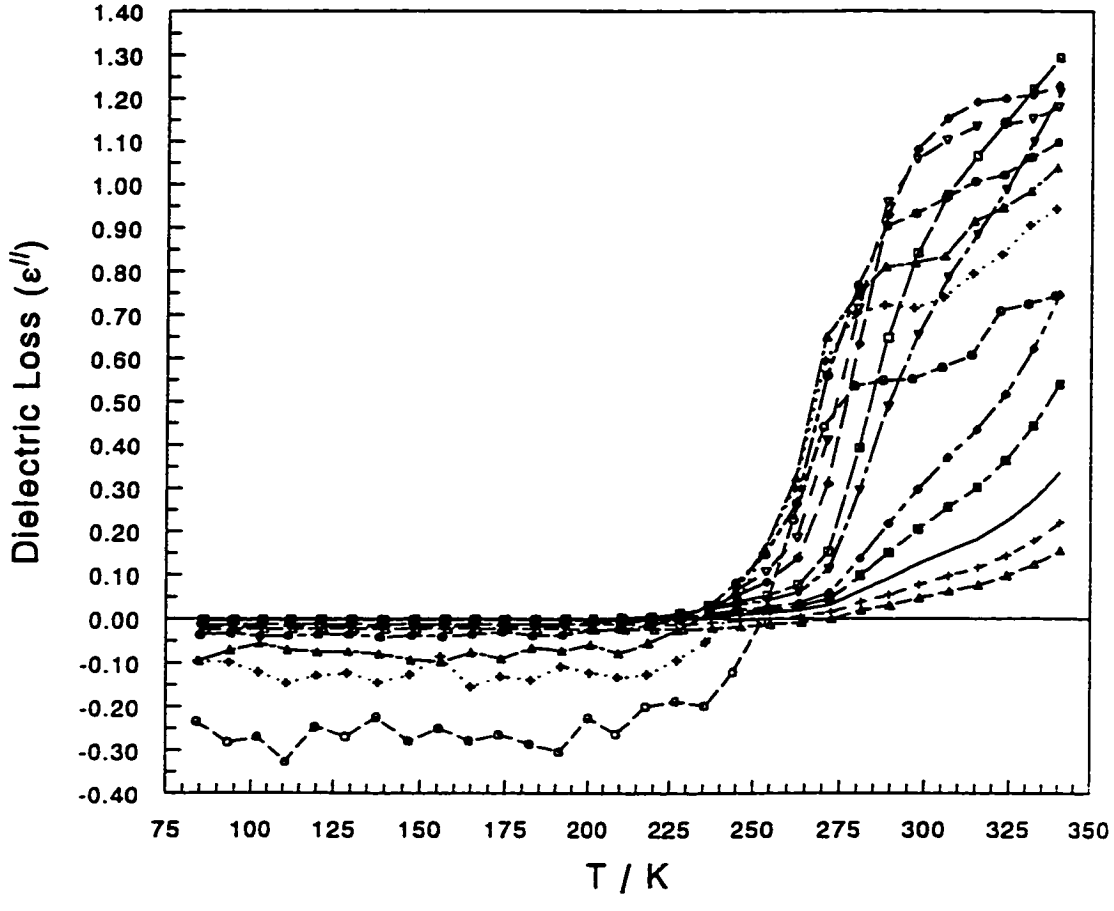

about the average being calculated. This was done in order to obtain a measure of the reproducibility of the capacitance and dissipation measurements taken by the LCR meter under a particular set of conditions. These uncertainties, along with the uncertainty in the area ratio of the ring electrode to the disk electrode as determined in Section 6.6, were propagated throughout the calculation of the dielectric constant and dielectric loss of the powder. Furthermore, in converting these powder values to bulk values using equations (7.10) and (7.11), the uncertainties in the measured powder dielectric constant and loss along with the uncertainty in the volume fraction of solid in the sample (Table 7.1(b)) were fully propagated throughout the calculations. The resulting uncertainties in the final dielectric constant and loss values are shown for the NaCl measurements for a few frequencies in Figure 7.7 and Figure 7.8, respectively. Where no error bar is shown, the uncertainty is equal to or less than the size of the symbol used to represent the data point.

Evidence for interfacial polarization relaxation at higher temperatures is also evident in the dielectric constant and dielectric loss curves obtained for KCl, which are shown in Figures 7.9 and 7.10, respectively. The KCl measurements were not carried out to as high a temperature as the NaCl measurements, but it is clear that the onset of interfacial relaxation in KCl occurs at a higher temperature than for NaCl, reflecting the different properties (especially electrical conductivities) of the two solids.

No interfacial polarization effects in the form of large dielectric constants and losses were observed for KBr, NH_4Br, and NH_4Cl over the temperature range and frequencies employed for the measurements. This perhaps reflects the difficulty for the cations in these compounds to hop into vacancies in the crystal lattice to provide a

Figure 7.7. Dielectric constant curves for NaCl as a function of temperature for four frequencies showing the experimental uncertainty (± 1 standard deviation) in the calculated bulk data using error bars. The lines are for guiding the eye. + 100 Hz, ○ 1 kHz, ▲ 10 kHz, ▽ 100 kHz.

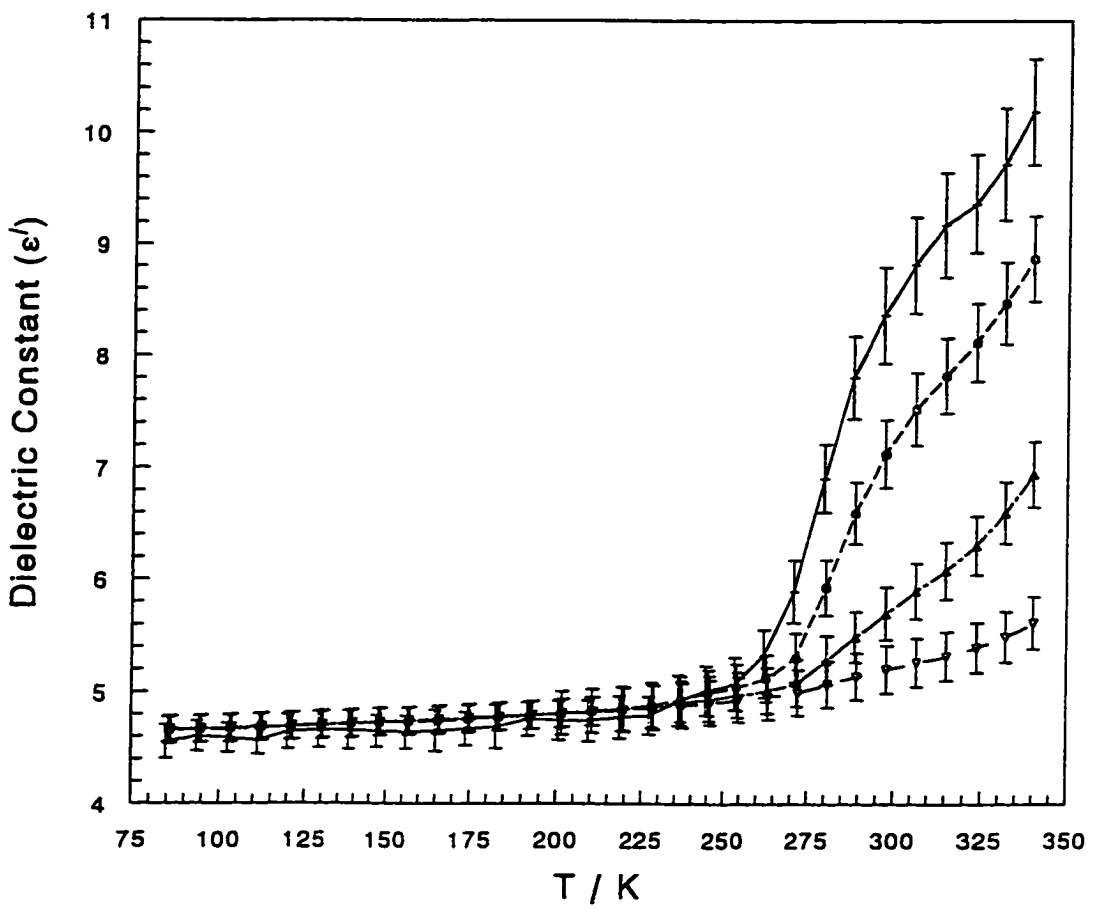

Figure 7.8. Dielectric loss curves for NaCl as a function of temperature for four frequencies showing the experimental uncertainty in the calculated bulk data using error bars. Where no error bar is shown, the uncertainty is equal to or less than the size of the symbol used to represent the data point. The lines are guides for the eye. + 100 Hz, O 1 kHz, ▲ 10 kHz, ▽ 100 kHz.

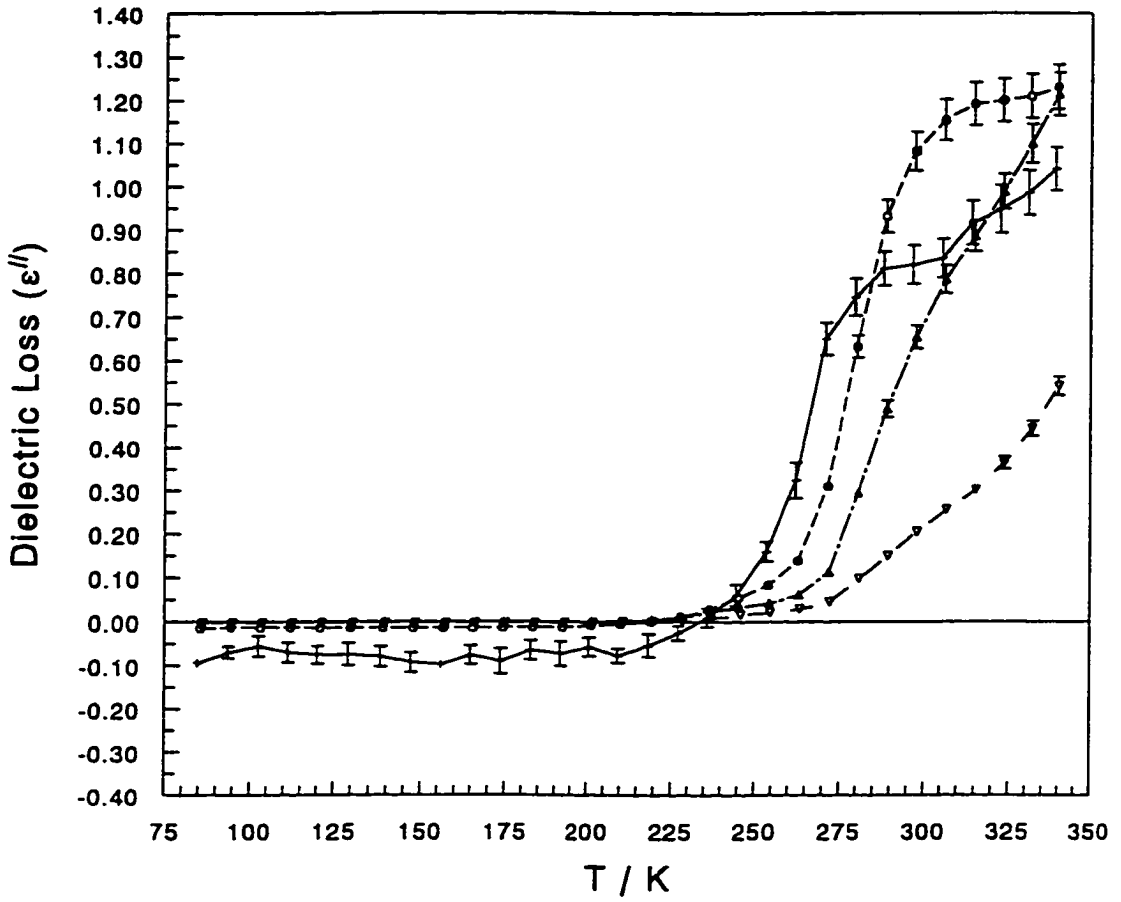

Figure 7.9. Dielectric constant curves for KCl as a function of temperature for several frequencies. The data plotted are bulk data obtained by converting the measured powder data using Böttcher's formula. The lines are for guiding the eye. ▵ 70 Hz, ○ 80 Hz, + 100 Hz, ▲ 200 Hz, ● 1 kHz, ▿ 10 kHz, ◇ 100 kHz, □ 250 kHz, ▼ 800 kHz.

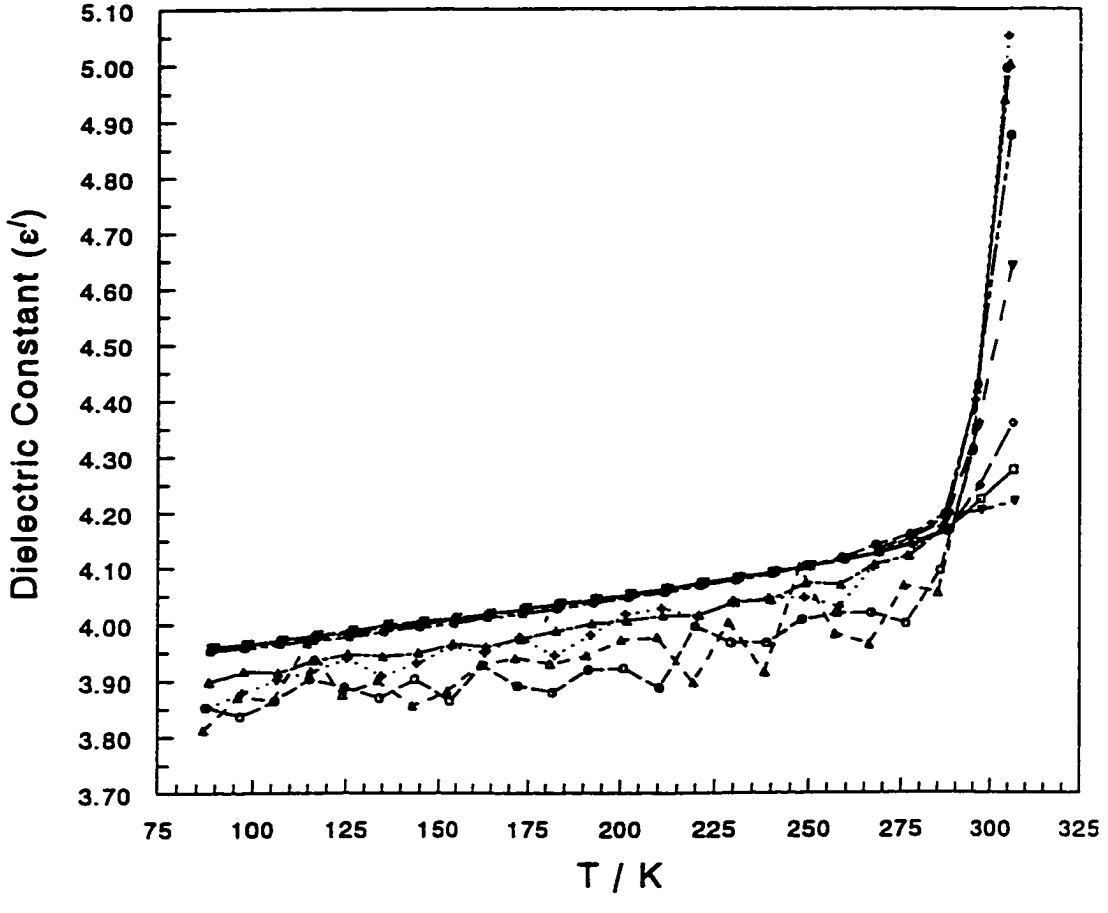

Figure 7.10. Dielectric loss curves for KCl as a function of temperature for several frequencies. The data plotted are bulk data converted from the measured powder data using Böttcher's formula. The lines are for guiding the eye. ▲ 200 Hz, ● 1 kHz, ▿ 10 kHz, ◇ 100 kHz, □ 250 kHz, ▼ 800 kHz.

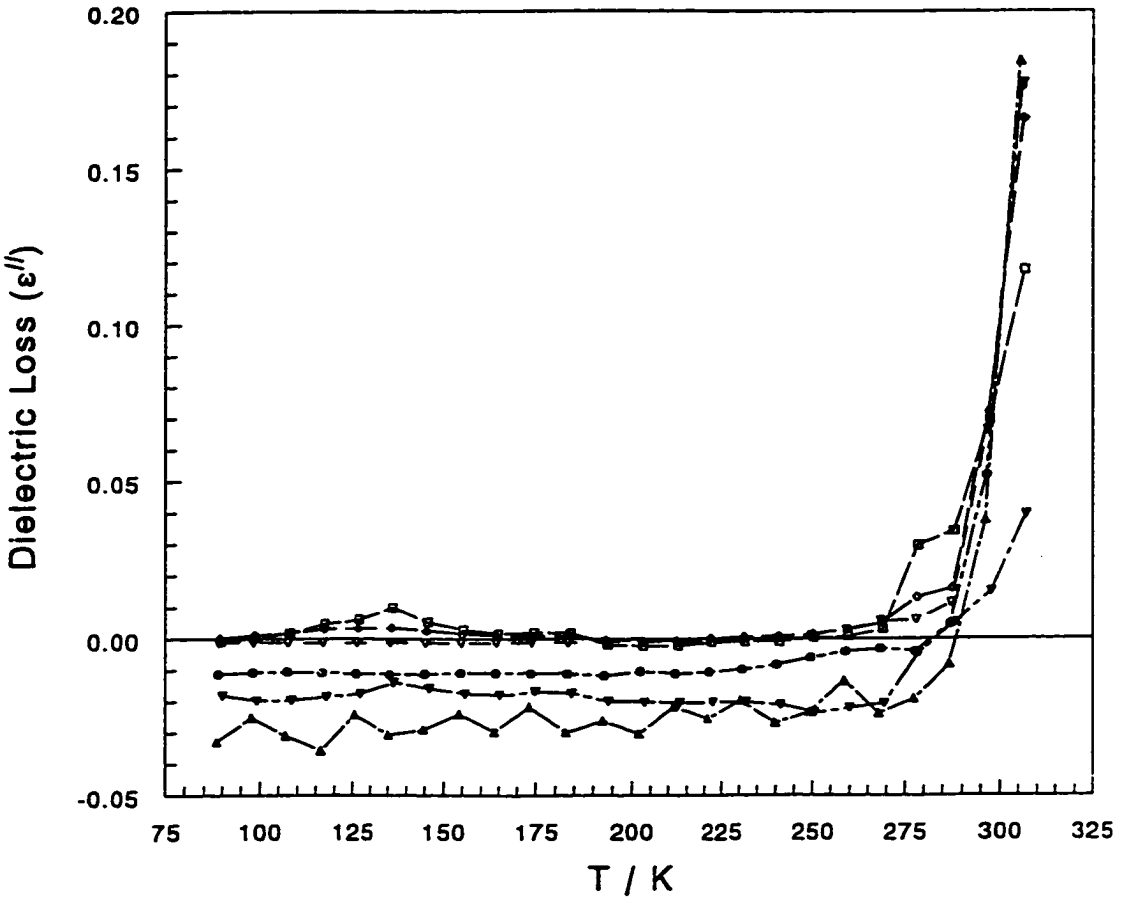

mechanism for electrical conduction. The measured dielectric constant curves for these three compounds were coincident for all frequencies studied within the experimental uncertainty, and no appreciable dielectric losses were observed at any of the temperatures or frequencies studied. The measured dielectric constant results (corrected using Böttcher's formula) for KBr, NH_4Br, and NH_4Cl are presented as a function of temperature for a single frequency in Figures 7.11, 7.12, and 7.13, respectively. Error bars in these figures reflect the determined experimental uncertainty for a particular data point.

While the measured dielectric constant curve for KBr shows no anomalous features, there are definite anomalies in the dielectric constant curves for NH_4Br and NH_4Cl. The anomaly in the NH_4Br curve begins at about 225 K and continues to 270 K while the anomaly in the NH_4Cl curve ranges from 245 K to 300 K. These anomalies are characteristic of the occurrence of phase transitions in these compounds, and in fact, such transitions are well-known in the literature.[38,363,364] At T = 235 K, NH_4Br undergoes a phase transition from a low-temperature tetragonal phase to a high-temperature cubic phase,[364] and at T = 243 K, NH_4Cl exhibits an order-disorder transition between two different cubic phases.[364] In fact, this phase transition in NH_4Cl is one of the most extensively studied of all order-disorder phase transformations. In the low temperature phase of NH_4Cl, the NH_4^+ ions are orientationally ordered in the cubic lattice, but above the transition temperature the ammonium ions are disordered between two possible orientations with respect to a cubic lattice of Cl^- ions. These phase transitions give rise to the observed steps in the measured dielectric constant curves for NH_4Br and NH_4Cl.

Figure 7.11. Dielectric constant data for KBr as a function of temperature at a frequency of 1 kHz. The data shown are bulk data obtained by converting the measured powder data using Böttcher's formula. Error bars reflect the experimental uncertainty for each data point. The literature value[322] of the dielectric constant of KBr at room temperature is 4.88.

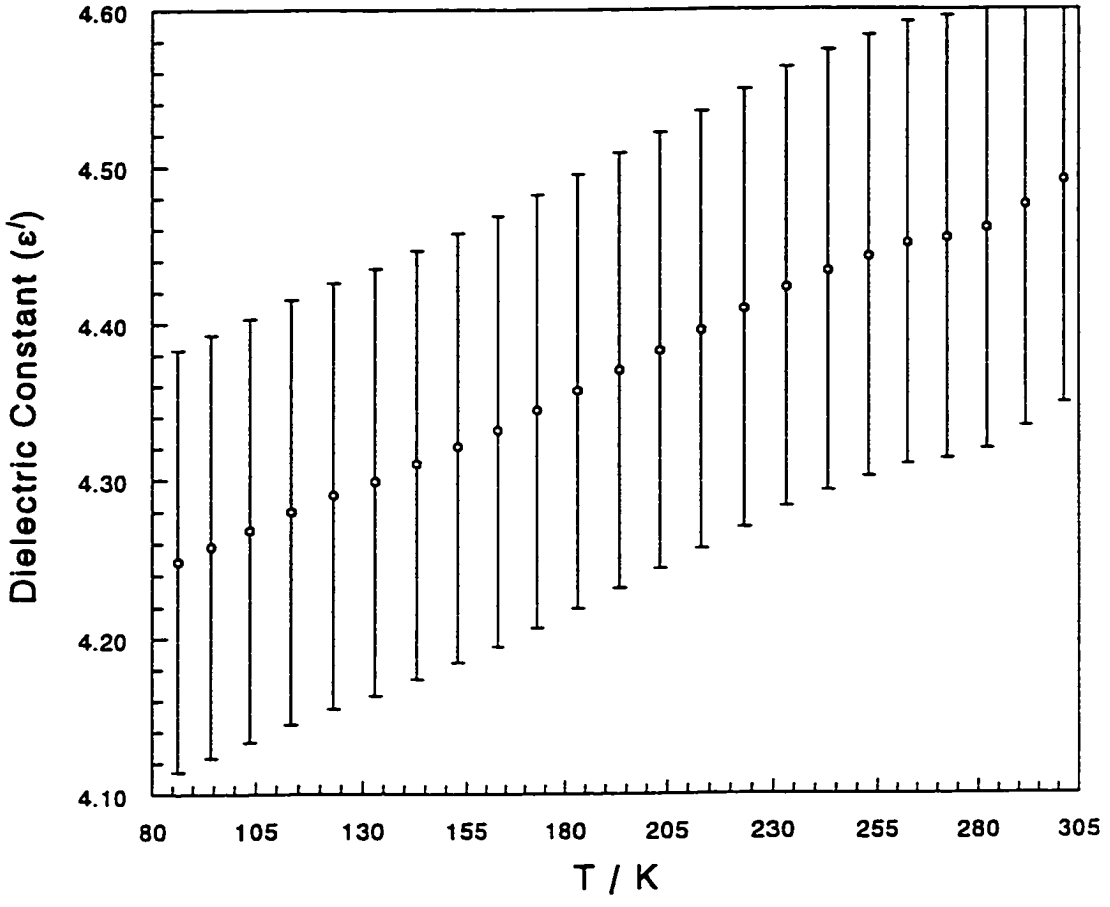

Figure 7.12. Dielectric constant data for NH_4Br as a function of temperature at a frequency of 10 kHz. The data shown are bulk data obtained by converting the measured powder data using Böttcher's formula. Error bars reflect the experimental uncertainty for each data point. The literature value[322] of the dielectric constant of NH_4Br at room temperature is 7.1.

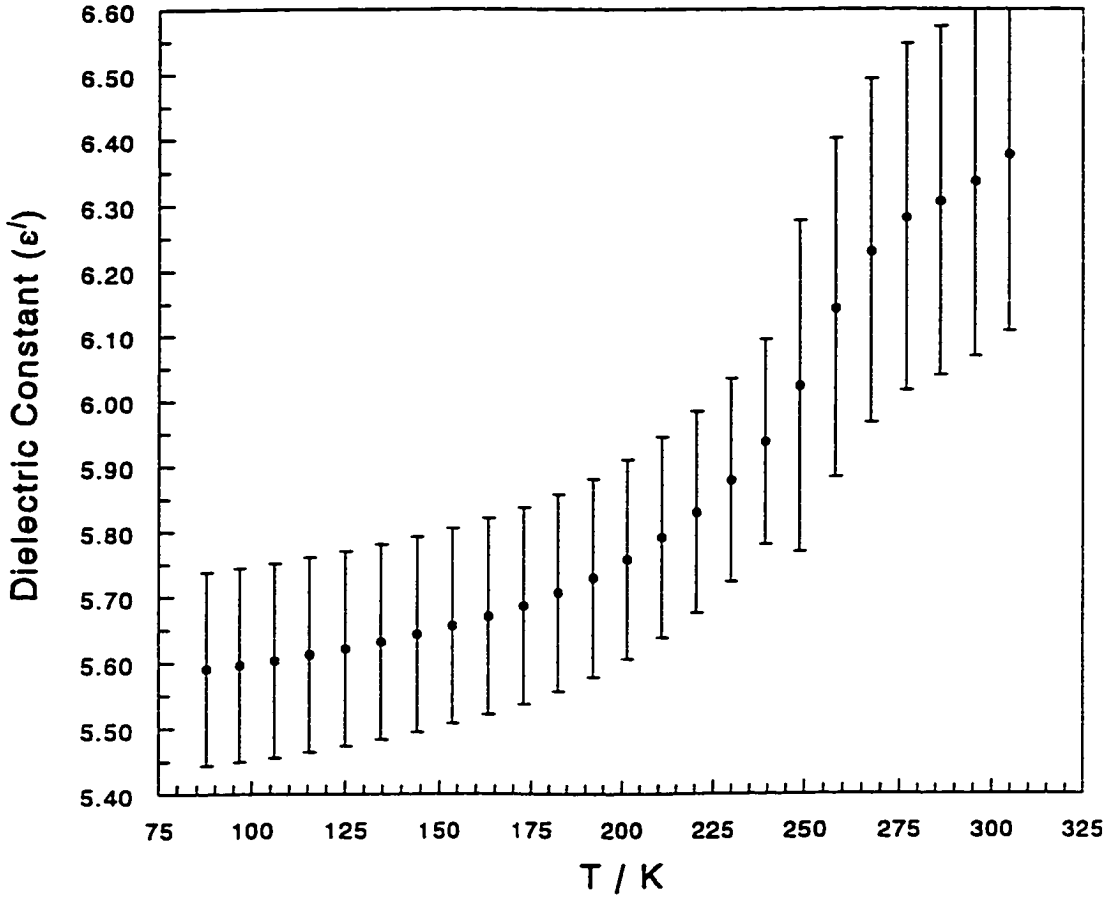

Figure 7.13. Dielectric constant data for NH_4Cl as a function of temperature at a frequency of 100 kHz. The data shown are bulk data obtained by converting the measured powder data using Böttcher's formula. Error bars reflect the experimental uncertainty for each data point. The literature value[322] of the dielectric constant of NH_4Cl at room temperature is 6.9.

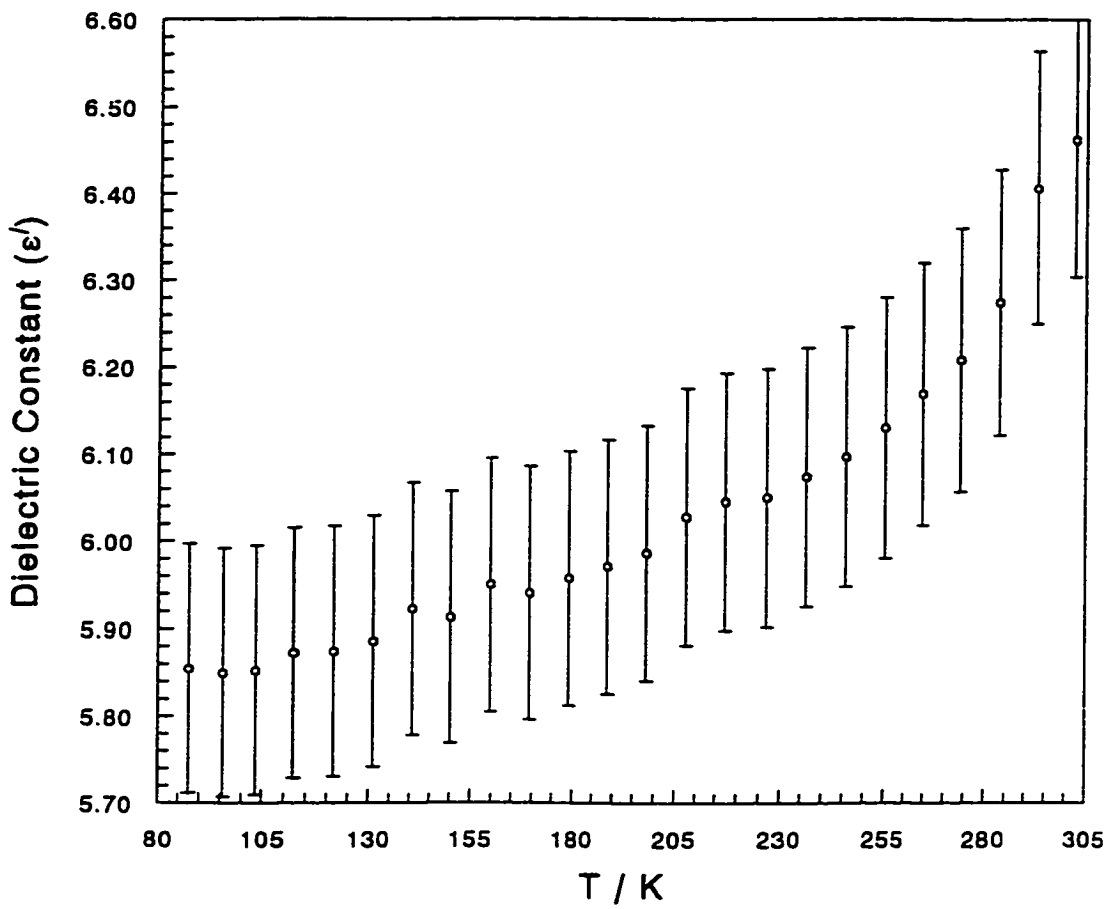

Similar anomalies in the dielectric constant curves for powdered samples of these two compounds have been reported in the literature.[359]

The results for NH_4Br and NH_4Cl are good examples of the utility of measurements by this dielectric relaxation apparatus in detecting polymorphic phase transitions in solids. However, the dielectric anomalies indicating the phase transitions in these compounds occurred over a 45 K to 55 K range. This likely reflected the kinetics of the transitions and the existence of temperature gradients within the sample, coupled with the rather fast heating rates that were used for these measurements (0.8 to 0.9 $K \cdot min^{-1}$). This suggested that much slower heating rates would be desirable in all future measurements, especially for the proper detection and observation of phase transition anomalies.

The uncertainties in the measured values of the dielectric constant and loss have already been partially discussed in terms of errors for a single run with a particular sample. However, at least three runs were performed for each sample and a comparison of the results obtained from the separate runs would provide an estimate of the reproducibility in the dielectric measurements that could be achieved with the experimental setup. Such a comparison was done for all the runs performed for every sample, and the results will now be summarized. For each sample at all measured temperatures, the reproducibility in the dielectric constant results over several runs was within $\pm$ 3.5% for a measuring frequency of 100 Hz, $\pm$ 1.4% for 1 kHz, $\pm$ 1.5% for 10 kHz, $\pm$ 0.7% for 100 kHz, and $\pm$ 1.0% for 800 kHz. A similar analysis of the dielectric loss results revealed a reproducibility within at least $\pm$ 6% at all frequencies

and temperatures employed in the experiments. These reproducibility values listed represent the highest deviations that were observed between runs. In most cases, the reproducibility was better than the percentages listed.

For the case of NH_4Cl, measurements were done on two separate samples, and therefore, a comparison of the data obtained for the two NH_4Cl pellets would enable an estimation of the reproducibility between different samples of the same compound. Such a comparison yielded reproducibilities in the measurement of the dielectric constant of $\pm$ 1.2% at a frequency of 100 Hz, and $\pm$ 0.5% at frequencies of 1 kHz, 10 kHz, 100 kHz, and 800 kHz, over all of the temperatures measured. Again, these numbers reflect the maximum deviations observed between results for the two samples.

The reproducibility data just presented indicate that the precision of the results obtained with the dielectric relaxation apparatus is fairly good. The accuracy of the measured data must also be considered. This can be discussed through a consideration of the results that were presented in Table 7.2. Böttcher's formula was used to convert the powder dielectric data to bulk data. The results in Table 7.2 indicate that the values obtained by the use of Böttcher's formula are consistently lower than the literature bulk values from measurements on single crystals by 6.8% to 14.1%. Thus, there appears to be a systematic inaccuracy in the overall method used to obtain the final bulk dielectric constant values. This could arise from several factors including inadequacies in the model used in deriving Böttcher's formula, the fact that the particles in the powdered sample are not perfectly spherical as required by Böttcher's formula, possible imperfect contact between the faces of the powder sample and the electrodes, and effects due to slight non-

parallelism of the sample faces. By the method used for determining the bulk dielectric constants from measurements of powders using the dielectric relaxation apparatus, accuracy of about 14% or better should be expected.

Accuracy in the measured dielectric loss data was much more difficult to evaluate since literature values of dielectric loss were not readily available. Furthermore, since powder samples were measured, literature dielectric loss values for powder samples would be needed for comparison to include the effects of interfacial dielectric loss which is prevalent in powder samples such as NaCl. Even if such literature values exist, they would depend on the volume fraction of solid in the sample, which would add to the comparison difficulties. It would be expected that the accuracy in the loss would be close to or slightly less than the accuracy in the dielectric constant.

7.5.3 Analysis of NaCl Interfacial Relaxation

The relaxation of the interfacial polarization in NaCl that is observed at high temperatures in Figures 7.5 and 7.6 could be analyzed using one of the methods described in Sections 4.3.4 and 4.3.5. The relaxational nature of this process is clearly evident when the dielectric constant and dielectric loss are plotted as a function of frequency at a constant temperature, an example of which is shown in Figure 7.14. Since the cell heater was kept on during the capacitance and dissipation factor measurements over the whole frequency range, the data plotted in Figure 7.14 are not exactly

Figure 7.14. (a) Dielectric constant and (b) dielectric loss data for NaCl plotted as a function of frequency at ~ constant temperature. Actually, the data were measured over a small temperature range from 338.6 K to 340.7 K. The shapes of the curves are characteristic of the relaxation of a polarization mechanism in the NaCl dielectric (*cf.* Figure (4.11)).

(a)

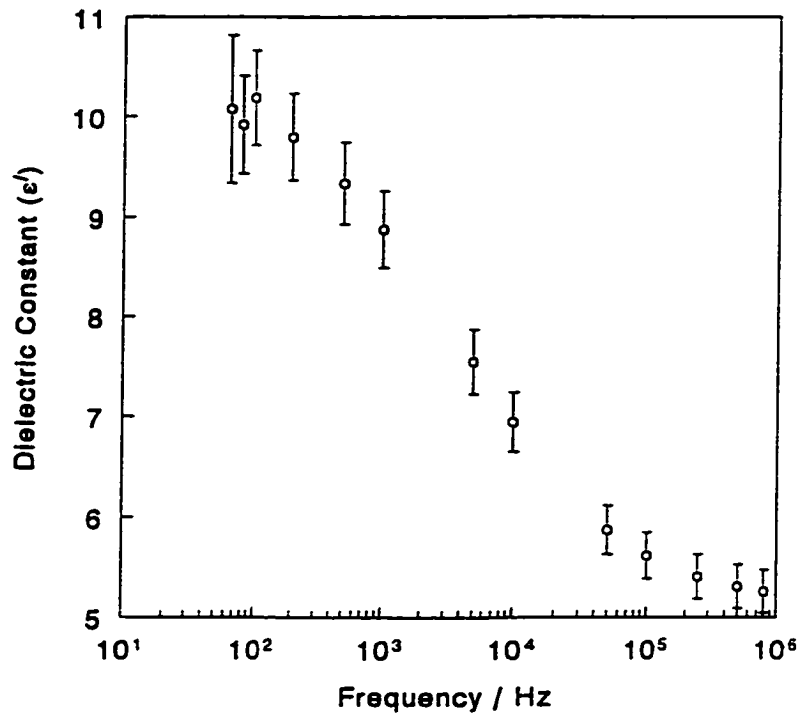

(b)

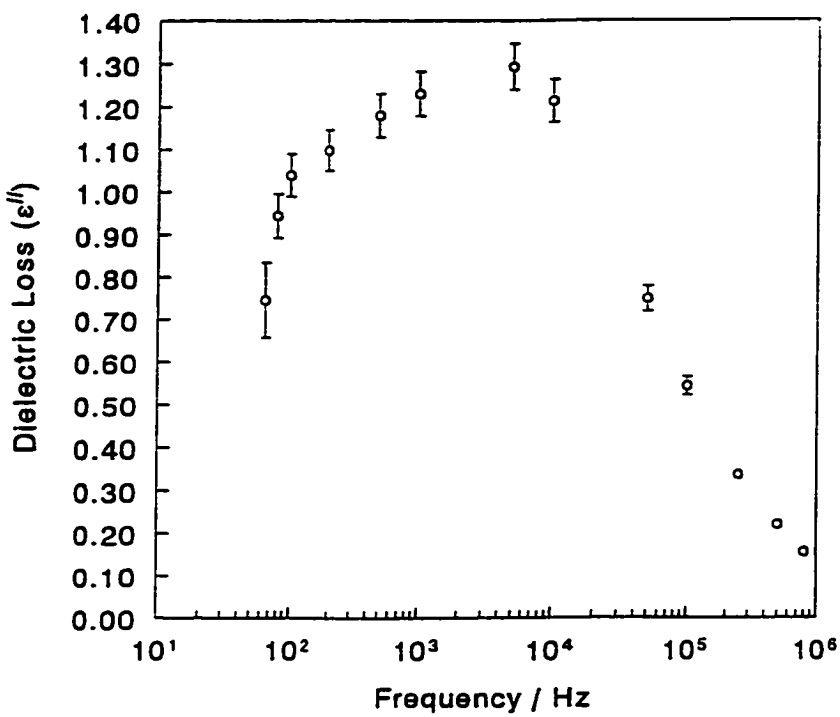

isothermal, but were measured over a small range in temperature from 338.6 K to 340.7 K.

The curves in Figure 7.14 are at least somewhat similar in shape to the theoretical Debye curves indicating a relaxation process that were presented as Figure 4.11 in Section 4.3.4. To determine which relaxational model would work best for the analysis of the NaCl interfacial relaxation, Cole-Cole plots were made by plotting the dielectric loss *versus* the dielectric constant for all frequencies at constant temperature (actually over an approximately 2 K temperature range). Cole-Cole plots were done for each NaCl 65 Hz to 800 kHz measurement series over a small temperature interval for temperatures above $T = 287$ K. An example is shown in Figure 7.15, where the data plotted were measured at 11 frequencies in the 65 Hz to 800 kHz frequency range over a temperature interval from 305.3 to 307.1 K. The curved line in the figure is the result of fitting the data to the equation of a circle.

It is clear from the circular fit in Figure 7.15 that the centre of the circle lies below the x-axis which, as explained in Section 4.3.5, indicates that the data are best represented by a model involving a distribution of relaxation times, rather than a single relaxation time. The data were analyzed in the context of the Cole-Cole equation for a dispersion process involving a distribution of relaxation times (equation (4.49))[237] which contains two parameters: α_{cc} and τ_o. The parameter α_{cc} represents the relaxation time distribution and can have values between 0 and 1, with a larger α_{cc} value indicating a more extensive relaxation time distribution. The parameter τ_o is an average relaxation time about which the distribution is symmetrically spread.

Figure 7.15. An example of a Cole-Cole plot for the NaCl dielectric constant and dielectric loss data over the temperature interval from 305.3 K to 307.1 K. The curved line was the result of fitting the data to the equation of a circle.

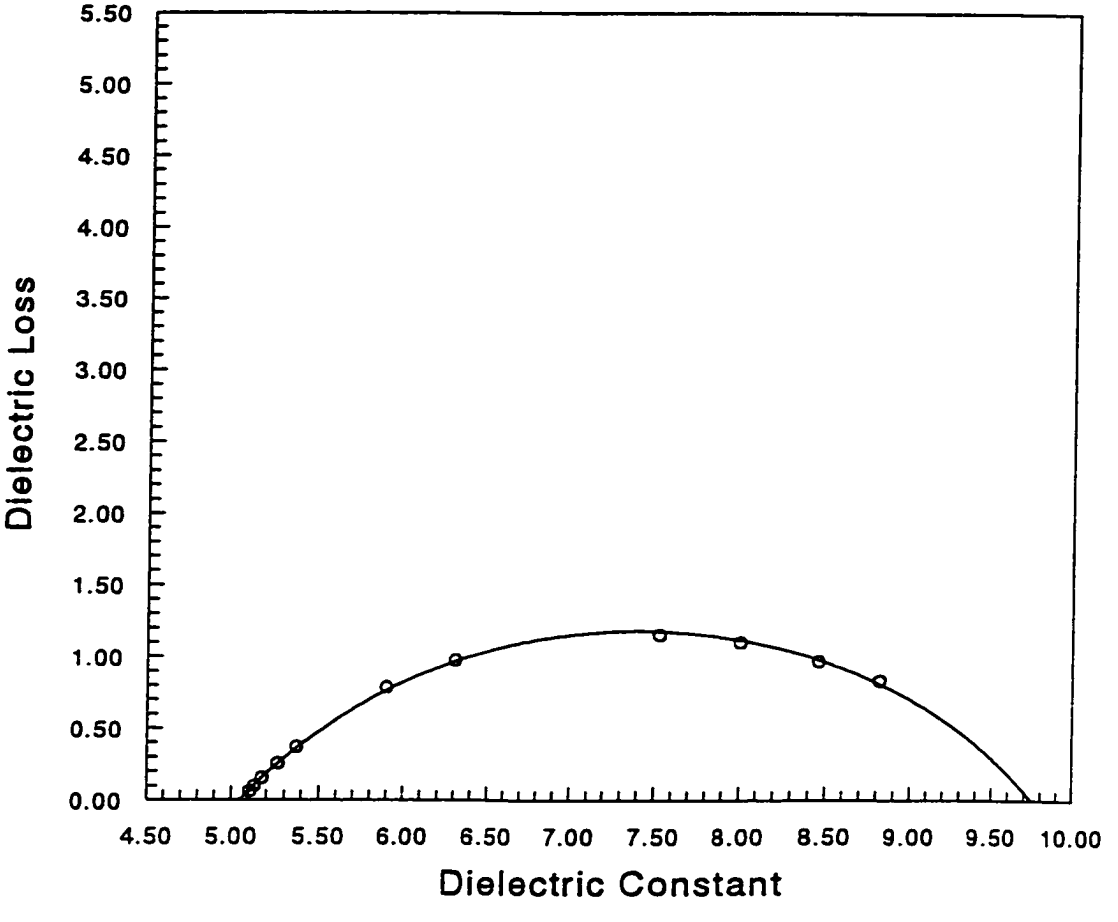

As was shown in Figure 4.14 of Section 4.3.5, α_{cc} can be obtained from the angle of intersection of the x-axis and the radius of the circle joined to ϵ_∞. This angle of intersection could be obtained from the best fit parameters for the centre of the circle and its radius. If the circle has centre (a,b) and radius r, α_{cc} can be found from simple trigonometry (see Figure 4.14), *i.e.*,

$$\sin\left[\frac{\alpha_{cc}\pi}{2}\right] = \frac{|b|}{r}, \tag{7.16}$$

and thus,

$$\alpha_{cc} = \frac{2}{\pi}\arcsin\left[\frac{|b|}{r}\right]. \tag{7.17}$$

The parameter α_{cc} was found for all of the Cole-Cole plots from the parameters of the circular fits and the results are shown in Table 7.3, where the temperatures listed are average temperatures for the data in a particular Cole-Cole plot. The uncertainties obtained in the fitted circular parameters were propagated throughout the calculation of α_{cc}, and these uncertainties in α_{cc} are included in Table 7.3. The values of α_{cc} vary over the temperature range studied from 0.388 to 0.492.

The relaxation time parameter for a particular Cole-Cole plot was determined using the procedure[237] described in Section 4.3.5 whereby the segments u and v (see Figure 4.14) were calculated for each data point in the Cole-Cole plot and a graph was made of $\ln(v/u)$ versus $\ln\omega$ (where $\omega = 2\pi f$ is the angular frequency). An example of such a plot is shown in Figure 7.16 for the Cole-Cole plot data from Figure 7.15. The slope of such a plot should be a straight line with slope $1-\alpha_{cc}$ and intercept $(1-\alpha_{cc})\ln\tau_o$.

Table 7.3. The parameter α_{cc}, describing the relaxation time distribution, determined from each Cole-Cole plot made for the NaCl dielectric data. The temperature listed is the average temperature for the data in a particular Cole-Cole plot, and the uncertainty listed for the temperature indicates the range.

T_{avg} / K	α_{cc}
288.9 ± 0.9	0.405 ± 0.011
297.6 ± 0.9	0.388 ± 0.016
306.2 ± 0.9	0.407 ± 0.016
314.9 ± 0.9	0.434 ± 0.036
323.3 ± 0.8	0.447 ± 0.040
331.6 ± 0.8	0.464 ± 0.053
339.6 ± 1.0	0.492 ± 0.078

Figure 7.16. A plot used to determine the relaxation time parameter (τ_o) for the NaCl data plotted in Figure 7.15.

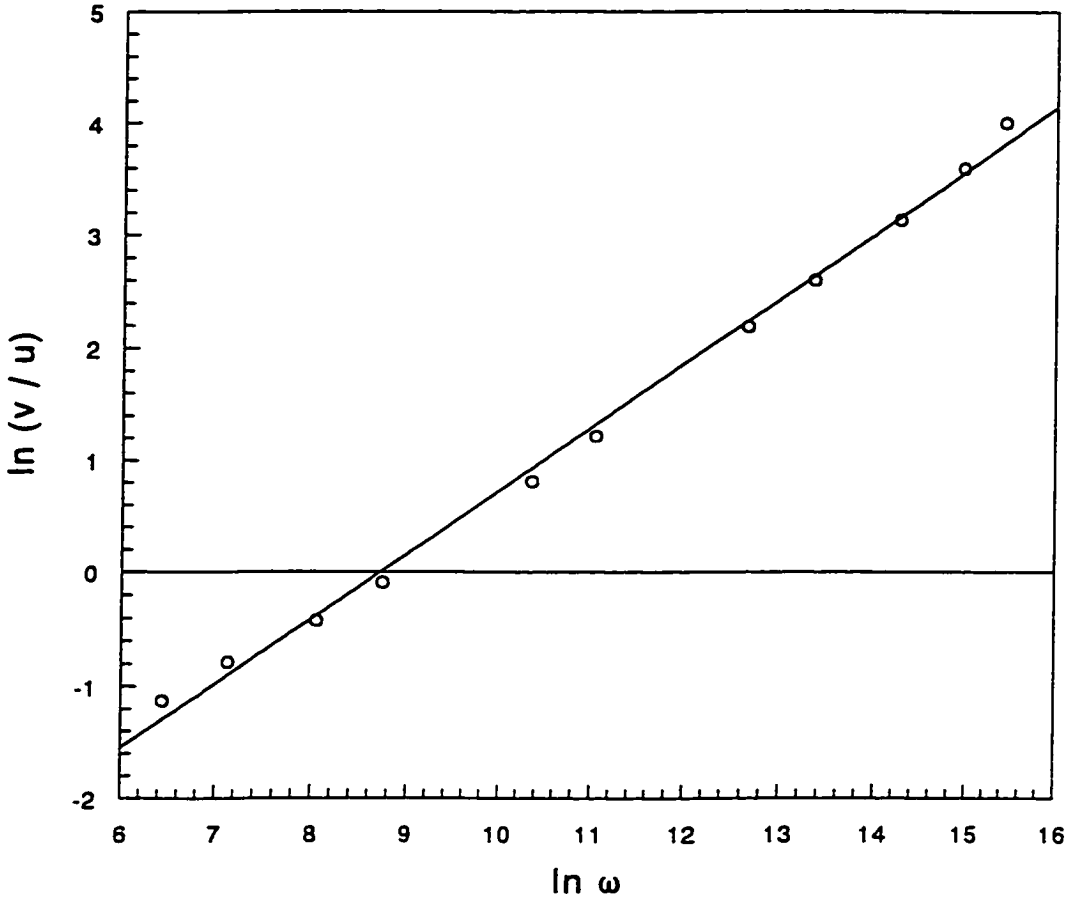

Thus, if m was the slope of such a plot and y_{int} was the intercept, the parameter τ_o could be calculated from the equation

$$\tau_o = e^{y_{int}/m}. \qquad (7.18)$$

This procedure was performed for all of the Cole-Cole plots and the resulting values of τ_o, along with their corresponding uncertainties, are listed in Table 7.4.

If the temperature dependence of the relaxation time followed Arrhenius behaviour, a plot of $\ln\tau_o$ *versus* $1/T$ should be linear and the activation energy for the relaxation process and the pre-exponential factor could be obtained from the slope and intercept, respectively, of the plot. This was done for the relaxation time data presented in Table 7.4 as shown in Figure 7.17, where the best fit line is also drawn. The behaviour of the data plotted in Figure 7.17 is reasonably linear. The activation energy and pre-exponential factor obtained from the slope and intercept of the best-fit line were 18.1 $\pm$ 1.7 kJ·mol^{-1} and (1.5 $\pm$ 0.9) x 10^{-7} s, respectively. These values represent the kinetic parameters for interfacial polarization in the powder NaCl sample.

7.6 Summary

The measurement and analysis of the dielectric properties of the well-known ionic salts NaCl, KCl, KBr, NH_4Cl, and NH_4Br allowed for a useful test of the dielectric relaxation apparatus and provided valuable information concerning the polarization mechanisms which exist in powder ionic samples. Based upon these measurements, an

Table 7.4. The relaxation time parameter (τ_o) at different temperatures determined from each Cole-Cole plot made for the NaCl dielectric data. The temperature listed is the average temperature for the data in a particular Cole-Cole plot, and the uncertainty listed for the temperature indicates the range.

T_{avg} / K	τ_o / s
288.9 ± 0.9	(3.16 ± 0.76) x 10^{-4}
297.6 ± 0.9	(2.05 ± 0.50) x 10^{-4}
306.2 ± 0.9	(1.66 ± 0.47) x 10^{-4}
314.9 ± 0.9	(1.57 ± 0.44) x 10^{-4}
323.3 ± 0.8	(1.22 ± 0.39) x 10^{-4}
331.6 ± 0.8	(1.15 ± 0.40) x 10^{-4}
339.6 ± 1.0	(9.0 ± 3.2) x 10^{-5}

Figure 7.17. Arrhenius plot describing the temperature-dependence of the relaxation time data for NaCl from Table 7.4. The line shown was determined by a least-squares fit.

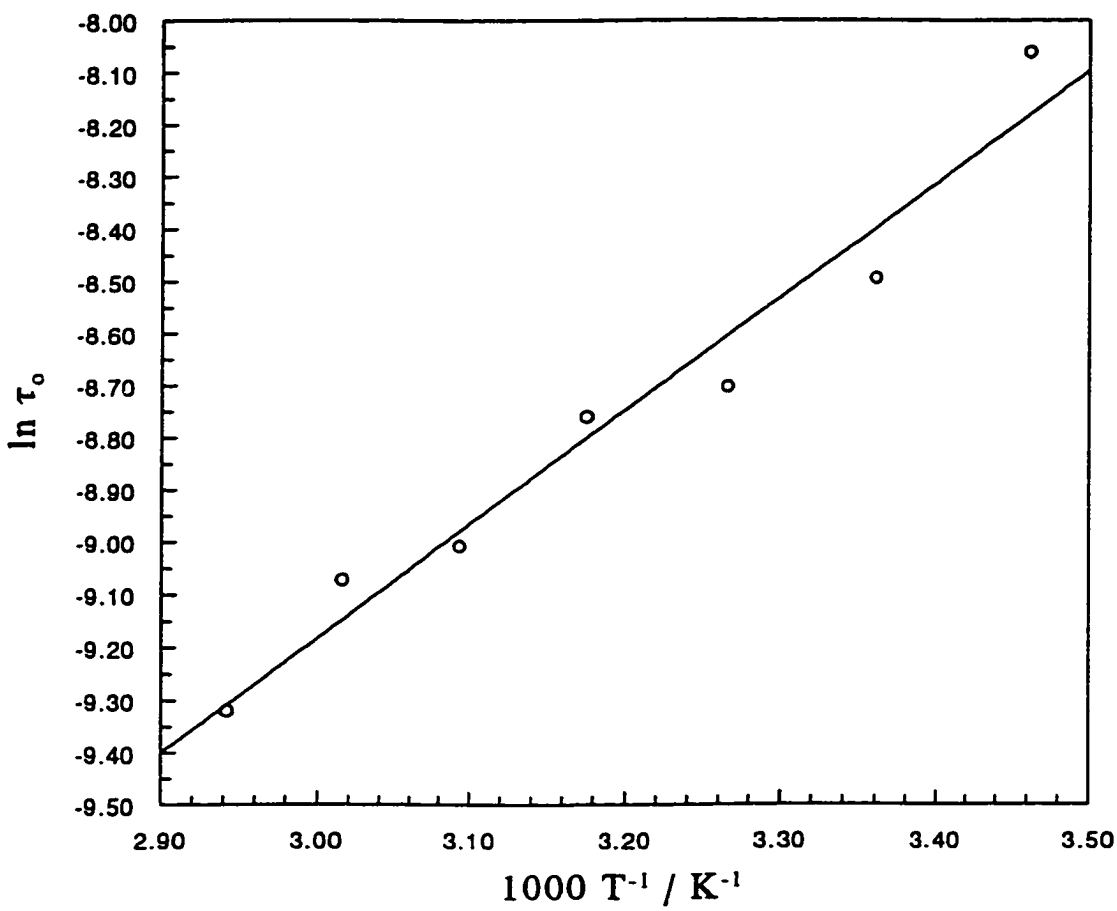

appropriate conversion formula could be chosen to convert the measured powder dielectric data to values representative of the bulk solid (Böttcher's formula). Electrical conductivity and interfacial polarization can contribute greatly to the dielectric constant and loss at low frequencies and higher temperatures. The measurement of NH_4Cl and NH_4Br provided an opportunity to observe the features in a dielectric constant curve indicating the occurrence of a polymorphic phase transition. Finally, enough data could be collected for the powder NaCl sample to observe the relaxation of the interfacial polarization in NaCl, and an analysis of these data allowed for the determination of the kinetic parameters which characterize this relaxation process.

Chapter 8: Dielectric Measurements of NaOH and NaOD

8.1 Introduction

With the design, construction, calibration, and testing of the dielectric relaxation apparatus satisfactorily completed, along with the knowledge gained concerning the measurement of powdered ionic salts as described in the last chapter, it was time to utilize the apparatus for its originally intended purpose: the measurement and analysis of the dielectric properties of NaOH and NaOD.

As was discussed for several examples in Section 4.3.6, the analysis of dielectric relaxation from a dipole reorientational process can provide kinetic information, and thus, enable a determination of the temperature at which the reorientational motion becomes too slow compared to the laboratory timescale to be observed. Frozen-in disorder was postulated for NaOH to explain the difference in the low-temperature behaviour of sodium hydroxide compared to its deuterated counterpart, NaOD. The observation of relaxational behaviour in the dielectric measurements of NaOH and the kinetic information obtained from the analysis of the dielectric relaxation curves would help test the postulate of frozen-in disorder and also allow for an estimation to be made of the temperature of a glassy-phase transition in NaOH (if any), indicating the onset of frozen-in disorder.

No conclusive evidence for a glassy-phase transition was found from calorimetric measurements of NaOH as described in Chapter 5. The results and analysis of dielectric

measurements of NaOH, coupled with the calorimetric data, would provide a firm basis upon which the likelihood of residual entropy in NaOH can be judged. Regardless, however, valuable insight should be gained concerning the anomalous low-temperature behaviour in NaOH from dielectric relaxation measurements, especially when compared to similar measurements performed on NaOD.

8.2 NaOD Measurements

8.2.1 Sample Preparation and Purity

As discussed in Section 5.4.1, when preparing samples of any of the alkali-metal hydroxides or deuteroxides for measurement, special precautions have to be taken to preserve their purity since they are highly corrosive, and they readily absorb moisture and carbon dioxide from the air. All manipulations in the preparation of the sample of NaOD had to be done under inert atmosphere conditions.

The NaOD sample was prepared using a 40 mass% solution of NaOD (listed as 99.9 atom% D) dissolved in D_2O purchased from the Aldrich Chemical Company. A quantity ($\sim$ 25 g) of this solution was placed into a ($\sim$ 30 mL) zirconium crucible under a dry nitrogen atmosphere inside a glove bag. The crucible was placed in a vacuum-sealed sublimator apparatus and heated at $T \sim 220$°C for several days under vacuum to evaporate all of the D_2O and dry the solid left behind. The resulting white granular

chunks that were obtained were crushed to a fine powder with a mortar and pestle under a dry nitrogen atmosphere.

In order to evaluate the purity of the NaOD powder, it had to be tested for monohydrate ($NaOD \cdot H_2O$ or $NaOD \cdot D_2O$) and carbonate (Na_2CO_3) impurities, and the isotopic purity (% deuteration) had to be determined. Just as described for the NaOH sample in Section 5.4.1, the hydrate and carbonate impurity contents were determined by differential scanning calorimetry. A DSC sample of the NaOD powder was made and thermal analysis was carried out using a Perkin-Elmer Pyris-1 DSC covering the temperature range from 40°C to 310°C. The percentages of water and Na_2CO_3 impurities were found in a similar manner as described for the NaOH calorimetric sample in Section 5.4.1, with the assumption that the enthalpy of fusion of $NaOD \cdot H_2O$ (or $NaOD \cdot D_2O$) was equal to the known enthalpy of fusion of $NaOH \cdot H_2O$ (61.54 $J \cdot g^{-1}$).[287] The mass percentages of water and carbonate impurities in the NaOD sample were found to be 1.6% and 0.81%, respectively. As explained in Section 5.4.1, these percentages represent upper limits to the true contents of these impurities in the sample.

The isotopic purity of the NaOD was determined in the following manner: A series of four standard solutions of NaOH in D_2O (Aldrich Chemical Co., the isotopic purity of the D_2O was listed as 99.9% D) was prepared of known concentration ranging from 0.460 M to 2.30 M. A solution of the NaOD sample in D_2O was similarly prepared of concentration within the range of concentrations of the four standard NaOH solutions. The same volume of each solution was placed in a separate NMR tube. An NMR tube was also prepared containing an equal volume of only the D_2O solvent. Proton NMR

spectra were run for each of the six samples using an EM-360 60 MHz NMR spectrometer.

All other conditions being equal, the area of a signal peak in a ^1H NMR spectrum is proportional to the number of protons in the sample which give rise to the signal (provided the relevant nuclei are allowed sufficient time to relax between pulses). Each of the samples of the standard solutions (NaOH in D_2O) measured by proton NMR contained a known number of protons, so a measurement of the area of the single peak in each spectrum (integration) enabled a calibration curve to be determined of peak area *versus* moles of protons in the sample. The measurement of the proton peak from the neat D_2O sample allowed for the determination of its isotopic purity, and the area of this peak was included in the calibration curve for zero moles of protons in the sample (*i.e.*, on the *y*-axis). A best fit line was calculated through the points on the calibration curve by a linear least-squares analysis. The measured signal area of the NaOD in D_2O sample enabled the determination of the number of moles of protons in the NaOD NMR sample from the calibration curve. By knowing the volume of the NaOD solution in the NMR sample as well as the amounts of NaOD and D_2O used to make up the original solution, the isotopic purity of the powder NaOD sample could be calculated. The isotopic purity of the NaOD as determined by this method was found to be (94 ± 6) mol%.

To ensure scrupulously dry conditions during the pressing of the NaOD powder to form pellets suitable for measurement, the preparation of the NaOD pellets was done inside a glove box with an atmosphere of dry nitrogen. The pressed powder samples of the ionic compounds described in the last chapter were obtained using a hydraulic press.

However, size constraints prohibited the use of the hydraulic press in the glove box. Therefore, the NaOD powder samples were pressed in the glove box by loading some of the NaOD powder into a die and piston device and applying pressure using an Arbor press and brute force. This procedure resulted in pressed pellets of NaOD that were suitable for measurement with the dielectric relaxation apparatus.

One of these pellets was loaded into the dielectric measurement cell under a helium atmosphere, suspended from the cryostat and wired up, evacuated, and cooled down to ~ 80 K with liquid nitrogen. The mass of this pellet was measured to be 0.324 ± 0.004 g, with a diameter of 17.08 ± 0.02 mm, and a thickness of 1.12 ± 0.02 mm. The calculated density of the pellet using this data was 1.263 ± 0.027 $g \cdot cm^{-3}$.

In order to calculate the volume fraction of NaOD in the pressed powder sample by equation (7.15), it was necessary to know the bulk density of NaOD. This value could not be found in the literature, so it was calculated from literature neutron-diffraction crystallographic data[140] for NaOD at T = 293 K. The crystallographic density thus obtained was 2.084 $g \cdot cm^{-3}$.

However, this density does not reflect the presence of vacancies, dislocations, and other defects in the crystal lattice that invariably exist. Since NaOH and NaOD have almost identical crystal structures at room temperature,[141] a correction factor to take into account the presence of defects was determined for NaOH from a comparison of the "true" bulk density of NaOH with the crystallographic density calculated from crystallographical data for NaOH in the literature. The crystallographic density of NaOH (ρ_{cryst}) was calculated from three literature reports of NaOH crystallographical data[141,160,162]

and the average density obtained was 2.0193 ± 0.0021 g·cm^{-3}. The bulk density of NaOH determined from macroscopic measurements (ρ_{macro}) is listed in the literature[361] as 2.130 g·cm^{-3}. A correction factor (η) was therefore calculated in the following manner:

$$\eta = \frac{\rho_{macro}}{\rho_{cryst}} = 1.0548 \pm 0.0011 . \qquad (8.1)$$

This correction factor was applied to the crystallographic density for NaOD to obtain its macroscopic bulk density taking into account the presence of defects as follows:

$$\rho_{macro}^{NaOD} = \eta \times \rho_{cryst}^{NaOD} = 2.198 \pm 0.002\, g \cdot cm^{-3} . \qquad (8.2)$$

Using this value along with the calculated density for the NaOD powder, the volume fraction of NaOD in the powdered sample (δ) was determined using equation (7.15) to be 0.575 ± 0.012.

8.2.2 Results and Discussion

Three runs were performed on the same NaOD sample using the dielectric relaxation apparatus covering the temperature range from 85 K to 340 K using twelve measurement frequencies between 80 Hz and 800 kHz. The only difference in the experimental conditions for the three runs was the heating rate. An average heating rate of 0.45 K·min^{-1} was used for the first run, with average heating rates of 0.30 K·min^{-1} and 0.15 K·min^{-1} being employed for the second and third runs, respectively.

The dielectric constant results for the third run are shown in Figure 8.1, which

Figure 8.1. Dielectric constant curves of NaOD as a function of temperature at several frequencies. The lines are simply guides for the eye. + 80 Hz, ▲ 100 Hz, ○ 200 Hz, ✦ 500 Hz, ▲ 1 kHz, ● 5 kHz, ▽ 10 kHz, ◇ 50 kHz, □ 100 kHz, ▼ 250 kHz, ◆ 500 kHz, ■ 800 kHz.

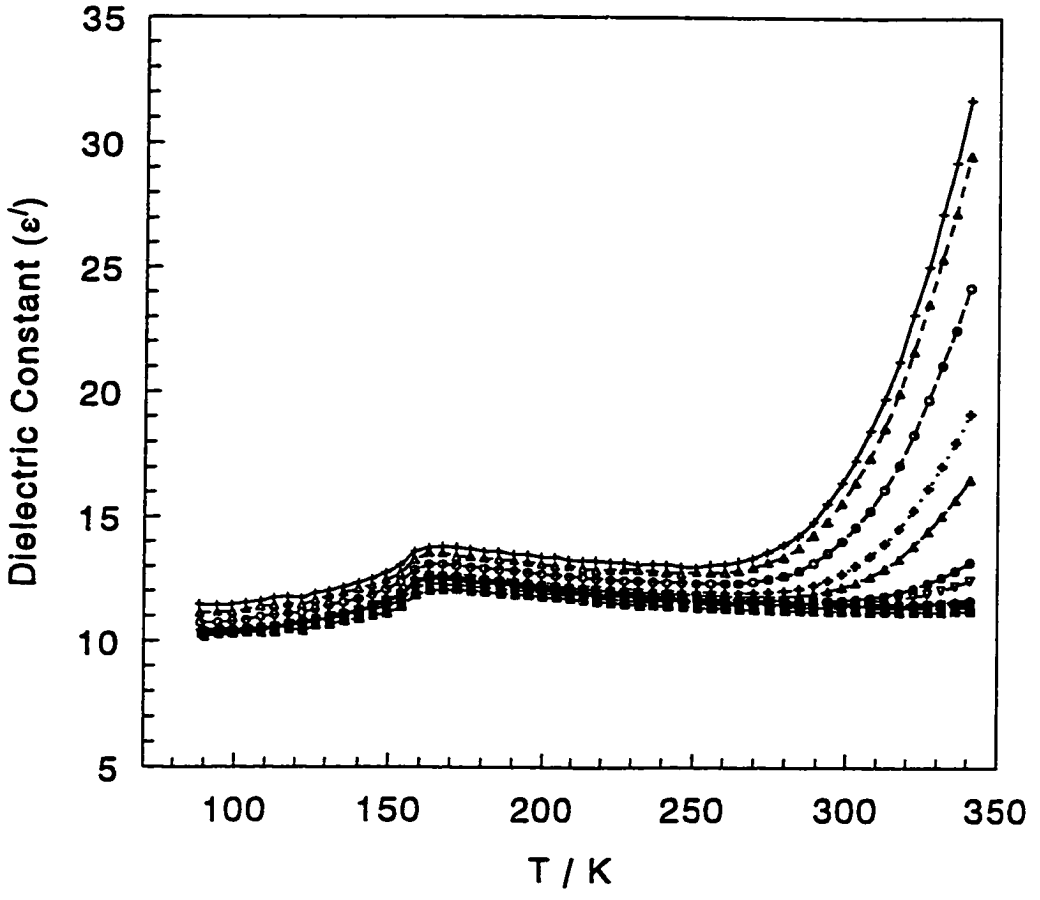

shows the dielectric constant of NaOD as a function of temperature for all of the frequencies measured. All of the dielectric data shown in this figure were obtained by conversion of the measured powder data using Böttcher's formula. Interfacial polarization effects are clearly evident in the low-frequency curves at temperatures above 260 K, which causes very large dielectric constants to be observed. The measured dielectric loss was zero within the experimental uncertainty for all frequencies at temperatures below 260 K. Above 260 K, high dielectric losses were observed, especially at the lower frequencies, due to conductivity and interfacial loss effects.

A more subtle anomaly is visible in all of the dielectric constant curves as a step near a temperature of 160 K. A close-up of this anomaly on an expanded scale is provided in Figure 8.2 for a frequency of 10 kHz. Error bars in this curve reflect the experimental uncertainty for each data point. Figure 8.2 reveals the anomaly as a lambda-shaped peak which is a characteristic feature of an antiferroelectric phase transition to a low-temperature antiferroelectric phase as discussed in Section 4.3.3. If the temperature of the transition is taken to be the temperature at which the maximum dielectric constant occurs, then a transition temperature of 160. $\pm$ 2 K is obtained.

The phase transition in NaOD is the low-temperature deuterium-induced phase transition which is the focus of this thesis. This is supported by the fact that the low-temperature phase in NaOD is known from crystallographic data to be antiferroelectric,[140] corresponding to the dielectric anomaly shown in Figure 8.2. Furthermore, the deuterium-induced phase transition temperature in NaOD has been determined previously from calorimetric measurements[152] (see discussion in Sections 3.1 and 3.2) to be 153.2

Figure 8.2. A close-up of the low-temperature anomaly in the dielectric constant curve of NaOD for a frequency of 10 kHz.

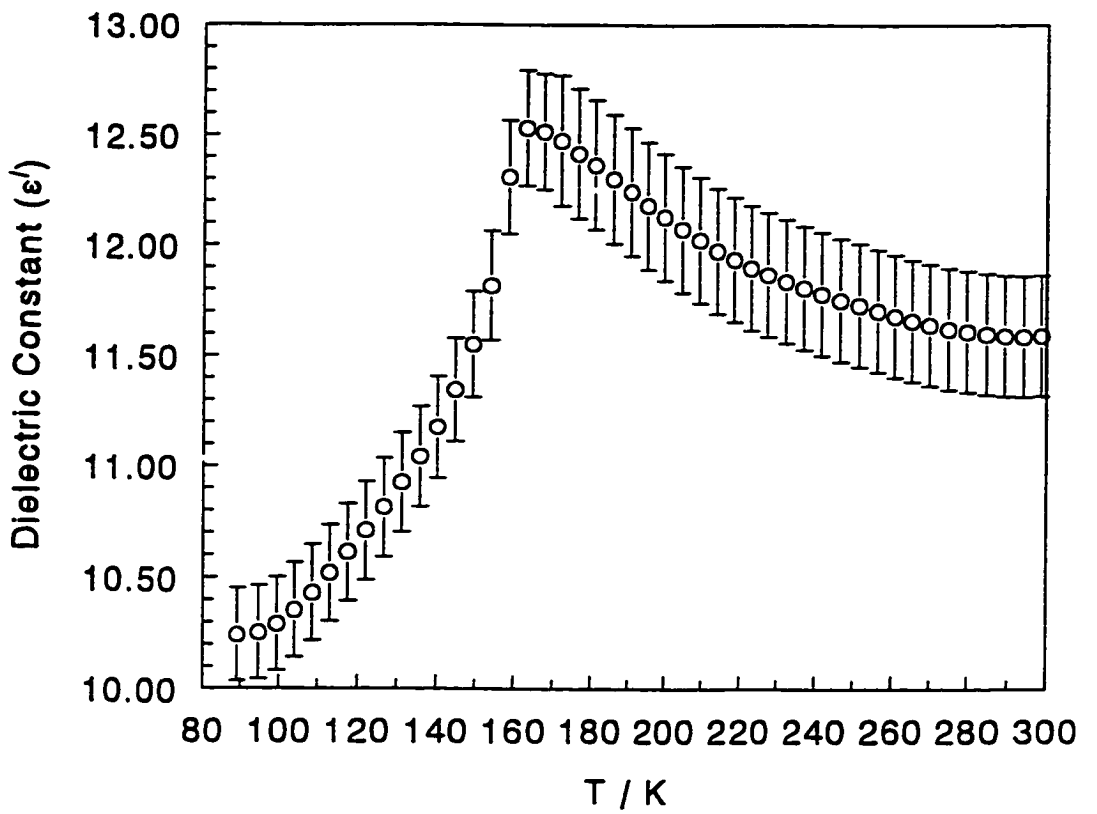

K which compares favourably with the dielectric phase transition temperature of 160 K determined here. It should be noted that in the first two runs with NaOD, lambda-shaped anomalies similar to Figure 8.2 were observed, but their maxima occurred at temperatures of 177 $\pm$ 2 K and 170 $\pm$ 2 K, for the first and second runs, respectively. The greater deviations of these temperatures from the true phase transition temperature, compared to the phase transition temperature obtained from the third NaOD run, can be correlated to the faster heating rates used for the first and second runs. This supports the conclusion reached in Chapter 7, *i.e.*, that slow heating rates should be used to accurately study phase transitions using the dielectric apparatus.

There is one report of previous NaOD dielectric measurements in the literature.[140] The plot of the results of this literature report was given as Figure 3.3. These literature results were obtained from an NaOD specimen formed by melting a sample between the conducting plates of a capacitor. These data also show a lambda-shaped anomaly in the dielectric constant curve for NaOD with a maximum near a temperature of 160 K. The authors neglected to mention the frequency at which their measurements were taken, however, so a detailed comparison with the present results is not possible.

The dielectric constant values above a ferroelectric or antiferroelectric phase transition are typically found to obey a Curie-Weiss Law, *i.e.*,[61]

$$\epsilon' = \epsilon_\infty + \frac{C}{T - T_o}, \qquad (8.3)$$

where ϵ_∞, C, and T_o are constants. This equation is analogous to the Curie-Weiss Law for ferromagnetism.

The dielectric constant data for NaOD at temperatures above the maximum in the lambda-shaped anomaly (up to T = 280 K) were fitted to equation (8.3) with values of 10.753 ± 0.053, 176 ± 15 K, and 71.0 ± 6.0 K being obtained for the fit constants ϵ_∞, C, and T_o, respectively. The result of such a fit is typically presented in the literature as a plot of $1/(\epsilon' - \epsilon_\infty)$ *versus* T, which, according to equation (8.3), should be a straight line. This type of plot is given for the NaOD data in Figure 8.3.

The value of T_o obtained from the analysis of the NaOD dielectric constant data is positive in contrast to the negative values of T_o that were obtained from a Curie-Weiss analysis for the antiferroelectric phase transitions observed for compounds in the $M_3(H,D)(XO_4)_2$ family described in Section 2.3.[61,63,64] Furthermore, the value of the Curie-Weiss constant (C) for NaOD is about an order of magnitude smaller than those determined for the $M_3(H,D)(XO_4)_2$ compounds.[61,63,64] Another known antiferroelectric compound is the well-studied lead zirconate ($PbZrO_3$), which is reported to have an antiferroelectric phase transition temperature of 506 K, and Curie-Weiss-Law constants of $C = 1.2 \times 10^5$ K and T_o = 458 K.[365,366]

It is possible that interfacial polarization affects the dielectric constants at the higher temperatures and has a detrimental influence on the fitted value of T_o. This was partially supported by performing fits to equation (8.3) excluding some of the higher temperature data points. This resulted in lower (but not negative) values of T_o being obtained, although the uncertainty in T_o increased considerably.

Even though NaOD and many deuterated compounds of the $M_3(H,D)(XO_4)_2$ family exhibit a low-temperature deuterium-induced phase transition which is not

Figure 8.3. Curie-Weiss plot for the NaOD dielectric data above the antiferroelectric phase transition temperature. The straight line is the result of a linear least-squares fit to the plotted data using equation (8.3).

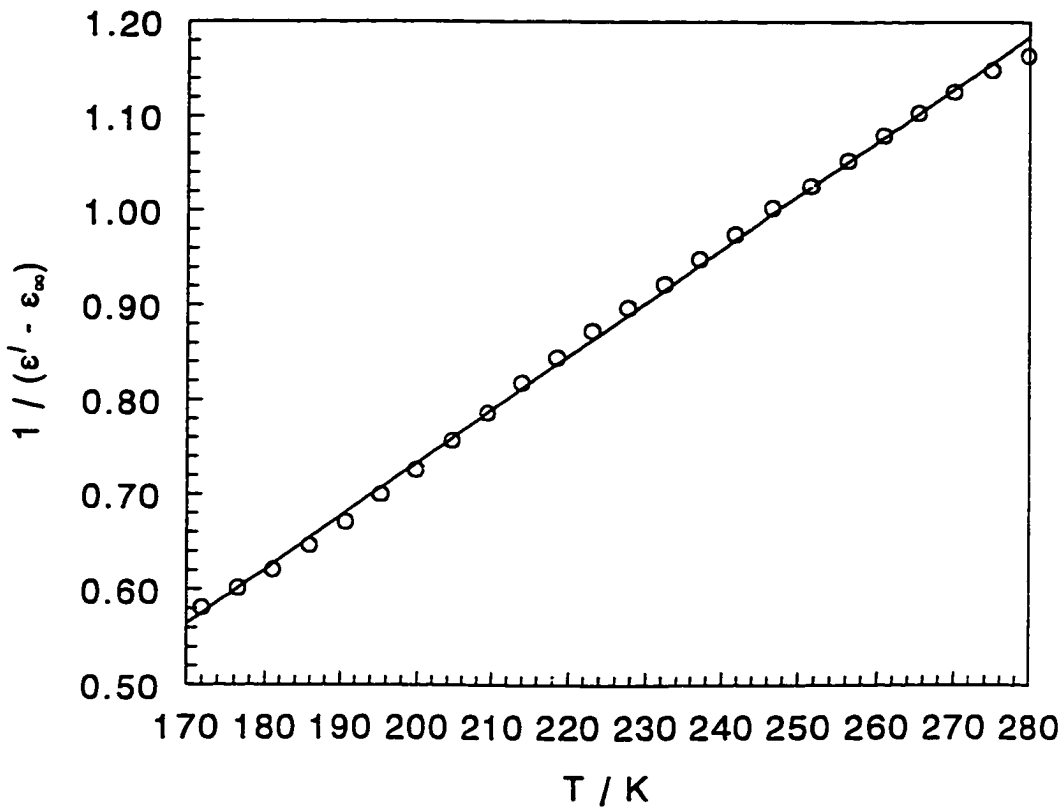

observed in the corresponding hydrogenated compound, the differences in the dielectric behaviour of the deuterium-induced phase transition in NaOD as suggested by the differences in the Curie-Weiss parameters, at the very least, suggest that different influences are likely responsible for the deuterium-induced polymorphism observed in NaOD as compared to the $M_3(H,D)(XO_4)_2$ compounds.

8.3 NaOH Measurements

8.3.1 Sample Preparation and Purity

The sodium hydroxide powder used for the dielectric relaxation measurements was prepared in a similar manner to that described in Section 5.4.1 for the NaOH sample used for the calorimetric experiments. A quantity of NaOH pellets (Aldrich Chemical Co., listed as 99.99% pure) was crushed into a fine powder with a mortar and pestle in a glove bag under dry nitrogen conditions. The powder ($\sim$ 8 g) was placed in a zirconium crucible in a sublimator apparatus and dried by heating the system to a temperature of $\sim$ 170°C under vacuum for two days.

A quantitative analysis for monohydrate ($NaOH \cdot H_2O$) and carbonate (Na_2CO_3) impurities in the resulting dried powder was done using differential scanning calorimetry in the same fashion as was done for the NaOH sample used for the calorimetric measurements (see Section 5.4.1) and for the NaOD sample used in the dielectric

measurements (see Section 8.2.1). The DSC measurements were taken with a Perkin-Elmer Pyris-1 differential scanning calorimeter. An analysis of the resulting measured monohydrate and carbonate eutectic enthalpies indicated impurity contents of 1.2 mass% H_2O and 0.53 mass% Na_2CO_3. As explained in Section 5.4.1, these values are upper limits to the actual percentages of these impurities in the sample.

Pressed pellets of the NaOH powder suitable for dielectric measurements were made following a procedure similar to that described for the formation of the NaOD pellets in Section 8.2.1. The NaOH pellets were pressed in a glove box with a dry nitrogen atmosphere using an Arbor press. Several NaOH pellets were made, and four of these were measured by the dielectric relaxation apparatus. The masses, linear dimensions, and volume fractions of the four measured NaOH pellets are listed in Table 8.1, where the volume fractions were calculated using equation (7.15) and the literature value for the bulk density of NaOH[361] (2.130 $g \cdot cm^{-3}$).

8.3.2 Results and Discussion

Several dielectric runs were done for each of the four pressed powder sodium hydroxide pellets listed in Table 8.1, most of which covered the temperature range between 80 K and 350 K, involving measuring frequencies from 80 Hz to 800 kHz. For sample #1, one run was performed using liquid helium as the cryogenic fluid, during which dielectric measurements of NaOH were taken from 12 K to 90 K. Heating rates

Table 8.1. (a) The masses and linear dimensions of each of the four NaOH pellets whose dielectric properties were measured by the dielectric relaxation apparatus. (b) These data were used to calculate the density of each powder sample which enabled the calculation of the volume fraction of NaOH in the sample using equation (7.15) along with the known bulk density of NaOH from the literature[361] (2.130 $g \cdot cm^{-3}$).

(a)

Sample #	Mass / g	Diameter / mm	Thickness / mm
1	0.669 ± 0.004	19.08 ± 0.02	1.61 ± 0.02
2	0.677 ± 0.004	19.08 ± 0.02	1.58 ± 0.02
3	0.762 ± 0.004	19.08 ± 0.02	1.82 ± 0.02
4	0.488 ± 0.004	19.08 ± 0.02	1.22 ± 0.02

(b)

Sample #	Powder Density / $g \cdot cm^{-3}$	Volume Fraction
1	1.453 ± 0.020	0.6823 ± 0.0094
2	1.499 ± 0.021	0.704 ± 0.010
3	1.464 ± 0.018	0.6873 ± 0.0085
4	1.399 ± 0.026	0.657 ± 0.012

during the dielectric experiments of NaOH varied for each run from 0.1 $K \cdot min^{-1}$ to 0.8 $K \cdot min^{-1}$. It was determined from the dielectric measurements of the common ionic salts (Chapter 7) and NaOD (Section 8.2) that slow heating rates are necessary to accurately study phase transitions. It was unknown before the measurements were taken whether or not a phase transition or a dielectric relaxation response would be observed in the dielectric measurements of NaOH. However, if such an event was observed, it would be highly desirable to optimize conditions as much as possible so that it could be characterized accurately. Thus, for most of the runs, a slow heating rate was usually chosen, *i.e.*, between 0.1 $K \cdot min^{-1}$ and 0.3 $K \cdot min^{-1}$.

The dielectric constant results for a run performed with NaOH sample #1 are shown in Figure 8.4. The dielectric constant curves shown are for several frequencies from 100 Hz to 800 kHz, where each data point was plotted after conversion of the measured powder data to bulk values using Böttcher's formula. The heating rate during this run was 0.7 - 0.8 $K \cdot min^{-1}$. Some scatter is evident at the lower frequencies which, as explained previously, is due to the difficulty of the LCR meter in measuring the electronic parameters of very high impedances.

As observed for most of the powder ionic salts studied using the dielectric relaxation apparatus, interfacial polarization gives rise to large dielectric constant values at high temperatures and low frequencies. These effects are observed for NaOH in Figure 8.4 at the lower frequencies of measurement at temperatures above $\sim$ 300 K.

As shown in Figure 8.4, the value of the dielectric constant of NaOH lies between $\sim$ 7.5 to 7.9 for all temperatures and frequencies where interfacial polarization effects

Figure 8.4. Dielectric constant curves of NaOH as a function of temperature for several frequencies. The data shown are the results of a measurement run performed on NaOH sample #1. The lines are merely for guiding the eye. + 100 Hz, ▲ 200 Hz, ● 500 Hz, ▽ 1 kHz, ◇ 5 kHz, □ 10 kHz, ▼ 100 kHz, ◆ 250 kHz, ■ 800 kHz.

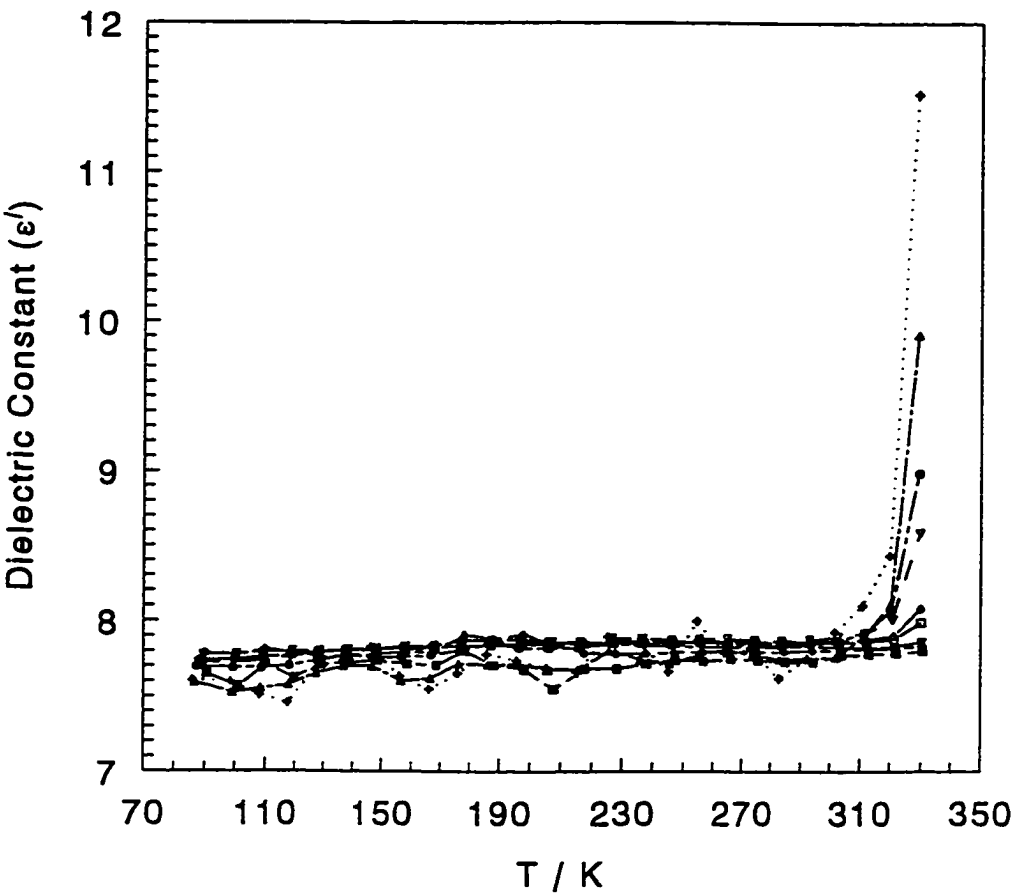

do not significantly affect the dielectric constant. There is one report of previous dielectric measurements for NaOH in the literature,[140] which were taken on a sample formed from an NaOH melt between two conducting electrodes. Results from this study were presented for temperatures between 100 K and 250 K, although the measuring frequency was not reported. A plot of these literature results was given in this thesis as Figure 3.3.[140] The dielectric behaviour of NaOH reported in the literature study is very similar to the behaviour exhibited by the results presented in Figure 8.4, *i.e.*, the dielectric constant changes little with temperature from 100 K to 250 K. Furthermore, the literature dielectric constant values vary between ~ 7.5 and 7.7 which is within the range of the results shown in Figure 8.4. Thus, despite the inaccuracies observed in the use of Böttcher's formula for conversion of the measured ionic powder data in Chapter 7, the use of Böttcher's formula on the powder data measured for NaOH gives results that are consistent with the literature.

A comparison of the dielectric constant values measured for the different samples of NaOH allowed for an estimation of the reproducibility of the measurements among the different samples. The reproducibility was determined for different temperatures and measuring frequencies. It was found that for all temperatures above liquid nitrogen temperature, the dielectric constant values for all the samples were within ± 8.5% for a measuring frequency of 100 Hz, ± 4.2% for 1 kHz, ± 2.9% for 10 kHz, ± 1.7% for 100 kHz, and ± 0.7% for 800 kHz. These percentages represent the maximum deviations that were observed in the dielectric constant measurements of the different samples. In most cases, the deviations were less than the percentages listed.

An example of the dielectric loss results obtained for NaOH is shown in Figure 8.5, which is from a run performed on sample #4. For all of the frequencies measured, the dielectric loss does not appreciably differ from zero from the lowest temperature measured ($\sim$ 85 K) to about 270 K. Above T = 270 K, the dielectric loss increases rapidly with increasing temperature for the lower frequencies, with a smaller rate of increase for the higher frequencies. For a given temperature above 270 K, the dielectric loss increases with decreasing frequency. The increase in the dielectric loss above 270 K is due to the effects of increased electrical conductivity at higher temperatures and interfacial polarization, which are also responsible for the increase in the dielectric constant of NaOH that was observed at high temperatures in Figure 8.4. Similar dielectric loss curves were obtained for all of the runs performed on all of the NaOH samples.

A plot of the dielectric loss as a function of frequency for the highest temperature measured in Figure 8.5 (actually, over the temperature range from 330.2 K to 330.9 K) is provided in Figure 8.6. Comparison with the similar plot that was given for the NaCl measurements in Chapter 7 (Figure 7.14(b)), shows that the NaOH measurements could not be carried out to a high enough temperature and/or a low enough measuring frequency in order to observe the peak in the dielectric loss curve. Because of this, there are insufficient data to analyze the relaxation of the interfacial polarization in the NaOH samples in a manner similar to the analysis done for NaCl in Section 7.5.3. In order to obtain statistically reasonable results from a Cole-Cole plot analysis of relaxation data, it is necessary that the data include enough measurements to cover at least one-half of

Figure 8.5. Measured dielectric loss curves of NaOH as a function of temperature for several frequencies. The data shown are from a run performed on NaOH sample #4. The lines are simply for guiding the eye. + 80 Hz, ▵ 100 Hz, ○ 200 Hz, ✦ 500 Hz, ▲ 1 kHz, ● 5 kHz, ▽ 10 kHz, ◇ 50 kHz, □ 100 kHz, ▼ 250 kHz.

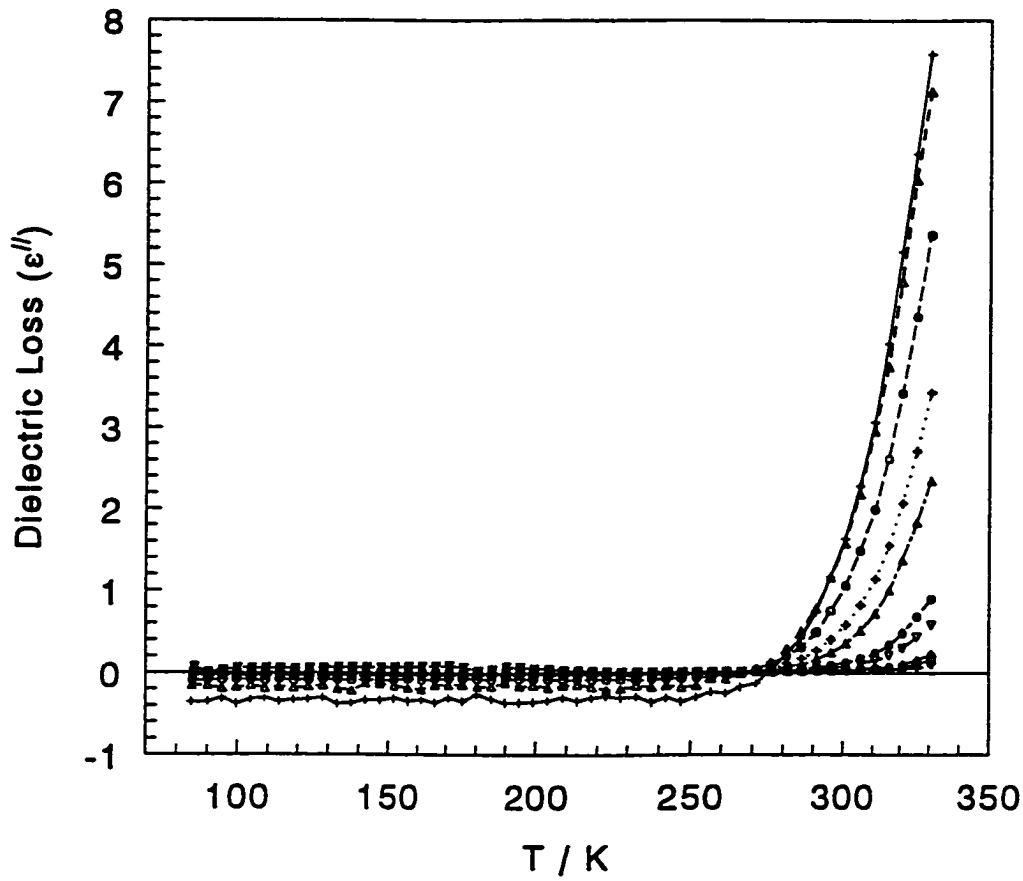

Figure 8.6. Dielectric loss data for NaOH sample #4 plotted as a function of frequency at ~ constant temperature. Actually the data were measured over a small temperature range from 330.2 K to 330.9 K. Error bars reflect the experimental uncertainty in each data point. Where no error bars are shown, the uncertainty is less than or equal to the size of the symbol used to represent the data point. Not enough of the dielectric loss curve is present to perform an analysis of the interfacial polarization in the NaOH sample.

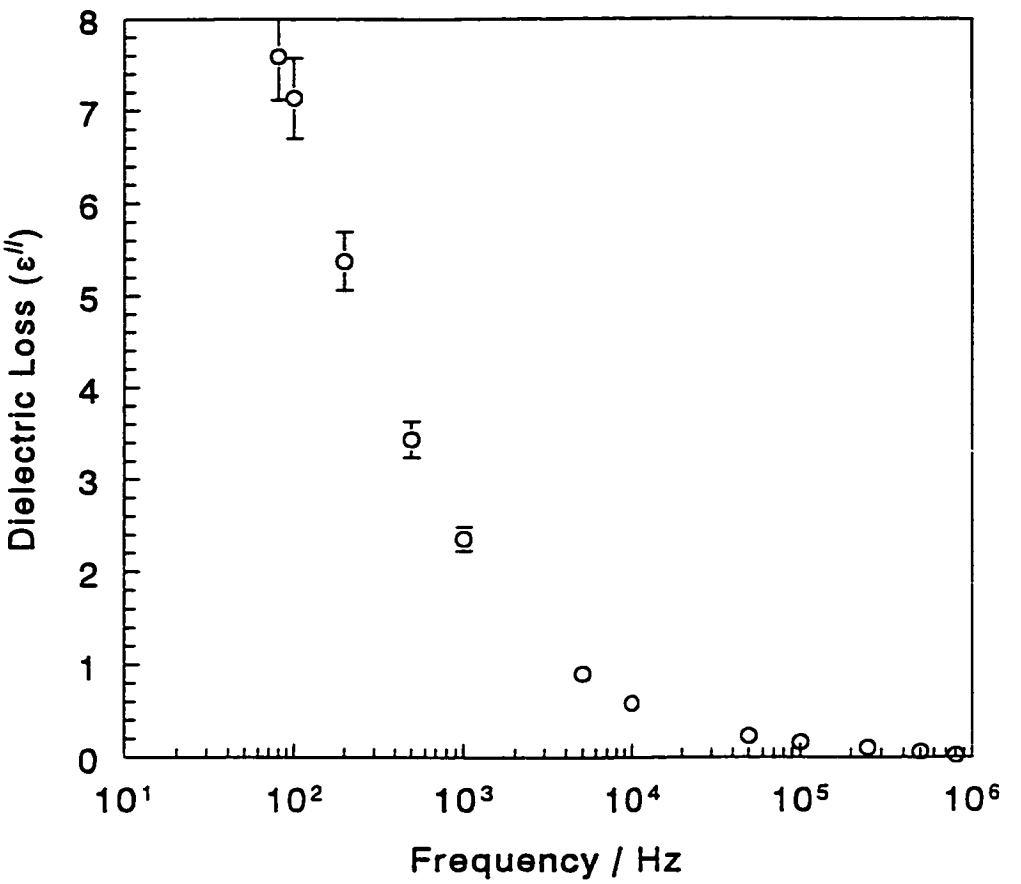

the range of the Cole-Cole plot semicircle. At the very least, this requires the observation of the maximum (or near the maximum) in the dielectric loss due to the relaxation process. While this was the case for the NaCl data (see Figure 7.14(b)), it is clearly not the case for the NaOH interfacial dielectric loss data as shown in Figure 8.6. Thus, a relaxation analysis of the interfacial polarization mechanism in NaOH could not be done.

A liquid helium run was done for sample #1 at temperatures from 12 K to 90 K using an average heating rate of 0.4 $K \cdot min^{-1}$, and the dielectric constant data obtained from this run are presented in Figure 8.7 for a frequency of 10 kHz. The dielectric constant data from this liquid helium run are very nearly continuous with the data obtained in the liquid nitrogen run shown in Figure 8.4: The dielectric constant at T = 89.08 K determined during the liquid nitrogen run was 7.74 at 10 kHz, while the dielectric constant determined from the liquid helium experiment at the same frequency and almost the same temperature (88.10 K) was 7.78, a deviation of only 0.6%. The dielectric losses measured during this liquid helium run did not differ significantly from zero over the entire temperature range measured for all measuring frequencies used.

No obvious anomalous dielectric behaviour is apparent in the dielectric constant data presented in Figure 8.4 and Figure 8.7, but a closer look reveals otherwise. A close-up of the NaOH dielectric data from Figure 8.4 is provided in Figure 8.8 for a frequency of 10 kHz. The noticeable feature of this curve is that the measured dielectric constant of NaOH does not increase monotonically with increasing temperature but rises to a peak near a temperature of 240 K and then starts to decrease. This feature was observed in almost all of the runs for every NaOH sample measured. The exceptions were the runs

Figure 8.7. Dielectric constant measured for NaOH sample #1 as a function of temperature for a frequency of 10 kHz. This run was performed using liquid helium as the cryogenic fluid. Error bars indicate the experimental uncertainty in each data point.

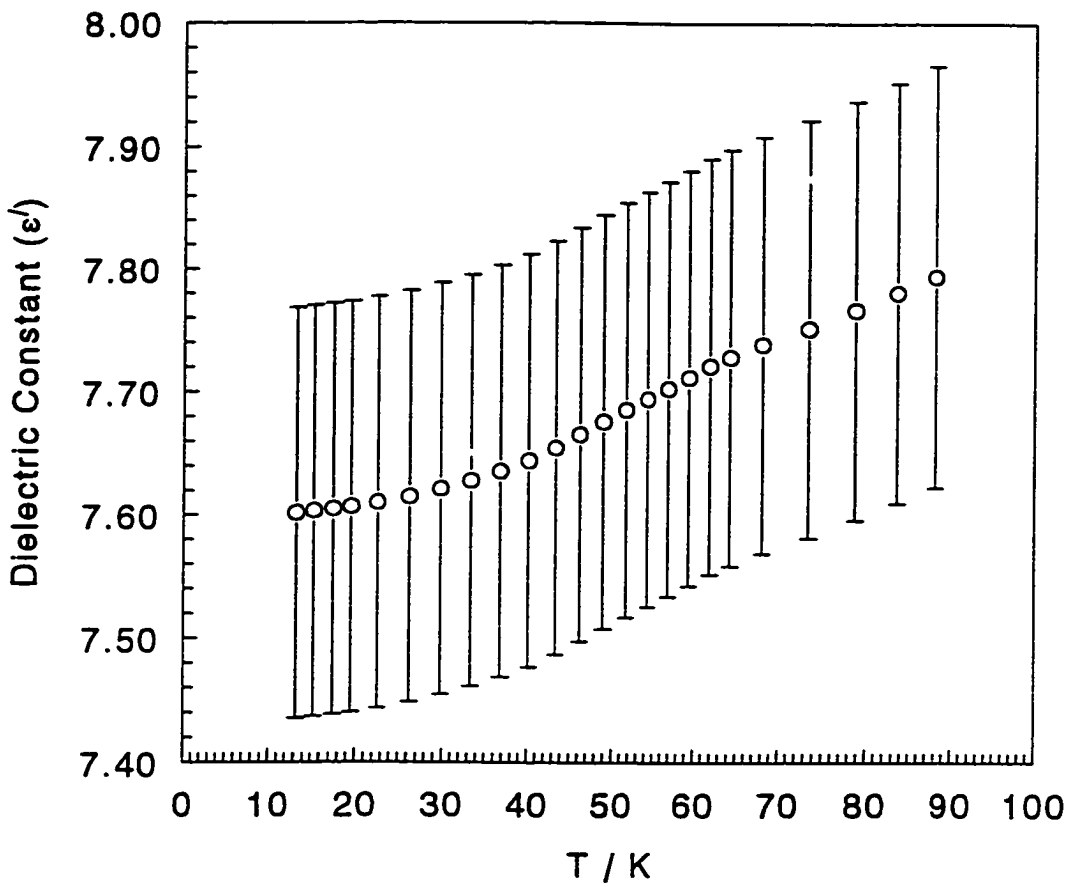

Figure 8.8. A close-up of the NaOH dielectric constant data from Figure 8.4 obtained for NaOH sample #1 at a frequency of 10 kHz. The heating rate during this run was 0.7 - 0.8 $K \cdot min^{-1}$. For each data point, the total experimental uncertainty is within $\pm$ 0.19. However, the uncertainty associated only with random errors in the dielectric constant measurements is within $\pm$ 0.018 (see text).

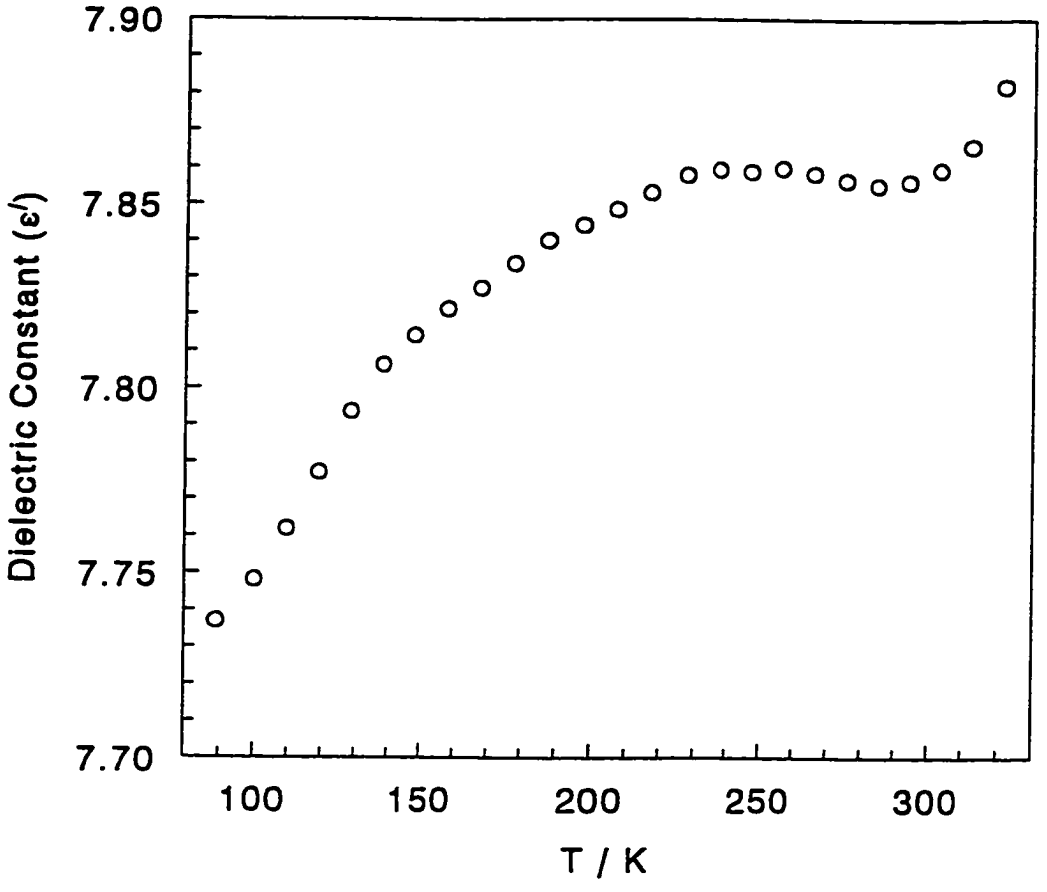

performed with NaOH sample #2. Only two runs were done with this pellet, as it was non-uniformly packed and clearly of poorer quality compared to the other pellets.

The total experimental uncertainty in the dielectric data presented in Figure 8.8 is within $\pm$ 0.19 for each data point. The total experimental uncertainty is subject to both systematic and random errors. Most of the total uncertainty is a result of the systematic uncertainty associated with the value of the volume fraction (δ), as listed in Table 8.1, which is propagated throughout the final calculations. In deciding whether or not the anomaly shown in Figure 8.8 is statistically real, only the random errors in the dielectric constant measurements should be considered, since only the random errors reflect the precision of a measurement. The experimental uncertainty associated with the random errors in the dielectric constant measurement is within $\pm$ 0.018 for all the data points shown in Figure 8.8. In light of this, it can be said that the anomaly apparent in the Figure 8.8 dielectric data is certainly more than just the reflection of random errors in the measurements.

This anomaly was more prominent in the dielectric experiments performed for samples #3 and #4. Figure 8.9 gives the dielectric constant determined during a run for NaOH sample #4 as a function of temperature at a frequency of 100 kHz. The heating rate used during this experiment was 0.15 $K \cdot min^{-1}$. The anomaly in this curve appears as a broad peak from $\sim$ 90 K to 230 K with a maximum in the dielectric constant near T = 170 K. The rising portion of the curve between 80 K and 170 K is similar to what would be expected for dielectric behaviour due to a polarization relaxation process. However, as shown in Figure 8.10, the rising portions of the curves for different

Figure 8.9. Dielectric constant of NaOH as a function of temperature measured for a frequency of 100 kHz. The results shown are from a run performed on NaOH sample #4. The heating rate during this run was 0.14 - 0.18 $K \cdot min^{-1}$. For each data point, the total experimental uncertainty is within $\pm$ 0.22. However, the uncertainty associated only with random errors in the dielectric constant measurements is within $\pm$ 0.018.

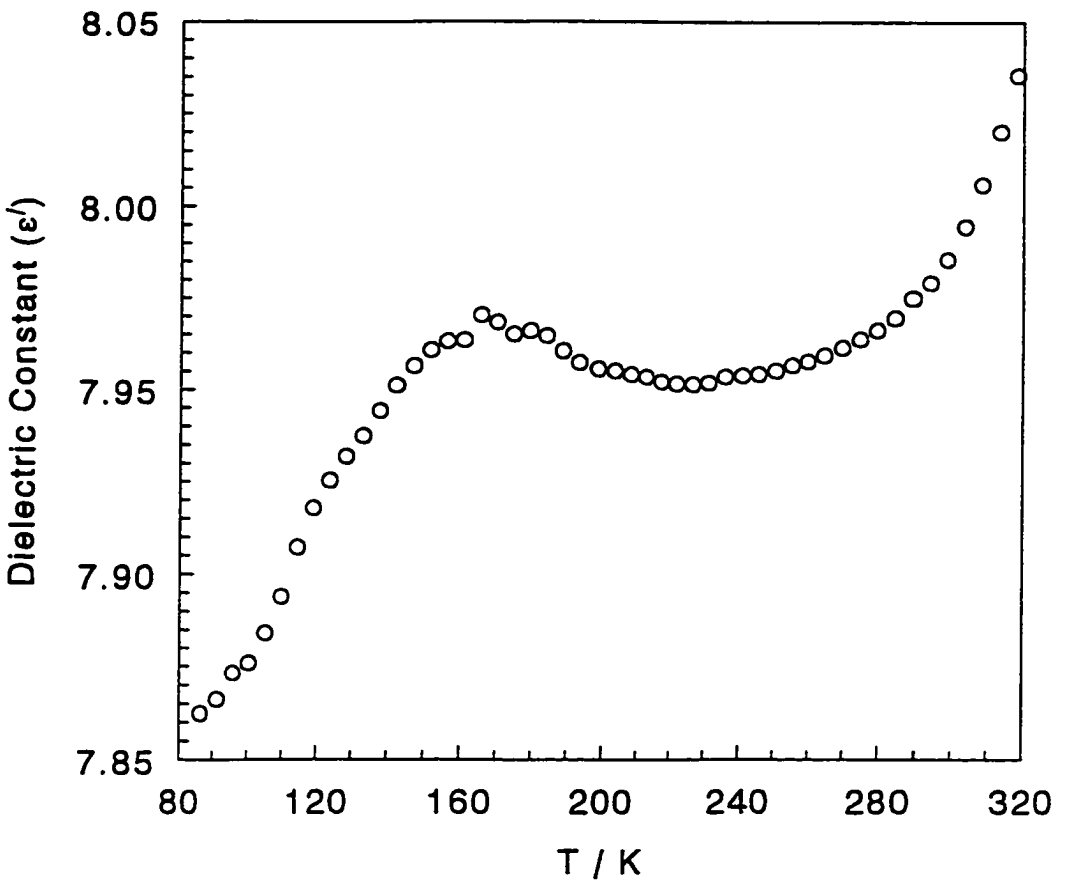

Figure 8.10. Dielectric constant of NaOH as a function of temperature for four different measuring frequencies. The data shown were obtained from measurements of NaOH sample #4. The heating rate during this run was 0.14 - 0.18 $K \cdot min^{-1}$. For each data point, the total experimental uncertainty in the dielectric constant is within $\pm$ 0.25. However, the uncertainty associated only with random errors in the dielectric constant measurements is within $\pm$ 0.018. The lines shown are simply guides for the eye. ● 5 kHz, ▿ 10 kHz, ◇ 50 kHz, ○ 100 kHz.

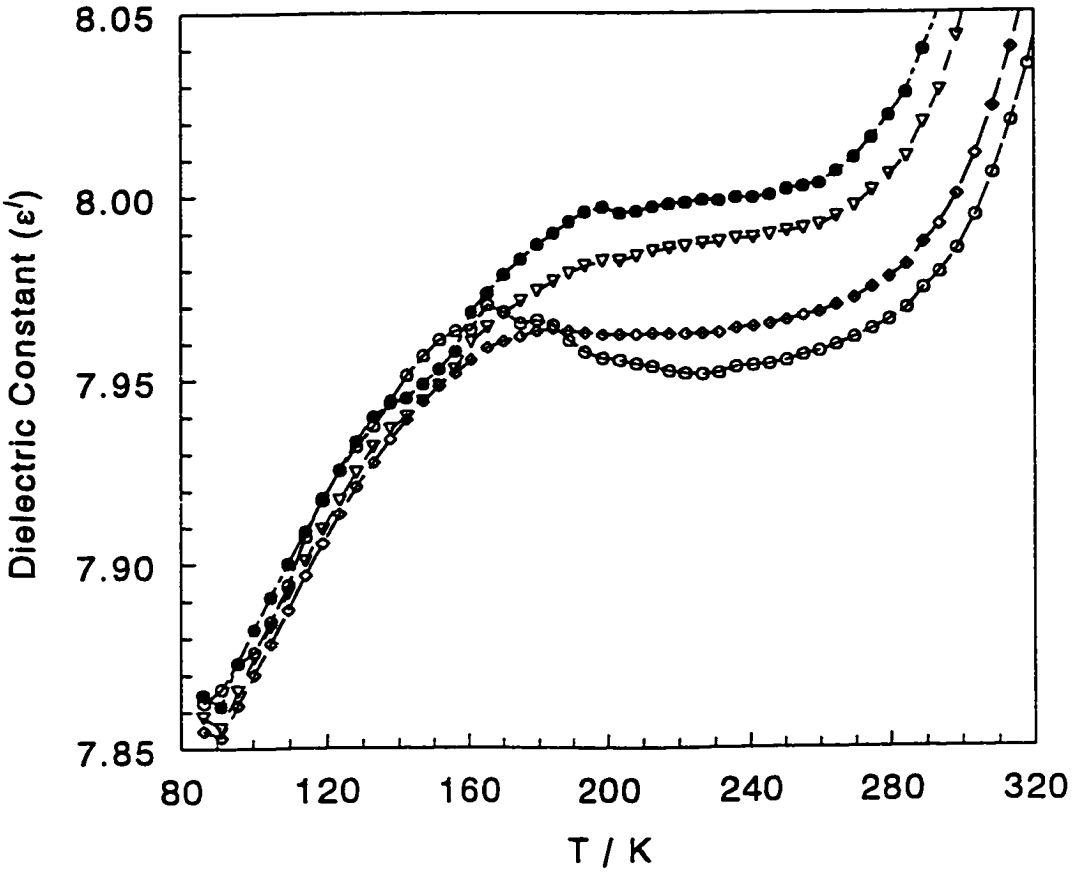

frequencies are very nearly coincident which is not characteristic of dielectric relaxation. Furthermore, if the curves in Figure 8.10 truly did arise from a dielectric relaxation process, dielectric losses would be expected. However, no appreciable dielectric losses were observed in this temperature region.

Since the tell-tale signs of a dielectric relaxation process were not observed in the NaOH dielectric measurements, some other factor must be responsible for the anomalous broad peak present in the dielectric constant curves for NaOH in the 80 K to 230 K temperature range. A phase transition might be suspected, but the shape of the NaOH anomaly does not closely resemble the lambda-shaped peak indicating a phase transition in the NaOD measurements, nor does it correspond to the anomalies observed in the dielectric constant curves of NH_4Br and NH_4Cl indicating the occurrence of phase transitions in these compounds (Chapter 7).

There is, however, a striking similarity between the broad peak found in the temperature-dependent dielectric constant measurements of NaOH and the anomalous peak reported in the dielectric constant curve for the compound $(NH_4)_3H(SO_4)_2$, as summarized in Section 2.3.1 (see Figure 2.1).[48] The broad peak at ambient pressure in the dielectric constant curve of $(NH_4)_3H(SO_4)_2$ centred at $\sim$ -25°C as shown in Figure 2.1, was found to be a prelude to a phase transition to a ferroelectric phase that would occur in $(NH_4)_3H(SO_4)_2$ under applied pressure.[50,51] As reported in the literature, when the dielectric constant of $(NH_4)_3H(SO_4)_2$ was measured as a function of temperature with the application of pressure, the anomalous broad peak became sharper, with a larger maximum, until, at a pressure of $\sim$ 5 kbar, the peak split into two sharp peaks (*i.e.*, two

transitions) with a new ferroelectric phase between them (named phase VI), with a second ferroelectric phase forming at still higher pressures (phase VII).[50,51] The broad hump observed in the dielectric constant curve of this compound at atmospheric pressure was thought to be the result of increased dipolar polarization due to a concerted fluctuation of dipoles within the solid that first increases and then decreases with decreasing temperature without diverging to form a ferroelectric phase.[51] It is interesting that the ferroelectric phases (phases VI and VII) are observed in the deuterated form of this substance ($(ND_4)_3D(SO_4)_2$) at atmospheric pressure.[54] Thus, the ferroelectric phases of $(NH_4)_3H(SO_4)_2$ can be induced by pressure or by deuteration. In fact, the phase diagrams for the protonated and deuterated forms of this salt (Figures 2.2 and 2.3, respectively) indicate that deuteration approximately corresponds to an increase in pressure of about 5 kbar.

The analogy between the behaviour of $(NH_4)_3H(SO_4)_2$ and its deuterated form, and the observed properties of NaOH/NaOD is remarkable. A low-temperature phase transition to an antiferroelectric phase is observed for NaOD at atmospheric pressure. No evidence is known to indicate that such a phase transition occurs in NaOH under ambient pressure. Yet, the dielectric constant of NaOH measured as a function of temperature does reveal an anomalous peak centred at ~ 170 K as shown in Figure 8.9, which is too broad to be the result of a phase transition taking place. By analogy with the atmospheric pressure dielectric measurements reported for $(NH_4)_3H(SO_4)_2$, however, this broad peak observed in the dielectric measurements of NaOH is most probably a prelude to the occurrence of a polymorphic phase transition to an antiferroelectric phase at higher

pressures. Carrying this line of reasoning further, this high-pressure antiferroelectric phase of NaOH should be analogous to the low-temperature antiferroelectric phase observed for NaOD at ambient pressure, although the measured dielectric data for NaOH does not, by itself, exclude the possibility that the high-pressure phase of NaOH alluded to by the broad peak may be ferroelectric.

Especially interesting were the results from three separate dielectric runs involving NaOH sample #4. The dielectric constant data collected from one of these runs are shown in Figure 8.11 for a frequency of 10 kHz (nearly identical curves were obtained for all of the frequencies measured) involving a heating rate of 0.15 $K \cdot min^{-1}$. The plot in this figure contains a small, fairly sharp lambda-shaped anomaly with a peak dielectric constant value occurring at a temperature between 190 K and 200 K. The anomaly in this plot appears to be superimposed on a dielectric constant curve which increases steadily with temperature indicative of normal temperature-dependent dielectric behaviour. The resemblance between the anomaly evident in the plot of Figure 8.11 and the lambda-shaped dielectric anomaly observed for NaOD when it undergoes its phase transition to a low-temperature antiferroelectric phase is unmistakable. The magnitude of the lambda-shaped anomaly observed in the dielectric data for NaOD is much larger, however, with an increase in dielectric constant from $T = 100$ K to the peak of the anomaly being over 2.2 units (representing a 22% increase), compared to < 0.15 units (1.8% increase) for the anomaly shown for the NaOH measurements in Figure 8.11.

Several extraneous possibilities were considered that could give rise to such an anomaly in the NaOH dielectric constant curves. First of all, it was thought that the

Figure 8.11. Dielectric constant of NaOH as a function of temperature measured during a run of NaOH sample #4 at a frequency of 10 kHz. The heating rate during this run was 0.13 - 0.18 $K \cdot min^{-1}$. For each data point, the total experimental uncertainty in the dielectric constant is within $\pm$ 0.25. However, the uncertainty associated only with random errors in the dielectric constant measurements is within $\pm$ 0.018.

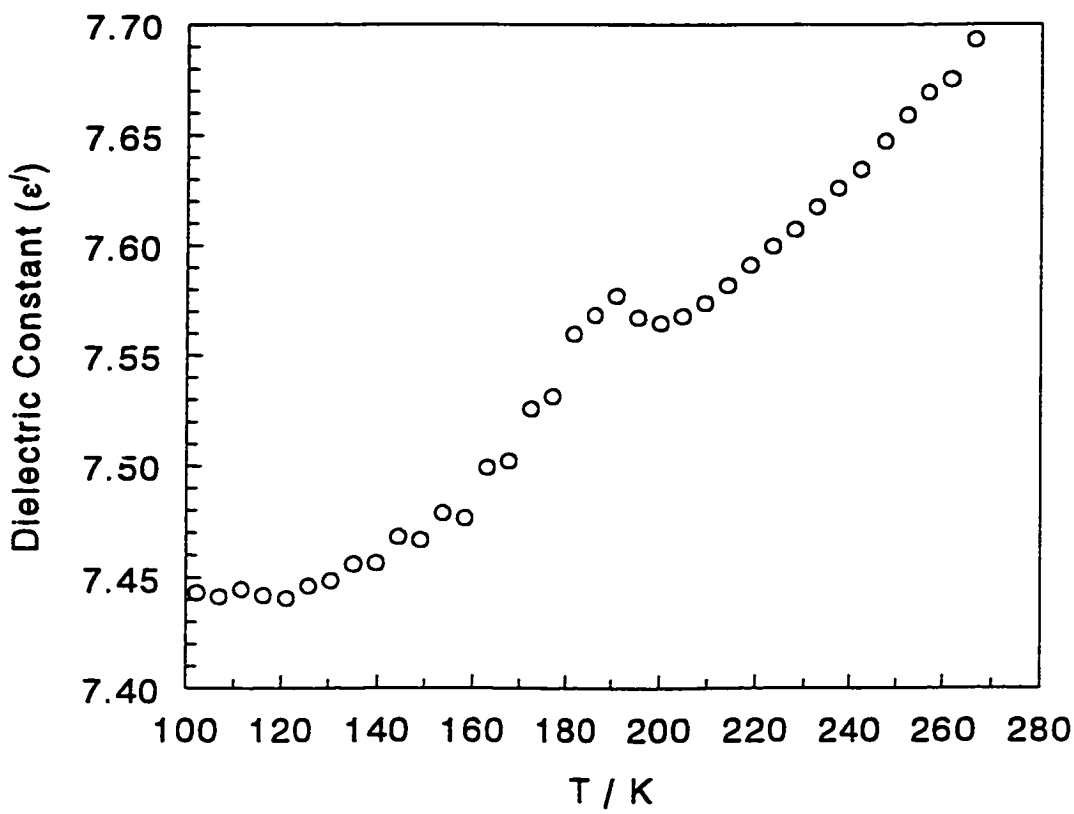

NaOH sample might have been contaminated with some NaOD, a small amount of which could account for the occurrence of the small anomaly when the NaOD impurity undergoes its low-temperature phase transition. However, all of the equipment used in the preparation of the NaOH sample was thoroughly cleaned and dried before use, and the electrodes of the sample cell were well-cleaned between samples, so the possibility of NaOD contamination is remote. Furthermore, the peak of the anomaly in Figure 8.11 occurs at a temperature at least 30 K above that observed for the NaOD dielectric anomaly in Figure 8.2, where an even slower heating rate was used in the experiment from which the NaOH data presented in Figure 8.11 were obtained, compared to the heating rate used to obtain the NaOD data in Figure 8.2. Therefore, it seems highly unlikely that the small lambda-shaped anomalies observed in three runs for the NaOH sample could be the result of NaOD contamination.

Other possibilities that were considered were the effects of the monohydrate and carbonate impurities in the NaOH sample. The amounts of these impurities in the sample were determined to be reasonably small using DSC as described in Section 8.3.1. If a phase transition occurred in $NaOH{\cdot}H_2O$ or Na_2CO_3 in the ~ 180 K to 200 K temperature range, this could account for the existence of the anomaly in the NaOH dielectric constant curve as shown in Figure 8.11 (and observed in at least two other runs). However, both $NaOH{\cdot}H_2O$ and Na_2CO_3 have been well-characterized by calorimetry.[139,202,367] A survey of the heat capacity data for these substances reported in the literature revealed that neither $NaOH{\cdot}H_2O$ nor Na_2CO_3 are known to undergo a phase transition or exhibit any other kind of thermal anomaly below 300 K.

An interesting possibility presented itself through the method by which the NaOH sample was prepared. Sodium hydroxide pellets were ground into a fine powder by manually grinding them with a mortar and pestle for about 15 minutes. There are many examples in the literature where the pressure and shear stresses caused by grinding substances in a mortar, ball mill, or other grinding devices causes a pressure-induced process to occur in the solid. Mechanical grinding of a solid in some cases has resulted in the formation of a high-pressure polymorphic phase that exists metastably when the pressure of the grinding action is released.[368,369,370,371] The pressure produced during the grinding of the calcite form of $CaCO_3$ resulted in the transformation to the high-pressure aragonite form which remained metastably when the grinding was stopped.[368] The onset of the appearance of the metastable form occurred after 0.5 hr of grinding with more being formed with longer grinding times. The pressure required to induce the calcite to aragonite phase transformation is about 3 kbar at room temperature.[372] Similar grinding experiments resulted in the high-pressure phases of PbO, PbO_2, MnF_2, Sb_2O_3, and BeF_2 being formed after several hours of grinding.[370] It has been estimated from these experiments that the maximum pressure exerted on a material that is ground in an automatic mortar is not less than 15 kbar.[370]

Other examples of processes induced by grinding are chemical reactions that are mechanically initiated by the grinding of mixtures of materials.[373] Also, the formation of a polymorphic phase of calcium carbide has been reported to occur by grinding.[374] Furthermore, the formation of amorphous solids from their corresponding crystalline forms is known to occur for several substances through the action of

grinding.[375,376,377] This process of solid-state amorphization has been observed for quartz,[375] some inclusion compounds,[376,377] and some organic compounds such as sucrose and phenolphthalein.[376,377] Amorphous metallic alloys also can be formed through the mechanical treatment of mixtures.[378,379]

Given the evidence from the literature that materials which are ground in a mortar are subjected to pressures on the order of several kilobars, it is possible that when the sample of NaOH was ground into a powder with a mortar and pestle, a small amount of a high-pressure phase was formed that remained in a metastable form when the grinding was stopped. From the phase diagram of NaOH shown in Figure 3.8 of Section 3.4,[172] it can be seen that pressures less than 10 kbar are required to produce the high-pressure phases IV and V. These pressures could have been produced in grinding. This phase diagram was deduced based upon high-pressure Raman spectroscopy measurements of NaOH, which also revealed that the high-pressure phase V of NaOH could be quenched upon the release of pressure, to exist metastably at ambient pressure.[172] Some pressure hysteresis was also observed for phase IV.[172]

Thus, it does seem possible that the formation of a small amount of a high-pressure form of NaOH occurred during the grinding process. The NaOH was further subjected to pressure during the pressing of the powder in a die and piston device to form the pressed powder pellet. If a small amount of NaOH did remain in a metastably compressed state after grinding and/or the pressing of the powder to form the pellet, at low temperatures a small amount of NaOH phase IV could have been formed. This phase is analogous to the low-temperature antiferroelectric phase IV of NaOD which exists in

equilibrium at ambient pressure. Assuming phase IV of NaOH is also antiferroelectric, the small amount of phase IV in the NaOH dielectric sample would be expected to exhibit a small lambda-shaped anomaly in its dielectric constant curve when it undergoes a phase transition to the high-temperature orthorhombic phase. According to the dielectric results shown in Figure 8.11, this phase transition took place at a temperature of ~ 190 K to 200 K. Thus, the existence of a metastable high-pressure phase of NaOH at low temperatures which formed as a result of grinding is a possible explanation for the observation of the small anomaly observed in the measured dielectric constant behaviour of the NaOH sample shown in Figure 8.11 (and observed in two other runs with this sample). The reason why this anomaly occurred only in some runs but not in others is still not understood.

8.4 Summary

The low-temperature phase transition in NaOD to its antiferroelectric phase is clearly evident in the results of the NaOD dielectric constant measurements through the observation of a characteristic antiferroelectric anomaly in the dielectric constant curve of NaOD. For NaOH, no analogous phase transition and no evidence for relaxation of the dipolar polarization mechanism was found in the results of the dielectric measurements. However, a broad peak centred near T = 170 K was observed in the temperature-dependent dielectric constant curve for NaOH which appears to foreshadow

the existence of a phase transition to a low-temperature antiferroelectric (or possibly ferroelectric) phase at higher pressures. A sneak preview of this phase transition was possibly provided at atmospheric pressure through the formation of a small amount of the high-pressure antiferroelectric phase in metastable form as a result of the pressures created during grinding of the NaOH sample with a mortar and pestle. This would account for the small lambda-shaped anomaly with a peak dielectric constant value occurring between T = 190 K and 200 K that was observed in some of the NaOH dielectric constant experiments.

Chapter 9: Overall Discussion

9.1 Residual Entropy in NaOH

A postulate of frozen-in disorder in NaOH was introduced as a possible explanation to account for the lack of a low-temperature phase transition in NaOH at atmospheric pressure analogous to the low-temperature phase transition observed in NaOD. This postulate was supported by a residual entropy calculation[200] for NaOH which suggested that NaOH possesses entropy at absolute zero amounting to 5.2 ± 1.3 $J \cdot K^{-1} \cdot mol^{-1}$. This residual entropy could arise from a freezing-in of the disorder of the hydrogen atoms in NaOH before a low-temperature phase transition could take place. The low-temperature phase transition in NaOD removes some disorder associated with the deuterium atoms. The removal of some disorder associated with the hydrogen atoms in NaOH might also be expected, but experimental observations reveal[140] that this does not happen by way of a low-temperature phase transition as observed for NaOD. The existence of residual entropy in NaOH would help to resolve this discrepancy, by indicating that this hydrogen-atom disorder does not get removed, but becomes frozen-in at low temperatures.

The residual entropy calculation[200] referred to in Section 4.1.4 was made based upon a single equilibrium constant value determined from the literature[201] for a reaction involving NaOH (equation (4.9)). This is not sufficient evidence to conclusively state that frozen-in disorder does exist in NaOH at low temperatures. The onset of frozen-in

disorder in a substance reveals itself through the observation of a glassy phase transition in its heat capacity curve. Such a glassy phase anomaly can be detected through the observation of characteristic relaxational effects (*e.g.*, thermal and dielectric) by the substance under study. Thus, some of the relaxational properties of NaOH were extensively studied in order to more confidently address the possibility of residual entropy in NaOH.

Several experiments were performed in this research work for this purpose. These experiments included an extensive adiabatic calorimetric study of NaOH to look for anomalous temperature drifts that are normally associated with a glassy phase transition. Also, dielectric relaxation measurements were done on several pressed powder samples of NaOH, using a newly constructed dielectric relaxation apparatus, in search of dielectric behaviour indicating a dipolar relaxational process that could be associated with frozen-in disorder in NaOH.

The results of the calorimetric study of NaOH were inconclusive. Some anomalies were observed in the measured temperature-drift behaviour as described in Chapter 5, but these could all be accounted for as being due to external factors involving the setup of the calorimeter, and not the NaOH sample.

The dielectric relaxation experiments of NaOH covered the temperature range from 12 K to 350 K at several frequencies between 80 Hz and 800 kHz. Throughout these experiments, the only relaxational process evident in the dielectric measurements of NaOH was the relaxation of the interfacial polarization. As explained in Chapters 7 and 8, the interfacial polarization is not an intrinsic property of bulk NaOH, but is a

result of the powder nature of the measured samples. No dispersion curves indicating the relaxation of a dipolar reorientational process were observed for any of the NaOH dielectric measurements.

The data obtained from the calorimetric and dielectric measurements of NaOH provided the necessary evidence for a firm judgement concerning the possibility of residual entropy in NaOH. Since no conclusive evidence for the existence of a glassy phase transition in NaOH was found from the calorimetric and dielectric relaxation measurements, it can be concluded that it is highly unlikely that frozen-in disorder exists in sodium hydroxide at low temperatures. Thus, residual entropy cannot be invoked as a possible explanation to account for the anomalous low-temperature behaviour of NaOH.

9.2 Deuterium-Induced Phase Transition in NaOD

Although evidence for a dipolar relaxational process was not found in the NaOH dielectric measurements, these experiments did reveal a broad anomaly in the dielectric constant curve for NaOH centred near $T = 170$ K. This anomaly was too broad to be the result of a phase transition taking place. By comparison, dielectric measurements of NaOD showed a very sharp lambda-shaped anomaly near 160 K as a direct result of its deuterium-induced phase transition to a low-temperature antiferroelectric phase. The broad anomaly observed in the NaOH dielectric measurements resembles a similar anomaly observed in dielectric measurements reported for $(NH_4)_3H(SO_4)_2$.[48] From

dielectric measurements reported for $(NH_4)_3H(SO_4)_2$ performed as a function of temperature and pressure, this anomaly was found to be the signature of a phase transition that fully manifests itself only at higher pressures.[50,51] It is reasonable to conclude that the similar anomaly in the atmospheric pressure NaOH dielectric constant curve is also indicative of a phase transition that will occur only upon application of pressure. This high-pressure NaOH phase could be analogous to the low-temperature antiferroelectric phase of NaOD at atmospheric pressure, just as the high pressure ferroelectric phases in $(NH_4)_3H(SO_4)_2$ were analogous to similar phases observed for the deuterated form under ambient-pressure conditions. Possible support for this conclusion came from the observation of small antiferroelectric-like anomalies in the dielectric constant curves in some of the dielectric runs for NaOH. These could be the result of a small amount of the high-pressure antiferroelectric phase existing in the sample in metastable form at low temperatures, possibly created by the pressures inflicted upon the NaOH sample when it was ground during its preparation.

The existence of a high-pressure antiferroelectric phase transition in NaOH (alluded to by the dielectric measurements) analogous to the ambient-pressure antiferroelectric phase transition observed for NaOD was not unexpected. Pressure- and temperature-dependent Raman spectroscopy measurements of NaOH and NaOD reported in the literature (and summarized in Section 3.4),[172] revealed the existence of a high-pressure hydrogen-bonded form of NaOH (called phase IV, see Figure 3.8) whose Raman spectrum was similar to the ambient-pressure antiferroelectric hydrogen-bonded phase of NaOD. The dielectric measurements of NaOH and NaOD presented here

provide further evidence of this analogy.

From the phase diagrams of NaOH and NaOD derived from the literature Raman studies of these two compounds (see Figure 3.8), it is apparent that a pressure of less than 10 kbar can induce the transformation to the antiferroelectric phase IV in NaOH.[172] In fact, a shift of the temperature axis of the NaOH phase diagram by approximately 10 kbar to higher pressures would almost exactly reproduce the NaOD phase diagram. Thus, it appears that deuteration is approximately equivalent to an increase in pressure. This same conclusion was reached upon comparison of the phase diagrams of $(NH_4)_3H(SO_4)_2$ and its deuterated form $(ND_4)_3D(SO_4)_2$ (see Figures 2.2 and 2.3).[49,56] A similar equivalence between deuteration and the application of pressure has been observed for several systems, including NH_4Cl/ND_4Cl, NH_4Br/ND_4Br, and CH_4/CD_4.[380,381,382,383,384]

The pressure/deuteration equivalence of NaOH can at least be partially explained by the geometric effects which are observed when hydrogen atoms involved in hydrogen bonds are replaced with deuterium. These effects were first investigated extensively by Ubbelohde and co-workers,[102,385,386] with many subsequent studies being reported by others.[387,388,389] It was found that for most short hydrogen bonds, with the distance between the electronegative atoms involved in the H-bond (*e.g.*, oxygen-to-oxygen distance) in the range of 2.45 to 2.65 Å, an expansion of the hydrogen bond distance by as much as 0.07 Å was observed upon substitution of the hydrogen atom with deuterium.[389] This phenomenon was thoroughly reinvestigated by Ichikawa who introduced this "geometric isotope effect" as a possible explanation for the large deuterium-induced effects observed for the phase transition temperatures of many

hydrogen-bonded solids.[82,95,96] The geometric isotope effect was summarized in Section 2.3.4.

A different kind of geometric isotope effect is observed for the alkali-metal hydroxides and deuteroxides. Table 9.1 lists the unit-cell volumes of the alkali-metal hydroxides and deuteroxides as calculated from reported crystallographic data. For every hydroxide, a comparison of the volumes of the hydrogenated and deuterated forms reveals that the deuterated form has the smaller unit-cell volume. This implies a geometric effect which is opposite to that described first by Ubbelohde, and later by Ichikawa. For the alkali-metal hydroxides, substitution of the hydrogen atoms with deuterium results in shorter oxygen-to-oxygen distances and thus, there is potential for stronger hydrogen bonds to be formed in the low-temperature phases of the deuterated compounds. This is supported by vibrational spectroscopy measurements reported for KOH/KOD,[187] RbOH/RbOD,[182,183] and CsOH/CsOD,[182,183] which show that the deuterated compounds exhibit stronger (*i.e.*, shorter) hydrogen bonds in their low-temperature hydrogen-bonded phases compared to the analogous phases of the hydrogenated compounds.

The hydrogen-bond distances (oxygen-to-oxygen) in all of the low-temperature phases of the alkali-metal hydroxides and deuteroxides are very long.[141,143,144,145,160] Values which are reported for the oxygen-oxygen distances in the low-temperature phases of these compounds include 3.24 Å for KOD at 100 K,[143] 3.24 Å for RbOD at 185 K,[144] and 3.30 Å for CsOD at 77 K.[145] By comparison, the hydrogen-bond distance in ice is 2.76 Å at 273 K.[390]

Table 9.1. A listing of the unit-cell volumes of the alkali-metal hydroxides and deuteroxides (except LiOH and LiOD) as calculated from literature crystallographic data for each compound. For some of the compounds, data from more than one temperature and/or more than one source are given. No uncertainty is listed for data obtained from literature sources which neglected to provide uncertainties in the crystallographic dimensions.

Compound	Temperature / K	Unit-Cell Volume / Å^3	Reference
NaOH	294	131.518 ± 0.040	162
NaOH	297	131.472 ± 0.080	160
NaOH	298	131.653 ± 0.080	141
NaOD	293	130.70	140
KOH	293	88.31[a]	170
KOD	295	87.98 ± 0.43[a]	143
RbOH	213	194.749 ± 0.079	144
RbOD	208	192.885 ± 0.058	144
CsOH	293	236.915 ± 0.043	171
CsOH	293	235.58 ± 0.27	145
CsOD	293	233.588 ± 0.087	145
CsOH	77	224.531 ± 0.035	171
CsOD	77	222.702 ± 0.092	145

[a] $Z = 2$, whereas $Z = 4$ for all the other unit cells.

From crystallographic measurements of NaOH and NaOD, it has been reported that the interlayer distance in NaOD is smaller than that in NaOH by 0.3% to 0.6%, with the difference increasing with decreasing temperature.[141] It is likely that the interlayer distance in NaOH (oxygen-oxygen distance between the layers is 3.488 Å at room temperature[160]) is very close to the upper limit at which a hydrogen-bonded interaction can occur. The shorter interlayer distance in NaOD gives it a distinct advantage towards the possibility of forming a hydrogen-bonded low-temperature phase. Thus, it is likely that the potential hydrogen-bond distance in NaOH is just outside of a threshold limit below which hydrogen bonds can form, while the corresponding distance in NaOD is just below this limit.

While substitution of deuterium for hydrogen in NaOH causes a contraction of the interlayer distance, the same effect could be achieved by the application of pressure on NaOH, which naturally tends to contract lattice parameters. This was confirmed by high-pressure studies of NaOH and NaOD which showed that NaOH forms a hydrogen-bonded phase under an applied pressure of ~ 10 kbar, as summarized in Section 3.4.[172] This high-pressure phase of NaOH gave a Raman spectrum analogous to that measured for the hydrogen-bonded phase of NaOD.[172] Thus, the equivalence of deuteration and pressure observed for NaOH can be at least partially accounted for by the contraction of lattice parameters which occurs with either pressure or deuteration. By this argument, one could regard the lack of a low-temperature phase transition in NaOH as being due to the fortuitous occurrence of an interlayer oxygen-oxygen distance which is just slightly too long for hydrogen bonds to form at ambient pressure. The contraction of this distance

upon substitution of the hydrogen atom with deuterium results in an oxygen-oxygen distance in NaOD which appears to be just short enough to form hydrogen bonds and enables NaOD to undergo the low-temperature deuterium-induced phase transition at atmospheric pressure.

No explanation has been put forth which satisfactorily accounts for the geometric effects associated with deuterium substitution. Several postulates have been made, however. Qualitatively, it has been suggested that the overall geometric effects associated with deuterium substitution are the result of two competing factors.[391]

A contraction of the hydrogen-bond length on deuteration would occur due to an increase in dipole moment.[391] A theoretical explanation of this effect has been reported,[392] based upon the reorientation of molecular dipoles that would occur due to the librational vibrational modes in a substance. A quantum-mechanical calculation of the expectation value of the dipole moment shows that a deuterated compound will have a slightly larger dipole moment in the equilibrium direction compared to the analogous hydrogenated compound.[392] This is a consequence of the different librational frequencies of the isotopomeric compounds and the larger moment of inertia of the deuterated compound. The larger dipole moment in the deuterated compound would tend to cause stronger (*i.e.*, shorter) hydrogen bonds to be formed because of the stronger electrostatic attraction that would exist between the greater dipole moment and an electronegative acceptor atom.[392,393] The contraction effect of deuteration also has been explained as resulting from the lower vibrational frequency of bonds containing deuterium because of the larger mass of deuterium compared with hydrogen.[394] This permits the closer approach of nearby

electronegative atoms to form stronger hydrogen bonds.

On the other hand, a tendency for expansion of the hydrogen-bond length upon deuteration results from the difference in the zero-point energies of hydrogen and deuterium.[386,391,395] The greater overlap of wavefunctions between two wells in the double-well potential of a hydrogen bond for hydrogen compared with deuterium will result in greater hydrogen density at the centre between the two electronegative atoms. The increased hydrogen density at the centre will tend to attract both electronegative atoms resulting in a shorter hydrogen bond for hydrogen compared with deuterium.[395] Substitution with deuterium leads to less density in the centre and the hydrogen bond becomes longer.

The expansion effect would be the dominant one for short hydrogen bonds, while the effect causing contraction would predominate for long hydrogen bonds,[391,396] as for the alkali-metal hydroxides and deuteroxides. Another explanation reported in the literature relates the expansion/contraction geometric effects associated with deuteration to the differing vibrational amplitudes of the O-H *versus* O-D stretching and librational modes.[397,398] For short hydrogen bonds, the influence of the stretching modes is dominant and thus, a shorter (stronger) hydrogen bond will result for hydrogen compared with deuterium. The opposite trend is observed for long hydrogen bonds because librational modes (which tend to weaken the hydrogen bond) have a dominating influence. In this case, a shorter (stronger) hydrogen bond will be observed for the deuterated compound because of the smaller amplitude of the O-D librational mode compared to the corresponding O-H librational mode. Several more quantitative theories for the geometric

effects associated with deuterium substitution also exist in the literature.[103,104,399,400]

9.3 Entropy Removal in NaOH

As determined by adiabatic calorimetry, the deuterium-induced phase transition which occurs in NaOD at $T = 153$ K has an associated entropy change[152] of 0.864 $J \cdot K^{-1} \cdot mol^{-1}$, which is almost totally due to a change in the disorder of the deuterium atoms. Thus, cooling NaOD through the phase transition removes about 0.864 $J \cdot K^{-1} \cdot mol^{-1}$ of entropy associated with the deuterium atoms. Given the similarities in the polymorphic behaviour and structures of NaOD and NaOH at high temperatures,[141] it would be expected that, upon cooling, the hydrogen atoms in NaOH would have to remove a similar amount of disorder before absolute zero is reached, in order to obey the third law of thermodynamics. The distinct absence of a low-temperature phase transition in NaOH, analogous to that in NaOD, clearly indicates that this does not happen by way of a phase transition, at least not at ambient pressure.[140]

The possible explanation that was proposed in Section 3.5 to resolve this entropy-removal problem suggested that the extra disorder of the hydrogen atoms in NaOH does not get removed upon cooling, but becomes frozen-in at low temperatures. This would give rise to residual entropy in NaOH. However, as the detailed experimental work performed on NaOH in this thesis has shown, residual entropy is unlikely in sodium hydroxide. Thus, some mechanism other than a phase transition must exist in NaOH at

low temperatures by which the extra entropy associated with the hydrogen atoms can be removed.

An important clue as to the nature of this entropy-removal mechanism was revealed when the low-temperature heat capacities of NaOH and NaOD were compared. Figure 9.1 gives the heat capacities of both compounds from $T \sim 20$ K to 60 K.[139,152] For NaOH, two sets of data are plotted: one set are heat capacity data for NaOH reported in the literature,[139] and the second set consists of the low-temperature heat capacity values determined for NaOH during this thesis work, as described in Chapter 5.

It is clearly evident from the data plotted in Figure 9.1 that at low temperatures the heat capacity of NaOH is greater than that of NaOD. At higher temperatures the opposite is true, *i.e.*, the heat capacity of NaOD is greater, as can be seen in Figure 3.2. The higher heat capacity of NaOH over NaOD at low temperatures is contrary to what is expected from consideration of purely vibrational and rotational contributions to the heat capacity, the reason for which will now be explained.

The spacing between vibrational levels for a diatomic molecule in the harmonic oscillator approximation is given by[401]

$$\nu = \frac{1}{2\pi}\sqrt{\frac{k_f}{\mu}}\,, \tag{9.1}$$

where ν is the classical frequency of vibration and also corresponds to the spacing between vibrational energy levels, k_f is the force constant for the vibration, and μ is the reduced mass. The classical frequency of vibration for polyatomic vibrational modes has

Figure 9.1. Low-temperature heat capacities for NaOH[139] and NaOD.[152] Two sets of data are plotted for NaOH. The lines are the results of separate best-fit ninth-order polynomials to the literature NaOH data and to the NaOD data. ○ NaOH data from this thesis work, + NaOH data from reference (139), ● NaOD data from reference (152).

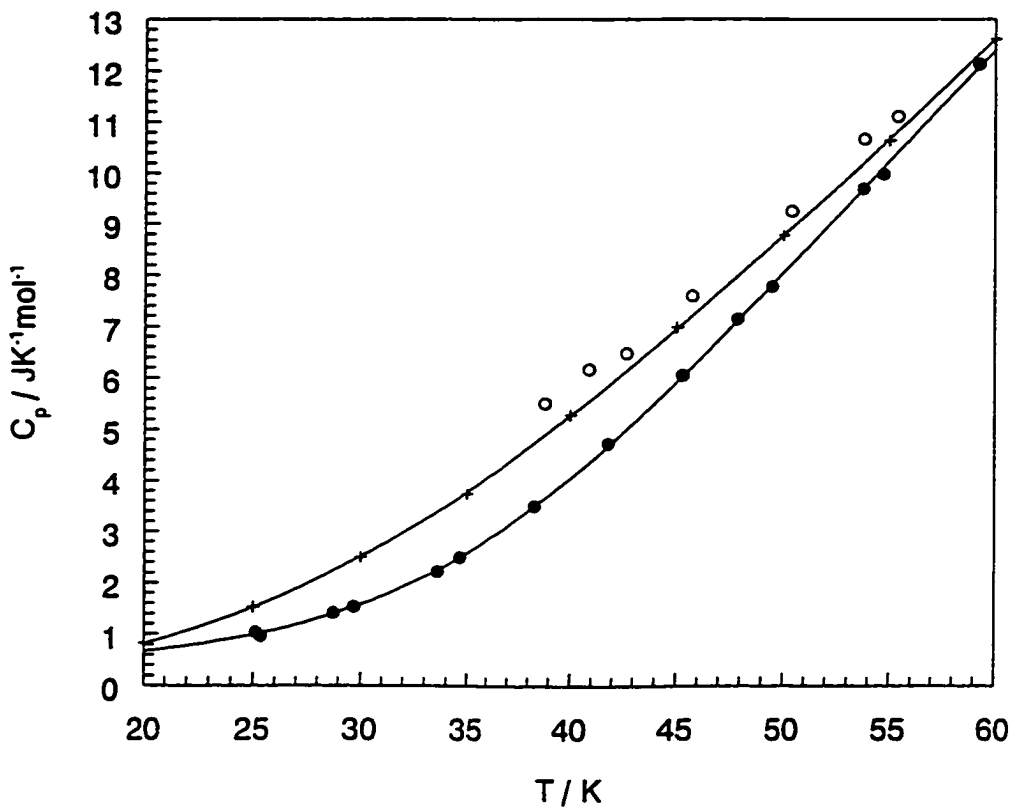

a similar mass dependence. The important point is that the classical frequency of vibration (spacing between vibrational levels) as given by equation (9.1) will decrease when the mass of the atoms involved in the vibration increases. Since the deuterated form of a compound has a higher mass than the hydrogenated form, the vibrational energy levels must be more closely spaced for the D-compound as compared to the H-compound. A schematic diagram showing this difference in the spacing of the vibrational energy levels is given in Figure 9.2.

An examination of Figure 9.2 indicates that because of the greater density of energy levels for the deuterated form over its hydrogenated counterpart, the deuterated compound can access more energy levels for a given amount of thermal energy (k_BT). Since the heat capacity (at constant volume) is defined as the rate of change of the internal energy with a change in temperature, it is evident that the deuterated form should have a higher heat capacity because the energy levels of the D-form are more closely spaced than for the analogous H-form.

This can be shown more quantitatively by an examination of the Einstein equation for the heat capacity, which is useful for describing the contribution to the heat capacity from the optic vibrational modes in the crystal, *i.e.*,[254,255]

$$C_v = 3R\left[\frac{\theta_E}{T}\right]^2 \frac{e^{\theta_E/T}}{(e^{\theta_E/T}-1)^2}, \qquad (9.2)$$

where θ_E is the Einstein characteristic temperature, given by

Figure 9.2. A schematic diagram showing the difference in the vibrational energy-level distributions for a hydrogenated compound *versus* its corresponding deuterated form (within the harmonic oscillator approximation). The quantity k_BT represents a given amount of thermal energy available to excite a molecule of each compound.

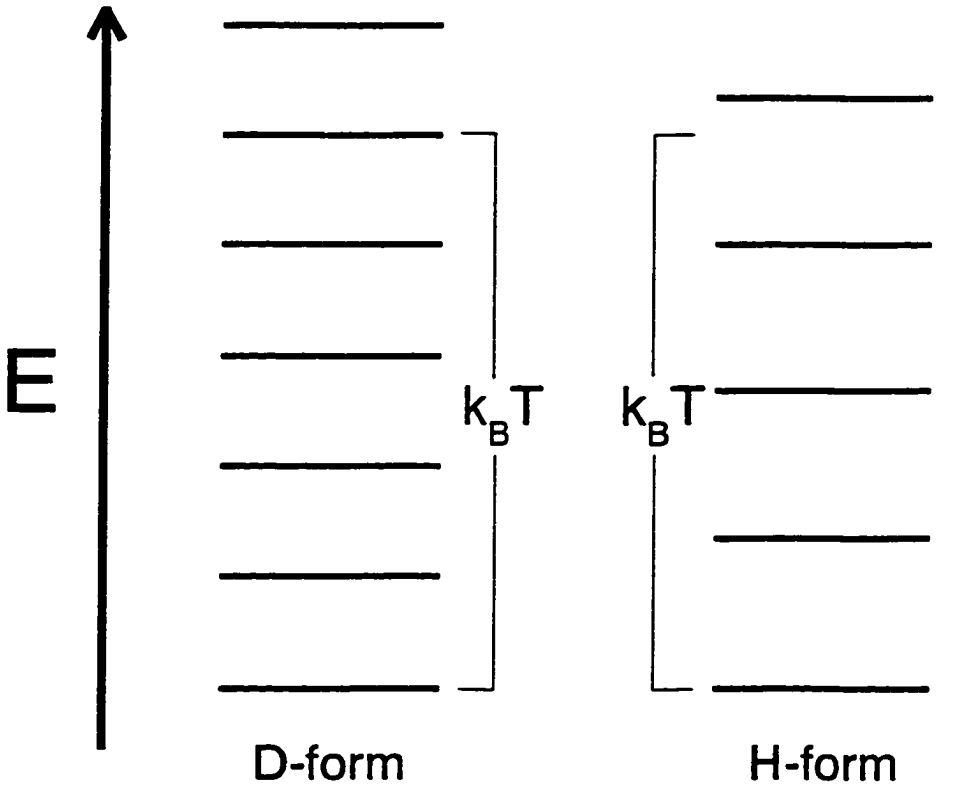

$$\theta_E = \frac{h\nu}{k_B}, \tag{9.3}$$

h is Planck's constant, and ν is the classical frequency of vibration as given by equation (9.1). Because of the greater mass of a deuterated substance, the classical frequency of vibration will be smaller. This means that the Einstein temperature for the deuterated compound will be smaller than that for the hydrogenated compound. From an examination of the θ_E-dependence of equation (9.2), it can be shown that for a given temperature, a smaller Einstein temperature will give rise to a larger heat capacity value. A similar argument can be made using the Debye equation for the heat capacity (equation (5.12)).[254,256] Thus, from vibrational considerations, the heat capacity of the deuterated form of a compound should have a higher heat capacity than the corresponding hydrogenated form.

The same conclusion can be reached from a consideration of rotational contributions to the heat capacity. The spacing between the rotational levels of a substance decreases when the mass increases, so by a similar argument as that used when discussing vibration, the same conclusion can be reached: the deuterated compound should have the higher heat capacity.

Despite all of the arguments just presented, the data in Figure 9.1 show that at low temperatures, the heat capacity of NaOH is greater than that of NaOD. This means that NaOH must have access to extra low-lying energy levels which cannot be accessed by NaOD. A major difference between deuterium atoms and hydrogen atoms is the greater ability of hydrogen atoms to undergo quantum-mechanical tunnelling. Recall from

Section 2.3.3 that the tunnelling interaction causes a splitting of the associated vibrational or rotational levels. Thus, it is likely that access to tunnelling energy levels in NaOH gives rise to its larger heat capacity as compared to NaOD at low temperatures.

To more firmly establish the extraneous nature of the apparent excess heat capacity of NaOH at low temperatures as indicated in Figure 9.1, the heat capacity data for both NaOH and NaOD were subjected to a detailed analysis, through which the component contributions to the heat capacity were calculated. From purely vibrational considerations, the experimentally measured value of the heat capacity (C_p) can be written as

$$C_p = C_v(acoustic) + C_v(optic) + (C_p - C_v), \qquad (9.4)$$

where $C_v(acoustic)$ is the contribution from the acoustic modes as described by the Debye model (equation (5.12)), $C_v(optic)$ is the contribution from the optic modes as described by the Einstein model (equation (9.2)), and the third term on the right-hand side of equation (9.4) is the C_p - C_v correction, which for isotropic materials is given by equation (5.4).

In determining the C_p - C_v correction, an approximation was made in that both NaOH and NaOD were considered to be isotropic compounds. This is strictly not correct, since NaOH is orthorhombic at all temperatures below 300 K, while NaOD is orthorhombic between room temperature and the phase transition at T = 153 K, with a monoclinic structure below the transition temperature. For anisotropic materials, the determination of the C_p - C_v correction requires knowledge of the components of the elastic constant and thermal expansion tensors,[402] neither of which have been reported for

NaOH or NaOD. Thus, an isotropic correction for both compounds was calculated. The error inherent in such an assumption should not significantly affect the overall heat-capacity analysis, since the C_p - C_v correction is typically very small at low temperatures.

Other assumptions also had to be made in calculating the C_p - C_v correction by equation (5.4). Since isothermal compressibility data for NaOH and NaOD have not been reported, the value for another ionic salt, NaCl, was used instead.[403] Also, there are limited volume data as a function of temperature available for use in determining the coefficient of thermal expansion. The scarce crystallographic volume data for NaOH[141,160,162] and NaOD[140] were fitted to separate quadratic equations. The extrapolated volume at absolute zero was determined by assuming that the volume *versus* temperature curve for NaOH and NaOD at low temperatures had a similar form to that for KOH and KOD, for which reported temperature-dependent crystallographic data are more extensive.[143,162] For NaOH, all of the experimental heat capacity data from the lowest measured temperatures to 310 K were used in the analysis, whereas for NaOD, only the experimental data below T = 110 K and between T = 180 K and 310 K were considered, as these data were deemed to be free from the effects of the polymorphic phase transition at 153 K. The calculated C_p - C_v correction values were very small for NaOH and NaOD below 100 K (< 0.12 $J \cdot K^{-1} \cdot mol^{-1}$) rising to a value of ~ 1.5 $J \cdot K^{-1} \cdot mol^{-1}$ at 300 K.

The contribution from the acoustic modes to the heat capacity should be nearly identical for both NaOH and NaOD, especially at low temperatures, since the Debye temperature of a crystal is proportional to the velocity of sound through the crystal, and

to the cube root of the number density of atoms in the crystal,[404] the values of which are very similar for both solids. A simple calculation using low-temperature crystallographic data for NaOH and NaOD confirms this,[140,162] giving

$$\theta_D\,(NaOD) \approx 0.962\,\theta_D\,(NaOH)\,, \qquad (9.5)$$

where $\theta_D(NaOD)$ and $\theta_D(NaOH)$ are the Debye temperatures of NaOD and NaOH, respectively. This slight difference between the Debye temperatures of NaOH and NaOD is not enough to cause any appreciable difference in the acoustic-mode heat capacities of the two compounds in the temperature region of interest.

The heat capacity contribution from the optic modes should be different for NaOH and NaOD, since the internal vibrational frequencies will be lower for a vibrational mode involving the deuterium atom in NaOD *versus* the corresponding mode in NaOH involving vibrational motion of the hydrogen atom. The frequencies of the fundamental vibrational modes in NaOH and NaOD have been determined using Raman and infrared spectroscopy.[405,406] The contribution from each mode was calculated using the measured frequencies and the Einstein heat capacity model, which is typically a valid representation of optic-mode heat capacity.[407]

The C_p - C_v correction data were used to convert the experimental NaOH and NaOD C_p values to C_v values. The literature values[139] for the heat capacity of NaOH shown in Figure 9.1 were used throughout these calculations, since these extended to lower temperatures than the data obtained in this thesis work. The contribution from all of the optic modes was then subtracted ($C_v(optic)$), using the data reported by Kanesaka, Tsuchida, and Kawai,[406] since it was more complete than the other available data set.[405]

The remaining heat capacity values should contain only the contribution from the acoustic modes, which will be nearly identical for both compounds, plus any non-vibrational contributions. However, subtraction of $C_v(optic)$ gave an unphysical result at low temperatures: for NaOH below $T \sim 40$ K, and for NaOD below ~ 50 K, the remaining heat capacity was negative.

At these low temperatures, the only optic modes which are significantly excited to appreciably contribute to the total heat capacity are the low-frequency modes (~ 100 cm^{-1}), the heat capacity contributions of which are the most sensitive to errors in frequency determinations. However, the frequencies of these modes would have been difficult to determine accurately from the reported vibrational spectra, since many of them appeared as shoulders superimposed on a broad absorption.[406] In fact, the two literature reports which gave normal-mode vibrational data for NaOH reported Raman frequencies for the low-frequency modes that differed by as much as 23 cm^{-1} for the same vibrational mode.[405,406] It is, therefore, likely that errors in the frequency determinations of the low-frequency modes gave rise to the negative heat capacity calculated at low temperatures upon subtraction of $C_v(optic)$.

It was possible to resolve this problem because the three lowest frequency modes in the vibrational spectra of NaOH and NaOD do not directly involve vibrational motion of the hydrogen or deuterium atoms, as could be observed from the reported vibrational assignments of each mode.[406] Thus, these three modes should have very similar frequencies for both substances. In fact, the reported frequencies for these three modes differed by at most 1 cm^{-1} for NaOH *versus* NaOD.[406] Therefore, subtraction of the

optic-mode heat capacity contributions from all the modes except for the three-lowest frequency modes should provide a common baseline for both compounds from which the existence of a non-vibrational contribution to the heat capacity of NaOH could be evaluated.

The heat capacities of NaOH and NaOD obtained after conversion of the experimental C_p values to C_v values followed by subtraction of all the optic-mode contributions except for the three lowest-frequency modes are shown for low temperatures in Figure 9.3(a). For the purposes of comparison, the experimentally determined low-temperature C_p values are given in Figure 9.3(b). In the absence of non-vibrational contributions to the heat capacity, one would expect the curves for NaOH and NaOD in Figure 9.3(a) to coincide. The data presented in this figure show that this is not the case. The NaOH heat capacity shown in Figure 9.3(a) is noticeably higher than that for NaOD, in a similar fashion as the difference exhibited by the experimental NaOH and NaOD heat capacities (C_p values) shown in Figure 9.3(b). The difference between the NaOH and NaOD heat capacities plotted in Figure 9.3(a) is larger at $T = 60$ K than the difference between the experimental heat capacities at the same temperature. This is likely due to errors in the frequency assignments of higher-frequency modes (> 200 cm^{-1}) which contribute significantly to the heat capacity at higher temperatures. From the results of this analysis, it is evident that the heat capacity of NaOH is greater than that of NaOD at low temperatures because NaOH has exclusive access to extra energy levels of non-vibrational origin, which are likely due to tunnelling.

The extra heat capacity of NaOH because of access to tunnelling levels imparts

Figure 9.3. (a) Low-temperature heat capacity values (C_v) of NaOH (○) and NaOD (●) obtained after conversion of the experimental C_p values[139,152] to C_v values and subsequent subtraction of $C_v(optic)$ excluding contributions from the three lowest-frequency optic modes. (b) Low-temperature experimentally determined heat capacity (C_p) values of NaOH (○) and NaOD (●).[139,152]

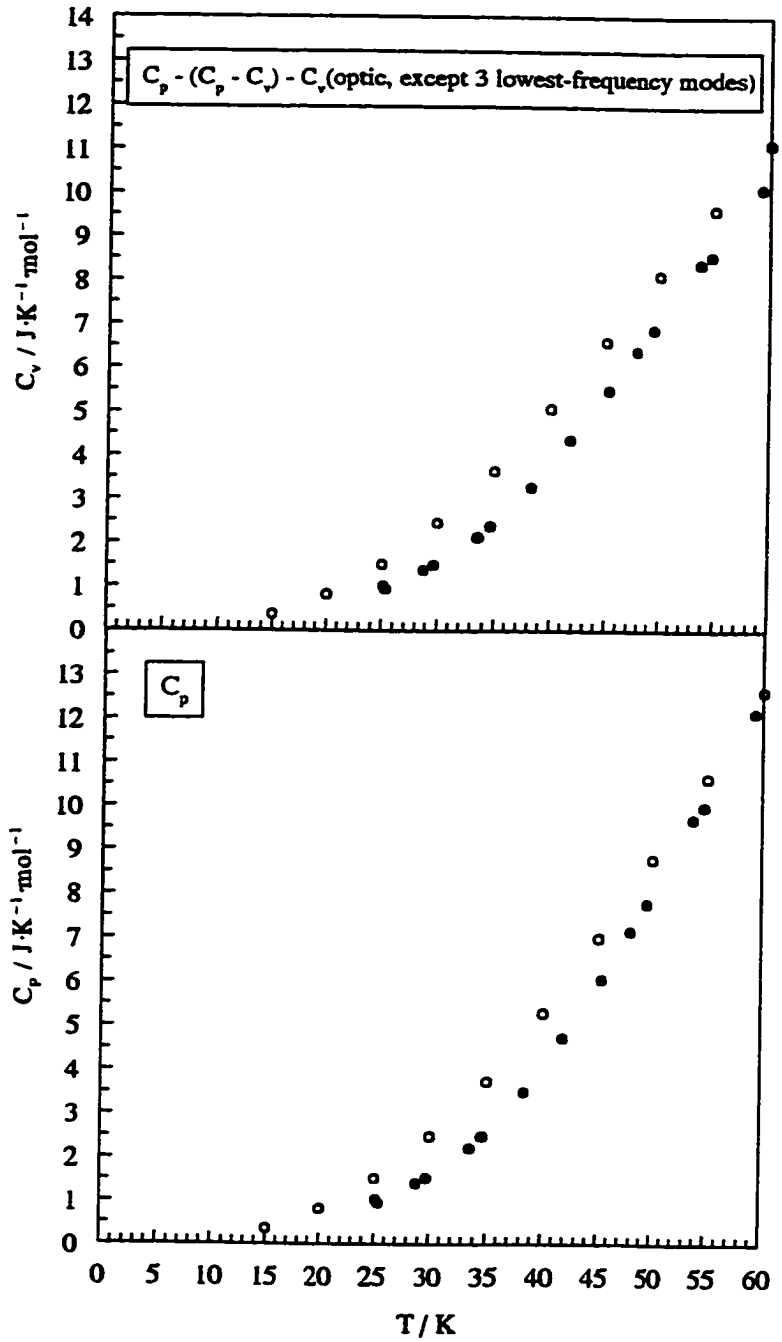

upon NaOH an extra amount of entropy compared to NaOD at low temperatures. This extra amount of entropy for NaOH can be found by determining the excess heat capacity of NaOH relative to NaOD as a function of temperature. This can be estimated using the heat capacity of NaOD as a baseline and taking the difference between the heat capacities of NaOH and NaOD. Again, for this purpose, the literature values for the heat capacity of NaOH shown in Figure 9.1 were used,[139] since these extended to lower temperatures than the data obtained in this thesis work.

The heat capacity data for NaOH from T = 15 K to 90 K and for NaOD from T = 25 K to 90 K were satisfactorily fit to ninth-degree polynomials by a linear least-squares fitting procedure. The excess heat capacity of NaOH as a function of temperature was then determined by subtracting the fitted polynomial for NaOD from the fitted polynomial representing the NaOH heat capacity data. The excess heat capacity of NaOH (ΔC_p) so determined is plotted in Figure 9.4 at 1 K intervals. The excess heat capacity reaches a maximum value of 1.239 $J \cdot K^{-1} \cdot mol^{-1}$ at T = 38.18 K, then decreases with increasing temperature until 64.39 K, when it increases to a small maximum at T = 75.09 K and decreases thereafter.

In order to determine the excess entropy (ΔS_{excess}) of NaOH, $\Delta C_p/T$ (the excess encraty) must be determined, since the two quantities are related by

$$\Delta S_{excess} = \int_{T_1}^{T_2} \frac{\Delta C_p}{T} dT . \qquad (9.6)$$

A plot of $\Delta C_p/T$ *versus* T is shown in Figure 9.5 at 1 K temperature intervals. As shown by equation (9.6), the area under this plot will give the excess entropy of NaOH. The

Figure 9.4. The excess heat capacity of NaOH at low temperatures. The excess heat capacity was obtained by subtracting the heat capacity of NaOD at a given temperature from the heat capacity of NaOH at the same temperature.

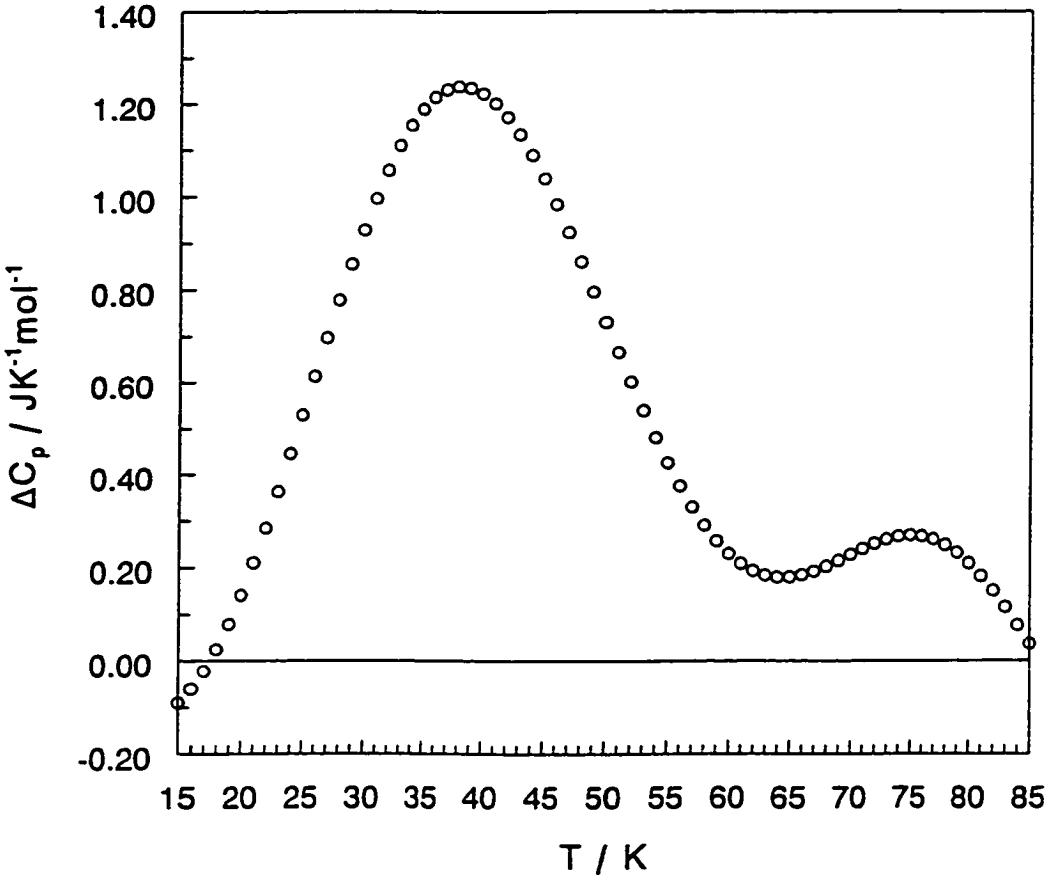

Figure 9.5. A plot of the excess heat capacity divided by temperature for NaOH. The area under this plot represents the low-temperature excess entropy of NaOH as defined by equation (9.6).

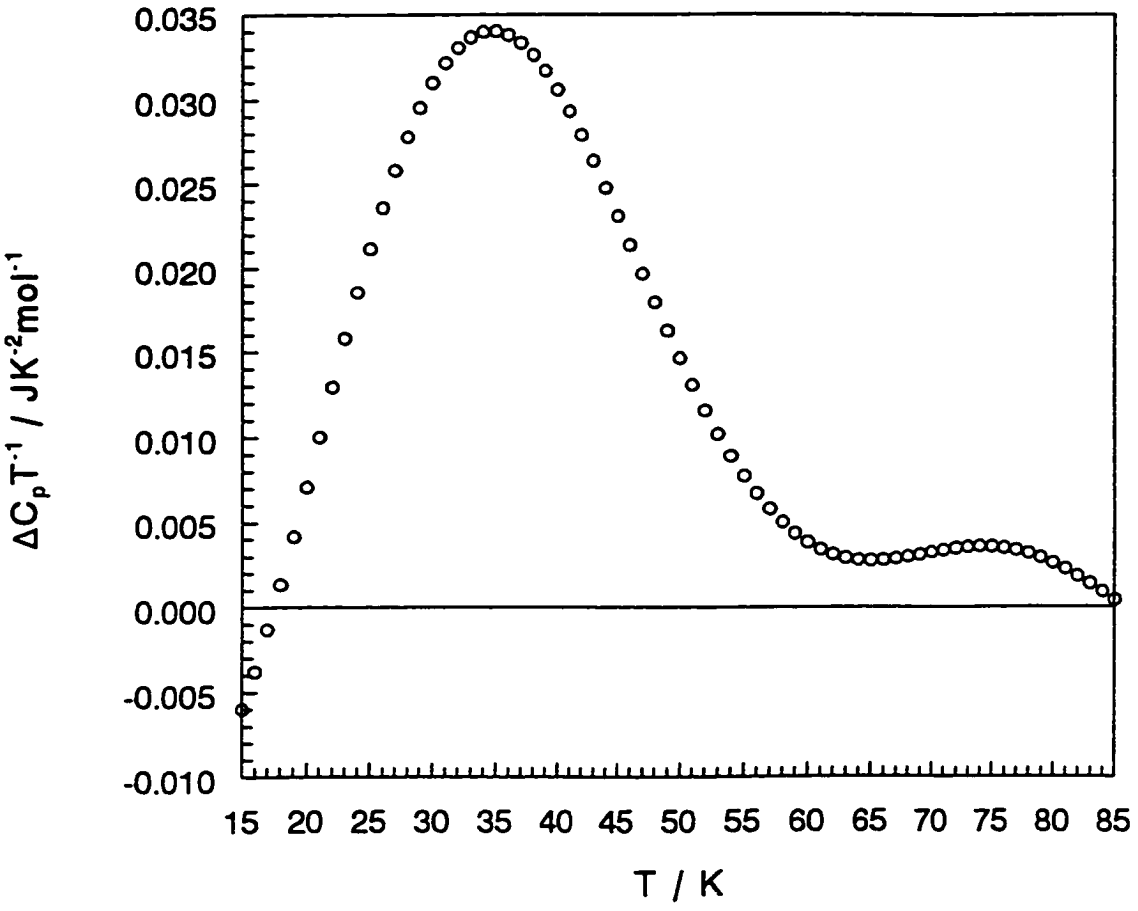

excess entropy of NaOH was determined as a function of temperature by integrating the curve shown in Figure 9.5 for various values of T_2, using T_1 as the temperature where $\Delta C_p/T$ is zero, *i.e.*, T_1 = 17.50 K. A plot of the excess entropy of NaOH as a function of temperature is shown in Figure 9.6. The excess entropy increases gradually with temperature until reaching a maximum value of about 0.93 $J \cdot K^{-1} \cdot mol^{-1}$.

The likely source of the excess heat capacity of NaOH is the thermal depopulation upon cooling of the split energy levels due to quantum-mechanical tunnelling. The heat capacity for such a situation involving two energy levels is given by the Schottky heat capacity equation, *i.e.*,[408,409]

$$C_v = \frac{Rd\left[\frac{\Delta E}{RT}\right]^2 e^{\Delta E/RT}}{(e^{\Delta E/RT} + d)^2}, \tag{9.7}$$

where ΔE is the energy difference between the two energy levels and d is their degeneracy ratio (defined in this case as the degeneracy of the excited state divided by the degeneracy of the ground state). If the two energy levels are considered to be split-tunnelling vibrational levels, both should be non-degenerate, and the degeneracy ratio (d) should therefore be equal to one. However, an attempt to fit all of the excess heat capacity data of Figure 9.4 to equation (9.7) by fixing d = 1 and using only ΔE as the fitting parameter was unsuccessful. Fitting only the excess heat capacity data between T = 18 K to 30 K to the Schottky equation with d = 1 did give a reasonable fit with a best-fit $\Delta E/R$ = 165.47 ± 0.84 K. This best-fit curve is shown in Figure 9.7.

The fitted Schottky curve shown in Figure 9.7 fits the data from T = 18 K to 30 K reasonably well, but deviates from the actual data by a large amount for temperatures

Figure 9.6. A plot of the excess entropy of NaOH as a function of temperature. This curve was calculated by determining the area under the curve in Figure (9.5) at different temperatures.

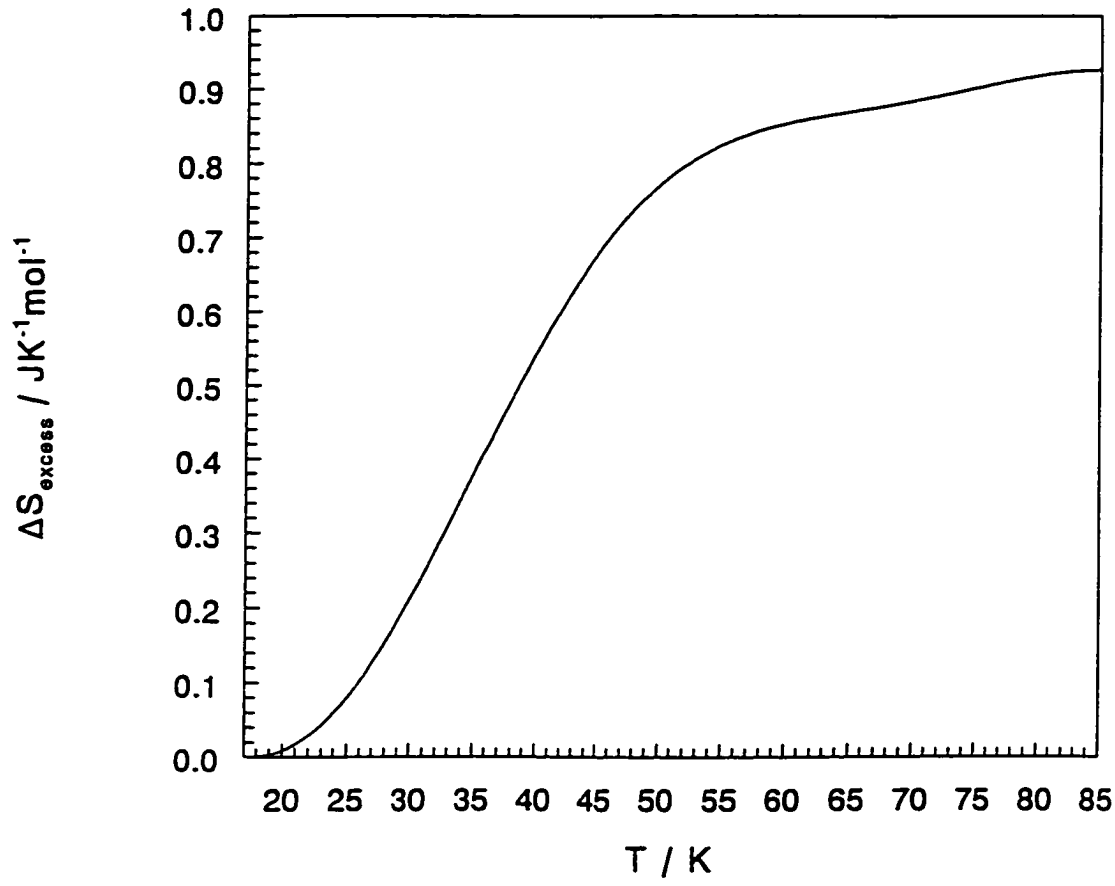

Figure 9.7. The best-fit curve obtained by fitting the excess heat capacity data of NaOH to the Schottky equation using a degeneracy ratio of one ($d = 1$). Only the data from $T = 18$ K to 30 K were used for the fit. The open circles represent the experimental NaOH excess heat capacity data.

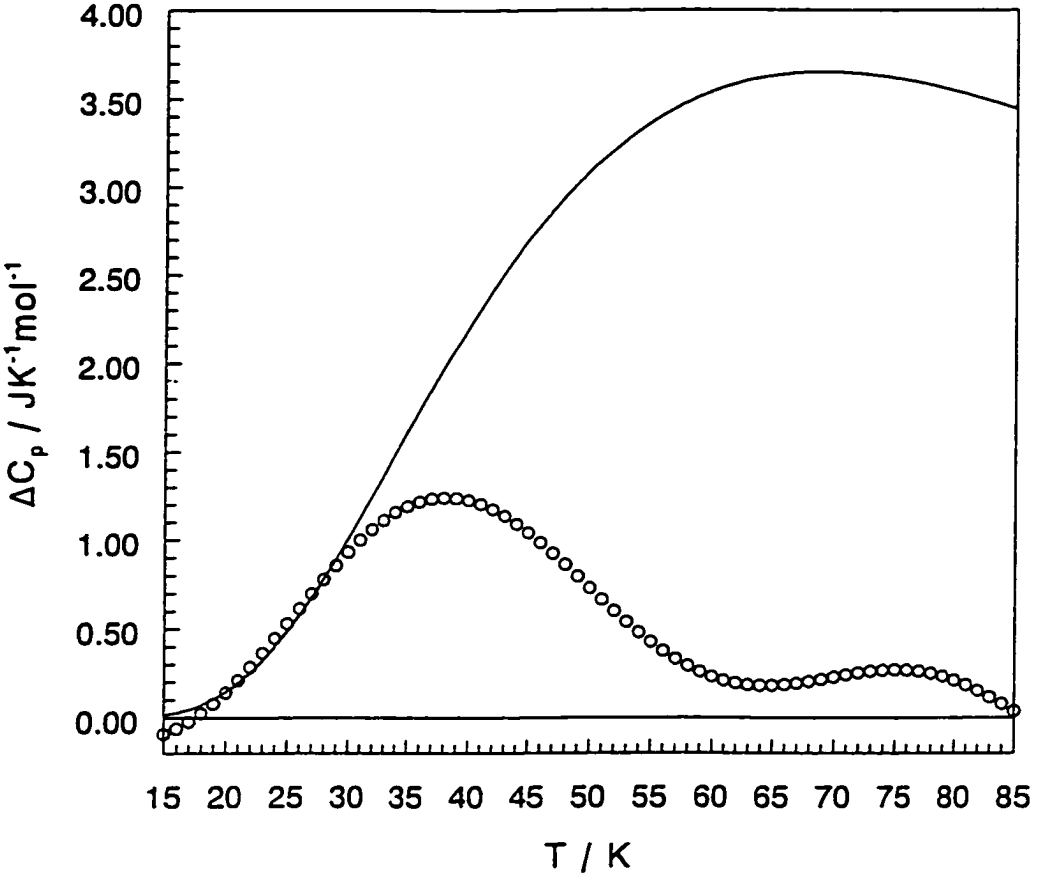

above 30 K. It would be desirable to fit the excess heat capacity data using a model which fits the data reasonably over a larger temperature range. One attempt to do this involved modelling the data using the Schottky equation with the degeneracy ratio (d) as a free parameter. Fitting all of the excess heat capacity data from Figure 9.4 to this model gave the unsatisfactory fit shown in Figure 9.8, defined by the best-fit parameters $\Delta E/R = 70.1 \pm 5.5$ K and $d = 0.173 \pm 0.012$. A fit to the data from $T = 18$ K to 30 K using the same model was also performed with resulting fitted parameters of $\Delta E/R = 153.4 \pm 4.4$ K and $d = 0.744 \pm 0.078$. However, this fit was not noticeably better than the fit obtained using ΔE as the only free parameter and fixing $d = 1$ (Figure 9.7).

A method suggested in the literature[257] for modelling excess heat capacity data similar to that shown in Figure 9.4 assumes that ΔE is not the same for all molecules, but is statistically distributed about a most probable value ΔE_m. A Gaussian distribution function g(ΔE) was introduced such that the fraction of molecules with a ΔE value between ΔE and $\Delta E + d\Delta E$ is g(ΔE)dΔE, where g(ΔE) is given by

$$g(\Delta E) = \frac{1}{\sigma\sqrt{2\pi}} e^{-\frac{1}{2}\left(\frac{\Delta E - \Delta E_m}{\sigma}\right)^2}, \qquad (9.8)$$

where σ is the standard deviation of the distribution. Thus, the contribution to the excess heat capacity (dC_v) from the molecules with a given ΔE is

$$dC_v = \frac{R\left[\frac{\Delta E}{RT}\right]^2 e^{\Delta E/RT}}{\left(e^{\Delta E/RT} + 1\right)^2} g(\Delta E)\, d\Delta E. \qquad (9.9)$$

The total excess heat capacity can be obtained from integrating equation (9.9) from - ∞

Figure 9.8. The best-fit curve obtained by fitting the excess heat capacity data of NaOH to the Schottky equation where both the degeneracy ratio (d) and the energy difference (ΔE) were allowed to vary as free parameters. All of the excess heat capacity data were used to obtain this fit. The open circles represent the experimental excess heat capacity data of NaOH over NaOD.

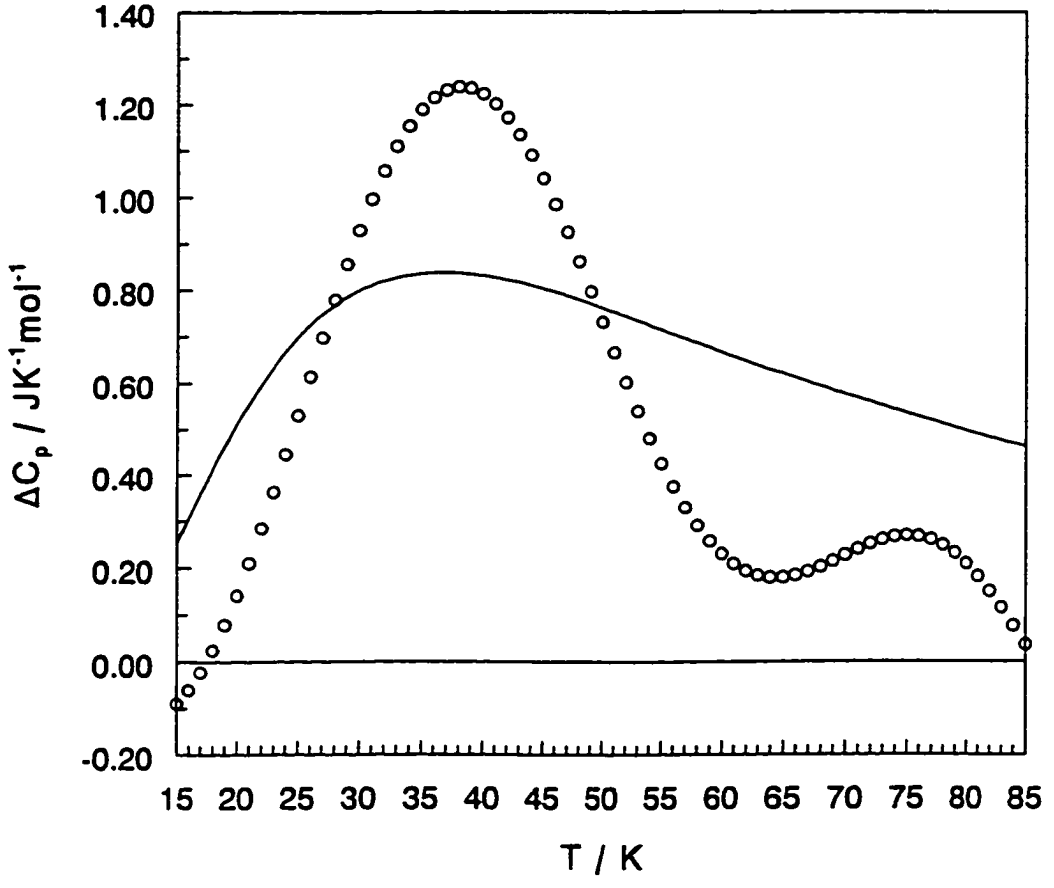

to + ∞, *i.e.*,

$$C_v = \int_{-\infty}^{\infty} \frac{R\left[\frac{\Delta E}{RT}\right]^2 e^{\Delta E/RT}}{\left(e^{\Delta E/RT} + 1\right)^2} g(\Delta E)\, d\Delta E . \qquad (9.10)$$

The Gaussian distribution function defined by equation (9.8) is non-zero for all values of ΔE in the open interval from - ∞ to + ∞. However, a ΔE value less than zero is unphysical, and thus, practically, the integral is performed for ΔE values from 0 to ∞. Typically, the error introduced by this procedure is of no consequence, since the contribution to the integral from ΔE values less than zero is negligible.

Fitting data to an equation of the form of equation (9.10) requires software that will perform a nonlinear least-squares fit to a function defined by an integral. Most fitting programs are not equipped to perform such a fitting procedure. In light of this, a computer program was written in the QuickBASIC language to fit data to a function defined by an integral using nonlinear least-squares analysis. This program combined known algorithms[279,280] for doing numerical integration and performing a general nonlinear least-squares fit. Practically, a computer cannot integrate up to a value of infinity. Nevertheless, the program was designed to integrate up to a ΔE value of 1×10^{20} K, which for the required purpose was close enough to infinity. However, problems were encountered because of the nature of the particular integrand involved (equation (9.10)) and the computer's limitations in dealing with very small and very large numbers. For this reason, the integration could only be performed for ΔE values from 0 K to 400 K. This was not deemed to be a problem, since over the range of temperatures

considered, the value of the integrand of equation (9.10) is negligible (less than 10^{-40}) for ΔE values greater than 400 K.

An attempted fit of equation (9.10) to all of the excess heat capacity data was again unsuccessful. However, a fit was obtained for the data from T = 18 K to 30 K with best-fit parameters of $\Delta E_m/R$ = 183.4 K and σ = 16.4 K being calculated. The fitted curve obtained by this procedure is shown along with the original data in Figure 9.9. The quality of this fit appears to be no better (actually, a bit worse) than the fit from Figure 9.7, obtained using just the regular Schottky equation (equation (9.7)). The limitations of the computer program used could be at least partially responsible for the poor quality of this fit for temperatures below T = 30 K.

Another fitting model used assumed that the value of ΔE is the same for all molecules but is allowed to vary with temperature in a Gaussian-type fashion, *i.e.*,

$$\Delta E = \Delta E_{max}\, e^{-\frac{1}{2}\left(\frac{T - T_{max}}{\sigma}\right)^2}, \qquad (9.11)$$

where ΔE_{max} is the maximum value of ΔE occurring at temperature T_{max}. All of the excess heat capacity data from T = 19 K to 82 K were successfully fitted to the Schottky equation (9.7) using a temperature-dependent value of ΔE given by equation (9.11). The best-fit parameters obtained were $\Delta E_{max}/R$ = 35.04 $\pm$ 0.60 K, T_{max} = 44.17 $\pm$ 0.44 K, and σ = 13.75 $\pm$ 0.42 K. The fitted curve is shown with the original excess heat capacity data in Figure 9.10. The fit is not perfect, but it certainly provides a much better representation of the excess heat capacity data over a larger temperature range as compared to the other fitting equations used. However, a physical interpretation of the

Figure 9.9. The fitted curve obtained by fitting the NaOH excess heat capacity data to equation (9.10) which assumes that a Gaussian distribution of ΔE values exists among the NaOH molecules in the solid. Only the data from T = 18 K to 30 K were used to obtain the fit. The open circles represent the experimental excess heat capacity data of NaOH over NaOD.

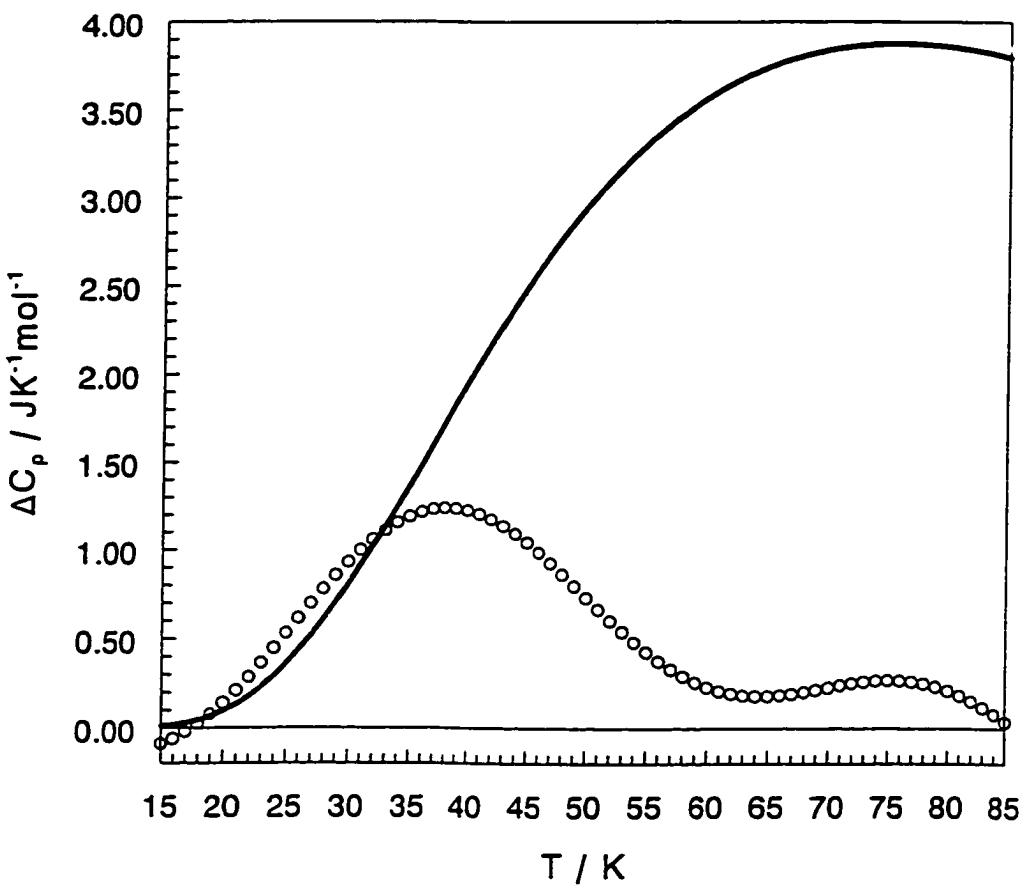

Figure 9.10. The best-fit curve obtained for the excess heat capacity data of NaOH using the Schottky equation and assuming that ΔE is the same for all molecules but varies with temperature in a Gaussian fashion. All of the heat capacity data from T = 19 K to 82 K were used to obtain this fit. The open circles represent the original NaOH excess heat capacity data.

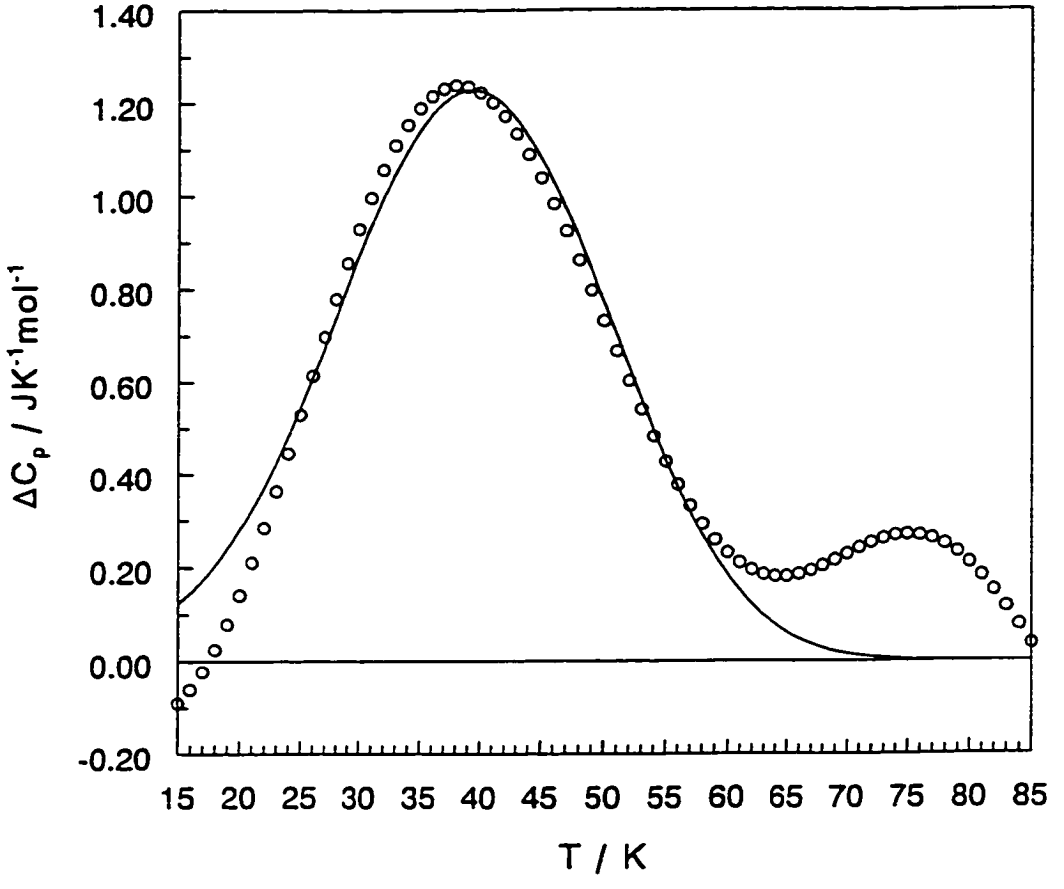

model proposed by equation (9.11) is, as yet, unclear.

The source of the excess heat capacity observed for NaOH at low temperatures likely involves a tunnelling mechanism. The total excess entropy that is realized by NaOH due to this mechanism was shown in Figure 9.6 to be $\sim$ 0.93 $J \cdot K^{-1} \cdot mol^{-1}$. Estimating the uncertainty in this value is difficult, since it is based upon using the heat capacity of NaOD as a baseline to determine the excess heat capacity of NaOH. It is likely that the heat capacity of NaOD does not perfectly represent the purely vibrational and rotational contributions to the heat capacity of NaOH. The NaOD heat capacity would provide an adequate baseline at lower temperatures, where the only optic modes which contribute significantly to the heat capacity (frequency less than 250 cm^{-1}) have the same frequency for NaOH and NaOD. At higher temperatures ($T >$ $\sim$ 50 K), higher-frequency optic modes which have different frequencies for NaOH and NaOD begin to contribute significantly to the heat capacity so that the use of the NaOD heat capacity as a baseline from which to determine the excess heat capacity of NaOH becomes less accurate at higher temperatures. The accuracy of the NaOH and NaOD heat capacity values was listed in the literature[139,152] to be within $\pm$ 1%. However, the excess heat capacity values were calculated by taking the (small) difference between two relatively large heat capacity values, so the relative error in the excess heat capacity data is much larger than $\pm$ 1%. It is reasonable to assume that the accuracy in the excess entropy value calculated for NaOH is no better than $\pm$ 20%, *i.e.*, $\Delta S_{excess} = 0.93 \pm 0.19$ $J \cdot K^{-1} \cdot mol^{-1}$.

The entropy change[152] of the deuterium-induced phase transition in NaOD at $T =$

153.2 K is 0.864 ± 0.005 $J \cdot K^{-1} \cdot mol^{-1}$. This differs from the excess entropy calculated for NaOH by 8%. In fact, the entropy change during the NaOD phase transition is within the uncertainty of the low-temperature excess entropy calculated for NaOH. Thus, NaOD removes some entropy associated with its deuterium atoms by undergoing a phase transition, while NaOH seems to remove a similar amount of entropy associated with its hydrogen atoms through a more gradual process at low temperatures, most likely involving thermal depopulation of tunnelling levels.

This provides further evidence against the existence of residual entropy in NaOH. It has been shown through the existence of excess heat capacity in NaOH at low temperatures that the disorder of the hydrogen atoms in NaOH does get removed gradually before absolute zero is reached. Through this gradual process, the hydrogen atoms in NaOH would all occupy the lowest-energy tunnelling level at absolute zero, and the system would therefore be in a single quantum state ($\Omega = 1$).[257] Therefore, the entropy of NaOH at $T = 0$ K would be $S = R\ln\Omega = 0$. Thus, NaOH does not possess residual entropy.

Quantum-mechanical tunnelling of the hydrogen atoms in NaOH could play two important roles in helping to explain the seemingly anomalous low-temperature behaviour of NaOH: Tunnelling helps to suppress a low-temperature phase transition through quantum-mechanical delocalization that reduces the effective dipole-dipole ordering interaction between neighbouring hydroxide ions. Tunnelling also provides a mechanism by which the extra entropy of the hydrogen atoms, incurred by the suppression of the phase transition, is removed before absolute zero is reached.

Support for this argument is provided by low-temperature calorimetric data reported for KOH and KOD.[153] As discussed in Chapter 3, both of these compounds undergo a low-temperature phase transition to an antiferroelectric hydrogen-bonded low-temperature monoclinic phase. The transition entropies of the low-temperature transitions for both compounds are very similar: 1.01 ± 0.02 $J \cdot K^{-1} \cdot mol^{-1}$ for KOH, and 1.046 ± 0.006 $J \cdot K^{-1} \cdot mol^{-1}$ for KOD.[153] This means that similar amounts of disorder are removed for the hydrogen atoms in KOH and the deuterium atoms in KOD through their low-temperature phase transitions. Thus, it would be expected that KOH has no need for excess heat capacity at low temperatures as a mechanism for entropy removal since all of the required entropy is removed by the phase transition. A comparison of the low-temperature heat capacities of KOH and KOD show that this is indeed the case. At low temperatures the heat capacity of KOH is slightly less than that of KOD,[153] which is the isotopic behaviour expected when only rotational and vibrational degrees of freedom contribute to the heat capacity.

The existence of excess heat capacity at low temperatures seems to be a common feature of all substances exhibiting a deuterium-induced phase transition that have been studied by adiabatic calorimetry. This has been shown for $Rb_3(H,D)(SO_4)_2$,[129] $Rb_3(H,D)(SeO_4)_2$,[257] $(N(H,D)_4)_2TeCl_6$,[111,112] $(N(H,D)_4)_2PbCl_6$,[110] and the organic compound 5-bromo-9-hydroxyphenalenone.[134] A comparison of the published heat capacity data of the hydrogenated and deuterated forms of $(N(H,D)_4)_2PtCl_6$[108,109] and $(N(H,D)_4)_2PdCl_6$[106,107] also indicates that the hydrogenated compound has a higher heat capacity than the deuterated form at low temperatures. In all cases, the excess heat capacity of the

hydrogenated compound at low temperatures is due to the ability of the hydrogen atoms in these compounds to access exclusive energy levels (probably related to hydrogen atom tunnelling). This provides a mechanism for entropy removal for the hydrogen atoms which do not remove entropy through a phase transition in contrast to the corresponding deuterated compounds.

The compound $(NH_4)_2SeCl_6$ and its deuterated counterpart provide a slightly different variation to this argument. As discussed in Section 2.4, both $(NH_4)_2SeCl_6$ and $(ND_4)_2SeCl_6$ have low-temperature phase transitions as shown by adiabatic calorimetry.[118] The anomalous effect of deuteration shows up by the difference in the phase transition temperatures (T_{trs} = 24.5 K for the H-form, and T_{trs} = 48.2 K for the D-form), and especially by the difference in the transition entropies. The transition entropy for the deuterated compound is ~ eight times as much as for the hydrogenated compound ($\Delta_{trs}S$ = 12.1 $J \cdot K^{-1} \cdot mol^{-1}$ for the D-form *versus* $\Delta_{trs}S$ = 1.50 $J \cdot K^{-1} \cdot mol^{-1}$ for the H-form).[118] A comparison of the low-temperature heat capacities of both compounds (below the phase transition temperature of the H-form) again shows that the heat capacity of the H-form is greater than that of the D-form. The extra degrees of freedom (probably tunnelling) giving rise to the excess heat capacity of $(NH_4)_2SeCl_6$ provide a mechanism of entropy removal for the NH_4^+ ions to help compensate for the much smaller entropy change during the low-temperature phase transition, compared to the entropy change during the phase transition for the deuterated compound.

9.4 Some Final Remarks

From the discussion presented in this chapter, it can be said that the seemingly anomalous low-temperature behaviour of NaOH arises because of several factors. The hydrogen-bonded phases of the alkali-metal hydroxides and deuteroxides involve hydrogen bonds which are very long (> 3.2 Å).[141,143,144,145,160] The existence of a low-temperature phase transition in NaOD, which does not occur in NaOH at atmospheric pressure, arises because the relevant geometric parameters of NaOH and NaOD are fortuitously close to a limit where hydrogen bonds will or will not form.

It should be noted that the geometric effects relevant to explain the behaviour of NaOH/NaOD (shortening of hydrogen bond upon deuteration) are opposite to the geometric isotope effect described by Ichikawa *et al.*[82,95,96] (lengthening of H-bond with deuteration) to explain the effects of deuterium substitution on phase transitions, as summarized in Section 2.3.4. Different geometric effects apply depending on the potential length of the hydrogen bonds in the substance under question.[391,396,397,398] For NaOH/NaOD, the distance between the two oxygen atoms which would participate in hydrogen bonding is very long, whereas for the other hydrogen-bonded substances exhibiting anomalous deuterium-induced phase transition behaviour (see Chapter 2), the hydrogen bonds are short. Ichikawa's geometric isotope effect applies only for short hydrogen-bond lengths in the range of 2.45 Å to 2.65 Å.

Tunnelling also seems to play a role in the low-temperature properties of NaOH as a mechanism of entropy removal. Tunnelling would also tend to prevent a phase

transition from taking place through quantum-mechanical delocalization that would reduce the dipolar interaction. Thus, both tunnelling and geometric effects are responsible for the anomalous behaviour of NaOH compared to its deuterated counterpart, NaOD.

The research work presented in this thesis has focused mainly on a single example of a deuterium-induced phase transition which occurs in NaOH/NaOD. However, as summarized in Chapter 2, many other examples exist. Fundamental to determining the properties of substances is the intermolecular potential. According to the Born-Oppenheimer approximation (Section 2.2), the intermolecular potential does not depend on the nuclear mass, and thus, should not change with isotopic substitution. However, the zero-point energy does depend on the nuclear mass, and therefore, the distribution of energy levels in the electronic potential will change with isotopic substitution. The effect of this will be most important for deuterium substitution, since the mass of a deuterium atom is twice the mass of a hydrogen atom. The energy levels for a hydrogenated compound will be higher in the potential well than for the deuterated form, which results in the greater ability of the hydrogenated compound to participate in quantum-mechanical tunnelling, and also leads to different geometric parameters for the hydrogenated/deuterated isotopomeric compounds. It is for these reasons that deuterium substitution has such a large effect on the polymorphic phase transition behaviour of some solids.

For some nuclei-specific solid-state experimental techniques such as solid-state NMR and neutron scattering, it is commonly advantageous to perform measurements on the deuterated form of a compound rather than the hydrogenated version because of

inherent advantages which arise that are related to the properties of the deuterium nucleus. It is sometimes tempting to assume that the results obtained from measurements of the deuterated compound will apply identically to the hydrogenated compound. As the results and discussion presented in this thesis show, such an assumption should be used with caution.

Chapter 10: Summary and Conclusions

All of the work presented in this thesis has been directed toward understanding the effects of deuterium substitution on the polymorphic phase transition behaviour of solids, especially where the deuterated form of a compound undergoes a low-temperature phase transition which is not observed for the hydrogenated form. The specific example of such a transition that was studied in this research work was the deuterium-induced phase transition which occurs at 153 K in NaOD,[138,152] that is absent in NaOH at ambient pressure.[140] Gaining insight into this phase transition discrepancy between NaOH and NaOD was the major focus of this thesis, in the hopes of learning more about the deuterium-induced phase transition phenomenon as a whole.

Frozen-in disorder or residual entropy was postulated for NaOH as a means to explain its anomalous low-temperature behaviour. Although a single residual entropy calculation for NaOH based upon a thermodynamic analysis supported this postulate,[200] further experimental testing was necessary. Evidence for a glassy phase transition in NaOH would have provided confirmation, since a glassy phase transition reflects the onset of frozen-in disorder in a substance. Detection of a glassy phase transition can be done by the techniques of adiabatic calorimetry and dielectric relaxation.

A detailed adiabatic calorimetry study of NaOH did not show conclusive evidence of a glassy phase transition. Although anomalous temperature drifts were observed during the calorimetric experiments, it was concluded that external factors were responsible for this behaviour. It was unlikely that these drifts were the result of thermal relaxation

effects occurring within the NaOH sample indicative of a glassy phase transition.

Since no equipment was available for measuring dielectric properties, an apparatus for performing dielectric relaxation measurements on powdered solid samples was designed and constructed. This apparatus consisted of a sample cell, resistance heater, platinum resistance thermometer, an immersion-type cryostat, and all of the necessary electronic components. The data acquisition process was automated by interfacing the electronic measuring devices to a computer. The whole set-up was tested by performing measurements on powder samples of some common ionic salts. These experiments also brought to light the concerns which must be addressed when measuring dielectric properties of powdered ionic solids.

The dielectric relaxation apparatus was used to measure the dielectric properties of powder samples of NaOH and NaOD as a function of temperature and electric-field frequency. The dielectric constant results for NaOD revealed its low-temperature deuterium-induced phase transition as a lambda-shaped anomaly with a peak near T = 160 K, which is characteristic of a phase transition to a low-temperature antiferroelectric phase. By contrast, no such anomaly was observed in the dielectric constant measurements of NaOH.

The observation of the relaxation of a dipolar polarization process in the dielectric measurements of NaOH would be evidence of the existence of a glassy phase transition. However, no such evidence was found in the NaOH dielectric measurements. This result coupled with the results of the calorimetric experiments indicated that residual entropy does not exist in NaOH at low temperatures.

The NaOH dielectric constant measurements did reveal a broad anomaly with a peak at $T \sim 170$ K which is very similar to an anomaly found in the dielectric measurements reported for $(NH_4)_3H(SO_4)_2$.[48] By analogy with $(NH_4)_3H(SO_4)_2$,[50,51] the anomaly in the dielectric constant curve of NaOH is likely a prelude to a phase transition which will occur at higher pressures. In fact, high-pressure Raman studies[172] reported for NaOH and NaOD show that NaOH undergoes a low-temperature phase transition at a pressure of $\sim$ 10 kbar to a hydrogen-bonded phase analogous to the deuterium-induced phase transition observed in NaOD at atmospheric pressure. Some of the NaOH dielectric results provided possible evidence for the observation of this high-pressure phase at ambient pressure in metastable form.

Although it was proven that residual entropy does not exist in NaOH, the apparent equivalence of deuteration and pressure for NaOH pointed the way toward an explanation of the discrepancy between the low-temperature behaviour of NaOH compared to NaOD. Substitution of deuterium for hydrogen in any of NaOH, KOH, RbOH, or CsOH, results in a shorter oxygen-to-oxygen distance between neighbouring layers in the solid structure.[141,143,144,145,170,171] This allows for stronger hydrogen bonds to be formed in the low-temperature phases of the deuterated alkali-metal hydroxides.[182,183,187] The geometric effects associated with deuterium substitution are related to the quantum-mechanical differences between hydrogen and the more massive deuterium isotope.[386,391,392,395,396]

The oxygen-to-oxygen distances that could potentially be used to form hydrogen bonds are very long in all of the alkali-metal hydroxides and deuteroxides (> 3.2 Å).[141,143,144,145,160] For NaOH, the stable structure is such that the potential hydrogen-bond

distance seems to be fortuitously located just outside the limit where a hydrogen-bonded interaction can occur. The oxygen-oxygen distance between the layers in NaOD is only slightly less than that for NaOH.[141] However, the difference in the oxygen-oxygen distances in NaOD and NaOH is great enough to enable a hydrogen-bonded phase to form in NaOD, but not in NaOH. The application of pressure decreases the interlayer distance in NaOH and allows for the transformation to the low-temperature hydrogen-bonded phase.[172]

Further insight into the low-temperature behaviour of NaOH came from a comparison of the low-temperature heat capacities of NaOH and NaOD.[139,152] Contrary to normal expectations for the effect of isotopic substitution on the heat capacity, at low temperatures the heat capacity of NaOH was greater than that of NaOD. Exclusive access by NaOH to quantum-mechanical tunnelling levels would explain the excess heat capacity observed for NaOH. The greater ability of the lighter hydrogen atom to undergo tunnelling would help to prevent a phase transition in NaOH from taking place through quantum-mechanical delocalization of the dipolar interaction. Tunnelling also provides a mechanism of entropy removal for NaOH so that it has zero entropy at $T = 0$ K (*i.e.*, no residual entropy).

Thus, geometric effects and tunnelling differences between hydrogen and deuterium play important roles in explaining the existence of a low-temperature phase transition in NaOD which does not occur in NaOH at atmospheric pressure. Both of these effects are related to the different quantum-mechanical energy-level distributions of hydrogen *versus* deuterium associated with their differences in mass. The Born-

Oppenheimer approximation indicates that the intermolecular potential should not change with isotopic substitution. However, it is the position of the energy levels within the potential which makes all the difference in causing the occurrence of deuterium-induced effects on the polymorphic phase-transition behaviour of solids.

Chapter 11: Future Work

The final chapters of a Ph.D. thesis should provide some form of closure to the research problem that was extensively studied in the thesis. Science was born out of the need or urge to understand the workings of our world and the universe. Yet, it is part of the allure of science that no aspect of scientific research can ever be considered fully closed. Research directed toward the study of a specific problem will, inevitably, point the way toward other avenues of research, sometimes in different directions. The research work presented in this thesis is no exception.

An interesting extension of this thesis work would be the study of $NaOH_{1-x}D_x$ isotopic solid solutions, for several values of x. These could readily be studied using the dielectric relaxation apparatus. This apparatus was shown in Section 8.2.2 to be fully capable of detecting and characterizing the low-temperature phase transition in fully deuterated (or nearly fully deuterated) NaOD. Introducing NaOD into an NaOH crystal (increasing x) should lower the overall effective tunnelling frequency of the crystal and reduce quantum effects. A critical deuterium content (x_{crit}) should be observed above which the low-temperature phase transition occurs, with the phase transition temperature increasing with increasing deuterium content (increasing x). Such studies would provide more insight into the extent of the influence of quantum effects, and the overall nature of this phase transition. Similar studies have been reported for $K_3H_{1-x}D_x(SO_4)_2$, $Rb_3H_{1-x}D_x(SO_4)_2$, and $Rb_3H_{1-x}D_x(SeO_4)_2$ solid solutions.[71,72]

The dielectric measurements of NaOH shown in Figure 8.11 of Section 8.3.2

revealed evidence that could be interpreted as the formation of a metastable high-pressure form of NaOH at low temperature and ambient pressure. It would be interesting to attempt a structure determination of this metastable phase of NaOH to discover if it is indeed analogous to the low-temperature antiferroelectric phase of NaOD. In addition, dielectric measurements of NaOH as a function of applied pressure would allow for the characterization of the high-pressure polymorphic phase transition in NaOH alluded to by the broad anomaly centred at $T \sim 170$ K observed in the NaOH dielectric measurements.

For the purposes of this research, the dielectric relaxation apparatus was built solely to measure the dielectric properties of NaOH and NaOD. Yet, it is now available to study just about any powdered solid. As described in Section 4.3, dielectric measurements can provide a wealth of information concerning the properties of solids, including the detection of polymorphic phase transitions, glassy phase transitions, ferroelectric and antiferroelectric phases, and the study of reorientational dynamics. Studies by dielectric measurements provide a fitting complement to other solid-state measuring techniques.

Solids which could be chosen for study using the dielectric relaxation apparatus include the other alkali-metal hydroxides and deuteroxides. Such studies have been reported for KOH, KOD, CsOH, and CsOD, but only over a limited temperature range at a single unknown frequency.[170,171] Low-temperature dielectric measurements have not been reported for LiOH, LiOD, RbOH, or RbOD. Measurements of the rubidium compounds would be especially interesting, since it is known from structural studies that

the low-temperature phases in RbOH and RbOD are ferroelectrically ordered.[144] Dielectric analyses of the deuterium-induced phase transitions in the $(NH_4)_2MCl_6$ family of compounds (Section 2.4) also have not been reported.

Generally, the ability of the dielectric relaxation apparatus to detect and characterize the relaxation of the dipolar polarization associated with reorientational motion is a definite asset in the study of solids. Kinetic parameters for the reorientational process occurring in a particular solid giving rise to the relaxation can be readily obtained from frequency- and temperature-dependent dielectric measurements.

An extension of the measurement capabilities of the apparatus can also be envisioned. Because the capacitance of the ring electrode in the sample cell of the dielectric relaxation apparatus is sensitive to the thickness of the sample, it is possible that the apparatus could be used to measure the thermal expansion of solid samples. Measurement of the capacitance of the ring electrode as a function of temperature should reflect the dimensional changes of the sample. The apparatus would have to be calibrated with the known thermal expansion of brass, since the dimensions of the brass ring electrode would also change with temperature.

Detailed low-temperature heat capacity measurements have not been reported for RbOH and RbOD, nor have extensive calorimetric measurements been reported for CsOH and CsOD. Characterization of the low-temperature polymorphic phase transitions in these compounds by calorimetry would be useful, especially an accurate determination of the entropy change which occurs during these transitions, which could be compared to the entropy changes reported for the low-temperature phase transitions in NaOD,[152]

KOH,[153] and KOD.[153]

The geometric effects associated with the substitution of hydrogen with deuterium should be further investigated through extensive theoretical studies (*e.g.*, *ab initio* calculations). Optimized geometries for several compounds and their deuterated analogues would help bring to light the conditions under which substantial geometric effects would be expected. Charge calculations would enable the examination of dipole moment changes which could occur with deuteration, especially in compounds which form hydrogen bonds.

References:

1. H. Kamerlingh Onnes, *Trans. Far. Soc.* **18**, 145 (1922).

2. W.H. Keesom, *Proc. Roy. Acad. Amsterdam*, **29**, 1136 (1926).

3. A.D. Buckingham, *Phil. Trans. R. Soc. Lond. B.* **272**, 5 (1975).

4. A.D. Buckingham and B.D. Utting, *Ann. Rev. Phys. Chem.* **21**, 287 (1970).

5. F. London, *Trans. Far. Soc.* **33**, 8 (1937).

6. J.O. Hirschfelder, C.F. Curtiss, and R.B. Bird, Molecular Theory of Gases and Liquids. John Wiley and Sons, Inc., New York, 1965, p. 22-35.

7. H. Margenau and N.R. Kestner, Theory of Intermolecular Forces (2nd edition). Pergamon Press, Oxford, 1971.

8. J.O. Hirschfelder, editor, Intermolecular Forces (Advances in Chemical Physics Vol. XII), Interscience Publishers, New York, 1967.

9. K.J. Laidler and J.H. Meiser, Physical Chemistry (2nd edition). Houghton Mifflin, Toronto, 1995, p. 807-814.

10. J.C. Bailar, H.J. Emeleus, Sir R. Nyholm, and A.F. Tortman-Dickenson, editors, Comprehensive Inorganic Chemistry. Pergamon Press, Oxford, 1973, Vol. 1, Ch. 5, p. 139.

11. C.A. Burrus, *J. Chem. Phys.* **28**, 427 (1958).

12. C. Kittel, Introduction to Solid State Physics (6th edition). John Wiley and Sons, Inc., New York, 1986, Ch. 3.

13. J. Timmermans, *J. Chim. Phys.* **35**, 331 (1938).

14. C.N.R. Rao and K.J. Rao, Phase Transitions in Solids. McGraw-Hill, New York, 1978.

15. Reference (9), p. 178.

16. E. Whalley, J.B.R. Heath, and D.W. Davidson, *J. Chem. Phys.* **48**, 2362 (1968).

17. D.D. Klug, Y.P. Handa, J.S. Tse, and E. Whalley, *J. Chem. Phys.* **90**, 2390 (1989).

18. H. Suga, *Ann. NY Acad. Sci.* **484**, 248 (1986).

19. A. Polian and M. Grimsditch, *Phys. Rev. Lett.* **52**, 1312 (1984).

20. W.F. Giauque and M.F. Ashley, *Phys. Rev.* **43**, 81 (1933).

21. W.F. Giauque and J.W. Stout, *J. Am. Chem. Soc.* **58**, 1144 (1936).

22. M.J. Buerger, in Phase Transformations in Solids. R. Smoluchowski, J.E. Mayer, and W.A. Weyl, editors, John Wiley and Sons, New York, 1951.

23. H. Chihara, *Ber. Bunsenges. Phys. Chem.* **87**, 188 (1983).

24. A general discussion of the features and mechanism of this phase transition can be found in F. Liebau and H. Böhm, *Acta Cryst.* **A38**, 252 (1982).

25. P. Ehrenfest, *Commun. Kamerlingh Onnes Lab.*, Leiden Suppl. **75b** (1933).

26. W.H. Keesom and P.H. van Laer, *Physica*, **5**, 193 (1938).

27. A.B. Pippard, Elements of Classical Thermodynamics. Cambridge University Press, 1957, p. 136.

28. A.K. Cheetham and P. Day, editors, Solid State Chemistry: Techniques, Clarendon Press, Oxford, 1987.

29. J.L. Atwood, J.E.D. Davies, D.D. MacNicol, and F. Vögtle, editors, Comprehensive Supramolecular Chemistry. Pergamon Press, Oxford, 1996, Vol. 8.

30. A.R. West, Solid State Chemistry and its Applications. John Wiley and Sons, New York, 1990.

31. N.G. Parsonage and L.A.K. Staveley, Disorder in Crystals. Clarendon Press, Oxford, 1978.

32. G.H. Stout and L.H. Jensen, X-ray Structure Determination. John Wiley and Sons, New York, 1989.

33. G.E. Bacon, Neutron Scattering in Chemistry. Butterworths, London, 1977.

34. R.K. Harris, Nuclear Magnetic Resonance Spectroscopy: A Physicochemical View. John Wiley and Sons, New York, 1991.

35. J.K.M. Sanders and B.K. Hunter, Modern NMR Spectroscopy: A Guide for Chemists (2nd edition). Oxford University Press, New York, 1993.

36. C.S. Yannoni, P.P. Bernier, D.S. Bethune, G. Meijer, and J.R. Salem, *J. Am. Chem. Soc.* **113**, 3190 (1991).

37. E.A. Long and J.D. Kemp, *J. Am. Chem. Soc.* **58**, 1829 (1936).

38. F. Simon, *Annln. Phys.* **68**, 241 (1922).

39. C.C. Stephenson, R.W. Blue, and J.W. Stout, *J. Chem. Phys.* **20**, 1046 (1952).

40. C.C. Stephenson and J.G. Hooley, *J. Am. Chem. Soc.* **66**, 1397 (1944).

41. W. Reese and L.F. May, *Phys. Rev.* **167**, 504 (1968).

42. D.A. McQuarrie, Quantum Chemistry. University Science Books, Mill Valley, California, 1983, p. 469.

43. F.L. Pilar, Elementary Quantum Chemistry (2nd edition). McGraw-Hill, New York, 1990, p. 309.

44. M. Born and J.R. Oppenheimer, *Ann. Physik.* **84**, 457 (1927).

45. M. Ichikawa and T. Matsuo, *J. Mol. Struct.* **378**, 17 (1996).

46. R. Blinc, *J. Phys. Chem. Solids.* **13**, 204 (1960).

47. M. Ichikawa, K. Motida, and N. Yamada, *Phys. Rev. B.* **36**, 874 (1987).

48. K. Gesi, *Phys. Stat. Sol.*(a) **33**, 479 (1976).

49. K. Gesi, *Jpn. J. Appl. Phys.* **19**, 1051 (1980).

50. K. Gesi, *J. Phys. Soc. Jpn.* **41**, 1437 (1976).

51. K. Gesi, *J. Phys. Soc. Jpn.* **43**, 1941 (1977).

52. S. Suzuki, Y Oshino, K. Gesi, and Y. Makita, *J. Phys. Soc. Jpn.* **47**, 874 (1979).

53. S. Suzuki, *J. Phys. Soc. Jpn.* **47**, 1205 (1979).

54. K. Gesi, K. Ozawa, T. Osaka, and Y. Makita, *J. Phys. Soc. Jpn.* **44**, 689 (1978).

55. T. Osaka, Y. Makita, and K. Gesi, *J. Phys. Soc. Jpn.* **49**, 593 (1980).

56. K. Gesi, K. Ozawa, T. Osaka, and Y. Makita, *J. Phys. Soc. Jpn.* **49**, 1083 (1980).

57. K. Gesi, *J. Phys. Soc. Jpn.* **42**, 1785 (1977).

58. K. Gesi, *J. Phys. Soc. Jpn.* **43**, 1949 (1977).

59. T. Osaka, Y. Makita, and K. Gesi, *J. Phys. Soc. Jpn.* **46**, 577 (1979).

60. T. Fukami and R.H. Chen, *J. Phys. Chem. Solids.* **58**, 2113 (1997).

61. K. Gesi, *J. Phys. Soc. Jpn.* **48**, 886 (1980).

62. K. Gesi, *J. Phys. Soc. Jpn.* **50**, 3185 (1981).

63. M. Endo, T. Kaneko, T. Osaka, and Y. Makita, *J. Phys. Soc. Jpn.* **52**, 3829 (1983).

64. M. Komukae, T. Osaka, T. Kaneko, and Y. Makita, *J. Phys. Soc. Jpn.* **54**, 3401 (1985).

65. M. Fukai, T. Matsuo, and H. Suga, *Solid State Commun.* **84**, 545 (1992).

66. T. Matsuo, K. Kohno, and M. Ichikawa, *J. Korean Phys. Soc. (Proc. Suppl.)* **29**, S432 (1996).

67. M. Fukai, Doctoral Thesis, Osaka University, Japan.

68. A. Titze, G. Hinze, and R. Böhmer, *Phys. Rev. B.* **57**, R666 (1998).

69. Y. Moritomo and Y. Tokura, *Jpn. J. Appl. Phys.* **32**, 309 (1993).

70. G.A. Samara, *Phys. Rev. Lett.* **27**, 103 (1971).

71. K. Gesi, *J. Phys. Soc. Jpn.* **61**, 162 (1992).

72. Y. Moritomo, Y. Tokura, N. Nagaosa, T. Suzuki, and K. Kumagai, *Phys. Rev. Lett.* **71**, 2833 (1993).

73. Y. Noda, S. Uchiyama, K. Kafuku, H. Kasatani, and H. Terauchi, *J. Phys. Soc. Jpn.* **59**, 2804 (1990).

74. S. Fortier, M.E. Fraser, and R.D. Heyding, *Acta Cryst.* **C41**, 1139 (1985).

75. M. Ichikawa, S. Sato, M. Komukae, and T. Osaka, *Acta Cryst.* **C48**, 1569 (1992).

76. M. Ichikawa, T. Gustafsson, and I. Olovsson, *Acta Cryst.* **C50**, 330 (1994).

77. I.P. Makarova, I.A. Verin, and N.M. Shchagina, *Sov. Phys. Crystallogr.* **31**, 105 (1986).

78. R. Melzer, R. Sonntag, and K.S. Knight, *Acta Cryst.* **C52**, 1061 (1996).

79. S. Suzuki and Y. Makita, *Acta Cryst.* **B34**, 732 (1978).

80. B.V. Merinov, N.B. Bolotina, A.I. Baranov, and L.A. Shuvalov, *Sov. Phys. Crystallogr.* **33**, 824 (1988).

81. B.V. Merinov, A.I. Baranov, and L.A. Shuvalov, *Sov. Phys. Crystallogr.* **35**, 200 (1990).

82. M. Ichikawa, T. Gustafsson, and I. Olovsson, *J. Mol. Struct.* **321**, 21 (1994).

83. J.D. Bernal and R.H. Fowler, *J. Chem. Phys.* **1**, 515 (1933).

84. L. Pauling, *J. Am. Chem. Soc.* **57**, 2680 (1935).

85. M. Ichikawa, T. Gustafsson, K. Motida, I. Olovsson, and K. Gesi, *Ferroelectrics*, **108**, 307 (1990).

86. Y. Noda, H. Kasatani, Y. Watanabe, H. Terauchi, and K. Gesi, *J. Phys. Soc. Jpn.* **59**, 3249 (1990).

87. Y. Noda, H. Kasatani, Y. Watanabe, and H. Terauchi, *J. Phys. Soc. Jpn.* **61**, 905 (1992).

88. M. Ichikawa, T. Gustafsson, and I. Olovsson, *Acta Cryst.* C48, 603 (1992).

89. M. Tanaka and Y. Shiozaki, *Acta Cryst.* **B37**, 1171 (1981).

90. M. Ichikawa, T. Gustafsson, and I. Olovsson, *Acta Cryst.* **B48**, 633 (1992).

91. M. Ichikawa, T. Gustafsson, and I. Olovsson, *Solid State Commun.* **78**, 547 (1991).

92. Y. Noda, Y. Watanabe, H. Kasatani, H. Terauchi, and K. Gesi, *J. Phys. Soc. Jpn.* **60**, 1972 (1991).

93. Y. Noda, I. Tamura, H. Nakao, R. Matsuo, and Y. Kuroiwa, *J. Phys. Soc. Jpn.* **63**, 1803 (1994).

94. T. Matsuo, *Order/Disorder in Solids.* **9**, 6 (1993).

95. M. Ichikawa, *Acta Cryst.* **B34**, 2074 (1978).

96. M. Ichikawa, *Chem. Phys. Lett.* **79**, 583 (1981).

97. M. Ichikawa and K. Motida, *J. Phys. Soc. Jpn.* **56**, 3750 (1987).

98. M.I. McMahon, R.J. Nelmes, W.F. Kuhs, R. Dorwarth, R.O. Piltz, and Z. Tun, *Nature.* **348**, 317 (1990).

99. M. Ichikawa and K. Motida, *J. Phys. Soc. Jpn.* **57**, 2217 (1988).

100. M. Ichikawa, T. Gustafsson, and I. Olovsson, *Solid State Commun.* **87**, 349 (1993).

101. M.I. McMahon, R.O. Piltz, and R.J. Nelmes, *Ferroelectrics.* **108**, 277 (1990).

102. J.M. Robertson and A.R. Ubbelohde, *Proc. R. Soc.* **A170**, 222 (1939).

103. E. Matsushita and T. Matsubara, *Prog. Theor. Phys.* **67**, 1 (1982).

104. C. Totsuji and T. Matsubara, *J. Phys. Soc. Jpn.* **63**, 2760 (1994).

105. M. Prager, W. Press, A. Heidemann, and C. Vettier, *J. Chem. Phys.* **80**, 2777 (1984).

106. J.E. Callanan, R.D. Weir, and E.F. Westrum, Jr., *Ber. Bunsenges. Phys. Chem.* **96**, 1585 (1992).

107. J.E. Callanan, R.D. Weir, and E.F. Westrum, Jr., *J. Chem. Thermodynamics*, **24**, 1001 (1992).

108. R.D. Weir and E.F. Westrum, Jr., *J. Chem. Thermodynamics.* **22**, 1097 (1990).

109. R.D. Weir and E.F. Westrum, Jr., *J. Chem. Thermodynamics.* **23**, 653 (1991).

110. H. Muraoka, T. Matsuo, and Y. Kume, *Solid State Commun.* **93**, 529 (1995).

111. Y. Kume, Y. Miyazaki, T. Matsuo, H. Suga, W.I.F. David, and R.M. Ibberson, *Europhys. Lett.* **16**, 265 (1991).

112. Y. Kume, Y. Miyazaki, T. Matsuo, and H. Suga, *J. Phys. Chem. Solids.* **53**, 1297 (1992).

113. Y. Kume, Y. Miyazaki, T. Matsuo, H. Suga, W.I.F. David, and R.M. Ibberson, *Physica.* **B180 & 181**, 594 (1992).

114. U. Kawald, S. Müller, J. Pelzl, and C. Dimitropoulos, *Solid State Commun.* **67**, 239 (1988).

115. R.G.S. Morfee, L.A.K. Staveley, S.T. Walters, and D.L. Wigley, *J. Phys. Chem. Solids.* **13**, 132 (1960).

116. J.E. Callanan, R.D. Weir, and E.F. Westrum, Jr., *J. Chem. Thermodynamics.* **22**, 149 (1990).

117. B.M. Powell and R.D. Weir, *J. Chem. Thermodynamics*. **24**, 1119 (1992).

118. Y. Kume, H. Muraoka, T. Matsuo, and H. Suga, *J. Chem. Thermodynamics*. **26**, 211 (1994).

119. W. Abriel, *Acta Cryst.* **C42**, 1113 (1986).

120. R.L. Armstrong, P. Dufort, and B.M. Powell, *Can. J. Phys.* **69**, 137 (1991).

121. C. Dimitropoulos, J. Pelzl, and F. Borsa, *Phys. Rev. B.* **41**, 3914 (1990).

122. I. Svare, A.M. Raaen, and G. Thorkildsen, *J. Phys. C: Solid State Phys.* **11**, 4069 (1978).

123. J.E. Tuohi, E.E. Ylinen, and M. Punkkinen, *Phys. Scr.* **13**, 253 (1976).

124. I. Svare, *J. Phys. C: Solid State Phys.* **10**, 4137 (1977).

125. M. Prager, A.M. Raaen, and I. Svare, *J. Phys. C: Solid State Phys.* **16**, L181 (1983).

126. O. Yamamuro, H. Muraoka, T. Ohta, T. Matsuo, Y. Kume, N. Onoda-Yamamuro, K. Oikawa, and T. Kamiyama, *J. Phys. Soc. Jpn.* **64**, 2722 (1995).

127. O. Yamamuro, K. Okishiro, T. Matsuo, N. Onoda-Yamamuro, K. Oikawa, T. Kamiyama, Y. Kume, and F. Izumi, *J. Chem. Phys.* **107**, 8004 (1997).

128. O. Knop, I.A. Oxton, and M. Falk, *Can. J. Chem.* **57**, 404 (1979).

129. T. Matsuo, *J. Korean Phys. Soc. (Proc. Suppl.)* **29**, S409 (1996).

130. T. Mochida, A. Izuoka, T. Sugawara, Y. Moritomo, and Y. Tokura, *J. Chem. Phys.* **101**, 7971 (1994).

131. T. Mochida *et al.*, unpublished; cited in reference (132).

132. Y. Moritomo, Y. Tokura, T. Mochida, A. Izuoka, and T. Sugawara, *J. Phys. Soc. Jpn.* **64**, 1892 (1995).

133. V.E. Bondybey, R.C. Haddon, and J.H. English, *J. Chem. Phys.* **80**, 5432 (1984).

134. T. Matsuo, A. Inaba, T. Mochida, A. Izuoka, and T. Sugawara, *Symp. Molecular Structure, Chemical Society of Japan*, Tokyo, Sept. 1994, paper 1P74.

135. J.H. Busch and J.R. de la Vega, *J. Am. Chem. Soc.* **108**, 3984 (1986).

136. Y. Yamamura, K. Saito, H. Matsuyama, and I. Ikemoto, *Chem. Phys. Lett.* **256**, 317 (1996).

137. T. Matsuo and H. Suga, *Solid State Commun.* **21**, 923 (1977).

138. D.T. Amm, T.J. Bastow, K. Jeffrey, R.D. Heyding, and S.L. Segel, *Thermochim. Acta.* **95**, 447 (1985).

139. L.E. Murch and W.F. Giauque, *J. Phys. Chem.* **66**, 2052 (1962).

140. T.J. Bastow, M.M. Elcombe, and C.J. Howard, *Solid State Commun.* **57**, 339 (1986).

141. H.-J. Bleif and H. Dachs, *Acta Cryst.* **A38**, 470 (1982).

142. A.P. Rollet and R. Cohen-Adad, *Rev. Chim. Miner.* **1**, 451 (1964).

143. B. Mach, H. Jacobs, and W. Schäfer, *Z. anorg. allg. Chem.* **553**, 187 (1987).

144. H. Jacobs, B. Mach, H.-D. Lutz, and J. Henning, *Z. anorg. allg. Chem.* **544**, 28 (1987).

145. H. Jacobs, B. Mach, B. Harbrecht, H.-D. Lutz, and J. Henning, *Z. anorg. allg. Chem.* **544**, 55 (1987).

146. See reference (31), p. 270-279, and references cited therein.

147. J.J. Rush, L.A. de Graaf, and R.C. Livingstone, *J. Chem. Phys.* **58**, 3439 (1973).

148. J.G. Smit, H. Dachs, and R.E. Lechner, *Solid State Commun.* **29**, 219 (1979).

149. D. Fontaine, R. Pick, and M. Yvinec, *Solid State Commun.* **21**, 1095 (1977).

150. L.V. Gurvich, G.A. Bergman, L.N. Gorokhov, V.S. Iorish, V. Ya. Leonidov, and V.S. Yungman, *J. Phys. Chem. Ref. Data.* **25**, 1211 (1996).

151. L.V. Gurvich, G.A. Bergman, L.N. Gorokhov, V.S. Iorish, V.Ya. Leonidov, and V.S. Yungman, *J. Phys. Chem. Ref. Data.* **26**, 1031 (1997).

152. M.A. White and S.A. Moore, *J. Chem. Phys.* **85**, 4629 (1986).

153. M.A. White, A. Perrott, D. Britten, and M.J.M. Van Oort, *J. Chem. Phys.* **89**, 4346 (1988).

154. R.J.M. Konings, E.H.P. Cordfunke, E.F. Westrum, Jr., and R. Shaviv, *J. Phys. Chem. Solids.* **51**, 439 (1990).

155. B. Mach, Ph.D. thesis, Universität Dortmund, Dortmund, W. Germany, (1984).

156. T. Ernst, *Z. Phys. Chem.* **B20**, 65 (1933).

157. H. Dachs, *Z. Kristallogr.* **112**, 60 (1959).

158. T. Ernst, *Nachr. Ges. Wiss. Göttingen, Math-phys. Kl.* 76 (1946); see *Chem. Abstr.* **43**, 8232c (1949).

159. H.-J. Bleif, Diplomarbeit. Univ. Tübingen. (1971).

160. H. Stehr, *Z. Kristallogr.* **125**, 332 (1967).

161. T.J. Bastow, D.T. Amm, S.W. Segel, and R.D. Heyding, *Z. Naturforsch.* **41a**, 283 (1986).

162. H. Jacobs, J. Kockelkorn, and T. Tacke, *Z. anorg. allg. Chem.* **531**, 119 (1985).

163. J.A. Ibers, J. Kumamoto, and R.G. Snyder, *J. Chem. Phys.* **33**, 1164 (1960).

164. H. Jacobs and B. Harbrecht, *Z. Kristallogr.* **156**, 59 (1981).

165. A.F. Wells, Structural Inorganic Chemistry (5th edition). Clarendon Press, Oxford, 1984, p. 632.

166. T.B. Douglas and J.L. Dever, *J. Res. Natl. Bur. Stds.* **53**, 81 (1954).

167. W.R. Busing, *J. Chem. Phys.* **23**, 933 (1955).

168. D.T. Amm, Ph.D. Thesis, Queen's University, Canada, 1985.

169. D.R. Stull, D.L. Hildenbrand, F.L. Oetting, and G.C. Sinke, *J. Chem. Eng. Data.* **15**, 52 (1970).

170. T.J. Bastow, M.M. Elcombe, and C.J. Howard, *Solid State Commun.* **59**, 257 (1986).

171. T.J. Bastow, M.M. Elcombe, and C.J. Howard, *Solid State Commun.* **62**, 149 (1987).

172. M.P. Krobok, P.G. Johannsen, and W.B. Holzapfel, *J. Phys.: Condens. Matter.* **4**, 8141 (1992).

173. D.T. Amm, S.L. Segel, R.D. Heyding, and B.K. Hunter, *J. Chem. Phys.* **82**, 2529 (1985).

174. I.J.F. Poplett and J.A.S. Smith, *J. Chem. Soc., Faraday Trans. 2.* **77**, 235 (1981).

175. D.T. Edmonds and J.P.G. Mailer, *J. Magn. Reson.* **36**, 411 (1979).

176. D.T. Amm and S.L. Segel, *J. Chem. Phys.* **80**, 4679 (1984).

177. T.J. Bastow, *J. Magn. Reson.* **63**, 590 (1985).

178. D.T. Amm, S.L. Segel, T.J. Bastow, and K.R. Jeffrey, *J. Chem. Phys.* **84**, 1 (1986).

179. D.T. Amm, S.L. Segel, T.J. Bastow, and K.R. Jeffrey, *Z. Naturforsch.* **41a**, 305 (1986).

180. D.T. Amm, S.L. Segel, and K.R. Jeffrey, *Can. J. Phys.* **64**, 22 (1986).

181. T.J. Bastow, S.L. Segel, and K.R. Jeffrey, *Solid State Commun.* **78**, 565 (1991).

182. H.D. Lutz, J. Henning, H. Jacobs, and B. Mach, *J. Mol. Struct.* **145**, 277 (1986).

183. J. Henning, H.D. Lutz, H. Jacobs, and B. Mach, *J. Mol. Struct.* **196**, 113 (1989).

184. J.W. Otto and W.B. Holzapfel, *J. Phys.: Condens. Matter*, **7**, 5461 (1995).

185. D.M. Adams and J. Haines, *J. Phys. Chem.* **95**, 7064 (1991).

186. D.M. Adams, A.G. Christy, and J. Haines, *J. Phys. Chem.* **96**, 8173 (1992).

187. R.G. Snyder, J. Kumamoto, and J.A. Ibers, *J. Chem. Phys.* **33**, 1171 (1960).

188. C.W.F.T. Pistorius, *Z. Physik. Chem.* **65**, 51 (1969).

189. H.P. Beck and G. Lederer, *Angew. Chem. Int. Ed. Engl.* **32**, 271 (1993).

190. H.P. Beck and G. Lederer, *J. Chem. Phys.* **98**, 7289 (1993).

191. E.R. Lippincott and R. Schroeder, *J. Chem. Phys.* **23**, 1099 (1955).

192. J.S. Loveday, W.G. Marshall, R.J. Nelmes, S. Klotz, G. Hamel, and J.M. Besson, *J. Phys.: Condens. Matter.* **8**, L597 (1996).

193. M.P. Krobok and W.B. Holzapfel, *J. Phys.: Condens. Matter.* **6**, 9789 (1994).

194. T.J. Bastow, private communication, 1986.

195. Reference (31), p. 113; p. 486-490.

196. J.O. Clayton and W.F. Giauque, *J. Am. Chem. Soc.* **54**, 2610 (1932).

197. M.W. Melhuish and R.L. Scott, *J. Phys. Chem.* **68**, 2301 (1964).

198. K.R. Nary, P.L. Kuhns, and M.S. Conradi, *Phys. Rev. B.* **26**, 3370 (1982).

199. G.N. Lewis and M. Randall, Thermodynamics and the Free Energy of Chemical Substances (1st edition). McGraw-Hill Book Co., New York, 1923, p. 448.

200. P.W. Bessonette, Honours B.Sc. Thesis, Department of Chemistry, Dalhousie University, Halifax, Canada (1991).

201. H. Hayashi, S. Yoshizawa, and Y. Ito, *J. Electroanal. Chem.* **124**, 229 (1981).

202. M.W. Chase Jr., C.A. Davies, J.R. Downey Jr., D.J. Frurip, R.A. McDonald, and A.N. Syverud, JANAF Thermochemical Tables (3rd edition), *J. Phys. Chem. Ref. Data.* **14**, Suppl. #1 (1985).

203. G.E. Gibson and W.F. Giauque, *J. Am. Chem. Soc.* **45**, 93 (1923).

204. F.E. Simon and F. Lange, *Z. Phys.* **38**, 227 (1926).

205. K.K. Kelley, *J. Am. Chem. Soc.* **51**, 1400 (1929).

206. K. Adachi, H. Suga, and S. Seki, *Bull. Chem. Soc. Jpn.* **41**, 1073 (1968).

207. H Suga, *J. Chem. Thermodynamics.* **25**, 463 (1993).

208. O. Haida, T. Matsuo, H. Suga, and S. Seki, *J. Chem. Thermodynamics.* **6**, 815 (1974).

209. Y. Tajima, T. Matsuo, and H. Suga, *Nature.* **299**, 810 (1982).

210. Y. Tajima, T. Matsuo, and H. Suga, *J. Phys. Chem. Solids.* **45**, 1135 (1984).

211. T. Atake, H. Suga, and H. Chihara, *Chem. Lett.* 567 (1976).

212. T. Matsuo, H. Suga, W.I.F. David, R.M. Ibberson, P. Bernier, A. Zahab, C. Fabre, A. Rassat, and A. Dworkin, *Solid State Commun.* **83**, 711 (1992).

213. S.S. Chang, *J. Res. Nat. Bur. Stds.* **78A**, 387 (1974).

214. H. Suga and T. Matsuo, *Pure & Appl. Chem.* **61**, 1123 (1989).

215. H. Suga, *J. Chim. Phys.* **82**, 275 (1985).

216. H. Suga, *Pure & Appl. Chem.* **67**, 1815 (1995).

217. Reference (30), p. 534-540.

218. R.A. Serway, Physics for Scientists and Engineers (2nd edition). Saunders College Publishing, Toronto, 1986, p. 586.

219. C.J.F. Böttcher, Theory of Electric Polarization. Elsevier Publishing Co., Amsterdam, 1952.

220. H.A. Lorentz, Theory of Electrons. Leipzig, 1909.

221. P.W. Debye, Polar Molecules. Dover Publications, New York, 1929.

222. O.F. Mosotti, *Memorie Mat. Fis. Modena.* **24**, 49 (1850).

223. R. Clausius, Die mechanische Wärmtheorie, Vol. II, Braunschweig, 1897, p. 62.

224. L. Onsager, *J. Am. Chem. Soc.* **58**, 1486 (1936).

225. J.G. Kirkwood, *J. Chem. Phys.* **7**, 911 (1939).

226. H. Fröhlich, Theory of Dielectrics. Oxford University Press, London, 1949.

227. C.P. Smyth and W.S. Walls, *J. Chem. Phys.* **3**, 557 (1935).

228. C.P. Smyth and C.S. Hitchcock, *J. Am. Chem. Soc.* **56**, 1084 (1934).

229. W.F. Giauque and R.W. Blue, *J. Am. Chem. Soc.* **58**, 831 (1936).

230. D.C. Look, I.J. Lowe, and J.A. Northby, *J. Chem. Phys.* **44**, 3441 (1966).

231. J.H. Loehlin, P.G. Mennitt, and J.S. Waugh, *J. Chem. Phys.* **44**, 3912 (1966).

232. G. Busch, *Helv. Phys. Acta.* **11**, 269 (1938).

233. W.J. Merz, *Phys. Rev.* **76**, 1221 (1949).

234. A.R. von Hippel, Dielectrics and Waves. John Wiley and Sons, Inc., New York, 1954, p. 3-4.

235. H. Pellat, *Ann. Chim. Phys.* **18**, 150 (1899).

236. R.H. Cole, *J. Chem. Phys.* **23**, 493 (1955).

237. K.S. Cole and R.H. Cole, *J. Chem. Phys.* **9**, 341 (1941).

238. R.M. Fuoss and J.G. Kirkwood, *J. Am. Chem. Soc.* **63**, 385 (1941).

239. D.W. Davidson and R.H. Cole, *J. Chem. Phys.* **18**, 1417 (1950).

240. D.W. Davidson and R.H. Cole, *J. Chem. Phys.* **19**, 1484 (1951).

241. C.P. Smyth and C.S. Hitchcock, *J. Am. Chem. Soc.* **54**, 4631 (1932).

242. S. Kawada, *J. Phys. Soc. Jpn.* **44**, 1881 (1978).

243. S. Kawada and H. Dohata, *J. Phys. Soc. Jpn.* **54**, 477 (1985).

244. S. Kawada, *J. Phys. Chem. Solids.* **50**, 1177 (1989).

245. T. Matsuo, H. Suga, and S. Seki, *Bull. Chem. Soc. Jpn.* **41**, 583 (1968).

246. H. Suga, T. Matsuo, and S. Seki, *Bull. Chem. Soc. Jpn.* **38**, 1115 (1965).

247. T. Shimada, T. Matsuo, H. Suga, and F. Lüty, *J. Chem. Phys.* **85**, 3530 (1986).

248. W. Dultz, *Solid State Commun.* **15**, 595 (1974).

249. M. Sugisaki, T. Matsuo, H. Suga, and S. Seki, *Bull. Chem. Soc. Jpn.* **41**, 1747 (1968).

250. Y. Kondo, D. Schoemaker, and F. Lüty, *Phys. Rev. B.* **19**, 4210 (1979).

251. F. Lüty and J. Ortiz-Lopez, *Phys. Rev. Lett.* **50**, 1289 (1983).

252. See, for example, reference (9), p. 50.

253. D.C. Wallace, Thermodynamics of Crystals. John Wiley and Sons, New York, 1972, p. 7.

254. T.L. Hill, An Introduction to Statistical Thermodynamics. Addison-Wesley Publishing Co., London, 1960, Ch. 5.

255. A. Einstein, *Ann. Physik.* **22**, 180 (1907).

256. P. Debye, *Ann. Physik.* **39**, 789 (1912).

257. M. Fukai, A. Inaba, T. Matsuo, and H. Suga, *Solid State Commun.* **87**, 939 (1993).

258. G.K. White, Experimental Techniques in Low-Temperature Physics (3rd edition). Clarendon Press, Oxford, 1979, p. 276.

259. C.Y. Ho, editor, Specific Heat of Solids. Hemisphere Publishing Co., New York, 1988, p. 73-4.

260. W. Nernst and F.A. Lindemann, *Z. Elektrochem.* **17**, 817 (1911).

261. M.A. White, Thermal Analysis and Calorimetry Methods. Ch. 4 of reference (29), p. 179, and references cited therein.

262. S.C. Mraw and D.F. Naas, *J. Chem. Thermodyn.* **11**, 567 (1979).

263. J.E. Callanan, K.M. McDermott, R.D. Weir, and E.F. Westrum, Jr., *J. Chem. Thermodyn.* **24**, 233 (1992).

264. E.F. Westrum, Jr., *J. Thermal Anal.* **14**, 5 (1978).

265. E. Gmelin, *Thermochim. Acta.* **29**, 1 (1979).

266. T. Matsuo, *Thermochim. Acta.* **163**, 57 (1990).

267. G.N. Lewis and M. Randall, Thermodynamics (2nd edition). McGraw-Hill Book Co., New York, 1961, p. 64-65.

268. Reference (258), Ch. 4.

269. M.J.M. Van Oort and M.A. White, *Rev. Sci. Instrum.* **58**, 1239 (1987).

270. M. Sorai, K. Kaji, and Y. Kaneko, *J. Chem. Thermodynamics.* **24**, 167 (1992).

271. Z. Tan, G. Sun, Y. Sun, A. Yin, W. Wang, J. Ye, and L. Zhou, *J. Thermal Anal.* **45**, 59 (1995).

272. Y. Ogata, K. Kobayashi, T. Matsuo, and H. Suga, *J. Phys. E: Sci. Instrum.* **17**, 1054 (1984).

273. T. Matsuo and H. Suga, *Thermochim. Acta.* **88**, 149 (1985).

274. M. Oguni, K. Watanabe, T. Matsuo, H. Suga, and S. Seki, *Bull. Chem. Soc. Jpn.* **55**, 77 (1982).

275. O. Yamamuro, M. Oguni, T. Matsuo, and H. Suga, *Bull. Chem. Soc. Jpn.* **60**, 1269 (1987).

276. M.J.M. Van Oort, Ph.D. Thesis, Dalhousie University, Halifax, Canada (1987).

277. T.N.E. Greville, Theory and Applications of Spline Functions. Academic Press, New York, 1969.

278. L.L. Schumaker, Spline Functions: Basic Theory. John Wiley and Sons, New York, 1981.

279. W.H. Press, B.P. Flannery, S.A. Teukolsky, and W.T. Vetterling, Numerical Recipes (FORTRAN version). Cambridge University Press, Cambridge, 1989, p. 86-89.

280. J.C. Sprott, Numerical Recipes: Routines and Examples in BASIC. Cambridge University Press, Cambridge, 1991, p. 43.

281. Reference (258), p. 268.

282. F. Gronvold, *J. Thermal Anal.* **13**, 419 (1978).

283. K. Clusius and L. Schachinger, *Z. Angew. Physik.* **4**, 442 (1952).

284. R. Hultgren, R.L. Orr, P.D. Anderson, and K.K. Kelley, Selected Values of Thermodynamic Properties of Metals and Alloys. John Wiley and Sons, New York, 1963, p. 133-7.

285. E.F. Westrum, Jr., C. Chou, D.W. Osborne, and H.E. Flotow, *Cryogenics*. **7**, 43 (1967).

286. D.R. Lide, editor, CRC Handbook of Chemistry and Physics (71st edition). CRC Press Inc., Boca Raton, 1990-1991, p. 5-65.

287. R. Cohen-Adad, M.T. Saugier, and J. Said, *Rev. Chim. Miner.* **10**, 631 (1973).

288. Y.S. Touloukian, R.W. Powell, C.Y. Ho, and P.G. Klemens, Thermophysical Properties of Matter. Plenum Press, New York, 1970, Vol. 1, p. 561.

289. L. Hartshorn, Radio-Frequency Measurements By Bridge and Resonance Methods. Chapman and Hall Ltd., London, 1941, p. 38-40.

290. A.F. Kip, Fundamentals of Electricity and Magnetism (2nd edition). McGraw-Hill Book Co., New York, 1969, p. 193-4.

291. W.D. Cooper, Electronic Instrumentation and Measurement Techniques. Prentice-Hall, Inc., New Jersey, 1970, p. 181.

292. Reference (289), Chapter II.

293. C. Kittel, Introduction to Solid-State Physics (4th edition). John Wiley and Sons, New York, 1971, p. 460.

294. F. Franks, editor, Water: A Comprehensive Treatise. Plenum Press, New York, 1972, Vol. 2, p. 431.

295. Reference (289), Chapter XII.

296. N.E. Hill, W. E. Vaughan, A.H. Price, and M. Davies, Dielectric Properties and Molecular Behaviour, Van Nostrand Reinhold Co., London, 1969, Chapter 2.

297. S.R. Gough. E. Whalley, and D.W. Davidson, *Can. J. Chem.* **46**, 1673 (1968).

298. S.R. Gough, *Can. J. Chem.* **50**, 3046 (1972).

299. M.G. Broadhurst and A.J. Bur, *J. Res. Natl. Bur. Stds.* **69C**, 165 (1965).

300. E.W. Greenfield, *Rev. Sci. Instrum.* **13**, 489 (1942).

301. A.H. Scott and H.L. Curtis, *J. Res. Natl. Bur. Stds.* **22**, 747 (1939).

302. Reference (289), p. 104-7.

303. D.G.W. Goad and H.J. Wintle, *Meas. Sci. Technol.* **1**, 965 (1990).

304. R.N. Work, *Rev. Sci. Instrum.* **26**, 1171 (1955).

305. A.J. Nanassy, *Rev. Sci. Instrum.* **36**, 756 (1965).

306. S.R. Gough, *J. Phys. E: Sci. Instrum.* **15**, 530 (1982).

307. R.G. Heydon, *J. Phys. E: Sci. Instrum.* **17**, 377 (1984).

308. O. Yamamuro, T. Matsuo, and H. Suga, *J. Incl. Phenom.* **8**, 33 (1990).

309. A.H. Scott and W.P. Harris, *J. Res. Natl. Bur. Stds.* **65C**, 101 (1961).

310. R.D. McCammon and R.N. Work, *Rev. Sci. Instrum.* **36**, 1169 (1965).

311. S.P. Tay and S. Walker, *J. Chem. Phys.* **63**, 1634 (1975).

312. Reference (289), p. 192.

313. J.G. Powles and C. P. Smyth, in Physical Methods of Organic Chemistry (3rd edition). A. Weissberger, editor, Interscience Publishers, Inc., New York, 1959, Vol. I, Ch. XXXVIII, p. 2570.

314. M. Honda, The Impedance Measurement Handbook. Yokogawa-Hewlett-Packard Ltd., 1989, p. 3-1.

315. G.K. White, *Cryogenics.* **1**, 151 (1961).

316. R. Pott and R. Schefzyk, *J. Phys. E: Sci. Instrum.* **16**, 444 (1983).

317. Y.S. Touloukian and E.H. Buyco, Thermophysical Properties of Matter. Plenum Press, New York, 1970, Vol. 4, p. 348.

318. Reference (219), p. 184.

319. D.E. Gray, editor, American Institute of Physics Handbook (3rd edition). McGraw-Hill Book Co., New York, 1972, p. 5-131.

320. I.S. Grigoriev and E.Z. Meilikhov, editors, Handbook of Physical Quantities. CRC Press, Boca Raton, 1997, p. 675.

321. K.F. Young and H.P.R. Frederikse, *J. Phys. Chem. Ref. Data.* **2**, 313 (1973).

322. D.R. Lide, editor, CRC Handbook of Chemistry and Physics (78th edition). CRC Press, Boca Raton, 1997-1998, p. 12-48.

323. F.C. Brown, The Physics of Solids. W.A. Benjamin, Inc., New York ,1967, Chapter 8, p. 227.

324. C.P. Smyth, Dielectric Behaviour and Structure. McGraw-Hill Book Co., New York, 1955, p. 135-9.

325. V.V. Daniel, Dielectric Relaxation. Academic Press Inc., London, 1967, p. 176.

326. Reference (323), Chapter 10, p. 295.

327. Reference (30), Chapter 13, p. 452.

328. Reference (30), Chapter 9, p. 318.

329. Reference (234), p. 228

330. R.W. Dreyfus, *Phys. Rev.* **121**, 1675 (1961).

331. R.J. Meakins, *Prog. Dielect.* **3**, 151 (1961).

332. R.G. Breckenridge, *J. Chem. Phys.* **18**, 913 (1950).

333. Y. Haven, *J. Chem. Phys.* **21**, 171 (1953).

334. J.S. Dryden and R.J. Meakins, *Disc. Faraday Soc.* **23**, 39 (1957).

335. T. Ninomiya, *J. Phys. Soc. Jpn.* **15**, 1601 (1960).

336. P. Varotsos and D. Miliotis, *J. Phys. Chem. Solids.* **35**, 927 (1974).

337. J.S. Dryden and D.A.A.S. Narayana Rao, *J. Chem. Phys.* **25**, 222 (1956).

338. R.G. Breckenridge, *J. Chem. Phys.* **16**, 959 (1948).

339. B.W. Henvis, J.W. Davisson, and E. Burstein, *Phys. Rev.* **82**, 774 (1951).

340. Reference (296), p. 58-60, 282-4.

341. J.C. Anderson, Dielectrics. Reinhold Publishing Co., New York, 1964, p. 52, 92-7.

342. L.K.H. van Beek, *Prog. Dielect.* **7**, 69 (1967).

343. J.C. Maxwell, Electricity and Magnetism (3rd edition). Oxford University Press, London, 1892, p. 452.

344. K.W. Wagner, *Arch. Elektrotechn.* **2**, 371 (1914).

345. L. Hartshorn and J.A. Saxton, *Handb. Phys.* **16**, 706 (1958).

346. Reference (219), p. 415-20.

347. C.J.F. Böttcher and P. Bordewijk, Theory of Electric Polarization (2nd edition). Elsevier Scientific Publishing Co., Amsterdam, 1978, p. 476-87.

348. J.A. Reynolds and J.M. Hough, *Proc. Phys. Soc.* **70B**, 769 (1957).

349. D. Polder and J.H. Van Santen, *Physica.* **12**, 257 (1946).

350. D. Halliday and R. Resnick, Fundamentals of Physics. John Wiley and Sons, Inc., New York, 1970, p. 495.

351. J.W. Rayleigh, *Phil. Mag.* **34**, 481 (1892).

352. C.J.F. Böttcher, *Rec. trav. chim.* **64**, 47 (1945).

353. D.A.G. Bruggeman, *Ann. Physik.* **24**, 636 (1935).

354. H. Looyenga, *Physica.* **31**, 401 (1965).

355. W. Niesel, *Ann. Physik.* **10**, 336 (1952).

356. O. Wiener, *Abh. math. phys. Kl. Sächs. Akad. Wiss.* **32**, 509 (1912).

357. C.A.R. Pearce, *Brit. J. Appl. Phys.* **6**, 358 (1955).

358. W.I. Higuchi, *J. Phys. Chem.* **62**, 649 (1958).

359. J.H. Bruce, *Trans. Far. Soc.* **35**, 706 (1939).

360. D.C. Dube and R. Parshad, *J. Phys. D.* **3**, 677 (1970).

361. R.C. Weast, editor, CRC Handbook of Chemistry and Physics (61st edition). CRC Press, Inc., Boca Raton, 1980-1981, p. B-73.

362. See, for example, R.S. Burington and C.C. Torrance, Higher Mathematics (1st edition). McGraw-Hill Book Co., New York, 1939, p. 564-5.

363. F. Simon, C. von Simson, and M. Ruhemann, *Z. Physik. Chem.* **129**, 339 (1927).

364. Reference (31), p. 311-328, and references cited therein.

365. G. Shirane, E. Sawaguchi, and Y. Takagi, *J. Phys. Soc. Jpn.* **6**, 208 (1951).

366. H.D. Megaw, Ferroelectricity in Crystals. Methuen and Co., Ltd., London, 1957, p. 111.

367. C.T. Anderson, *J. Am. Chem. Soc.* **55**, 3621 (1933).

368. J.H. Burns and M.A. Bredig, *J. Chem. Phys.* **25**, 1281 (1956).

369. H. Bode and E. Voss, *Z. Elektrochem.* **60**, 1053 (1956).

370. F. Dachille and R. Roy, *Nature.* **186**, 34 (1960).

371. M. Senna and H. Kuno, *J. Am. Ceram. Soc.* **54**, 259 (1971).

372. J.C. Jamieson, *J. Chem. Phys.* **21**, 1385 (1953).

373. P.G. Fox, *J. Mater. Sci.* **10**, 340 (1975).

374. M.A. Bredig, *J. Phys. Chem.* **46**, 801 (1942).

375. R.C. Ray, *Proc. R. Soc.* **A102**, 640 (1923).

376. I. Tsukushi, O. Yamamuro, and T. Matsuo, *Solid State Commun.* **94**, 1013 (1995).

377. I. Tsukushi, O. Yamamuro, and T. Matsuo, *Prog. Theor. Phys. Suppl.* **126**, 89 (1997).

378. C.C. Koch, O.B. Cavin, C.G. McKamey, and J.O. Scarbrough, *Appl. Phys. Lett.* **43**, 1017 (1983).

379. E. Hellstern and L. Schultz, *Appl. Phys. Lett.* **49**, 1163 (1986).

380. W. Press, J. Eckert, D.E. Cox, C. Rotter, and W. Kamitakahara, *Phys. Rev. B.* **14**, 1983 (1976).

381. C.W. Garland, K.J. Lushington, and R.C. Leung, *J. Chem. Phys.* **71**, 3165 (1979).

382. A. Hüller, *Faraday Discuss. Chem. Soc.* **69**, 66 (1980).

383. J.W. Stewart, *J. Phys. Chem. Solids.* **12**, 122 (1959).

384. M.S. Constantino and W.B. Daniels, *J. Chem. Phys.* **62**, 764 (1975).

385. A.R. Ubbelohde, *Proc. R. Soc.* **A173**, 417 (1939).

386. A.R. Ubbelohde and K.J. Gallagher, *Acta Cryst.* **8**, 71 (1955).

387. R.G. Snyder and J.A. Ibers, *J. Chem. Phys.* **36**, 1356 (1962).

388. W.C. Hamilton and J.A. Ibers, *Acta Cryst.* **16**, 1209 (1963).

389. W.C. Hamilton and J.A. Ibers, Hydrogen Bonding in Solids. W.A. Benjamin, Inc., New York, 1968, p. 104, and references cited therein.

390. H.D. Megaw, *Nature.* **134**, 900 (1934).

391. K.J. Gallagher in Hydrogen Bonding. D. Hadzi, editor, Pergamon Press, London, 1959, p. 45.

392. T. Matsuo, Y. Tajima, and H. Suga, *J. Phys. Chem. Solids.* **47**, 165 (1986).

393. A.C. Legon and D.J. Millen, *Chem. Phys. Lett.* **147**, 484 (1988).

394. A.R. Ubbelohde, *Trans. Far. Soc.* **32**, 525 (1936).

395. R.E. Rundle, *J. de Phys.* **25**, 487 (1964).

396. S.N. Vinogradov and R.H. Linnell, Hydrogen Bonding. Van Nostrand Reinhold Co., New York, 1971, p. 124.

397. H.D. Lutz and H. Möller, *J. Mol. Struct.* **295**, 147 (1993).

398. H.D. Lutz, K. Beckenkamp, and H. Möller, *J. Mol. Struct.* **322**, 263 (1994).

399. C.E. Nordman and W.N. Lipscomb, *J. Chem. Phys.* **19**, 1422 (1951).

400. T.R. Singh and J.L. Wood, *J. Chem. Phys.* **50**, 3572 (1969).

401. Reference (42), p. 163.

402. Reference (253), p. 26.

403. S.N. Vaidya and G.C. Kennedy, *J. Phys. Chem. Solids.* **32**, 951 (1971).

404. M.T. Dove, Introduction to Lattice Dynamics. Cambridge University Press, Cambridge, 1993, p. 72.

405. A. Giessler, G. Schaack, and H. Bleif, *Phys. Stat. Sol.*(b) **104**, 151 (1981).

406. I. Kanesaka, M. Tsuchida, and K. Kawai, *J. Raman Spectrosc.* **13**, 253 (1982).

407. R.A. Smith, Wave Mechanics of Crystalline Solids (2nd edition). Chapman and Hall, Ltd., London, 1969, p. 342.

408. E.S.R. Gopal, Specific Heats at Low Temperatures, Plenum Press, New York, 1966, p. 102.

409. Reference (259), p. 64.

IMAGE EVALUATION TEST TARGET (QA-3)

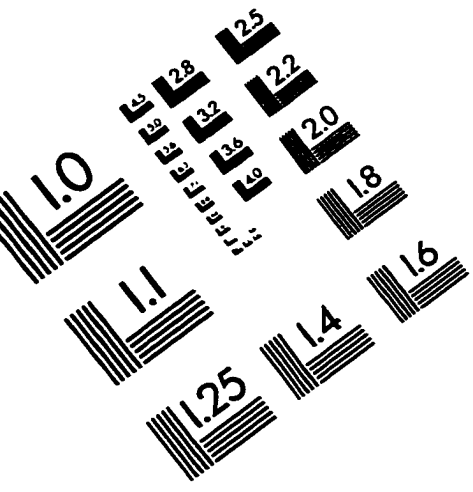

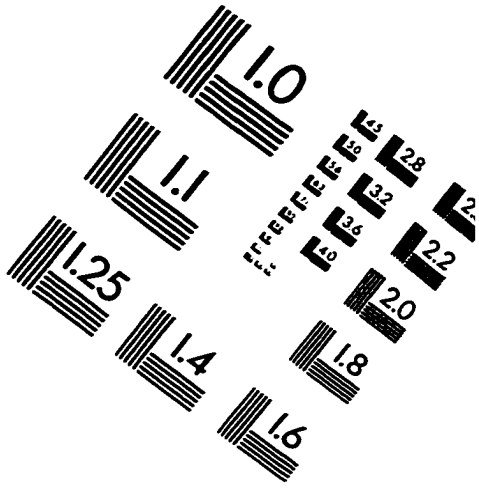

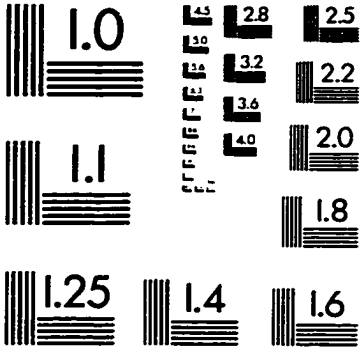

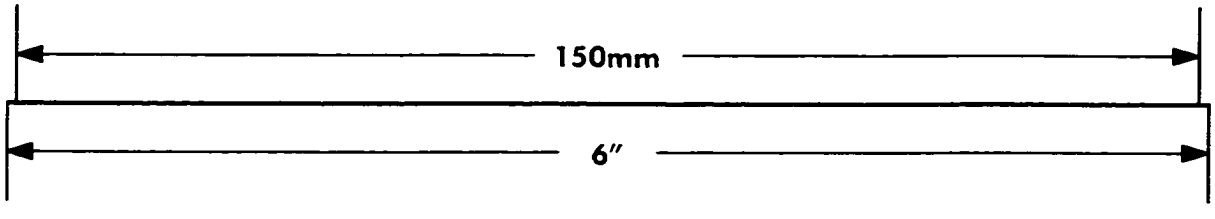

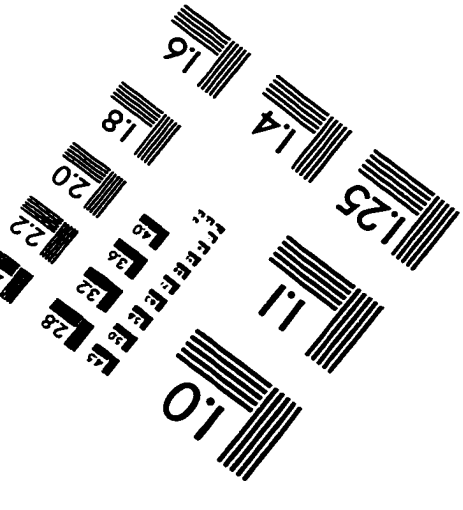

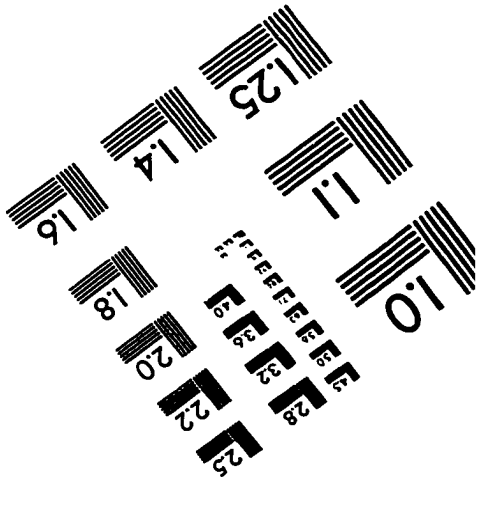

APPLIED IMAGE, Inc
1653 East Main Street
Rochester, NY 14609 USA
Phone: 716/482-0300
Fax: 716/288-5989